CO_2 methanation on Ni-Fe based catalysts: Mechanistic and structured reactor study

by

Huong Lan Huynh

Thesis submitted in fulfilment of
the requirements for the degree of
PHILOSOPHIAE DOCTOR
(PhD)

Faculty of Science and Technology
Department of Energy and Petroleum Engineering
2021

University of Stavanger
NO-4036 Stavanger
NORWAY
www.uis.no

ISBN: 978-82-8439-030-7
ISSN:1819-1387
PhD: Thesis UiS No. 607

Acknowledgements

To begin with, I would like to express my gratitude to my supervisor, Professor Zhixin Yu, for giving me the opportunity to conduct my PhD study. Without your thorough guidance and continuous encouragement, I would have not completed my PhD thesis.

I would like to thank all my lab-mate, especially my senior fellow PhD candidates Dori Kalai and Kristian Stangeland who have been my great mentors since I joined the Catalysis group. My experiments would not be successful without your pioneering work. I also thank the bachelor and master students Anderson Camacho, Sarah Shariff and Vladislav Volkov, and our new lab member PhD candidate Song Lu, I highly appreciate your assistance in the experimental works.

To all the staff and engineers at TN-IEP and the workshop, I am extremely grateful to receive the massive support throughout my three-year PhD work. My special thanks go to Hilde Jonsbråten, Kim Vorland, Jorunn Vrålstad, Caroline Einvik, Emil Kristiansen, Johannes Jensen, Caroline Rudd, Sivert Drangeid, Reidar Korsnes, Jon Arne Evjenth, Thomas Olsen, Dagfinn Sleveland, Inger Johanne Olsen, Ola Ketil Siqveland and others for your expertise, for always being available and for your good humor that made my PhD work so much easier. To Wakshum Tucho for helping me with the microscopy analysis. To all my friends at UiS-KE building for all the joyful moments we shared.

To my collaborators, Jie Zhu and Guanghui Zhang (Dalian, China) for your help on the advanced spectroscopy analysis; and Yongli Shen (Tianjin, China) for the great support on DFT calculations.

To my life partner Jonatan Byman, for the mental health support and for being a patient graphic illustrator. Finally, to my family in Vietnam, the Gundersen, the Le-Karvonen, the Byman, and all my close friends for their unconditional love and support.

Abstract

The clean energy transition towards renewable energy sources has increased the need for large-scale and long-term energy storage systems. Power-to-Gas concept offers the solution to convert surplus electrical power into gaseous energy carriers. Via catalytic CO_2 methanation, methane (CH_4) or synthetic natural gas (SNG) can be produced from renewable H_2 and captured CO_2. SNG is an effective energy carrier with high heating value, and is one of the most promising chemical compounds for energy storage. Although CO_2 methanation is a mature reaction, rational design and synthesis of new catalytic materials have always been necessary for the improvement of industrial process efficiency.

Based on recent advances in the development of catalysts and reactors for CO_2 methanation, bimetallic Ni-Fe catalysts have been employed throughout this work. Herein, powder particle Ni-Fe/(Mg,Al)O_x catalysts were prepared from hydrotalcite (layered double hydroxides, LDHs) materials via rapid coprecipitation method. Ni-Fe alloy supported catalysts exhibited higher activity in CO_2 methanation at a low temperature of 250-350 ºC than Ni supported catalysts, especially at a Fe/Ni ratio of 0.25. By combining in-situ spectroscopy studies and density functional theory calculations, the promoting effect of Fe was revealed. A moderate addition of Fe alloying with Ni facilitated CO_2 activation via hydrogenation to formate (*HCOO) intermediates and lowered the overall energy barrier for CH_4 formation. The reaction mechanism was proposed that $*CO_2 \rightarrow *HCOO \rightarrow *HCO \rightarrow *CH \rightarrow *CH_4$ was the most energetically favorable pathway for CO_2 methanation over Ni-based catalysts.

Subsequently, the effect of total metal concentration on the physico-chemical properties and catalytic behavior of Ni-Fe/(Mg,Al)O_x catalysts was investigated. By increasing metal concentration, a larger amount of

catalyst mass per batch was produced while the catalytic activity was maintained. Hence, it is very promising possible for the large-scale production of earth-abundant Ni-Fe supported catalysts for commercial applications of CO_2 methanation.

For the implementation of laboratory research into industrial practice, monolithic catalyst is commonly used because of the low pressure drop, the tunable thickness of catalytic layer, excellent heat and mass transfer and high throughput (high gas flow rates) compared to that of conventional fixed-bed catalysts. The preparation method of Ni-Fe catalysts on ceramic honeycomb substrates was developed. By urea hydrolysis, NiFe-CO_3 LDHs layers were in-situ grown on the washcoated substrate, which subsequently derived to form the final Ni-Fe monolithic catalyst for CO_2 methanation. Alumina colloidal solution was found to be a better washcoating material than silica. It was also found that the best performing monolithic catalysts were prepared at a metal concentration of 0.25 M.

Due to the exothermic nature of CO_2 methanation, the reactor development for better heat management has been focused on. Generally, the formation of hot-spots in fixed-bed reactors could reduce CH_4 yield, accelerate catalyst deactivation, and potentially cause thermal runaway. However, hot-spots could also be utilized to achieve outstanding CO_2 methanation performance in monolithic reactors at low temperatures and high gas rates. Temperature profiles were examined by experimental observation and computational fluid dynamic simulation, and hot-spot formation was identified. Due to high thermal conductivity, hot-spots were transferred along the reactor bed, thus could boost the CO_2 conversion of low-activity monolithic catalysts. A strategic bed packing configuration combining low and high activity monolith was proposed. A high methane yield of ~83%, less severe hot-spot formation and stable CO_2 methanation performance at high gas rates was achieved.

List of Publications

I. CO_2 Methanation
H. L. Huynh and Z. Yu
Chapter 9 of Chemical Valorization of Carbon Dioxide (Royal Society of Chemistry book)
Invited book chapter, to be submitted.

II. CO_2 Methanation on Hydrotalcite-Derived Catalysts and Structured Reactors: A Review
H. L. Huynh and Z. Yu
Energy Technology **2020**, *8*, 1901475
DOI: 10.1002/ente.201901475

III. Promoting effect of Fe on supported Ni catalysts in CO_2 methanation by in situ DRIFTS and DFT study
H. L. Huynh, J. Zhu, G. Zhang, Y. Shen, W. M. Tucho, Y. Ding, and Z. Yu
Journal of Catalysis **2020**, *392*, 266-277
DOI: 10.1016/j.jcat.2020.10.018

IV. Synthetic natural gas production from CO_2 and renewable H_2: Towards large-scale production of Ni-Fe alloy catalysts for commercialization
H. L. Huynh, W. M. Tucho, X. Yu, and Z. Yu
Journal of Cleaner Production **2020**, 121720
DOI: 10.1016/j.jclepro.2020.121720

V. Structured NiFe catalysts derived from in-situ grown layered double hydroxides on ceramic monolith for CO_2 methanation
H. L. Huynh, W. M. Tucho, and Z. Yu
Green Energy & Environment **2020**, *5*, 423-432

DOI: 10.1016/j.gee.2020.09.004

VI. Bed packing configuration and hot-spot utilization for low-temperature CO_2 methanation on monolithic reactor
H. L. Huynh, W. M. Tucho, Q. Shen and Z. Yu
Chemical Engineering Journal **2022**, *428*, 131106
DOI: 10.1016/j.cej.2021.131106

This dissertation is based on the above six publications which are referred to in the text as Paper I-VI.

Conference Presentations and Proceedings

I. **H. L. Huynh** and Z. Yu. CO_2 methanation over Ni-Fe alloy catalysts: an in-situ study. *Oral presentation* at the Norwegian Catalysis Symposium 2019, Bergen, Norway, 4-6 December 2019.

II. **H. L. Huynh** and Z. Yu. Power-to-Gas technology: Large-scale preparation of Ni-Fe supported catalysts for CO_2 methanation. *Oral presentation* at the International Conference on Energy, Ecology and Environment (ICEEE) 2019, Stavanger, Norway, 23-26 July 2019.

III. **H. L. Huynh** and Z. Yu. Low temperature CO_2 methanation over Ni-Fe hydrotalcite-derived catalysts synthesized by rapid coprecipitation. *Poster presentation* at the 17th International Conference on Carbon Dioxide Utilization (ICCDU) 2019. Aachen, Germany, 23-27 June 2019.

Table of Contents

Table of Figure

List of Tables

1 Introduction

Climate change concerns are growing bigger every year due to the continuous and ever-increasing emissions of carbon dioxide (CO_2), mostly as waste material from fossil-based energy systems. Humanity has always relied on fossil fuels as the primary energy sources. However, to achieve the ambitious goal of reducing carbon emissions, our energy system is inevitably experienced a clean transition from fossil fuels (i.e., coal, oil, and natural gas) to renewable energy sources ("renewables" hereafter).

1.1 Clean energy transition towards renewables

The global energy system has undergone considerable changes from using coal and traditional biomass to natural gas, nuclear power, and renewables, following the wave of technological innovations. Since 2000, there has been a surge in investment in renewables for power generation, particularly in Europe, United States, and China. Because electricity production and heat generation based on fossil fuels emit the largest amount of CO_2, accounting for 42% of the global CO_2 emissions, the transformation of the power sector has been focused.[1]

Renewables-based power generation technologies have significantly accelerated the clean energy transition. Since the late 1990s, wind power has been invested and now accounts for over 5% of the global power. The development of solar photovoltaic (PV) was slower, but it has sharply increased in recent years. In 2019, over 710 TWh of electricity was produced by solar PV, attributed to 2.5% of global electricity demand. Significant declines in capital cost started from 2010 could explain the rapid growth of wind and solar PV technologies.[2]

In Europe, the power sector is shifting towards renewables as can be seen by the increasing share of wind, solar PV and biomass sources in the gross electricity production from 20% in 2010 to 32% in 2018. It is

expected that half of the electricity in the European power sector will be generated by renewables in 2030.[3]

1.2 Power-to-Gas technology

Renewables-based power generation encounters one main problem - volatile production - due to the intermittency of wind or solar power. Different energy policy road maps in different regions (e.g., Germany, Denmark, Great Britain, or Spain) have created more difficulties to balance the strong fluctuations of power production. Future climatic prognosis systems may be able to predict electricity production, however, the integration problem has not completely been solved. On the other hand, it is not sustainable if the system could be shut-down when the renewables supply was excessive.[4]

Another solution has been proposed that surplus electricity can be stored for future use in energy storage systems such as pumped hydro storage, batteries, supercapacitors, compressed air, flywheels, or in the chemical form of synthetic natural gas via Power-to-Gas (PtG) technology.[5] Among them, PtG offers large energy capacity, high volumetric density, system benefits, flexible site-specific modifiability, decentralized application possibility and prolonged storage duration (from days to months).[4] To provide a safe and cheap power supply in a long term, renewables-based power generation stations should be simultaneously coordinated with available grid and storage facilities. The development of a chemical energy storage system via PtG technology is therefore of great importance.

The PtG concept, as illustrated in Fig. 1.1, is to convert excessive renewable electricity into a gaseous chemical energy carrier. In the first stage, hydrogen (H_2) is produced by water electrolysis. In the second stage, the green H_2 reacted with external CO_2 sources to produce methane (CH_4) via methanation reaction.[5-6] The produced methane is called synthetic or substitute natural gas (SNG), an effective energy

carrier with high heating value. With the existing infrastructure including pipeline networks, storage facilities, and filling stations, SNG can be distributed and stored without additional expenses. This is an advantage of using SNG as an energy carrier compared to hydrogen, for instance.[6]

On the one hand, PtG technology can converge the value chains of both gas and electricity sectors into one energy system, as shown in Fig. 1.1, allowing flexible handling and storage of surplus renewable electricity.[7] On the other hand, the process also tackles greenhouse gases emission by large-scale recycling of captured CO_2. The produced SNG by PtG process can also be considered as renewable natural gas with a low carbon footprint, which could be a great contributor to the future decarbonizing and net zero energy system.[8]

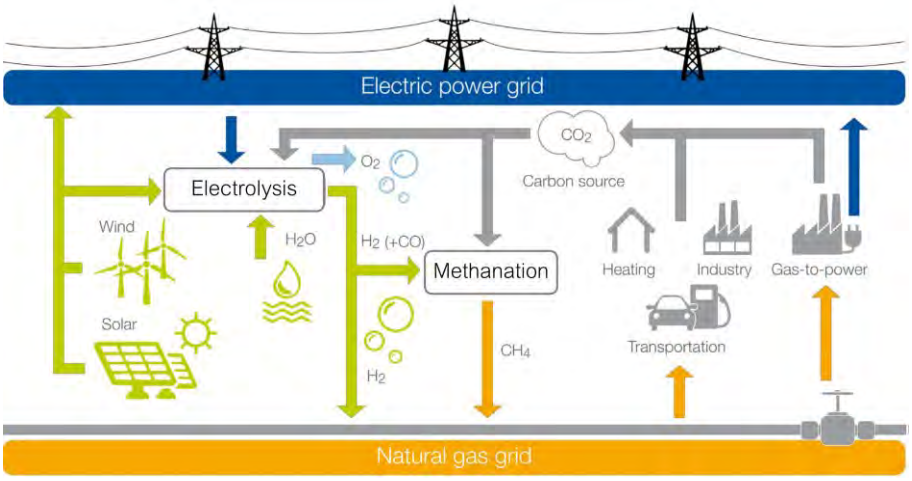

Figure 1.1 The Power-to-Gas concept with electrolysis and methanation unit.[7]

The PtG concept was initiated by Japanese researchers in 1994,[9] although other sources[10] stated that the first project "continuous CH_4 production from H_2 and CO_2" based on biological methanation was located at Higashi-Hiroshima (Japan) in 1988. Nevertheless, the current leader in PtG technologies is Europe, particularly Germany, Denmark

and Switzerland.[11] One of the largest existing plants is the Audi e-gas plant in Werlte (Germany), under operation since 2013, where H_2 is produced from alkaline electrolyzers (6 MW) powered by an offshore wind park in the North Sea.[12] Currently, the drawback of PtG technology is the high costs (mainly at the electrolysis unit). For the methanation unit, catalytic methanation is preferred due to its scale-up capability and lower costs. However, improvements are still needed in the development of catalyst and reactor design for better heat management to enhance the overall energy efficiency of the PtG process.

1.3 The revival of CO_2 methanation

CO_2 methanation, was discovered in 1902 by the French chemist and Nobel laureate Paul Sabatier,[13-14] thus sometimes it was also called the Sabatier reaction (Eq. 1.1).

$$CO_2 + 4H_2 \leftrightarrow CH_4 + 2H_2O \qquad \Delta H_{298K} = -165.0 \text{ (kJ/mol)} \qquad (1.1)$$

CO_2 methanation has been merely used to remove catalyst-poisoning traces of CO_2 and CO from H_2-rich gas for ammonia production in the 1950s.[15] But later, the Sabatier reaction has become important for SNG production. Traditionally, SNG is produced from coke oven gas, or syngas from coal or wood, or biomass.[16] However, due to the oil crisis of the 1970s, considerable efforts had been put into the application of CO_2 (and CO) methanation for SNG synthesis. In recent years, the interest in catalytic CO_2 methanation has significantly grown particularly because it is a part of the PtG process. Moreover, the Sabatier reaction has also been employed for space exploration missions via applications such as propellant production on Mars or air revitalization system.[17-19]

Nickel (Ni) was first found as the catalyst for the Sabatier reaction. Up to now, despite noble metals (e.g., ruthenium) with excellent activity, the earth-abundant Ni-based catalysts have always been the most attractive active metal of choice for industrial applications due to its affordable

price. However, Ni-based catalysts exhibited poor catalytic activity at temperatures below 350 °C.[14] While the reaction is thermodynamically favoured at low temperatures, kinetic limitations hindered high conversion of CO_2 and CH_4 yield. Tremendous efforts have been devoted to improving the activity, selectivity and stability of Ni-based catalysts for CO_2 methanation, especially at low temperatures.

1.4 Objectives and scope of the study

This thesis is a continuation of such efforts with an emphasis on the rational design and synthesis of Ni-Fe based catalysts and reactors for CO_2 methanation.

A comprehensive overview of reaction thermodynamics, mechanisms, kinetics, catalysts and reactors for CO_2 methanation (**Paper I**) together with the current research on Ni-based catalysts derived from hydrotalcite (HT) materials and structured reactors have been presented (**Paper II**). Bimetallic catalysts were selected as the main approach to enhance the catalytic performance of Ni-based catalysts. By taking advantage of density functional theory (DFT) calculations, Fe alloying with Ni was identified as an effective catalyst to substitute noble-metal catalysts for CO_2 methanation.

As the promoting effect of Fe on Ni-based catalysts was highly dependent on the amount of Fe addition, a series of Ni-Fe catalysts was prepared at different Fe/Ni ratios, which was derived from hydrotalcite (HT) materials (also called layered double hydroxides, LDHs). The catalysts were extensively studied by different ex-situ and in-situ characterization methods combined with DFT calculations. The promoting effect of Fe on Ni-based catalysts for CO_2 methanation is revealed. The reaction mechanism of the Ni-Fe catalytic system is also elucidated based on experimental and theoretical observations (**Paper III**).

The preparation method of Ni-Fe supported catalysts was further developed by studying the effect of metal concentration on the catalytic performance. The catalysts were prepared by rapid coprecipitation at different metal concentrations from 0.25 M to 2.5 M. Physiochemical properties and catalytic behaviors of all catalysts were investigated. The results allow us to evaluate the possibility of catalyst production on a large scale for industrial applications (**Paper IV**).

As hot-spot formation has always been the main challenge for the exothermic Sabatier reaction, reactor development is very important. The structured reactor has emerged as a promising concept for CO_2 methanation at industrial relevant conditions. Monolithic catalysts embedded with Ni-Fe active sites were prepared by a novel preparation method. To improve the surface area of the ceramic honeycomb substrate, a colloidal solution (alumina or silica) was used. The active Ni-Fe sites were derived from in-situ grown LDHs materials via urea hydrolysis on the washcoated substrates. The catalytic activity for CO_2 methanation was evaluated in a structured reactor (**Paper V**).

Subsequently, different metal concentrations were used to optimize the catalyst loading and to find the best performing Ni-Fe monolithic catalyst. Experimental studies on the thermal profile of monolithic reactor during reaction were carried out and verified by computational fluid dynamics (CFD) simulations. Different bed packing strategies, different gas rates and different input temperatures were applied to understand the effect of catalytic activity on the thermal profiles. Although hot-spot formation is undesirable, the potential of utilizing hot-spot to boost the conversion of low-activity catalysts has also been demonstrated **(Paper VI)**.

2 Literature review

In this chapter, fundamental principles and the current state of research on CO_2 methanation catalysts and reactors are reviewed as the relevant background of the present work.

2.1 Thermodynamics

CO_2 methanation (Eq. 1.1) is a highly exothermic reaction that is thermodynamically favoured at low temperatures and high pressures. Alongside, three main side reactions could also occur, namely reverse water gas shift (RWGS), CO methanation and reverse dry reforming (Eqs. 2.1-2.3, respectively). Other side reactions such as Boudouard reaction, CO_2 reduction, CO_2 reduction, methane pyrolysis and alkanes/alkenes formation could also be considered (Eqs. 2.4-2.9, respectively), as summarized in Table 2.1.

Table 2.1 Possible side reactions occur during CO_2 methanation.

Reaction name	Reaction formula	ΔH_{298K} (kJ/mol)	Eq.
Reverse water gas shift	$CO_2 + H_2 \leftrightarrow CO + H_2O$	41.2	(2.1)
CO methanation	$CO + 3H_2 \leftrightarrow CH_4 + H_2O$	-206.1	(2.2)
Reverse dry reforming	$2CO + 2H_2 \leftrightarrow CH_4 + CO_2$	-247.4	(2.3)
Boudouard reaction	$2CO \leftrightarrow C + CO_2$	-172.5	(2.4)
CO_2 reduction	$CO_2 + 2H_2 \leftrightarrow C + 2H_2O$	-90.1	(2.5)
CO reduction	$CO + H_2 \leftrightarrow C + 2H_2O$	-131.3	(2.6)
Methane pyrolysis	$CH_4 \leftrightarrow C + 2H_2$	74.9	(2.7)
Formation of alkanes	$nCO + (2n+1)H_2 \leftrightarrow C_nH_{2n+2} + nH_2O$	-	(2.8)
Formation of alkenes	$nCO + 2nH_2 \leftrightarrow C_nH_{2n} + nH_2O$	-	(2.9)

By Gibbs free energy minimization method,[20] the equilibrium product compositions (Fig. 2.1) at 1 atm and stoichiometric H_2/CO_2 molar ratio of 4 was calculated from a model consisted of 10 possible reactions. Methane was the main product at low temperatures of 200-300 ºC but gradually decreased as increasing temperatures. Accordingly, an increase of H_2 and CO_2 mole fraction was also observed from 200 ºC to 500 ºC. The RWGS reaction was responsible for CO formation, which was detected at temperatures above 450 ºC. This side reaction became significantly dominant at temperatures above 550 ºC as evidenced by the drop of CO_2 mole fraction to more CO.

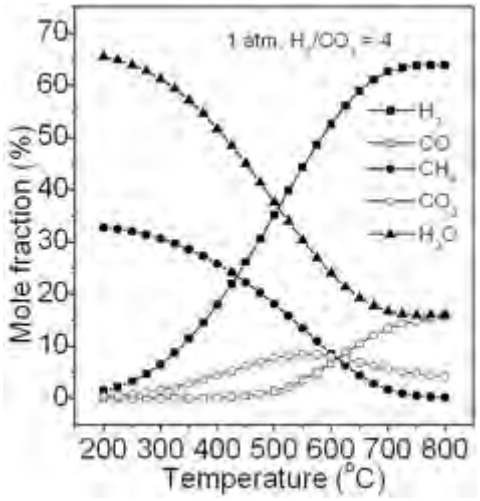

Figure 2.1 Product compositions of CO_2 methanation at thermodynamic equilibrium.[20]

Regardless of reaction temperature and H_2/CO_2 ratio, an increase in CO_2 conversion, CH_4 selectivity and yield was obtained when the pressure changed from atmospheric to 30 bar (Fig. 2.2). Notably, the influence of RWGS reaction on methane production was less significant at high pressures (10-100 bar).[20] Moreover, the impact of H_2/CO_2 ratio on CO_2 methanation was also studied. It was recommended that H_2/CO_2 ratio should not be lower than stoichiometric value of 4 to obtain high CH_4 yields and avoid carbon formation.[20-22]

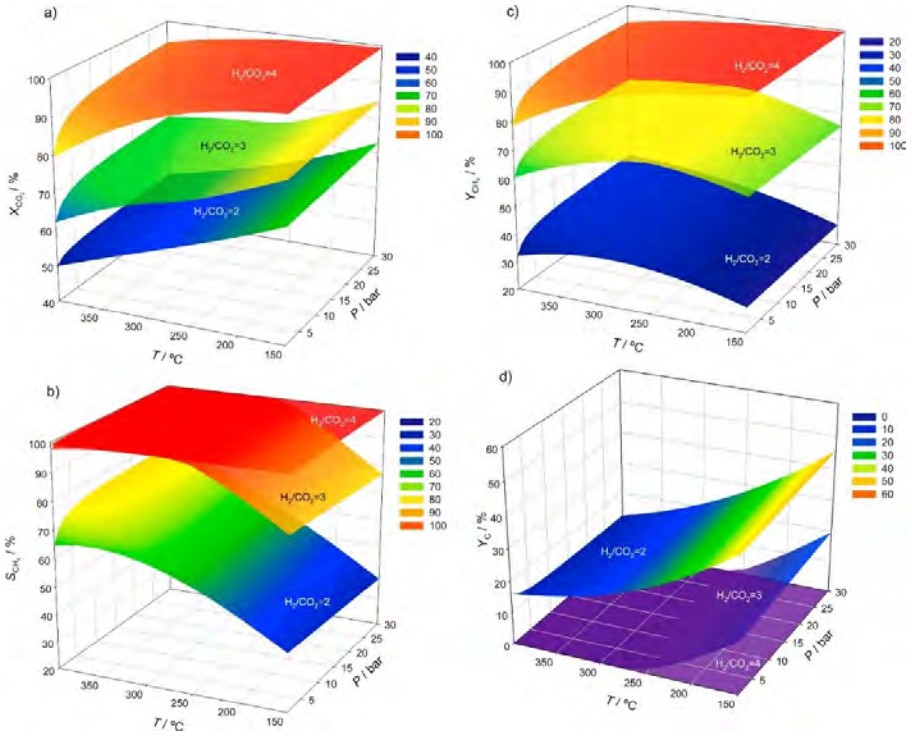

Figure 2.2 The influence of temperature, pressure, and H_2/CO_2 ratio on CO_2 methanation in terms of (a) CO_2 conversion, (b) CH_4 selectivity, (c) CH_4 yield and (d) carbon yield.[21]

2.2 Mechanism and kinetics

Although CO_2 methanation has been discovered for more than 100 years, the reaction mechanism is still under debate regarding the reaction intermediates, elementary steps, and rate-determining step (RDS).[23-26] The existing proposed mechanisms can be divided into two main pathways, i.e., associative, and dissociative route, which was based on the initial elementary step of adsorbed CO_2 molecules ($*CO_2$) as illustrated in Fig. 2.3. In the associative scheme, $*CO_2$ reacted with H* to form oxygenates intermediates like formate (*HCOO) or carboxylate (*COOH) and subsequently hydrogenated to CH_4, which is known as formate pathway and RWGS+CO-hydro (carboxylate) pathway, respectively. In the dissociative scheme, CO_2 firstly dissociated to

carbonyl (*CO) and *O via direct C-O bond cleavage, followed by *CO hydrogenation to CH_4 which was closely related to CO methanation mechanism. That is, *CO could undergo direct dissociation to C* and O* (direct C-O bond cleavage pathway) while it could also be hydrogenated to *HCO or *COH and eventually to CH_4 (similar to RWGS+CO-hydro pathway).

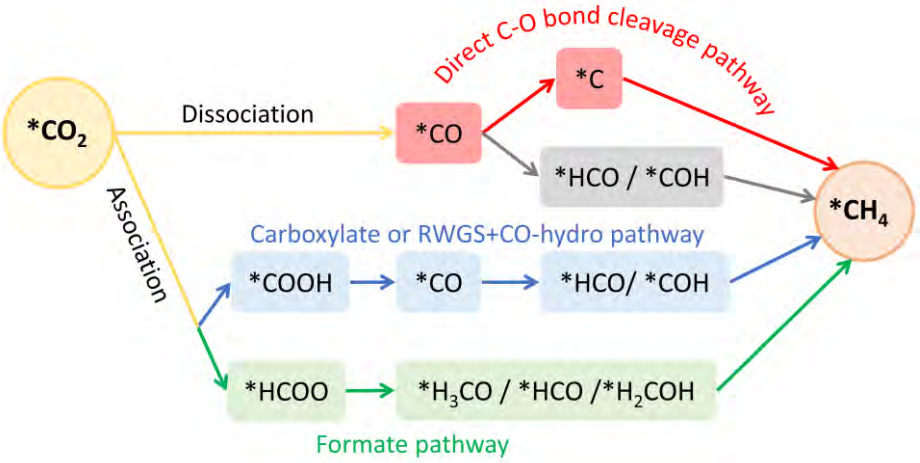

Figure 2.3 Possible reaction pathways of CO_2 methanation.

In the early 1900s, the classical Sabatier reaction over Ni was assumed to occur firstly via RWGS reaction, that CO_2 dissociatively adsorbed with H_2 to form CO and H_2O. Then CO methanation happened which *CO was directly hydrogenated or dissociated to atomic *C and further hydrogenated to CH_4. However, modern studies employing advanced techniques in both experiments (e.g., in-situ spectroscopy analysis) and computational DFT calculations have provided deeper insights into the reaction mechanism for CO_2 methanation.[26-28] The mechanism of CO_2 methanation on unsupported and supported catalysts is dedicatedly discussed in section 3 of **Paper I**.

As different proposed mechanisms were dependent on specific catalysts and reaction conditions, many various kinetic models were reported,

which is discussed in detail in section 4 of **Paper II**. While some models were based on the simple power-law equation (e.g., Ni/ kieselguhr[29], Ni/Y_2O_3-ZrO_2[30], Ru/Al_2O_3[31]), other kinetic studies applied complex mechanisms such as Langmuir-Hinshelwood (e.g., Ru/g-Al_2O_3[32], Ni/MgO[33], Ni/AlO_x[34], Ni/La_2O_3[35], Ni/Al_2O_3[36-37]) or Eley-Rideal (e.g., Ru/g-Al_2O_3[38]). Despite different reaction conditions, a relative kinetics comparison showed that Ni activity could be as good as Ru activity however at higher Ni loading and higher pressures.[22] Recently, as kinetic models are essential for reactor modelling, especially for large-scale production of methane, kinetic experiments have been conducted under industrially relevant conditions on state-of-the-art Ni/AlO_x catalysts by Koschany *et al*.[34] The reaction mechanism was assumed to follow $*CO_2$ dissociation to *CO and subsequent H-assisted dissociation to *CHO. The best-fit rate equation was derived by assuming *CHO formation as RDS, also included the inhibition influence of $*H_2O$ and *OH at temperatures of 453-613 K and pressures of 1-10 bar. This kinetic model was selected for the reactor modelling in this thesis.

Although Sabatier reaction is thermodynamically favored at low temperatures and elevated pressures, high conversion rates are difficult to be achieved at low-temperature region of 200-350 ºC due to kinetic limitations. Therefore, highly active, CH_4 selective and stable catalysts are extremely desired to produce SNG via CO_2 methanation.

2.3 Catalysts

Catalysts play a critical role in the conversion and selectivity of CO_2 methanation, which have been extensively reviewed in terms of active sites, supports, promoters and preparation methods.[39-43] Particularly, metal supported catalysts have been widely used for CO_2 methanation which consisted of active metals (noble or transitional metals), support materials (conventional and novel type) and sometimes promoters (e.g., second metal).

Noble metals, i.e., rhodium (Rh) and ruthenium (Ru) are highly recognized for their remarkable performance at low temperature. Several studies compared the activity and selectivity of noble metals on the same type of support and suggested that Ru and Rh are excellent for CH_4 production while platinum (Pt) and palladium (Pd) produce mainly CO through RWGS reaction.[44-45] Nevertheless, due to high cost and scarce availability, noble metals may not be favourable for industrial applications of the Sabatier reaction.

Transitional metals, i.e., cobalt (Co), nickel (Ni) and iron (Fe) generally have poorer activity and selectivity compared to noble metals. Co was suggested to have superior catalytic activity than Ru on SiO_2 supported catalysts in terms of CO_2 turnover frequency, however, its selectivity towards CH_4 was lower than Ru.[46] Although Co seems to be more active than Ni and Fe, the cost of Co is high (much higher than Ni and Fe). In contrast, Fe offers the most affordable price, but the monometallic Fe catalyst exhibited very low CH_4 selectivity. Fe-based catalysts are often used for C_2+ hydrocarbons synthesis via CO_2 Fischer-Tropsch reaction.[47] Ultimately, Ni with good CH_4 selectivity and low cost has always been the first choice for industrial applications.

2.3.1 Bimetallic Ni-Fe catalysts

Using second metal as a promoter is one of the most common approaches to improve the activity of Ni-based catalysts.[48-49] The addition of Fe to Ni has been reported as a promising strategy to achieve better catalytic performance and stability of methanation catalyst. It was first predicted by DFT calculations initiated by Nørskov *et al.*[50] Based on the calculated energies, NiFe and Ni_3Fe showed excellent activity compare to monometallic Ni and Fe, close to that of the best catalysts (i.e., Ru and Co).[51-52] Experimental investigations have also verified that Ni-Fe catalysts exhibited higher activity than their individual constituent in CO_2 hydrogenation (H_2/CO_2 = 91/9) at 250 ºC.[53] This bimetallic Ni-Fe catalytic system is very attractive because cheap Fe will further

contribute to the cost-effectiveness of Ni-based catalysts for industrial CO_2 methanation.

Studies on Ni-Fe catalysts for CO_2 methanation have been reported on different catalytic supports, i.e., Al_2O_3[54], TiO_2, SiO_2, Nb_2O_5, and ZrO_2 [55-56], while unsupported NiFe catalysts[57] were also investigated. The optimal composition of Fe in Ni-based catalysts to achieve the best promoting effect appears to be dependent on the support type and metal loading. Importantly, the amount of Fe addition plays a crucial role since a small amount of Fe boosted the production of CH_4 while a large amount of Fe promoted the formation of CO via RWGS reaction.[58]

Overall, most of these studies have confirmed the superiority of Ni-Fe alloy catalysts in CO_2 methanation compared to monometallic Ni catalysts. Besides, the Ni_3Fe/Al_2O_3 catalysts showed a more stable performance compared to commercial Ni methanation catalysts.[59] Based on kinetic measurements, Mutz *et al.* assumed the effect of Fe could be due to the synergetic effect of Ni-Fe alloy.[59] While the CO dissociation energy was used as a descriptor for CO and CO_2 methanation activity,[51, 60] the binding energy of adsorbed CO was proposed as the key descriptor for CO_2 hydrogenation to CH_4 (H_2/CO_2 = 2).[58] An improvement in CO_2 uptake capacity on alloy surfaces corresponding to the promoted CH_4 production has also been speculated.[61] Nevertheless, there is no consensus on the promotional effect of Fe on Ni, while the mechanism of CO_2 methanation on Ni-Fe alloy catalysts is not clearly understood.

2.3.2 *Metal supported catalysts derived from hydrotalcite materials*

Catalytic supports are very important because it affects the metal dispersion, basicity, SMSI, oxygen vacancies, catalyst structure, etc.[43] More details are discussed in section 5 of **Paper I**.

A common approach to improve catalytic performance is tuning the basicity of the support. Alkaline-earth oxides, such as MgO, are usually used to strengthen the basicity of the catalytic surface. The combination of MgO and Al_2O_3 (most commonly used support material), as anticipated, has been reported as the best support for CO_2 conversion reactions, such as dry reforming of methane, due to its high basicity, good thermal stability, large surface area and pore volume.[62] Metal sintering and carbon deposition are other challenges that lead to the deactivation of Ni-based catalysts in the exothermic Sabatier reaction. To address these problems, Ni active sites are often stabilized by well-defined crystalline structures (i.e., solid solution, spinel, perovskite, etc.), rigid mesoporous frameworks or core-shell structures.[63]

The aforementioned two approaches can be well covered by the layered double hydroxides (LDHs) or also called hydrotalcite (HT) materials. Ni-based on $(Mg,Al)O_x$ mixed oxide support can be prepared via HT precursors. HT has similar LDHs structures as the natural magnesium aluminium hydroxy carbonate $Mg_{0.75}Al_{0.25}CO_3(OH)_{0.125} \cdot mH_2O$. The general formula of LDHs is $[M_{1-x}^{2+}M_x^{3+}(OH)_2](A^{n-})_{x/n} \cdot mH_2O$, where M represents metals, and A is anion. The value of x (is equal to $M^{2+}/(M^{2+}+M^{3+})$ molar ratio) is preferred to be in the range of 0.2-0.33 to obtain a pure LDH phase and to avoid the formation of hydroxides and other compounds. Divalent cations can be Mg and/or other metals (e.g., Ni, Co, Fe), while trivalent cations are Al and/or other metals (e.g., Fe, In, Mn).[64-66] Because a wide range of cations and anions can be incorporated, HT materials have drawn much attention as promising precursors for heterogeneous catalyst design. As the cations in HT structures are well dispersed, the obtained mixed oxides upon thermal decomposition usually show a good distribution of metal active sites. Therefore, derivatives of HT precursors after calcination are often used as metal supported catalysts.[66] The phase transformation during calcination of the HT precursors and subsequent reduction of the mixed oxides are schematically illustrated in Fig. 2.4.

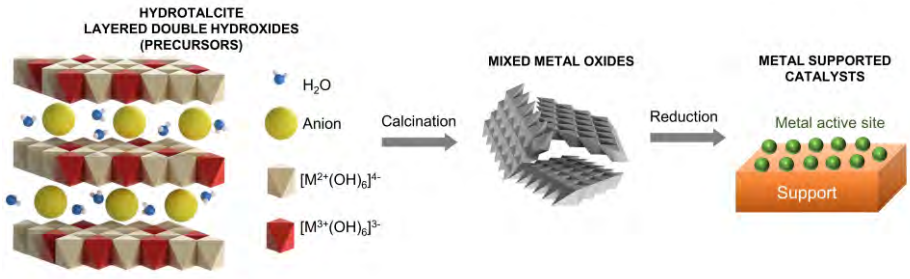

Figure 2.4 Preparation pathway of metal supported catalysts from HT/LDHs precursors.

A comprehensive review of recent applications of Ni-based HT-derived catalysts for CO_2 methanation is presented in section 2 of **Paper II**. In this thesis, Ni-Fe/(Mg,Al)O_x HT-derived catalysts were prepared by fast coprecipitation methods adapted from Tathod and Gazit.[67]

2.3.3 Structured catalysts

Applying laboratory research of CO_2 methanation catalyst and reactor into industrial practice is essential for the commercialization of PtG technology. One of the most recent development trends of methanation unit is structured reactors equipped with monolithic catalysts.[4] Honeycomb monolithic catalysts have been widely used for environmental applications, such as automotive catalysts, volatile organic compounds incinerators, etc.[68] The use of structured catalysts for other heterogeneous catalytic reactions like CO_2 methanation has been highly motivated. Monolithic catalysts offer many advantages over conventional pelletized catalysts, such as lower pressure drop associated with the high rates and small size of the reactor, which are typical concerns for gas-phase chemical processes. For CO_2 methanation, monolithic catalysts can handle large volumetric flow of CO_2 during industrial applications with more efficient heat and mass transfer.

In general, structured catalysts consist of a three-dimensional (3D) shaped support with a layer of catalytic material. The support materials

are ceramic-type (e.g., cordierite, Al_2O_3, MgO, SiO_2, SiC) or metallic-type (e.g., Al, Ni, Cu, Co, stainless steel, Inconel, FeCrAlloy) or carbon-type (e.g., activated carbon, reticulated vitreous carbon). Several 3D structural configurations are honeycomb, corrugated sheet, gauze, foam, fiber, wire packing or periodic open cellular structures.[69]

In terms of preparation methods, there are two types of structured catalysts. Catalysts in which an active phase is deposited on inert monolithic support are classified as coated catalysts, whereas catalysts in which the whole structure is made from the active compounds are bulk catalysts. Most structured catalysts used for CO_2 methanation are coated catalysts.

Cordierite ($2Al_2O_3.5SiO_2.2MgO$) is the most widely used ceramic material to produce commercial monoliths at different dimensions and cell densities. Cordierite has high thermal stability and low thermal expansion coefficient, but ultralow surface area. Therefore, it is advantageous to coat a layer of support material on cordierite to increase the surface area prior to the deposition of active catalyst layer. The active layer can be deposited by different methods such as impregnation or deposition-precipitation.[70]

Recently, a novel synthesis using urea hydrolysis to deposit LDHs layer in-situ on monolithic substrates as precursors for structured catalysts has been reported. In the presence of a basic retardant, i.e., urea, LDHs consisting of Ni-Al, Co-Al, Co-Fe, etc., were successfully coated on a variety of supports such as metal mesh and foams (e.g., Ni foam, Fe mesh, FeCrAl fiber, Al foils, etc.) with great potentials for different catalytic reactions.[71-75] Moreover, in-situ grown LDHs layers appeared to have strong adherence and mechanical stability between the layer and the metal substrate.[76-78] Notably, the formation of LDHs was influenced by different parameters such as reaction temperature, urea amount, metal concentration, and the ratio of trivalent and divalent ions.[79-80] However,

research on structured catalysts from in-situ grown precursors on the ceramic substrate via urea hydrolysis is rarely reported.

More details on the recent development of conventional and novel structured catalysts (and reactors) for CO_2 methanation are presented in section 3 of **Paper II**. In this thesis, ceramic honeycomb monoliths were selected to prepare Ni-Fe structured catalysts. Urea hydrolysis was applied to prepare in-situ grown NiFe-CO_3 LDHs precursors on washcoated substrates.

2.4 Reactor development

Fixed-bed reactors, also called packed-bed reactors, are commonly used for CO_2 methanation due to its simplicity and cost-effectiveness. The reactors provide more contact between the reactant gases and the catalyst granules/pellets. However, random maldistribution in the fixed-bed reactors causes nonuniform access of reactant gases to the catalytic surface, unexpected hot-spot formation, and possible thermal runaways of exothermic reactions, which are one of the most challenging problems of the methanation process. The overall process performance, CH_4 yield, CH_4 selectivity, and lifetime of catalysts are consequently reduced. Therefore, different reactor concepts focusing on improving heat management have been proposed.[81]

With inter-stage cooling installations, adiabatic fixed-bed reactors have been commercially developed but its complexity increased costs and hindered flexibility. Multi-tubular reactors with cooling fluids are alternative designs but temperature and pressure control are more difficult. In contrast, fluidized-bed and three-phase reactors promise effective heat removal and accurate temperature control. However, there are many drawbacks, e.g., catalyst loss, shortened lifetime or mass transfer resistance. Alternatively, micro-reactors, which are well-known for their excellent heat transfer in small channels have been used especially for space exploration missions. Recent advances in additive

manufacturing have reduced the cost of micro-reactors which makes it more attractive for commercial applications.[6]

A more practical option is structured reactors loaded with well-designed structured catalysts. The hydrodynamics in a structured reactor can be simplified as uniform laminar flow, enabling full access of reactant gases to the catalytic surface with a lower pressure drop due to channelling nature thus possibly diminishing mass transfer limitations.[68, 82] The tunable thickness of catalyst layer which affects the diffusion length could be beneficial to optimize the efficiency of the catalysts. Moreover, high volumetric rates of feed gases can be handled by structured reactors with improved heat and mass transfer, especially for better heat transfer since monolithic substrates typically have good thermal conductivity.[83] For instance, based on modelling studies, Schlereth *et al*. concluded that honeycomb monolithic reactors have superior performance in comparison with fixed-bed reactors in terms of heat transfer efficiency, although it was only applied on specific operating conditions of CO_2 methanation.[84]

Nevertheless, hot-spot formation is still a big problem for monolithic catalyst and reactor design. There has been an increase in the number of publications attempting to control a stable thermal profile in the reactor. For instance, Fukuhara *et al*. reported that under similar methanation conditions, honeycomb-type catalytic bed showed a flat temperature profile while granular-type catalytic bed showed a temperature rise of 20 ^{o}C due to poor heat dissipation of the conventional fixed bed.[85] However, at a higher gas rate, hot-spot formation was observed on the honeycomb monolithic bed. Great efforts to further improve heat and mass transfer along the monolithic bed have been devoted.[86] It was found that a less severe hot-spot formation could be obtained while high CO_2 conversion and CH_4 selectivity were maintained on a multi-stacked catalyst bed.[87] The researchers have been innovative by designing the bed packing configuration containing a sequence of coated and uncoated Ni/CeO_2 aluminum honeycomb-fin monolithic catalysts. Thus, the

catalytic activity was discretely distributed along the reactor bed length which resulted in an optimal heat transfer and reaction rate.

Kosaka *et al.* has recently reported that an increasing catalytic activity along the tubular catalyst bed could also prevent hot-spot formation compared to the uniform catalytic bed.[88-89] However, it was not anticipated that the performance of the low-activity catalysts was boosted by the observed hot-spots. Apparently, controlled hot-spot formation could be utilized for a more sustainable catalytic process and has been deliberately employed in certain reactor designs.[90-91] Therefore, it is important to fundamentally understand the effect of catalytic activity on hot-spot formation along the reactor bed.

3 Methodology

3.1 Catalyst preparation

3.1.1 Ni-Fe catalysts derived from hydrotalcite precursors

Ni-Fe/(Mg,Al)O_x catalysts in **Paper III** and **Paper IV** were derived from HT precursors, which were prepared by the coprecipitation method adapted from Tathod and Gazit.[67] All chemicals were analytical grade (Merck Millipore) and used as received without purification.

In a typical preparation, a metal nitrate solution (100 mL) containing a calculated amount of $Ni(NO_3)_2.6H_2O$, $Fe(NO_3)_3.9H_2O$, $Mg(NO_3)_2.6H_2O$ and $Al(NO_3)_3.9H_2O$ were quickly injected by a syringe into a 500-mL base solution containing a sufficient amount of NaOH and Na_2CO_3 under vigorous stirring at 60 ºC. The suspension was then aged under flowing N_2 gas at 85 ºC for 18 h. Subsequently, the gel-like mass was filtered, washed until the pH of the filtrate was neutral, and dried at 90 ºC overnight. The dried precursors were calcined at 600 ºC for 6 h in flowing synthetic air (heating rate of 5 K/min). The calcined catalysts in powder particles were pelletized, crushed and sieved to a particle size of 200-355 μm, as shown in Fig. 3.1.

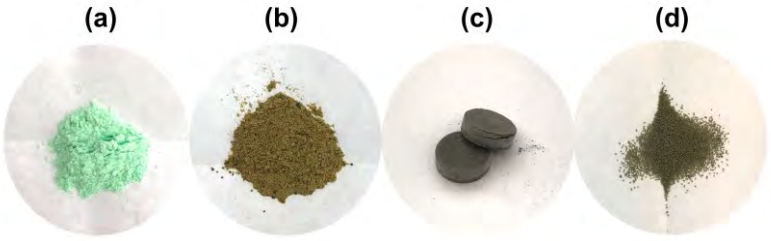

Figure 3.1 Photographs of (a) dry HT precursors, (b) calcined catalysts in (c) pellet form and (d) small granular form.

In all catalysts, the molar ratio between divalent and trivalent cations, i.e., (Ni+Mg)/(Al+Fe) ratio was fixed at 3 and the Ni loading was kept constant at 20 wt.%. In **Paper III**, different molar ratios of Fe/Ni were used, varied from 0 to 0.5. **In Paper IV**, the concentration of the metal nitrate solution was varied from 0.25 M to 2.5 M.

For certain characterization, reduced and passivated catalysts were required. The calcined catalysts were reduced in the reactor at 600 ºC for 4 h (heating rate of 5 K/min) in flowing 50% H_2/N_2 gas with a rate of 100 mL/min. Upon reduction, the samples were cooled down to room temperature in flowing N_2 (gas rate of 50 mL/min). Thereafter, synthetic air was added to adjust the oxygen content in the gas mixture from 0 vol.% to 0.1 vol.% and then 1 vol.% to passivate the catalysts.

3.1.2 Ni-Fe catalysts in-situ grown on ceramic honeycomb monoliths

Ni-Fe catalysts on washcoated monolithic substrates in **Paper V** and **Paper VI** were prepared by the following procedure. At first, the pure ceramic honeycomb substrates were washed with ethanol and water in an ultrasonic bath (3 times and 3 min each time) and dried at 90 ºC overnight prior to further synthesis steps.

The cylindrical honeycomb monoliths are commercial products (Versagrid™) supplied by Applied Ceramics Inc. (USA). It was made of cordierite ($MgO/SiO_2/Al_2O_3$ = 13.8/50/34 wt.%, and traces amount of iron and zinc oxide). The dimension of monoliths was 19 mm in diameter and 20 mm in length. The monoliths had 230 cells per square inch (cpsi), channel wall thickness of 200±50 μm, average pore diameter of 4.5 μm, open frontal area of 72%, and geometric surface area of 2220 m^2/m^3.

Secondly, a washcoat layer was deposited on the ceramic surface by dip coating method to increase its surface area. Colloidal solutions were used, i.e., Al_2O_3 (Alfa Aesar, 20 wt.% suspension in water) with particle

size of 50 nm and SiO_2 (LUDOX TM-50, 50 wt.% suspension in water) with particle size of 22-25 nm. In one typical dip coating cycle, the monolith was immersed in the colloidal solution for 3 min, and then dried at 250 ºC for 15 min. Several cycles were made to achieve the desired washcoat loading. Finally, the monolith was calcined at 600 ºC for 6 h (heating rate of 2 K/min) in a muffle furnace.

Thirdly, the washcoated monoliths were immersed in 45 mL of the stock solution containing $Ni(NO_3)_2.6H_2O$, $Fe(NO_3)_3.9H_2O$ and urea (Merck Millipore) at different molar concentrations from 0.05 M to 2 M. The molar ratio of Ni^{2+}/Fe^{3+} was maintained at 4 and the molar ratio of urea and metal ion was 9.9, corresponding to a urea/nitrate ion ratio of 4.5. The selected urea/metal compositions had been experimentally optimized to obtain a pure LDHs structure.

Finally, the stock solution and monoliths were transferred into a 90-mL Teflon-lined hydrothermal autoclave and heated at 110 ºC for 24 h. After cooling the autoclave to room temperature, the monolith was washed with deionized water and dried at 90 ºC for 1 h. Calcination was carried out at 600 ºC for 6 h (heating rate of 2 K/min) in a muffle furnace. Fig. 3.2 presents the monolith as fresh, as well as before and after reaction.

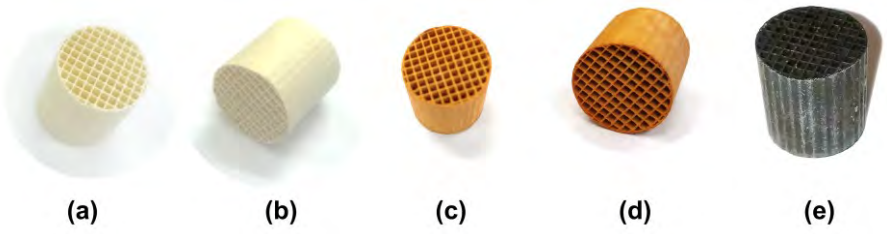

Figure 3.2 (a-b) Photograph of fresh cordierite monolith, (c-d) photograph of calcined monolith before reaction and (e) photograph of monolith after reaction.

For comparison, the same synthesis procedure was conducted without the addition of washcoated monoliths. The solid precipitate was collected by centrifugation, washed, and dried. The dry LDHs powders were subsequently calcined at 600 ºC for 6 h (heating rate of 2 K/min).

3.2 Catalyst characterization

3.2.1 N_2 physisorption

Information on the surface area, pore size and volume of the catalysts is obtained based on N_2 physisorption. The N_2 adsorption-desorption isotherms were determined at -196 ºC using Micromeritics Tristar II instrument. Prior to measurement, the sample (~120 mg) was degassed overnight at 150 ºC under vacuum. The surface area was calculated by the Brunauer-Emmett-Teller (BET) method in the pressure range of $0.05 < P/P_o < 0.3$.[92] The pore volume and pore size distribution were calculated from the desorption branch of the isotherms by the Barrett-Joyner-Halenda (BJH) method.[93]

3.2.2 Structure and morphology

3.2.2.1 Ex-situ and in-situ X-ray diffraction (XRD)

For the phase identification of precursors and catalysts, ex-situ X-ray diffraction (XRD) patterns were recorded on a Bruker D8 Advance micro-diffractometer using CuKα radiation source in the 2θ range of 5-90º at a step interval of 1 º/min. The *d*-spacing was calculated based on Bragg's law.[94] The average crystallite size *d* was calculated by the Scherrer's equation (Eq. 3.1), where K_F is the shape factor (0.9), λ is the wavelength of CuKα (1.5406 Å), θ is the diffraction angle of the peak and β represents the full width at half maximum of the peak (in radians).[94]

$$d = \frac{K_F \times \lambda}{\beta \times cos\theta} \tag{3.1}$$

In-situ XRD diffractograms were recorded to study the phase transitions of catalysts during reduction and reaction at atmospheric pressure. SmartLab 9 kW (Rigaku) diffractometer equipped with an XRK900 reactor chamber and a 1D/Dtex detector was used. The diffractometer

was operated at 45 kV and 200 mA using CuKα radiation source. About 50 mg of calcined catalyst was loaded in the sample holder and heated up to 600 ºC at a heating rate of 10 K/min under a flow of pure H_2 (30 mL/min) for reduction at atmospheric pressure. The diffractograms were subsequently recorded at 100-600 ºC at a scanning speed of 8 º/min (hold for 5 min at each temperature). When the temperature reached 600 ºC, the data were collected every 15 min for 90 min. The in-situ XRD measurement was continuously conducted under reaction conditions. A gas mixture of $CO_2/H_2/N_2$ = 17/69/14 vol.% (30 mL/min) was introduced after cooling the reduced sample down to 200 ºC. The XRD diffractograms were recorded during reaction at 200-350 ºC.

3.2.2.2 Scanning Electron Microscopy (SEM)

The morphology of the powder precursors was examined using Scanning Electron Microscopy (SEM) Gemini Supra 35VP (ZEISS). The dried powder samples were spread on carbon tape and coated with Pd plasma to inhibit charging.

The coating morphology of the monolithic catalysts was also examined by the same microscope equipped with energy-dispersive X-ray spectroscopy (EDS) for elemental mapping. Prior to analysis, the monolith was polished and coated with Pd plasma to inhibit charging.

3.2.2.3 Transmission Electron Microscopy (TEM)

The morphology was also studied by Transmission Electron Microscopy (TEM) JEM-2100F (JEOL) operating at 200 kV. The reduced-passivated powder samples were dissolved in ethanol, assisted by ultrasonic dispersion. A drop of the suspension was deposited on a holey carbon-coated copper grid and dried before it was inserted into the microscope.

3.2.2.4 Thermogravimetric analysis (TGA)

Thermogravimetric analysis (TGA) was conducted using Netzsch STA449 Jupiter F3 instrument. Approximately 10 mg of sample was used and the TG profiles were obtained when the sample was heated up from room temperature to 800 ºC at a heating rate of 10 K/min in flowing He (20 mL/min).

3.2.2.5 In-situ Diffuse Reflectance Infrared Fourier Transform Spectroscopy (DRIFTS)

In-situ diffuse reflectance infrared Fourier transform spectroscopy (DRIFTS) study was conducted on a Nicolet iS 50 (Thermo Scientific) FTIR spectrometer equipped with a mercury cadmium telluride detector cooled by liquid N_2. Prior to measurement, the calcined catalysts were reduced in 30% H_2/N_2 flow (15 mL/min) at 600 ºC for 90 min (heating rate of 10 K/min). Thereafter, the sample was cooled down to 200 ºC followed by N_2 purging for 10 min. For CO_2 adsorption study, a flow of CO_2/N_2 = 1/5 vol.% (6 mL/min) was introduced. For CO_2 methanation study, a gas mixture of $CO_2/H_2/N_2$ = 1/4/5 vol.% (10 mL/min) was used. The in-situ DRIFTS spectra were continuously collected at elevated temperatures of 200-350 ºC. Time-resolved DRIFTS study was also recorded every 1 min during CO_2 methanation at 300 ºC for 180 min.

3.2.3 Chemical properties

3.2.3.1 Inductively Coupled Plasma Optical Emission Spectrometry (ICP-OES)

The elemental compositions of catalysts were analyzed by the inductively coupled plasma optical emission spectrometry (ICP-OES) named OPTIMA 4300 DV (PerkinElmer). The dried samples were completely dissolved in a mixture of HCl and HNO_3 concentrated acid at a ratio of 3 and further diluted for analysis.

3.2.3.2 Temperature Programmed Reduction (TPR)

The reducibility of calcined catalysts can be understood by temperature programmed reduction (TPR) analysis. The experiment was carried out by Micromeritics Autochem II instrument equipped with a thermal conductivity detector (TCD). The calcined sample (in a sufficient amount to obtain reliable data[95-96]) was first degassed at 200 ºC for 30 min and then reduced using 10% H_2/Ar from 50 ºC to 950 ºC at a heating rate of 10 K/min.

3.2.3.3 Temperature Programmed Desorption (TPD)

The temperature programmed desorption (TPD) of CO_2 can be used to gain information on the basicity of metal supported catalysts. TPD experiment used the reduced catalysts from previous TPR measurement on the same instrument (Micromeritics Autochem II). A degassing step was carried out at 600 ºC in He for 30 min. A flow of 6% CO_2/Ar was then introduced for 1 h. Weakly adsorbed CO_2 was desorbed by He flow for 1 h. The CO_2-TPD was recorded by heating the sample to 800 ºC under He flow at a heating rate of 10 K/min. The same equipment was also used to measure TPR data of reduced catalysts to determine the reduction degree *f* by Eq. 3.2.[97]

$$f = \frac{\text{TPR peak area of calcined sample-TPR peak area of reduced sample}}{\text{TPR peak area of calcined sample}} \times 100 \qquad (3.2)$$

3.2.3.4 Hydrogen Chemisorption

By the assumption that H_2 chemisorption occurs only on Ni atom (one hydrogen atom per nickel atom), the dispersion of Ni active sites can be calculated by Eq. 3.3, where n_{H2} is the mol of H_2 uptake in chemisorption study, w_{Ni} is weight percentage, *f* is the reduction degree and M_{Ni} is the molar mass of Ni.[98]

$$\text{Ni dispersion (\%)} = \frac{\text{number of Ni at the surface}}{\text{total number of Ni}} = \frac{2 \times n_{H2} \times M_{Ni}}{w_{Ni} \times f/100} \times 100 \qquad (3.3)$$

H_2 chemisorption analysis was performed at 35 ºC on Micromeritics ASAP 2020 Plus instrument. Calcined samples (~200 mg) were degassed in He flow at 200 ºC for 2 h, reduced in H_2 flow at 600 ºC for 4 h (heating rate of 5 K/min), and cooled down to 35 ºC before measurement.

3.2.4 Mechanical properties of monolithic catalysts

The adherence of the coating layer on ceramic honeycomb substrates was evaluated by measuring its weight loss after ultrasonic treatment. The calcined monolithic catalyst was immersed in ethanol and then transferred to an ultrasonic bath (VWR, 45 kHz, 600 W) at room temperature for 30 min. After that, it was dried at 90 ºC for 1 h and the total weight loss was calculated.

3.3 Catalytic activity evaluation

3.3.1 Fixed-bed reactor setup for powder catalysts

The activity of catalysts in powder particles was studied on a stainless-steel fixed-bed reactor (**Paper III** and **Paper IV**). The reactor has an inner diameter of 4.5 mm and a length of 53 cm. It was heated by an electric oven (installed vertically) at atmospheric pressure, as shown in Fig. 3.3. The temperature was controlled by a type-K thermocouple installed in the bottom of the catalyst bed. The rate of reactant gases was regulated at standard conditions by calibrated mass flow controllers (Alicat). Water formed during the reaction was condensed by a cold trap. A partial outgas flow was split and vented while the other part was analyzed by an online gas chromatograph (GC, Agilent 7890A). The GC is equipped with packed columns and two TCD detectors. A simple schematic representing the reactor setup for catalytic activity test is illustrated in Fig. 3.4.

Figure 3.3 Photographs of fixed-bed reactor setup.

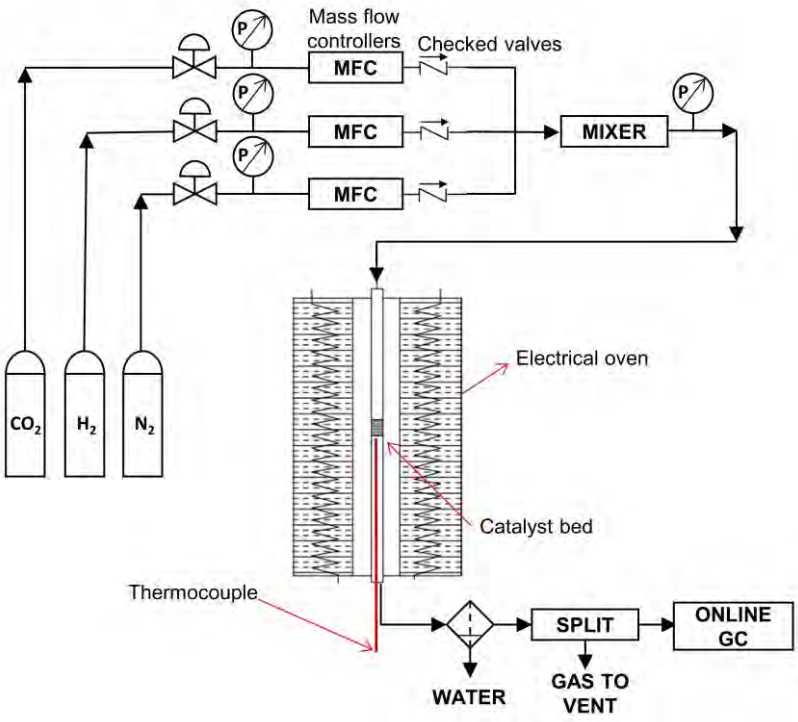

Figure 3.4 Schematic diagram of the reactor setup for catalytic tests.

In a typical experiment, 60 mg of calcined catalysts (200-355 μm) was diluted with 600 mg of silicon carbide (SiC, grit 45, particle size of 355 μm) and placed on the quartz wool, located above the thermocouple. Prior to reaction, the catalyst was reduced at 600 ºC for 4 h in 50% H_2/N_2 with a total flow of 100 mL/min. Thereafter, the reactor was cooled down in pure N_2 flow for 1 h. Residual H_2 from reduction was purged out from the reactor.

Subsequently, the reactant gases of $H_2/N_2/CO_2$ = 64/20/16 vol.% (i.e., H_2/CO_2 = 4/1) was introduced at 270 mL/min, corresponding to a weight hourly space velocity (WHSV) of 270 $L/g_{cat}/h$ (or 43.2 $L_{CO2}/g_{cat}/h$) and a gas hourly space velocity (GHSV) of 34,000 h^{-1} with regards to the catalytic bed length of 3 cm. The temperature-dependent activity tests were carried out at 200-450 ºC with a step of 50 ºC and a heating rate of 1 K/min. The condition was held for 1 h at each temperature to obtain a stable CO_2 conversion. A blank test was conducted and no significant conversion was found over SiC powder in the stainless-steel reactor.

For long-term stability evaluation, the catalysts were tested at the desired temperature for up to 100 h of time on stream (TOS).

3.3.2 Structured reactor for monolithic catalysts

The activity of monolithic catalysts was studied on a stainless-steel structured reactor (**Paper V** and **Paper VI**). The reactor has an inner diameter of 21.1 mm and a length of 67 cm. The reactor was horizontally installed and heated by an electric oven, as shown in Fig. 3.5, where the temperature was controlled by a type-K thermocouple inside the reactor. The schematic representing the reactor setup is shown in Fig. 3.6a. Since the outer diameter of the monolith was 19 mm, an in-house designed catalyst holder with an inner diameter of 19.1 mm (outer diameter of 21.1 mm) was used. Therefore, the structured catalysts were inserted in the holder and could be easily placed inside and removed from the reactor,

avoiding any potential for gas channelling. Fig. 3.6b illustrates the monolith inside the holder.

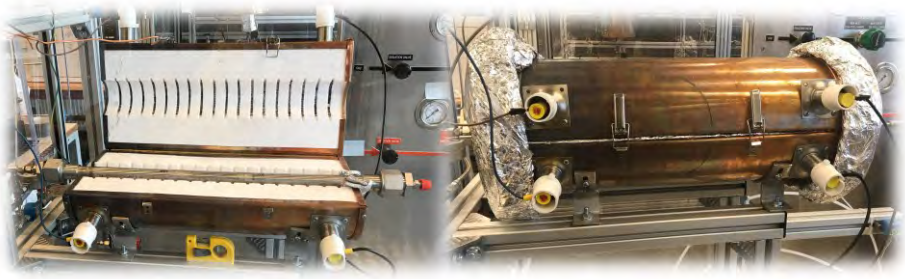

Figure 3.5 Photographs of structured reactor setup.

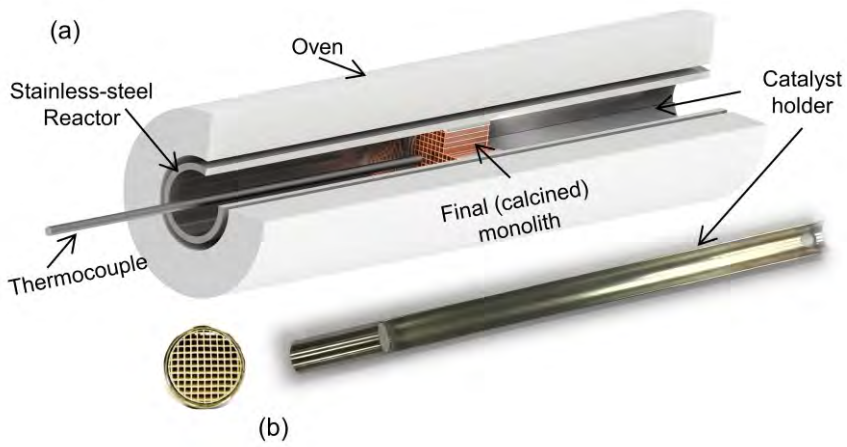

Figure 3.6 (a) Schematic diagram of structured reactor setup and (b) photograph of monolith located inside the holder.

Prior to the reaction, the monolithic catalyst was reduced at 600 ºC for 2 h in 50% H_2/N_2 with a total flow of 200 mL/min. Thereafter, the reactor was cooled down in pure N_2 flow for 2 h. Subsequently, a total flow of reactant gases of 500 mL/min was introduced, corresponding to a GHSV of 7,760 h^{-1}. The ratio of $H_2/N_2/CO_2$ was 64/20/16 vol.% (i.e., H_2/CO_2 = 4/1). The reaction was carried out at 200-500 ºC at ambient pressure and kept at each temperature for 1 h.

The gas mass flow controllers, gas inlet, outlet and splitting system, cold trap and GC used in the fixed-bed reactor setup were also employed in this setup. A blank test was conducted, and no conversion was found over pure cordierite monolith in the stainless-steel reactor.

3.3.3 Temperature profile study of structured reactor

For the study of temperature profiles along the catalytic bed, a multi-point thermocouple (Watlow) was installed to measure temperatures at 6 different positions, as illustrated in Fig. 3.7.

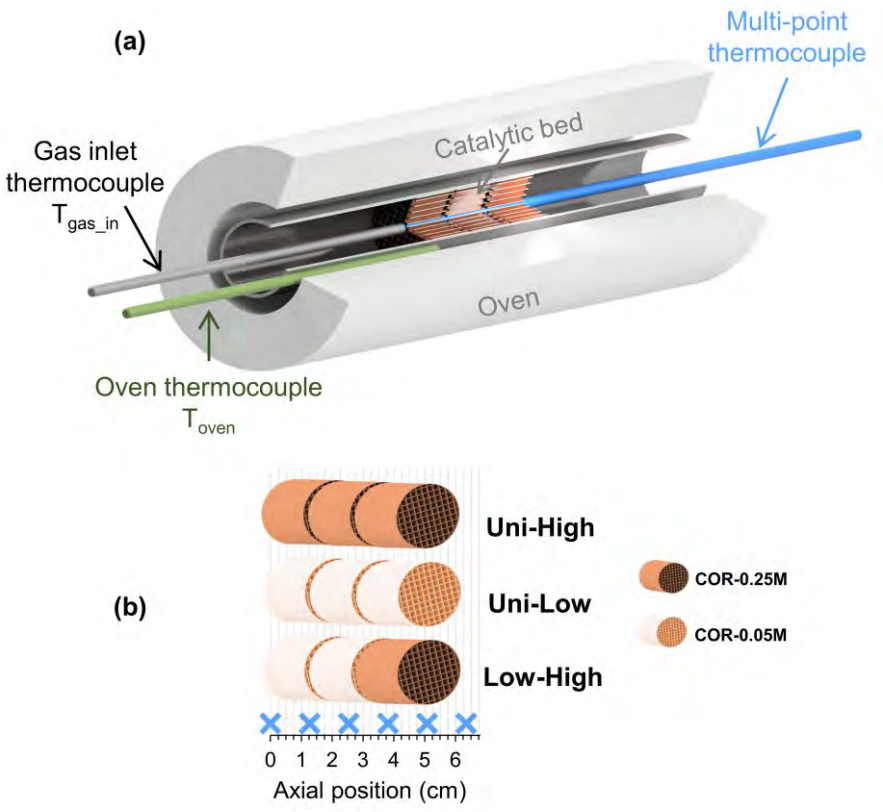

Figure 3.7 (a) Illustration of the upgraded structured reactor setup for temperature profile studies. (b) The axial position of measuring points by the multi-point thermocouple with respect to the gas inlet position of different bed packing configurations.

The catalytic bed contained three monoliths with a total length of 60 mm. The monoliths were drilled through at the center (hole diameter of 3 mm) so that the multi-point thermocouple could be inserted. The temperature of the oven was controlled by another thermocouple (T_{oven}) located outside of the reactor. Three different bed packing configurations were studied, including two beds with uniform catalytic activity and one bed with increasing catalytic activity. The temperature of the gas inlet was also monitored by the thermocouple at the gas inlet (T_{gas_in}). The reaction temperature was varied from 200 to 300 °C at ambient pressure with different gas rates of up to 3000 mL/min. The stability test was carried out at T_{oven} of 250 °C at a gas rate of 1500 mL/min for 100 h.

3.3.4 Catalytic performance indicators

The CO_2 conversion (X_{CO2}), CH_4 selectivity (S_{CH4}), and CH_4 yield (Y_{CH4}) CH_4 productivity or production rate of methane (P_{CH4}) were defined in Eqs. 3.4-3.7, where F^{in} and F^{out} are the molar rates in and out of the reactor (mol/h).

$$X_{CO2}\,(\%) = \frac{F_{CO2}^{in} - F_{CO2}^{out}}{F_{CO2}^{in}} \times 100 \tag{3.4}$$

$$S_{CH4}(\%) = \frac{F_{CH4}^{out}}{F_{CO2}^{in} - F_{CO2}^{out}} \times 100 \tag{3.5}$$

$$Y_{CH4}\,(\%) = \frac{F_{CH4}^{out}}{F_{CO2}^{in}} \times 100 \tag{3.6}$$

$$P_{CH4}\left(\mathrm{mol}/_{\mathrm{g_{cat}h}}\right) = \frac{F_{CH4}^{out}}{m_{cat}} \tag{3.7}$$

3.4 Density functional theory calculation

The Ni(111) and Ni4Fe(111) alloy were modeled using five-layered slab of (3×3) surface unit cell. The Ni(111) model is presented for NiFe-0 catalysts in **Paper III** (i.e., Ni-Fe/(Mg,Al)O_x HT-derived catalysts with

Fe/Ni ratio of 0). In the Ni4Fe model, Ni atoms were replaced with Fe atoms with a Fe/Ni ratio of ¼, representing NiFe-0.25 catalysts in **Paper III**, (i.e., Ni-Fe/(Mg,Al)O_x HT-derived catalysts with Fe/Ni ratio of 0.25).

Spin-unrestricted calculations were performed using DFT-D scheme provided by DMol3 code.[99-100] The exchange-correlation functional was expressed using the generalized gradient approximation (GGA)-Perdew, Burke, and Ernzerhof (PBE) functional.[101] Double numerical plus polarization (DNP) basis set was used throughout the calculation. The convergence criteria were set to be 1×10^{-5} Ha, 0.001 Ha $Å^{-1}$, and 0.005 Å for energy, force, and displacement convergence, respectively. A self-consistent field (SCF) density convergence with a threshold value of 1×10^{-5} Ha was specified. K-points were sampled using the 4×4×1 Monkhorst-Pack mesh for Ni and Ni-Fe alloys.

All the transition states (TS) were determined using the linear synchronous transit and quadratic synchronous transit methods. The TS structures were confirmed by using a local minimum search (after a small distortion of each TS in the reaction coordinate direction) to reach the reactants and products.[102] The desorption energy (E_{des}) of adsorbed species was calculated by Eq. 3.8, where E_{ads} and E_{surf} are the total energies of the isolated adsorbates in vacuum and the clean surface, respectively. E_{ads_surf} is the total energy of the adsorbed system.

$$E_{des} = E_{surf} + E_{ads} - E_{ads\_surf} \tag{3.8}$$

3.5 Computational fluid dynamics simulation

Numerical simulations were developed to verify the thermal profiles along the monolithic beds obtained from experimental studies. A discretized (13296 elements) 3D computational geometry of one-eighth of a monolith with the same dimensions as lab-scale experiments was built (Fig. 3.8), which consisted of channel blocks and porous walls. The

governing equations of the CFD models are reaction rate, continuity, momentum, mass, and energy equations as described in detail in Appendix F, Table S1-S3. All boundary conditions and parameters are also listed. The equations were solved by finite element based multiphysics simulation software COMSOL Multiphysics® version 5.5.

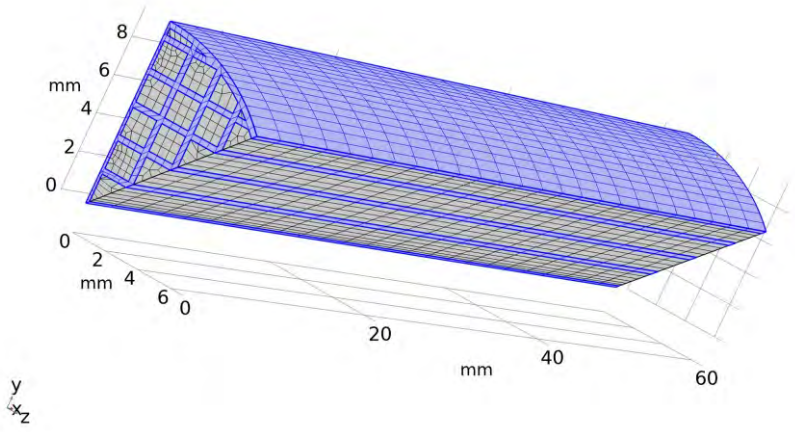

Figure 3.8 Discretized one-eighth of the full monolithic reactor geometry.

The model presents the channels in monolithic reactor with a pseudo-homogeneous approach. The reaction rate and equilibrium equation were adapted from Koschany *et al.*[34, 103] The fluid flow was assumed as a fully developed laminar flow with weak compressibility, and the average gas velocity was set at the inlet. The temperature-dependent transport properties of the multicomponent gas mixtures (heat capacity, thermal conductivity, and viscosity) were automatically calculated by the software with a mass-fraction weighted rule. The gas diffusivity was estimated using Fuller-Schettler-Giddings equations while the effective binary diffusion coefficients in the porous walls were calculated with the Bruggeman correction model.[104-106] Atmospheric pressure was applied, and the pressure drop was neglected. The energy equation defines the reacting gas temperature in the channels and conductive heat transfer in

the wall structure. The gas mixture was set at desired inlet temperature and heat generated from the reaction was the main heat source, while the ambient temperature was set as the oven temperature. Moreover, no-slip conditions were also applied together with a symmetric boundary condition since the modelling domain was reduced to one-eighth of the full reactor geometry.

4 Results and Discussion

4.1 The promoting effect of Fe on supported Ni catalysts (Paper III)

In this paper, a series of Ni-Fe/(Mg,Al)O_x hydrotalcite-derived catalysts was prepared at different Fe/Ni molar ratios to study the promoting effect of Fe. The catalysts were denoted as NiFe-*x*, where *x* is the Fe/Ni ratio varying from 0 to 0.5.

4.1.1 Catalyst characterization

4.1.1.1 XRD analysis of as-prepared precursors and calcined catalysts

As compared to the reference Mg-Al hydrotalcite material (JCPDS 01-089-0460), the XRD diffractograms of the as-prepared precursors (Fig. 4.1) showed similar characteristic diffractions and calculated lattice parameters (Appendix C, Table S1). Thus, it is confirmed the pure crystalline HT materials were successfully synthesized via the rapid coprecipitation method. An in-depth discussion on the structure of as-prepared HT precursors can be found in the next section 4.2.1.1.

Upon calcination, the precursors were fully decomposed into mixed metal oxides (Fig. 4.2), as overlapping reflections of NiO (JCPDS 01-089-5881), MgO (JCPDS 03-065-0476) and Al_2O_3 (JCPDS 01-073-1512) were observed. It has been reported that not only the rock-salt-type phase (NiO or MgO) but also crystalline spinels (e.g., $MgAl_2O_4$) would also be formed.[107] Therefore, the support in this work could be assumed to be in the mixed oxide (Mg,Al)O_x phase. Notably, the diffraction patterns of bimetallic Ni-Fe catalysts were similar to monometallic NiFe-0 catalyst. The increase of Fe content resulted in slightly poorer

crystallinity with smaller oxide crystallite sizes, as can be seen by the reduced intensity of the diffraction lines (Fig. 4.2).

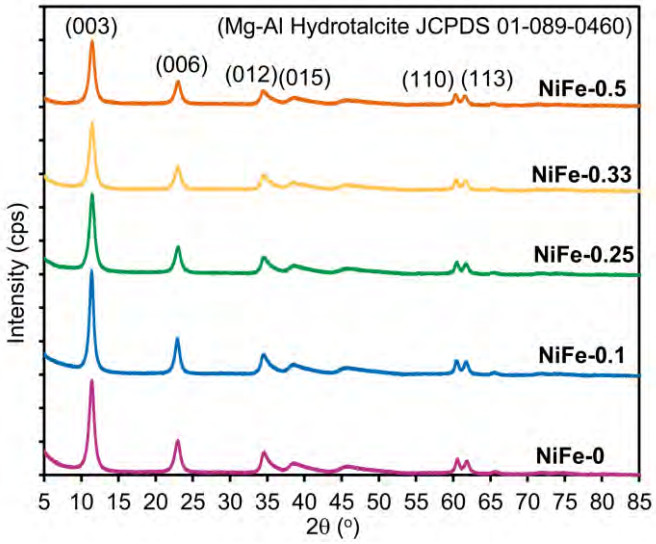

Figure 4.1 XRD diffractograms of HT precursors prepared at different Fe/Ni ratios.

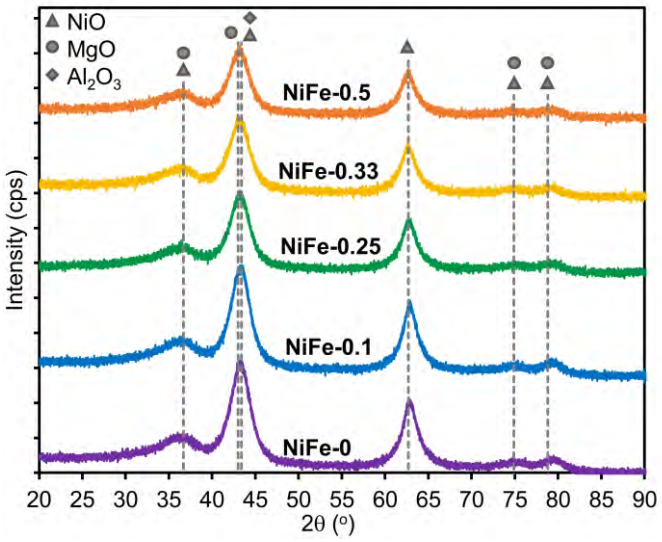

Figure 4.2 XRD diffractograms of the calcined catalysts prepared at different Fe/Ni ratios.

4.1.1.2 N_2 physisorption of calcined catalysts

The N_2 physisorption isotherms of calcined catalysts were type-IV isotherms with hysteresis loop at high P/P_o range (Appendix C, Fig. S2), attributed to mesoporous materials according to The International Union of Pure and Applied Chemistry (IUPAC) classification.[108] The pore size distribution of calcined catalysts (Appendix C, Fig. S3) further showed that calcined catalysts had mesopores in the range of 10-15 nm.

In general, all HT-derived catalysts had a relatively high surface area of 200-250 m^2/g and a large pore volume of 0.7-0.8 cm^3/g (Table 4.1). Interestingly, the increase of Fe content did not significantly affect the mesoporous texture of the catalysts.

Table 4.1 Textural properties of calcined catalysts.

Catalysts	BET Specific surface area (m^2/g)	BJH Pore volume (cm^3/g)	BJH Average pore size (nm)
NiFe-0	227.8	0.73	10.1
NiFe-0.1	240.0	0.77	11.0
NiFe-0.25	232.6	0.70	9.7
NiFe-0.33	247.3	0.72	9.7
NiFe-0.5	197.4	0.68	10.5

4.1.1.3 Elemental analysis

Elemental analysis of calcined catalysts by ICP-OES reveals the actual metal loading and Fe/Ni molar ratio, which was close to the nominal values (Table 4.2). Thus, Ni and Fe cations were confirmed to be successfully precipitated.

Table 4.2 Elemental compositions from ICP-OES of calcined catalysts.

Catalysts	Nominal Fe/Ni molar ratio	Ni (wt.%)	Fe (wt.%)	Fe/Ni molar ratio
NiFe-0	0	19.85	0	0
NiFe-0.1	0.1	19.84	1.87	0.1
NiFe-0.25	0.25	19.62	4.70	0.25
NiFe-0.33	0.33	18.83	6.39	0.36
NiFe-0.5	0.5	19.50	9.45	0.51

4.1.1.4 TPR study

The reduction behavior of calcined catalysts was investigated by H_2-TPR analysis (Fig. 4.3). For the monometallic NiFe-0 catalyst, only a single reduction peak at 810 ºC was observed, corresponding to the reduction of NiO to metallic Ni. It has been reported that the reduction temperature of pure NiO is at 290-340 ºC.[109] Other types of Ni^{2+} cations such as NiO aggregates or freely bounded NiO were not depicted. Thus, it is suggested that Ni was embedded in the $(Mg,Al)O_x$ structure and was harder to be reduced.[109-110]

For bimetallic Ni-Fe catalysts, the sequential reduction of Fe_2O_3 was not observed due to low Fe content,[111-112] and only small peaks at 350-400 ºC were detected in Fe-rich catalysts. This could be ascribed to the partial reduction of Fe_2O_3 to Fe_3O_4,[59, 113] whereas the reduction of Fe_3O_4 to Fe and NiO to Ni was overlapped at higher temperatures.[111-112] The main reduction peaks of Ni species shifted to lower temperatures with increasing Fe content. Therefore, it is anticipated that Fe addition could enhance the reducibility of the Ni-based catalysts.

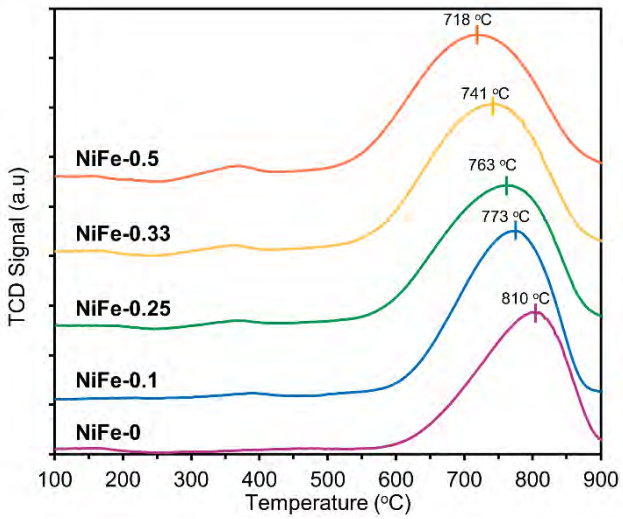

Figure 4.3 H_2-TPR profiles of the calcined catalysts.

4.1.1.5 In-situ XRD study during catalyst reduction

The in-situ XRD diffractograms of NiFe-0, NiFe-0.25, and NiFe-0.5 catalysts during reduction are shown in Fig. 4.4. For the monometallic catalyst, the diffraction line associated with metallic Ni(200) was detected at 2θ of 51.4° (JCPDS 03-065-2865) after the sample reached 600 °C for 15 min. The intensity of this line gradually increased during 90 min of reduction, indicating the growth of Ni particle from 5.3 nm to 9.1 nm (Appendix C, Table S2). Besides, the mixed oxide $(Mg,Al)O_x$ phase remained unchanged, demonstrating their irreducible nature.

As for NiFe-0.25 and NiFe-0.5 catalysts, the characteristic peak shifted to a lower angle of 50.85° and 50.75°, respectively. Correspondingly, the *d*-spacing obtained from the (200) reflection was in a linear correlation with the molar ratio of Ni/(Ni+Fe) (Appendix C, Fig. S4).[114] The lattice parameter appeared to be increased with increasing Fe content. The shift in peak position could confirm the formation of Ni-rich Ni-Fe fcc alloy upon reduction of NiFe-0.25 and NiFe-0.5 at 600 °C.[59, 114-116] Moreover,

the alloy crystals were smaller in size (5-6 nm) than Ni crystals (9 nm) (Appendix C, Table S2).

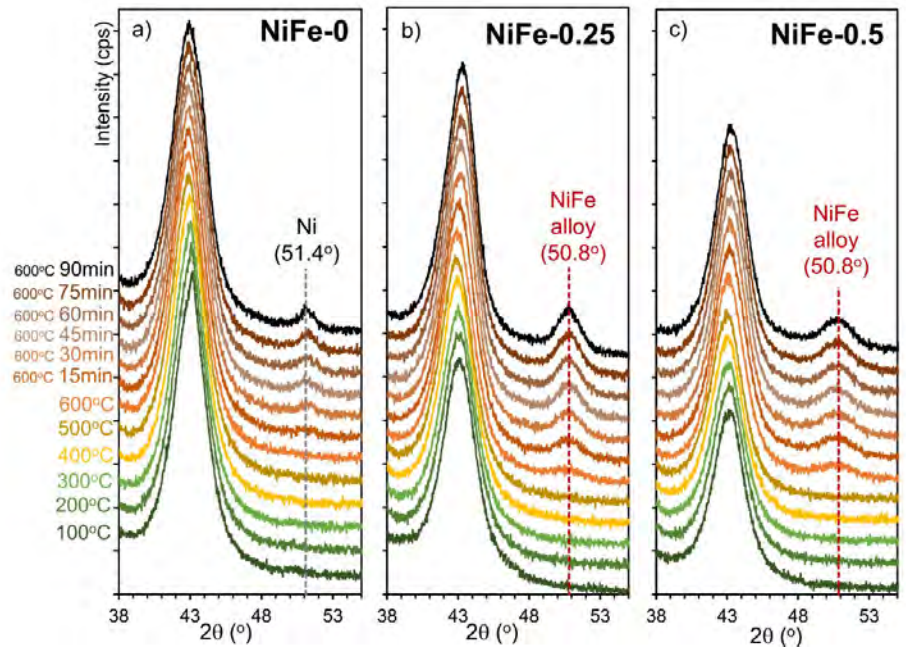

Figure 4.4 In-situ XRD diffractograms of (a) NiFe-0, (b) NiFe-0.25, and (c) NiFe-0.5 catalysts during reduction in pure H_2 at increasing temperatures and time.

4.1.1.6 Metal surface area and basicity

The maximum Ni surface area of 5.52 m^2/g was obtained from NiFe-0 catalyst based on H_2 chemisorption analysis. With increasing Fe content, the Ni surface area dramatically dropped to 0.1 m^2/g for NiFe-0.5 catalyst although the Ni loading was kept constant at 20 wt.% (Table 4.3). These results further confirmed the formation of Ni-Fe alloy which is inactive in H_2 chemisorption.[114]

CO_2-TPD analysis showed that the alloy catalysts exhibited stronger basicity than monometallic catalysts, due to the larger integrated area of the desorption profiles (Appendix C, Fig. S5). It reveals that Fe addition could enhance the total basicity of the catalysts. However, the impact of

different basic types (i.e., weak, medium, and strong) on the catalytic activity in CO_2 methanation remains disputable.[36, 117]

Table 4.3 H_2 chemisorption uptake and Ni surface area of reduced catalysts.

Catalysts	H_2 chemisorption uptake ($\mu mol/g_{cat}$)	Metal surface area (m^2/g)
NiFe-0	70.6	5.52
NiFe-0.1	50.1	3.91
NiFe-0.25	29.4	2.30
NiFe-0.33	16.4	1.28
NiFe-0.5	1.3	0.10

4.1.2 CO_2 methanation activity tests

4.1.2.1 Temperature programmed reaction study

The catalytic behavior of different Ni-Fe catalysts was firstly studied in temperature programmed reaction at atmospheric pressure. In terms of CO_2 conversion, Ni-Fe alloy catalysts were more active than monometallic Ni catalysts at low temperatures, particularly at 260-290 ºC (Fig. 4.5a). NiFe-0.25 achieved the highest CO_2 conversion of 53% at 270 ºC. As the temperature increased to 450 ºC, a decline of activity for all catalysts was observed.

During CO_2 methanation, the simultaneous RWGS reaction led to a competition between CO and CH_4 formation. At 250 ºC, the highest CH_4 selectivity was obtained from NiFe-0 catalyst (Fig. 4.5b). However, at 270-400 ºC, Ni-Fe alloy catalysts exhibited better CH_4 selectivity, particularly for NiFe-0.25 with selectivity higher than 97%. At a higher temperature of 400-450 ºC, a decrease in CH_4 selectivity was observed because the endothermic RWGS reaction was favored. Moreover, the addition of too large amount of Fe could have facilitated CO formation (i.e., NiFe-0.33 and NiFe-0.5 catalysts). It has been reported that

although Fe/(Mg,Al)O_x catalysts had very low activity in CO_2 methanation, the CO selectivity was very high (~100%).[60] Fe-rich Ni/ZrO_2 catalysts have also been found to significantly promote the RWGS reaction rather than CO_2 methanation.[58] Hence, it could be concluded that a high CH_4 yield could only be achieved over a suitable composition of Ni and Fe, particularly NiFe-0.25 catalyst in the low-temperature region.

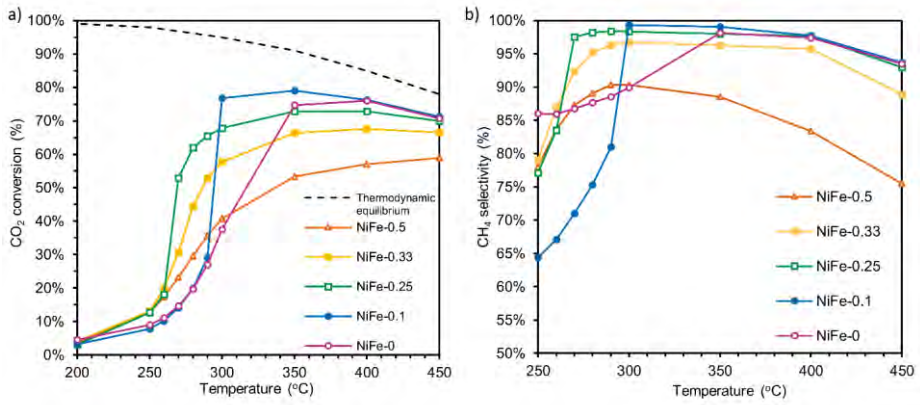

Figure 4.5 (a) CO_2 conversion and (b) CH_4 selectivity as a function of reaction temperature in CO_2 methanation ($H_2/CO_2/N_2$ = 64/16/20 vol.%, GHSV = 34,000 h^{-1}).

4.1.2.2 Long-term activity test

The best performing NiFe-0.25 catalyst was tested under high GHSV condition for more than 100 h of TOS at 300 °C. The formation rate of CH_4 was higher over NiFe-0.25 alloy catalyst compared to the monometallic NiFe-0 catalyst (Fig. 4.6). A slight decline in CO_2 conversion with 0.18%/h for NiFe-0 and 0.08%/h for NiFe-0.25 was observed. Both catalysts exhibited high stability and the deactivation rate was low compared to those reported in the literature.[59]

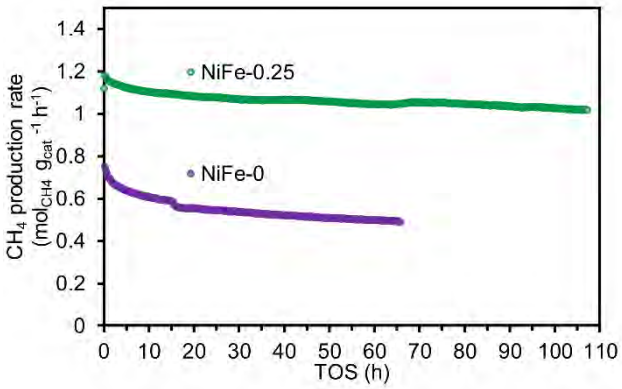

Figure 4.6 Methane production rate over NiFe-0.25 and NiFe-0 catalysts during long-term test at 300 °C ($H_2/CO_2/N_2$ = 64/16/20 vol.%, GHSV = 34,000 h^{-1}).

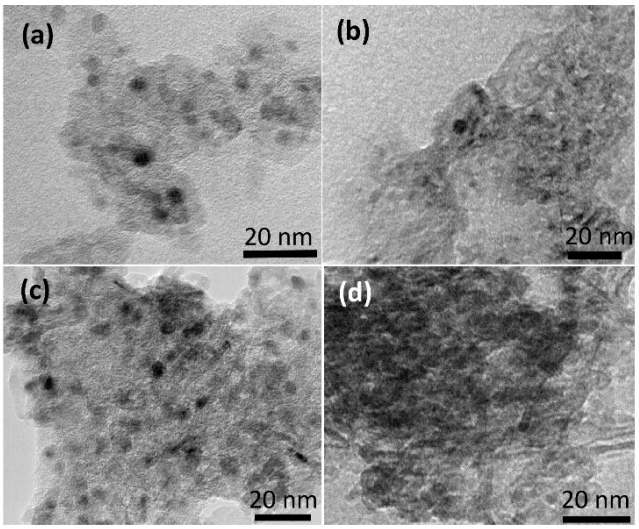

Figure 4.7 TEM images of (a) reduced-passivated NiFe-0, (b) reduced-passivated NiFe-0.25, (c) spent NiFe-0 and (d) spent NiFe-0.25 catalysts after the long-term stability test.

4.1.2.3 Catalyst deactivation study

TEM images of reduced-passivated NiFe-0 and NiFe-0.25 catalysts show that metallic particles (Ni and Ni-Fe alloy) were well dispersed on the support (Fig. 4.7.a and Fig. 4.7.b). The average particle sizes were close at 6.7±1.8 nm and 6.1±1.5 nm. TEM images of catalysts after long-term tests were also examined (Fig. 4.7.c and Fig. 4.7.d). The average particle sizes of the spent catalysts remained constant at 6.7±1.4 nm and 6.1±2.2 nm for NiFe-0 and NiFe-0.25, respectively. Since carbonaceous species were not observed, carbon formation, as well as metal sintering, are not the reason for the degradation of methanation activity.

In-situ XRD analysis was further used to study the phase changes during CO_2 methanation at increasing temperatures. In addition to previously identified mixed oxides and Ni or Ni-Fe phases, no carbon formation was observed in the in-situ XRD diffractograms (Appendix C, Fig. S6). The crystallite size of Ni and Ni-Fe alloy particles were almost unchanged during reaction at 200-350 ^{o}C. NiFe-0 catalyst maintained its metal crystallite size of approximately 9 nm, whereas Ni-Fe alloy crystallite size was stable in the range of 5-6 nm under reaction conditions at increasing temperatures (Appendix C, Table S2).

Furthermore, time-resolved in-situ DRIFTS spectra during CO_2 methanation were also recorded at 300 ^{o}C for 180 min over NiFe-0 catalysts (Appendix C, Fig. S7). While the intensity of vibration bands attributed to gaseous CH_4 species gradually reduced, linearly adsorbed *CO species on Ni was not detected during reaction. As a result, the presence of nickel carbonyl could not be confirmed.[118] Overall, metal sintering, carbon, and nickel carbonyl formation were likely not the reasons for catalyst deactivation on both Ni and Ni-Fe alloy catalysts.

4.1.3 In-situ DRIFTS study

4.1.3.1 In-situ DRIFTS during CO_2 adsorption

To identify surface species on the catalyst during CO_2 adsorption, the sample was in-situ reduced before exposure to CO_2 at increasing temperatures. Surface species are assigned as summarized in Table 4.4.

Table 4.4 Summary of infrared vibrational frequencies of observed surface species.

Species	**Frequencies (cm^{-1})**
Linear *CO_2	2350, 2035
Surface hydroxyl *OH	3600-3700
Bicarbonate *HCO_3	1220-1223, 1650-1668
Monodentate carbonate *CO_3	1360-1400
Formate *HCOO	1605, 2855
Carbonyl *CO	2210, 2035
Methane *CH_4	3015, 1305
Formyl *HCO	2735

For NiFe-0 catalyst, as the temperature increased, the intensity of *HCO_3 bands at 1223 and 1668 cm^{-1} gradually decreased, while the band of *CO_3 species only slightly reduced. Monodentate *CO_3 species were assumed to adsorb on strong basic sites of the catalyst, more stable and harder to remove at high temperatures. As for Ni-based on $(Mg,Al)O_x$ catalysts, it is anticipated that surface *OH species possibly provided weak basic sites to produce *HCO_3, whereas *O species with strong basic site facilitated the formation of monodentate *CO_3.[119]

In addition, similar surface species were detected over the NiFe-0.25 catalyst (Fig. 4.8b). Nevertheless, the most significant difference was the transition of *HCO_3 vibration bands to formate-related bands over Ni-Fe alloy catalysts, but not on NiFe-0 catalyst. The IR bands at 1605 cm^{-1} were ascribed to *HCOO species.[120-122] The formate species started to

appear at 290 °C, while the band intensity of *HCO_3 was decreased. Likewise, *HCOO species was detected at an even lower temperature of 250 °C on NiFe-0.5 (Appendix C, Fig. S8). It is suggested that Ni-Fe alloy provided a synergistic effect in the transformation of *HCO_3 to formate species.

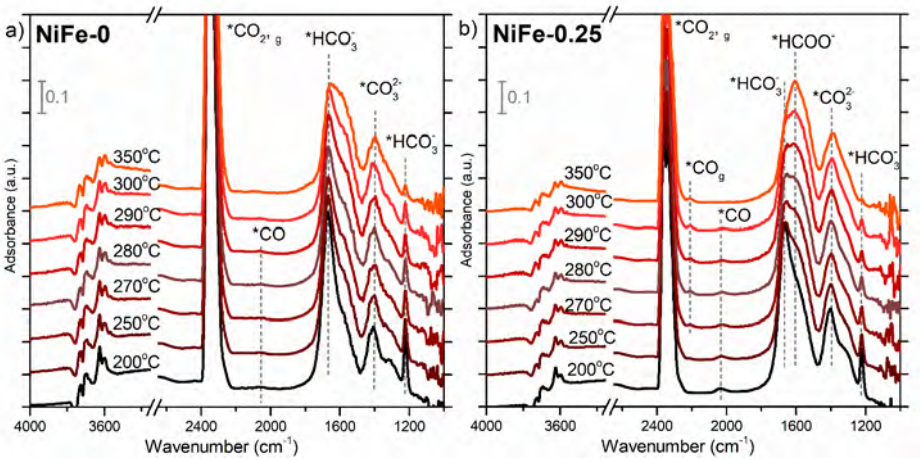

Figure 4.8 In-situ DRIFTS spectra of (a) NiFe-0 and (b) NiFe-0.25 catalysts under CO_2 adsorption condition (CO_2/N_2 = 1/5 vol.%) at increasing temperatures.

Moreover, linearly adsorbed *CO species on Ni surface (small IR bands at 2035 cm^{-1}) were detected at 200 °C but disappeared at higher temperatures of 250-350 °C. On the other hand, both linear and gaseous *CO species were found on the alloy catalysts (IR bands at 2210 cm^{-1}), especially on the Fe-rich NiFe-0.5 catalyst (Appendix C, Fig. S8). As the Fe content increased, a larger amount of gaseous *CO on the alloy surface was observed. This observation is in good agreement with previous reports that the binding energy of *CO was weaker on Ni-Fe alloy compared to Ni surface, thus *CO was desorbed easier.[58, 123] It can be speculated that the activation of *CO_2 via direct dissociation was promoted on Ni-Fe alloy surface compared to that on Ni surface. A DFT study has also reported that CO_2 activation by decomposition to *CO and *O was easier on Ni_3Fe surface than monometallic Ni surface.[114]

4.1.3.2 In-situ DRIFTS during CO_2 methanation

In-situ DRIFTS spectra of NiFe-0 and NiFe-0.25 catalysts during CO_2 methanation ($H_2/CO_2 = 4$) are presented in Fig. 4.9. The $*CH_4$ vibration on NiFe-0.25 appeared at low temperature of 200 °C, while the band intensity was always higher than on NiFe-0 at the same temperature. This further proves that the NiFe-0.25 catalyst performed higher activity in CO_2 methanation, in accordance with the temperature-dependent activity test results. Similar to the in-situ DRIFTS spectra during CO_2 adsorption, $*CO_3$, $*HCO_3$, gaseous $*CO_2$, and *OH species were all detected.

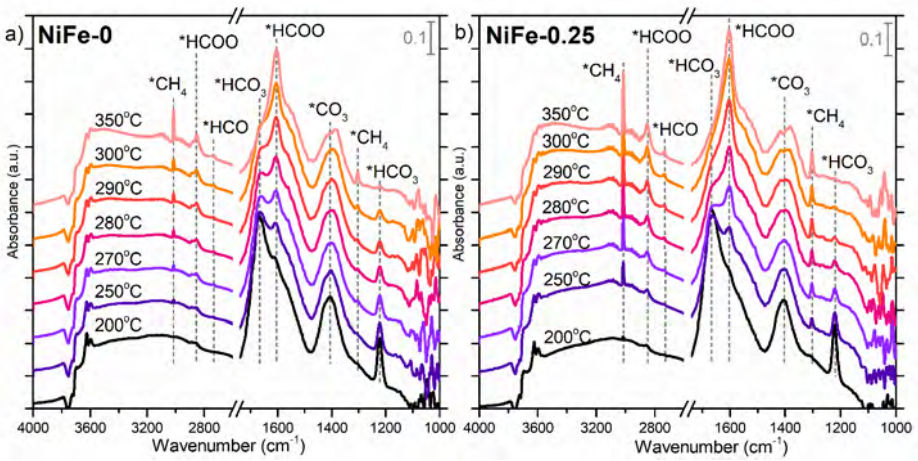

Figure 4.9 In-situ DRIFTS spectra of (a) NiFe-0 and (b) NiFe-0.25 catalysts under CO_2 methanation condition ($CO_2/H_2/N_2$ = 1/4/5 vol.%) at increasing temperatures.

As the temperature increased, a transition from $*HCO_3$ to *HCOO was observed over both catalysts. Small bands at 2855 cm^{-1} were attributed to the C-H stretching vibration from *HCOO species.[124] For NiFe-0, the peak of $*HCO_3$ decreased and disappeared at 300 °C, accompanied by the increase in intensity of *HCOO. For NiFe-0.25 catalyst, the disappearance of $*HCO_3$ readily occurred at 280 °C. Moreover, the IR bands at 2735 cm^{-1} could also be assigned to aldehyde hydrogen (formyl) *HCO species.[125-126]

Therefore, a formate pathway is highly plausible for CO_2 methanation of over Ni and Ni-Fe alloy catalysts on $(Mg,Al)O_x$ support. The addition of Fe to Ni-based catalysts would not interfere with this pathway since similar surface species were observed. The transition of $*HCO_3$ to *HCOO observed on both catalytic surfaces was assumed to follow the decomposition $*HCO_3 \leftrightarrow *HCOO+*O$. It is also possible that CO_2 was directly hydrogenated $*CO_2+*H \leftrightarrow *HCOO$ at elevated temperature, thus $*HCO_3$ formation was bypassed. *HCOO and *HCO could be the key intermediates in the reaction pathway of CO_2 methanation, while the RWGS could occur via direct CO_2 dissociation since gaseous CO species was found on Fe-rich (NiFe-0.5) catalyst during CO_2 adsorption and methanation (Appendix C, Fig. S8 and S9).

Based on the relative intensity of in-situ DRIFTS spectra, it further revealed that Ni-Fe alloy could accelerate the formation of *HCOO and *HCO intermediates compared to the monometallic (NiFe-0) catalyst (Appendix C, Fig. S10). *HCOO formation rate would be promoted by increasing Fe content (NiFe-0.5 > NiFe-0.25 > NiFe-0). However, the production rate of *HCO and CH_4 did not follow this trend (NiFe-0.25 > NiFe-0.5 > NiFe-0). Moreover, because Fe-based catalysts are active for the RWGS reaction,[127-128] tuning Fe content is therefore of great importance to achieve the best performance of Ni-Fe alloy catalysts for CO_2 methanation. The transformation of $*HCOO \rightarrow *HCO \rightarrow *CH_4$ could be the key to decipher the promoting effect of Fe in the Ni-Fe alloy catalysts.

4.1.4 Reaction mechanism via DFT calculations

To unravel the reaction mechanisms and the higher activity of Ni-Fe alloy compared to monometallic Ni catalysts in CO_2 methanation, DFT calculations were performed on the Ni(111) and Ni4Fe(111) (representing NiFe-0 and NiFe-0.25 catalysts, respectively, as shown in Appendix C, Fig. S11). Energetics of elementary reactions and the desorption energy of adsorbed species are presented in Appendix C,

Table S3 and Table S4, together with the stable geometries of reaction intermediates and its coordinates (Appendix C, Fig. S12, Fig. S13 and Table S5).

4.1.4.1 H_2 dissociation and diffusion

The dissociation of H_2 and diffusion of *H atom on the surface of catalyst directly determine whether the catalyst can provide enough *H atom for CO_2 methanation. Activation energy (E_a) for the dissociation of H_2 on Ni(111) and Ni4Fe(111) (Fig. 4.10a) was calculated and implied that H_2 dissociation was facile. The reaction energy (ΔE) for H_2 dissociation was between -19.2 to -30 kcal/mol, thus it can be speculated that formed *H atoms were relatively stable on both catalysts. The diffusion barriers for *H atom on Ni(111) and Ni4Fe(111) were estimated to be 12.0 and 16.0 kcal/mol, respectively (Fig. 4.10b). This indicates that the diffusion of *H atoms was relatively easy on both catalysts, suggesting the sufficient availability of *H atoms for CO_2 methanation.

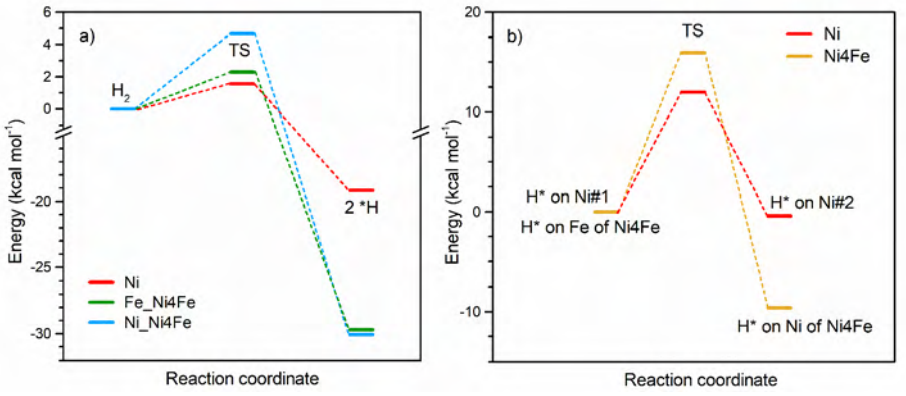

Figure 4.10 (a) H_2 dissociation pathway and (b) *H diffusion pathway on Ni and Ni4Fe surface.

4.1.4.2 CO_2 methanation on Ni and Ni-Fe alloy surface

Based on the in-situ DRIFTS observation and literature data,[25] possible pathways for CO_2 methanation to CH_4 and CO are proposed in Fig. 4.11. The initial step of CO_2 methanation could occur on either O-terminal to

produce *COOH (carboxylate pathway) or C-terminal to produce *HCOO (formate pathway). The direct C-O dissociation of CO_2 to *CO and *O is also possible. It is noteworthy that *COH can also be formed from *CO hydrogenation. However, it was not included in this thesis because *HCO (also written as *CHO) formation was more favorable.[129] Many studies assumed that *HCO is one of the key intermediates of CO_2 methanation,[58, 130] which has been observed previously in the in-situ DRIFTS study. Moreover, while *HCO intermediate can transform to *CHOH, *H_2CO, or *CH as intermediates for final product CH_4, *HCO dissociation (*HCO ↔ *CH+*O) was reported as the most favorable pathway.[58, 129]

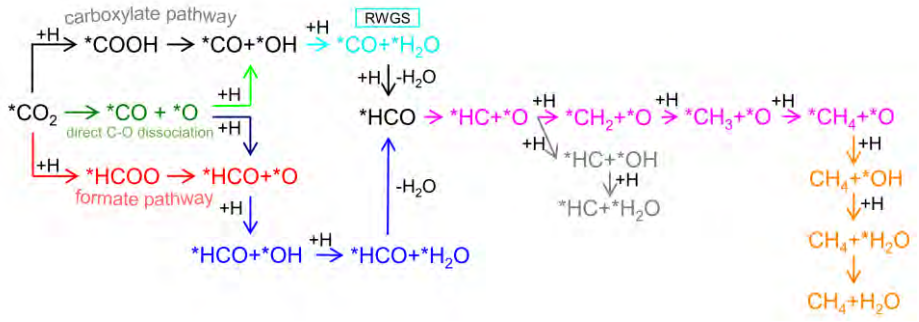

Figure 4.11 Plausible reaction pathways of CO_2 methanation.

Besides CO_2 methanation, the RWGS reaction can occur simultaneously and its mechanism can also be understood by DFT calculations. The side reaction could follow either the carboxylate pathway or direct CO_2 dissociation pathway since the dissociated *CO species (cyan route in Fig. 4.11) could desorb as a gaseous product while surface *O and *OH were removed as water.

The energy diagram of *HCO formation via COOH route with a partial contribution from the direct CO_2 dissociation on both Ni(111) and Ni4Fe(111) surface is presented in Fig. 4.12ab. Likewise, Fig. 4.12cd illustrates the energy diagram via the HCOO route and its partial direct CO_2 dissociation pathway.

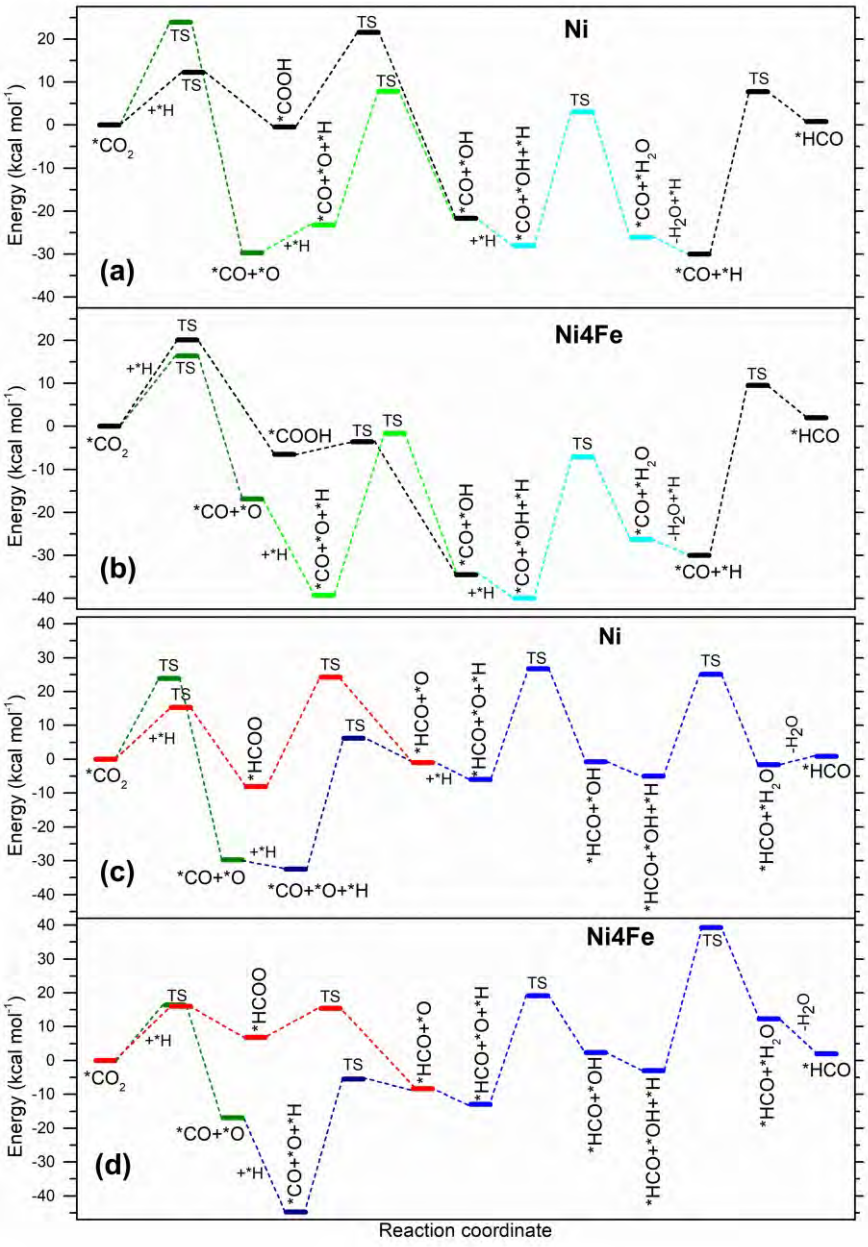

Figure 4.12 The energy diagram of *HCO formation via carboxylate pathway on (a) Ni and (b) Ni4Fe; via formate pathway on (c) Ni and (d) Ni4Fe. The CO_2 direct dissociation pathway is also included.

From the energy diagram (Fig. 4.12ab), it can be observed that Ni-Fe alloy easily promoted *CO_2 direct dissociation, compared to that of Ni-only catalyst, which was consistent with Kim *et al.*[114] and the in-situ CO_2 adsorption study. However, the subsequent hydrogenation of *O at (*CO+*O) state was difficult on both surfaces. In fact, the hydrogenation of *CO to *HCO was rather difficult due to high energy barrier (E_a of roughly 38-40 kcal/mol) via either COOH or direct dissociation pathway. On the contrary, *CO_2 was more likely to be hydrogenated to *HCOO with a moderate E_a of 15.2-16.0 kcal/mol (Fig. 4.12cd). Therefore, the transformation of *CO_2→*HCOO→*HCO was more facile than that of *CO_2→*CO→*HCO regardless of the catalytic systems.

Interestingly, for the C-O bond cleavage of *HCOO to *HCO, while an E_a of 32.3 kcal/mol was needed on Ni, only 8.5 kcal/mol was required for Ni4Fe alloy (Fig. 4.12cd). Hence, *HCO was formed much easier on Ni4Fe alloy surface than on Ni surface. Moreover, *HCOO appeared to be more stable on Ni surface and could be detected experimentally,[131] while Ni4Fe alloy was more active to produce *HCO. This could explain the higher formation rate of *HCOO and *HCO observed in the in-situ DRIFTS study.

It should be noted that *HCO intermediate was not stable and preferred to decompose back to *CO since the energy barrier of *HCO formation was much higher than its dissociation (Fig. 4.12ab). Thus, RWGS reaction was likely occurred following the COOH pathway. However, CO desorption was very difficult due to the strong binding of *CO to the metallic surfaces (E_{des} = 59.7 and E_{des} = 58.1 kcal/mol on Ni and Ni4Fe, respectively). Hence, steadily adsorbed *CO would occupy the active sites and deactivate the catalysts during reaction. In this study, *CO was formed and desorbed easier on Ni-Fe alloy compared to the Ni surface in both experiments and calculations. This could explain the more stable performance of NiFe-0.25 compared to NiFe-0 catalyst in the long-term test.

Fig. 4.13 illustrates the energy diagram of *HCO→*CH_4 transformation on Ni and Ni4Fe. Alloy surface seems to promote *CH formation better than Ni alone. When (*CH+*O) was hydrogenated, either *CH_2 or *OH could be formed. While *CH further yielded *CH_4, water could also be produced (Appendix C, Fig. S14, gray pathway). Since the formation of *CH_4 from *CH_3 required very high E_a (26.2-26.9 kcal/mol) on both surfaces, it could be the RDS of *HCO→*CH_4.

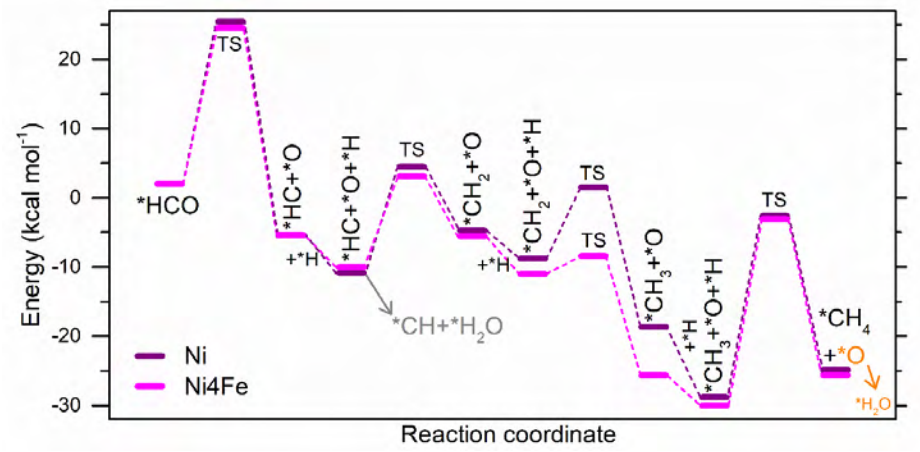

Figure 4.13 The energy diagram of *CH_4 formation from *HCO on Ni and Ni4Fe.

Finally, *CH_4 was desorbed to gaseous CH_4 as product on both catalytic surfaces. The energy diagram for water produced from *O at (*CH_4+*O) state is also presented in Appendix C, Fig. S14, orange pathway. The removal of *O by two steps hydrogenation is crucial because not only the active sites would be free from occupied *O, but *H_2O would also be produced as product of both RWGS reaction and CO_2 methanation. The formation of *H_2O via *OH+*H ↔ *H_2O required significantly high E_a compared to the formation of *CH_4, which agreed with Zhang *et al.*[132] However, *H_2O could also be formed via *OH+*OH ↔ *H_2O+*O at very low E_a (3.4 and 1.2 kcal/mol on Ni and Ni4Fe surface, respectively).

Microkinetic modelling on Ni(111) surface reported that HCO* ↔ CH*+O* was the main RDS for CO_2 methanation.[26] As mentioned above, the decomposition of *HCO was better promoted on Ni4Fe than on Ni surface due to a lower energy barrier. According to our DFT calculations, *HCO formation via *HCOO was the most energetically favorable pathway, especially on Ni4Fe alloy surface. Fe alloying with Ni at a certain molar ratio could result in an effective catalytic system that reduced the energy barrier for *CO_2 hydrogenation. The alloy surface further facilitated the dissociation of *HCO to *CH, thus accelerated the *CH_4 formation.

In addition, the desorption of *CO was easier on Ni4Fe than on Ni surface. While stably adsorbed *CO could block available sites on the surface, *O and *H_2O were also possible to occupy the Ni and NiFe active sites. The removal of *O via two-step hydrogenation to water is important. It was recently proposed that Fe could hinder Ni hydroxylation thus catalyst deactivation since it could be the preferential site for water production.[133-134] However, our DFT results showed that similar energy is required for *H_2O formation and desorption on both Ni and alloy surfaces. Further studies on the deactivation mechanism of Ni and Ni-Fe alloy are therefore highly recommended.

4.2 Effect of preparation parameter on the performance of Ni-Fe catalysts (Paper IV)

In this paper, Ni-Fe/(Mg,Al)O_x HT-derived catalysts were prepared via coprecipitation at different metal concentrations of 0.25 M, 1 M and 2.5 M. The catalysts were denoted as NiFe-*x*M, where *x* is the total metal concentration.

4.2.1 Catalyst characterization

4.2.1.1 XRD analysis of as-prepared precursors and calcined catalysts

In the XRD diffractograms of the as-prepared precursors (Fig. 4.14), common LDH diffraction peaks of MgAl-HT (JCPDS 01-089-0460) were detected, i.e., symmetric and sharp reflections of the basal (003), (006), (012) planes at 2θ of 11.4°, 22.9°, and 34.5°, respectively; broader and smaller peaks at 2θ of 38.5°, 45.6°, 60.5°, and 61.8° ascribed to the nonbasal (015), (018), (110) and (113) planes, respectively. No other phases were identifiable. Thus, it can be inferred that HT precursors with high purity and crystallinity were successfully synthesized regardless of metal concentrations.

It was reported that HT materials have layered structures in rhombohedral 3R symmetry and the parameters of a unit cell, *a* and *c*, could be derived from *d*(110) and *d*(003) spacing.[64] The thickness of one layer consisting of a brucite-like sheet and one interlayer could be estimated based on the *d*-spacing of the (003) plane. Meanwhile, the average cation-cation distance in the brucite-like layer could be correlated to the *d*-spacing of the (110) plane. The lattice parameters of as-prepared precursors are summarized in Table 4.5.

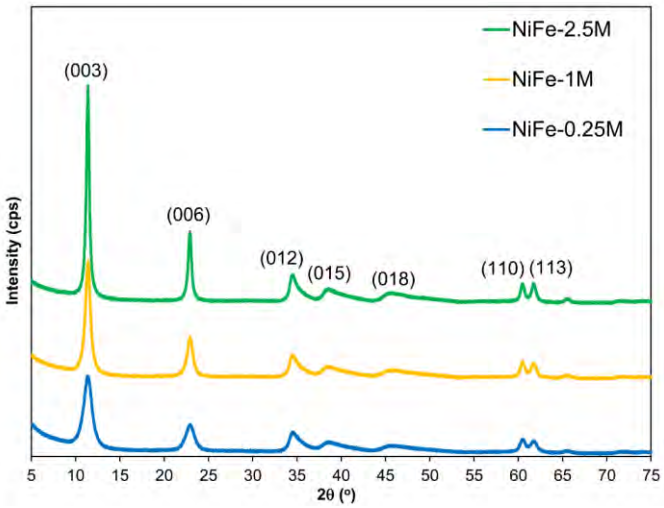

Figure 4.14 XRD diffractograms of HT precursors prepared at different metal concentrations.

Table 4.5 Physicochemical properties of as-prepared HT precursors.

	NiFe-0.25M	**NiFe-1M**	**NiFe-2.5M**	**Reference** [135]
Lattice cell parameter *a* (Å)*	3.06	3.06	3.06	3.07
Lattice cell parameter *c* (Å)*	23.31	23.29	23.29	23.81
Crystallite size (nm)	7.9	12.8	22.0	5.8
Mass obtained per batch (g)	1.90	7.66	18.77	-
BET surface area (m^2/g)	218.8	158.8	114.4	118.0
BJH pore volume (cm^3/g)	0.45	0.46	0.30	0.40

*$a = 2 \times d(110)$ and $c = 3 \times d(003)$

Interestingly, there was no significant difference in the lattice parameters between precursors prepared at different concentrations. Moreover, the unit cells of all precursors were slightly smaller than that of the reference material, $Mg_{0.75}Al_{0.25}CO_3(OH)_{0.125} \cdot 0.71H_2O$.[135] This could be due to the substitution of smaller Ni^{2+} ion for larger Mg^{2+} ion (i.e., radii of 0.69 Å

and 0.72 Å, respectively) in the layered structures. Thus, Ni (and Fe) cations were assumed to incorporate well into the HT structures.

The crystallite size of the precursors was calculated from the (003) reflection using Scherrer's equation (Table 4.5). The crystallite size was larger than that of the reference material. As the metal concentration increased, larger crystals were obtained. Furthermore, it can be seen that a significantly larger amount of catalyst mass was obtained by increasing the total metal concentration during coprecipitation (Table 4.5).

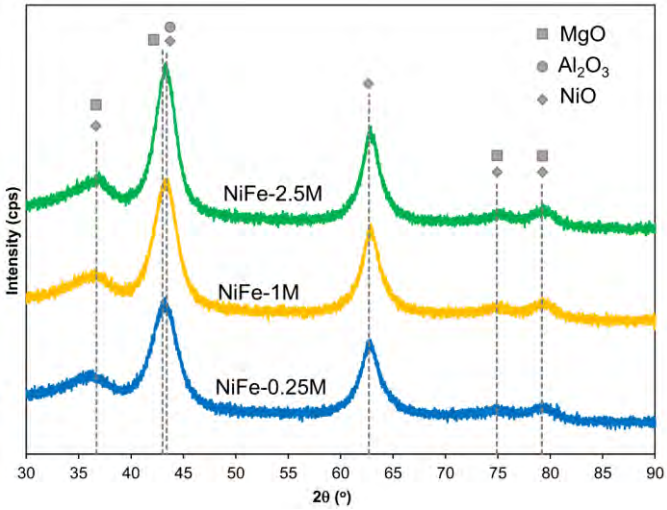

Figure 4.15 XRD diffractograms of calcined catalysts prepared at different metal concentrations.

Upon calcination, the HT structures were completely decomposed since only diffraction patterns of oxide phases were detected (Fig. 4.15). In this study, the main reflection peaks could be attributed to not only NiO (JCPDS 01-089-5881) but also MgO (JCPDS 03-065-0476) and Al_2O_3 (JCPDS 01-073-1512). However, it is difficult to distinguish these phases due to overlapped diffraction patterns. The XRD diffractograms of reduced-passivated NiFe-2.5M and NiFe-1M catalysts are shown in Fig. 4.16. The formation of Ni-Fe alloy was confirmed by the representative peak of Ni_3Fe (200) at 2θ of 51.2° (JCPDS 03-065-3244).

Diffraction peaks of MgO and Al_2O_3 were still apparent in the reduced-passivated samples. For both catalysts, the calculated crystallite size of Ni-Fe alloy was close to the oxide crystallite size of the calcined catalysts of ~5 nm (Table 4.6).

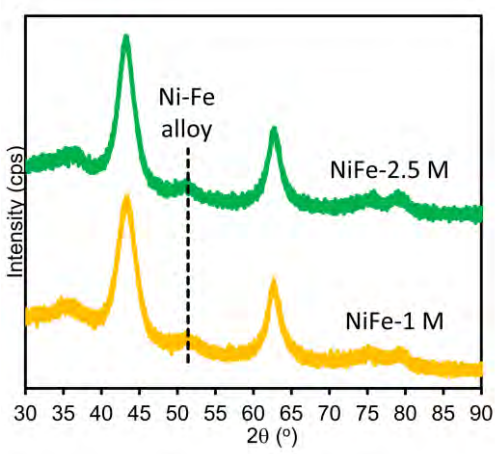

Figure 4.16 XRD diffractograms of reduced-passivated catalysts prepared at different metal concentrations.

Table 4.6 Physicochemical properties of calcined catalysts.

	NiFe-0.25M	**NiFe-1M**	**NiFe-2.5M**
Oxide crystallite size (nm)	4.6	4.9	5.1
BET surface area (m^2/g)	294.7	240.6	231.4
BJH pore volume (cm^3/g)	0.68	0.77	0.45
Ni surface area (m^2/g)	3.38	3.91	4.00
Reduction degree	66%	69%	68%
Ni dispersion	4.07%	4.48%	4.68%
Ni-Fe crystallite size (nm)	-	4.8	5.1

4.2.1.2 N_2 physisorption of calcined catalysts

The textural properties of calcined catalysts are summarized in Table 4.6. The N_2 adsorption-desorption isotherms showed a type-IV isotherm with hysteresis at high P/P_o range, which is characteristic of mesoporous materials (Fig. 4.17a). Compared to the textural properties of as-prepared precursors (Table 4.5), the calcined catalysts had higher surface area and pore volume. Upon calcination at 600 ^oC, the layered structures collapsed, resulting in higher surface area and larger pore channels. However, with increasing metal concentration, the surface area and pore volume decreased. Nevertheless, all calcined catalysts exhibited a high surface area (230-300 m^2/g) and pore volume (0.4-0.8 cm^3g) compared to conventional catalysts.[60]

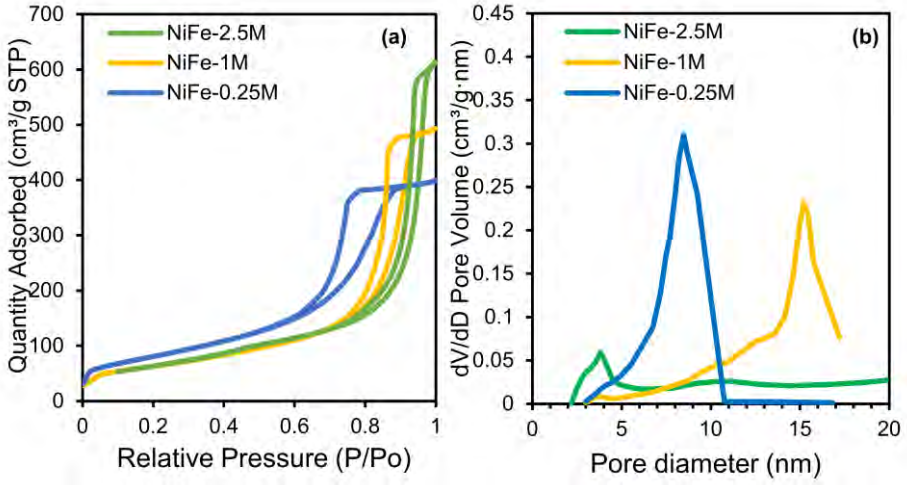

Figure 4.17 (a) N_2 physisorption isotherms and (b) BJH pore size distribution of calcined catalysts prepared at different metal concentrations.

Catalysts prepared by the rapid coprecipitation method also possessed a uniform pore structure according to their pore size distribution (Fig. 4.17b). The pore size of the calcined NiFe-0.25M catalyst was 8-10 nm, while the pore size of the calcined NiFe-1M catalyst was larger at 14-16 nm. Interestingly, the structure of the calcined NiFe-2.5M catalyst

consisted of significantly small pores of ~4 nm. It is worth mentioning that this tunable pore dimension by different metal concentrations in this study can be used in other reactions such as Fischer-Tropsch synthesis.[136]

4.2.1.3 TPR study

To study the reducibility of different catalysts, TPR analysis was conducted. All H_2-TPR profiles exhibited one intense peak at a high temperature range of 760-800 ºC (Fig. 4.18a), ascribed to the reduction of NiO species to metallic Ni. For catalysts prepared at higher metal concentrations, the reduction peaks slightly shifted to higher temperatures. However, it can be assumed that the reducibility of all three catalysts was similar, regardless of total metal concentrations.

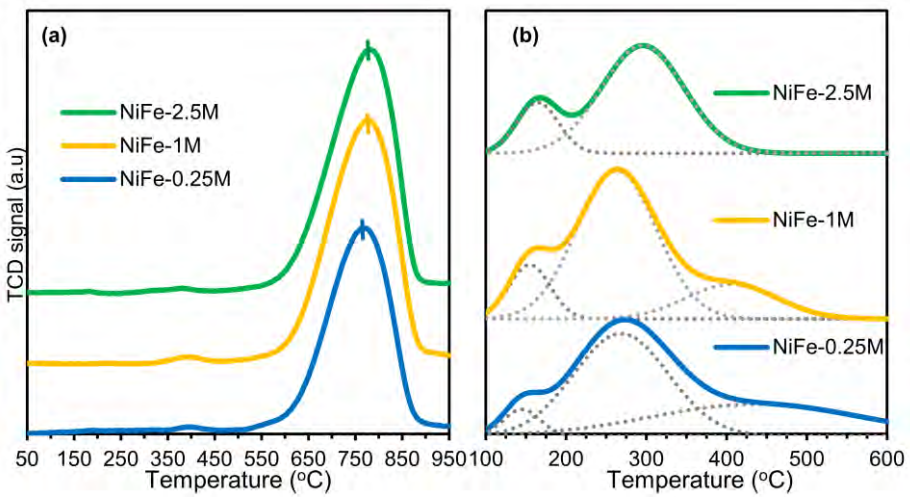

Figure 4.18 (a) H_2-TPR profiles of calcined catalysts and (b) CO_2-TPD profiles of reduced catalysts.

4.2.1.4 TPD study

CO_2-TPD analysis has been carried out to study the surface basicity. The desorption profiles (Fig. 4.18b) show three peaks corresponding to weak,

medium and strong basic sites.[119] The NiFe-1M catalyst possessed the highest total basicity among the others since its integrated area under the desorption line was the largest, which is expected to perform a better catalytic activity. However, the impact of different basic types (weak, medium, and strong) on the catalytic activity in CO_2 methanation remains ambiguous. The strong basic site was suggested to be the dominant factor,[117] while the weak basic site was assumed to be more responsible for the improvement of catalytic activity.[36]

4.2.1.5 Chemisorption study

The Ni surface area was calculated from the adsorbed amount of H_2 based on the chemisorption study. H_2 was assumed to adsorb only on Ni atoms and not Fe atoms. For the determination of metal dispersion, the reduction degree was calculated (Table 4.6), reconfirmed the similar reducibility of all catalysts. Moreover, as the metal concentration increased, the Ni-Fe alloy catalysts exhibited slightly higher Ni surface area and better Ni dispersion.

4.2.1.6 SEM & TEM characterization

The SEM characterization revealed an agglomerated morphology of NiFe-1M (Fig. 4.19a) and NiFe-2.5M HT precursors (Fig. 4.20ab). Spherical agglomerates were observed for both precursors. TEM images of the reduced-passivated catalysts show the highly dispersed Ni-Fe round-shaped particles (dark color) on the support (Fig. 4.19b and 4.20cd). The average particle size from the TEM images was obtained by measuring about 750-800 particles for each sample using ImageJ software. Notably, the increase in total metal concentration did not significantly affect the average size of Ni-Fe alloy particles, which was approximately 6.0±1.4 nm for NiFe-1M and 6.5±1.7 nm for the NiFe-2.5M catalyst. These results are also close to the crystallite size obtained from the XRD study.

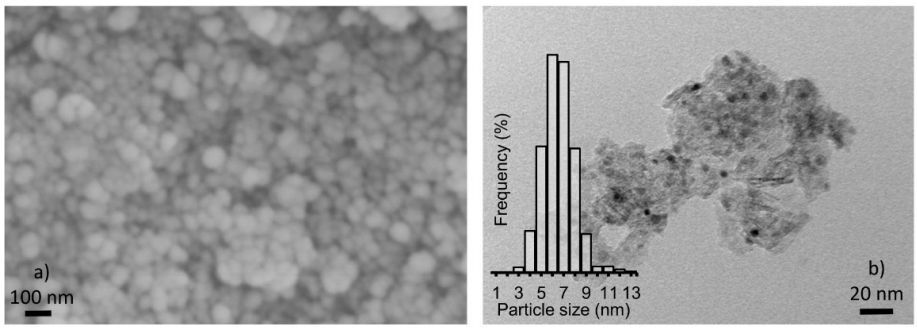

Figure 4.19 (a) SEM images of NiFe-1M HT precursors; (b) TEM bright-field images of reduced-passivated NiFe-1M catalyst. The inset in (b) is the particle size distribution.

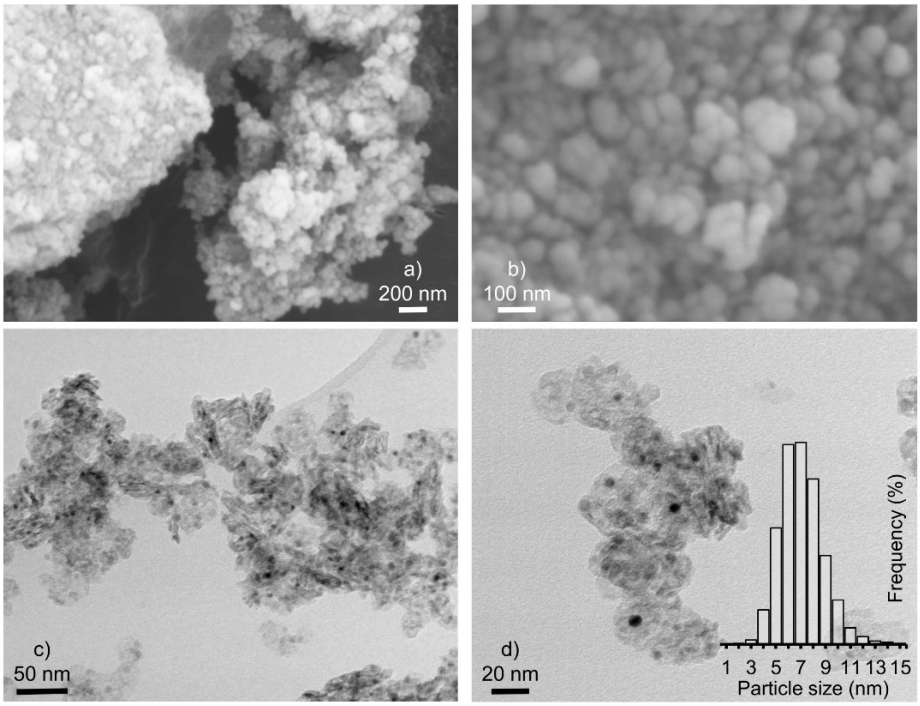

Figure 4.20 (a-b) SEM images of NiFe-2.5M HT precursors; (c-d) TEM bright-field images of reduced-passivated NiFe-2.5M catalyst. The inset in (d) is the particle size distribution.

4.2.2 CO_2 methanation activity tests

4.2.2.1 Temperature programmed reaction study

The activity of Ni-Fe/(Mg,Al)O_x catalysts prepared at different metal concentrations was studied in the temperature programmed reaction. Although Sabatier reaction was thermodynamically favored at low temperatures, kinetic limitations prevented the reaction to readily occur. As expected, poor performance at 200-250 °C is observed for all catalysts (Fig. 4.21a). From 250 °C to 300 °C, CO_2 conversions plunged up from approximately 10% to 73-79%. The conversions slightly declined at 350-450 °C because of the reaction thermodynamics.[20] The CH_4 selectivity reached 93-95% at 300-450 °C for all catalysts (Fig. 4.21b). The production of CH_4 was not significant at low temperatures of 200-250 °C. Meanwhile, a small amount of CO was also formed, probably from the RWGS reaction. The selectivity of CO increased at 400-450 °C because CO production via RWGS was thermodynamically favored at high temperatures.

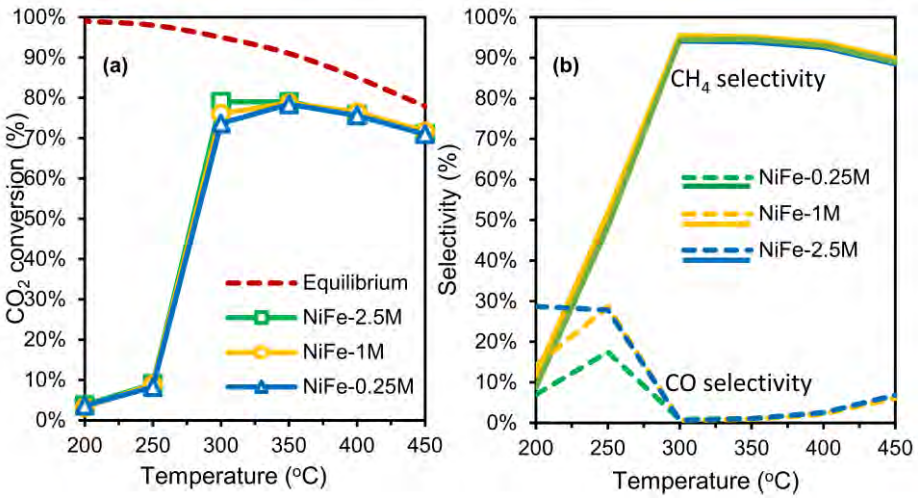

Figure 4.21 (a) CO_2 conversion and (b) CH_4 and CO selectivity of catalysts prepared at different metal concentrations in CO_2 methanation ($H_2/CO_2/N_2$ = 64/16/20 vol.%, GHSV = 34,000 h^{-1}).

Overall, the activity of all three catalysts were not significantly different. By increasing the total metal concentration up to 10 times higher, a larger amount of catalyst mass was obtained but their catalytic performance remained unchanged. This demonstrates the feasibility of large-scale preparation of catalysts by the proposed method in this study.

4.2.2.2 Long-term activity test

A long-term test of NiFe-1M catalysts was carried out at 300 °C at a GHSV of 34,000 h^{-1} or WHSV of 43.2 $L_{CO2}/g_{cat}/h$ (Fig. 4.22). The initial CO_2 conversion was 71.78% and reduced to 68.09% after 65 h TOS, corresponding to a deactivation rate of only 0.057%/h. Mutz *et al.*[59] reported a deactivation rate of 0.12%/h of 20 wt.% Ni/Al_2O_3 commercial catalysts in CO_2 methanation at 358 °C, 6 bar, and WHSV of 80.5 $L_{CO2}/g_{cat}/h$. Under the same condition but at 305 °C, the prepared 17 wt.% Ni_3Fe/Al_2O_3 catalysts showed a deactivation of 0.3%/h. Thus, Ni-Fe/(Mg,Al)O_x can be assumed to have better stability than the commercial and other alumina supported catalysts.

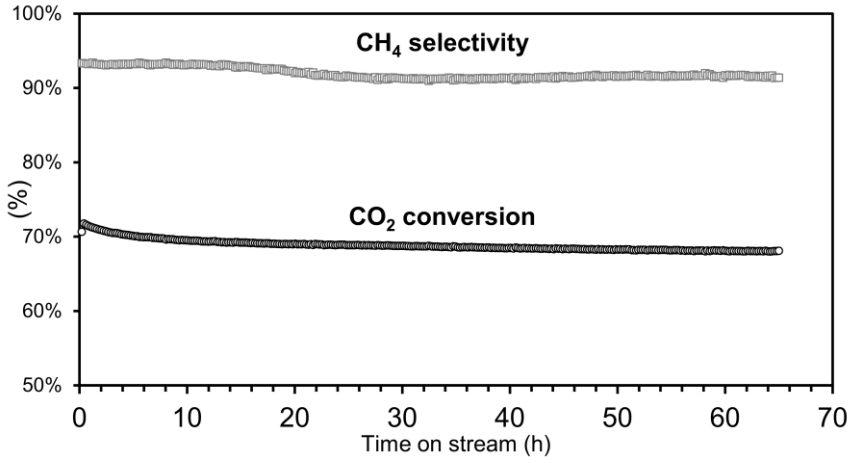

Figure 4.22 CO_2 conversion and CH_4 selectivity during a long-term test of NiFe-1M catalyst in CO_2 methanation at 300 °C ($H_2/CO_2/N_2$ = 64/16/20, GHSV = 34,000 h^{-1}).

4.3 Structured Ni-Fe catalysts derived from in-situ grown layered double hydroxides on ceramic monolith (Paper V)

This paper focused on the preparation of Ni-Fe monolithic catalysts. The ceramic substrate was washcoated with either alumina or silica colloidal (denoted as COR-AluCC and COR-SiCC, respectively). Subsequently, Ni-Fe LDHs precursors were in-situ grown on the washcoated substrate surface via urea hydrolysis at metal concentration of 0.05 M and 0.5 M. Characterizations were carried out comprehensively on the monolithic catalysts (denoted as COR-AluCC-*x*M and COR-SiCC-*x*M, where *x* is the total metal concentration) and the corresponding powder precursors (i.e., LDH-0.05M and LDH-0.5M).

4.3.1 Synthesis reproducibility

The first step of structured catalysts preparation was dip coating support materials (i.e., Al_2O_3 and SiO_2) onto cordierite monoliths using colloidal solutions. The weight gain of monoliths after several colloidal coating cycles is presented in Fig. 4.23. For Al_2O_3 coating, the washcoat layer reached 14±0.5 wt.% after three times of dip coating and drying. The weight gain of six different monoliths as shown in Fig. 4.23 demonstrates the high reproducibility of the synthesis procedure. On the other hand, one coating cycle was sufficient to achieve a washcoat layer of 17±1 wt.% for SiO_2, where the reproducibility was also confirmed by four monolith samples. Calcination was subsequently conducted for the fixation of the support materials onto cordierite. As a result, the weight of washcoat layers was reduced to 12 wt.% for COR-AluCC and 16 wt.% for COR-SiCC.

In the second step, NiFe-CO_3 LDHs were in-situ grown on the washcoated monoliths by urea hydrolysis at 110 ^oC for 24 h. After washing, drying, and calcination, the mixed oxides layer was fixed on the cordierite monoliths. Herein, the catalyst loading was defined as the

percentage of the catalytic mass (mixed oxides) on the weight of original monolith, as summarized in Table 4.7. It can be seen that Al_2O_3 was more advantageous for the deposition of the catalyst layer than SiO_2, even though SiO_2 was easier to be washcoated on the monolith.

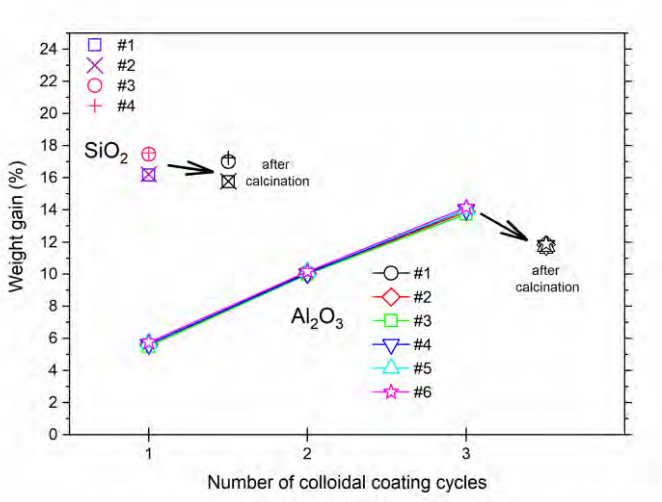

Figure 4.23 The weight gain of monoliths after colloidal coating and calcination.

Table 4.7 Synthesis parameters, mass of in-situ grown LDHs, catalyst loading and the adherence of structured catalysts.

Structured catalysts	Colloidal solution	Total metal concen-tration	Mass of LDHs (mg)	Catalyst loading (wt. %)	Adherence % (wt. loss %)
COR-AluCC-0.5M	Al_2O_3	0.5 M	175.8	2.85%	99.2% (0.8%)
COR-AluCC-0.05M	Al_2O_3	0.05 M	60.1	0.58%	99.6% (0.4%)
COR-SiCC-0.5M	SiO_2	0.5 M	112.8	2.24%	98.9% (1.1%)

4.3.2 Characterization of LDHs layer

XRD analysis was conducted on the dry powder precursors obtained after urea hydrolysis, as shown in Fig. 4.24. Because characteristic

diffraction peaks of LDHs structures (NiFe-CO_3 LDHs, JCPDS 00-051-0463) were observed for both LDH-0.5M and LDH-0.05M, it can be confirmed that NiFe-CO_3 LDHs with high crystallinity were successfully synthesized via urea hydrolysis.

Moreover, the XRD analysis of calcined LDHs confirmed that LDHs structures were completely transformed into mixed metal oxides since only diffraction patterns of $NiFe_2O_4$ (JCPDS 00-054-0964) and NiO (JCPDS 01-089-5881) were identified (Fig. 4.25).

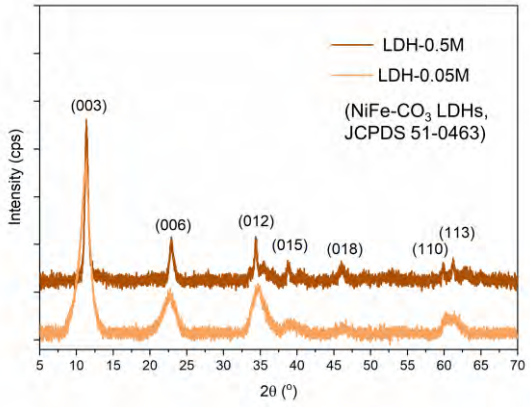

Figure 4.24 XRD diffractograms of NiFe-CO_3 LDHs prepared by urea hydrolysis.

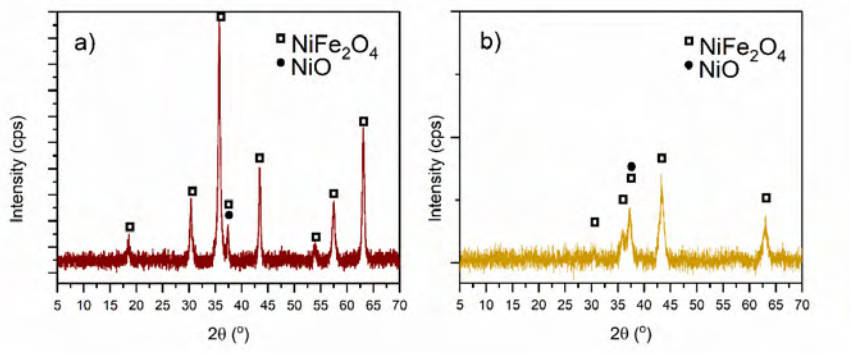

Figure 4.25 XRD diffractograms of calcined NiFe-CO_3 LDHs (a) LDH-0.5M and (b) LDH-0.05M.

For an inclusive comparison between LDHs precursors prepared at different metal concentrations, further characterizations of LDH-0.05M and LDH-0.5M precursors are presented in the next section 4.4.1.

4.3.3 Characterization of structured catalysts

4.3.3.1 Adherence tests

In industrial applications, monolithic catalysts may experience different severe stresses such as thermal, chemical, and mechanical stresses. For gas-phase processes like the methanation unit in PtG technology under stationary operating conditions, thermal and chemical stresses could be ruled out. However, mechanical stress can affect the amount of active phase on the washcoated monoliths. An ultrasonic vibration test is often used to estimate the effect of mechanical stress on the monoliths.[137] The adherence of the catalytic layer, calculated by the weight loss percentage, is reported in Table 4.7 for the calcined structured catalysts.

The adherence of the Ni-Fe oxides layer on alumina-washcoated cordierite substrate was relatively high at 99.2% for COR-AluCC-0.5M and 99.6% for COR-AluCC-0.05M. By using stock solutions of 0.05 M, less amount of LDHs was deposited, which could be the reason for the stronger anchoring forces on the substrate. On the other hand, the COR-SiCC-0.5M showed slightly weaker adhesion. Nevertheless, the catalyst layer prepared by hydrothermal synthesis on the ceramic monoliths had good mechanical stability, similar to those prepared on metallic monoliths.[76-77]

4.3.3.2 N_2 physisorption

It is well-known that cordierite monoliths have an ultralow BET surface area, which was 1.2 m^2/g in this study. After washcoating alumina and silica on the substrate, the surface area of COR-AluCC and COR-SiCC was larger at 18.3 m^2/g and 17.0 m^2/g, respectively (Table 4.8).

Thereafter, when LDH-0.5M precursor was grown on the monolith and calcined, the surface area of both COR-AluCC and COR-SiCC further increased to 30.7 m^2/g and 34.8 m^2/g, respectively. The pore volume of the final monolithic catalysts was larger than that of washcoated monoliths.

Table 4.8 Textural properties of the washcoated monoliths and final calcined structured catalysts.

Catalysts	BET specific surface area ($m^2/g_{\text{total COR}}$)	BJH pore volume (cm^3/g)
COR-AluCC	18.3	0.064
COR-SiCC	17.0	0.045
COR-AluCC-0.5M	30.7	0.069
COR-SiCC-0.5M	34.8	0.070

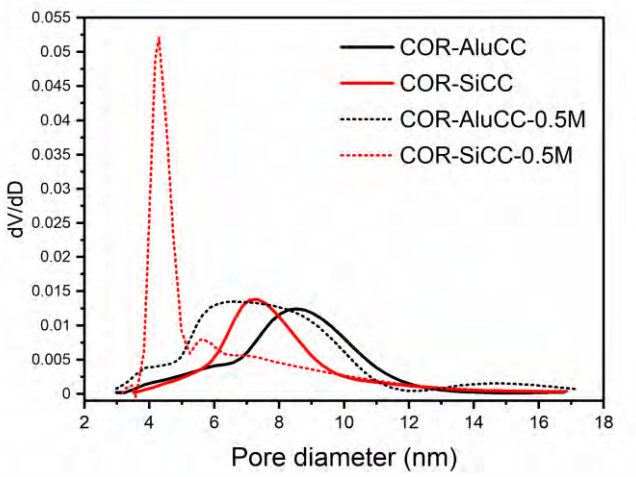

Figure 4.26 Pore size distribution of washcoated monoliths and final structured catalysts.

Cordierite monolith had a very low macropore volume with an average macropore size of 4.5 µm. In this study, the micro-mesopore size of washcoated and final monoliths was calculated from the N_2 physisorption isotherms using the BJH method (Fig. 4.26). The COR-AluCC washcoated monoliths had an average pore size of 9 nm, while it

was smaller at 7 nm for COR-SiCC. After LDHs layers were formed and calcined, the pore sizes were reduced for COR-AluCC-0.5M (6-9 nm). Meanwhile, a bimodal pore size distribution of 4 nm and 6 nm was observed for COR-SiCC-0.5M and the pore sizes were also reduced compared to that of the backbone COR-SiCC.

4.3.3.3 SEM characterization

The in-situ grown LDHs structure was examined by SEM characterization (Fig. 4.27). For COR-AluCC-0.5M, the monolithic surface contained numerous hexagonal platelets intercrossed with each other, which was typical morphology of LDHs prepared by urea hydrolysis.[138] The lateral size of these platelets was around 1 μm (900±100 nm), while the thickness was 30±10 nm. When LDHs were formed using a diluted stock solution, the hexagonal platelets were smaller with a lateral diameter at 300±50 nm, while the thickness was maintained at 35±10 nm (COR-AluCC-0.05M, Fig. 4.27b). For COR-SiCC-0.5M (Fig. 4.27c), the regular flower-like clusters of NiFe-CO_3 LDHs were 2-3 times smaller as compared to COR-AluCC-0.5M. The thickness of the platelets was about 20-30 nm while the lateral dimension was difficult to measure.

The morphology of the final monolithic catalyst was also of great interest. Fig. 4.27d reveals that although significantly reduced in lateral size, the mixed oxides particles were still in its original hexagonal shape after calcination. This is beneficial for the dispersion of Ni and Fe active sites. Moreover, the ordered interconnection between the platelets was maintained, providing sufficient exposed surface area for reactant molecules to access to the active sites.

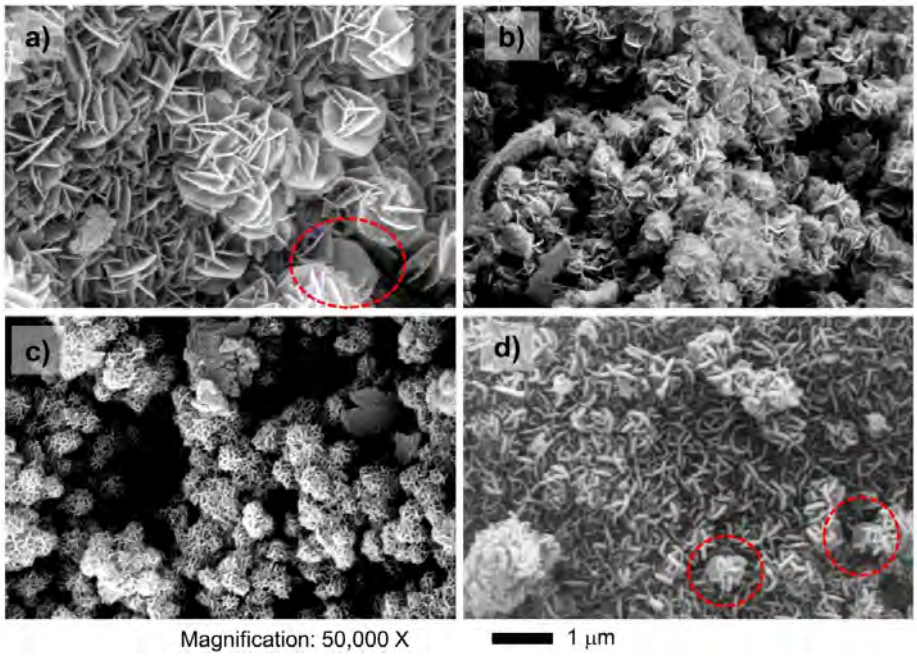

Figure 4.27 SEM images of in-situ grown LDHs on (a) COR-AluCC-0.5M, (b) COR-AluCC-0.05M, (c) COR-SiCC-0.5M and (d) calcined COR-AluCC-0.5M monoliths.

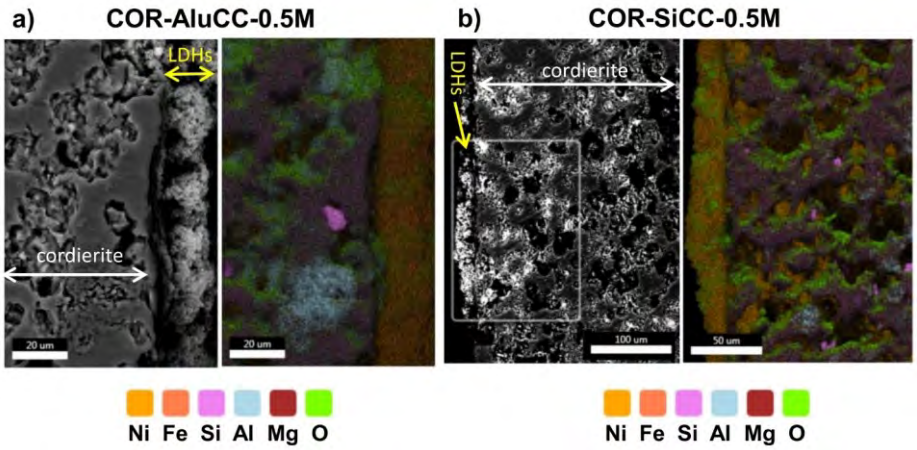

Figure 4.28 SEM images and corresponding EDS elemental mapping of the cross-sectional channel wall of (a) COR-AluCC-0.5M and (b) COR-SiCC-0.5M monoliths.

Furthermore, the cross-sectional SEM images of the channel wall were captured, and EDS elemental mapping was conducted. It is noteworthy that the washcoat layer using colloidal solutions of alumina and silica could not be differentiated from cordierite ($2MgO.5SiO_2.2Al_2O_3$). For COR-AluCC-0.5M, the deposition-precipitation of LDHs occurred on the porous exterior. Fig. 4.28a combined with Fig. 4.27a suggests that the LDHs platelets were grown perpendicularly on the cordierite surface, which could be explained by the evolution selection mechanism.[76]

The LDHs layer on COR-AluCC-0.5M was around 20 µm, which was relatively thin compared to the channel wall thickness of 200±50 µm. Moreover, the EDS mapping images show a spatial distribution of Ni and Fe on the LDHs region without visible segregation, demonstrating well-dispersed metal ions of LDHs. For COR-SiCC-0.5M, the thickness of LDHs layers located outside the cordierite wall was similar at 15-27 µm. However, the elemental mapping detected both Ni and Fe even inside the pores of cordierite, which was not the case for COR-AluCC-0.5M. Thus, it could be assumed that Ni and Fe were diffused into the porous structure and LDHs layer deposited both inside the pore and on the surface of the monolith. This further explains why smaller pores were obtained for COR-SiCC-0.5M from the pore size distribution analysis (Fig. 4.26).

LDHs could only deposit due to chemical bonding between the material itself and the substrate surface, especially on a polar substrate.[139] Reports showed that LDHs were not feasible to grow on an un-anodized aluminum substrate,[77] or FeCrAl-fiber without Al_2O_3 washcoat.[74] In this work, colloidal solutions with conductive properties should have played an important role in the anchoring of NiFe-CO_3 LDHs on the ceramic monoliths. In fact, SiO_2 nanoparticles (~25 nm, high viscosity) had a negative charge while Al_2O_3 nanoparticles (~50 nm, low viscosity) had a positive charge. The higher viscosity of silica colloidal could explain the successful ~17 wt.% loading after one washcoating cycle,

compared to three cycles of COR-AluCC.[140] Smaller silica particles could have diffused further inside the pore of cordierite monolith.

For COR-AluCC-0.05M, since a very diluted stock solution was used during urea hydrolysis, the in-situ grown LDHs layer at very low weight loading was unable to be observed from SEM imaging (Fig. 4.29). Although the thickness was not measurable, LDHs were found to be distributed on the surface of the porous cordierite, similar to COR-AluCC-0.5M.

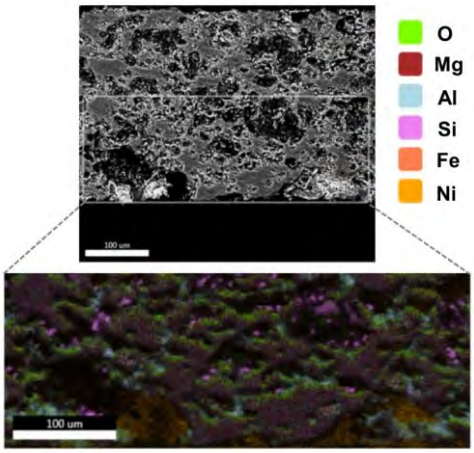

Figure 4.29 SEM images and corresponding EDS elemental mapping of the cross-sectional channel wall of COR-AluCC-0.05M monolith.

4.3.4 CO_2 methanation activity tests

The temperature programmed reaction was carried out at a total gas flow of 500 mL/min, corresponding to a GHSV of 7,760 h^{-1}. The active phase on the monoliths was assumed to be stable during the reaction at this high GHSV due to insignificant weight loss before and after reaction. Besides, the weight losses were mainly due to the reduction of oxides into metallic phases. It is also important to note that a high reproducibility was achieved in terms of preparation and activity test of structured catalysts.

The reproduced experimental data are reported in Appendix E, Table S1. and Fig. S1.

The catalytic performance was compared between COR-AluCC-0.5M COR-SiCC-0.5M monolithic catalysts to determine the more suitable washcoating colloidal solution for the preparation of structured catalysts. (The activity of COR-AluCC-0.05M will be presented in the next section 4.4.3 for a more inclusive comparison).

CO_2 conversion and CH_4 selectivity are shown in Fig. 4.30. On the one hand, both monolithic catalysts expectedly exhibited low activity at 200-250 °C. On the other hand, COR-AluCC-0.5M showed much higher CO_2 conversion and CH_4 selectivity compared to that of COR-SiCC-0.5M. At 300 °C, a CO_2 conversion of 70% was obtained on the former, while the latter only achieved 21%.

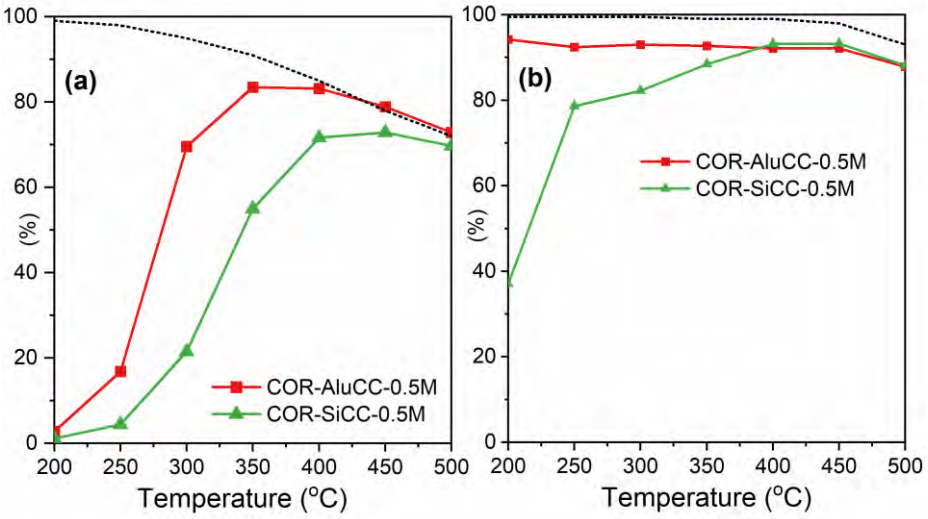

Figure 4.30 (a) CO_2 conversion and (b) CH_4 selectivity of structured catalysts in CO_2 methanation at atmospheric pressure, GHSV of 7,760 h^{-1}, $H_2/N_2/CO_2$ = 64/20/16 vol.%. The thermodynamic equilibrium of CH_4 selectivity is also included for comparison.

As the EDS elemental mapping (Fig. 4.28b) revealed a large amount of Ni and Fe penetrated inside the pore structure of COR-SiCC-0.5M, the

active sites would be more difficult to be reached by gaseous molecules. As a result, the diffusion path could be extended from the exterior (20 μm) to the whole channel wall thickness (200±50 μm). It could be used to explain the poorer performance of COR-SiCC-0.5M. However, it is noteworthy that the superior activity of COR-AluCC-0.5M could be due to the stronger metal-support interaction of Al_2O_3 than SiO_2.[141-142]

As a result, alumina colloidal solution was continuously used as washcoating material for the preparation of monolithic catalysts in **Paper VI.**

4.4 Hot-spot utilization by strategic bed packing for low-temperature CO_2 methanation (Paper VI)

Monolithic Ni-Fe catalysts with different catalytic activities were prepared by varying the total metal concentration during urea hydrolysis. The monoliths and corresponding powder precursors are denoted as COR-*x*M and LDH-*x*M, respectively, where *x* is the total metal concentration.

4.4.1 Characterization of LDHs prepared at different metal concentrations

4.4.1.1 XRD analysis of as-prepared LDHs

The XRD diffractograms of dry precursors (Fig. 4.31) showed that highly crystalline LDHs materials were formed by using metal concentrations of up to 1 M. Characteristic peaks of LDHs structures were observed for all samples except for LDH-2M, e.g., symmetric and sharp reflections at 2θ of 11.5°, 23.3°, and 34.5° could be ascribed to the basal (003), (006), (012) planes, respectively, as compared to the specific NiFe-CO_3 LDHs, (JCPDS 00-051-0463). LDH-0.25M had the best crystallinity, thus probably was the most perfect LDH structure. For LDH-2M, the precursor was amorphous since no diffraction peaks were observed.

It has been reported that LDHs synthesized at high metal concentrations had poorer crystallinity.[143] Moreover, to form a pure LDHs structure, the Fe^{3+}/Ni^{2+} molar ratio should be in the range of 0.2-0.33.[64, 144-145] However, at high Fe^{3+} concentrations, it was more favorable for Fe^{3+} ion to precipitate as insoluble $Fe(OH)_3$ in aqueous ammonia.[146] Perhaps, the amorphous structure of LDH-2M was due to the excessive total metal concentration.

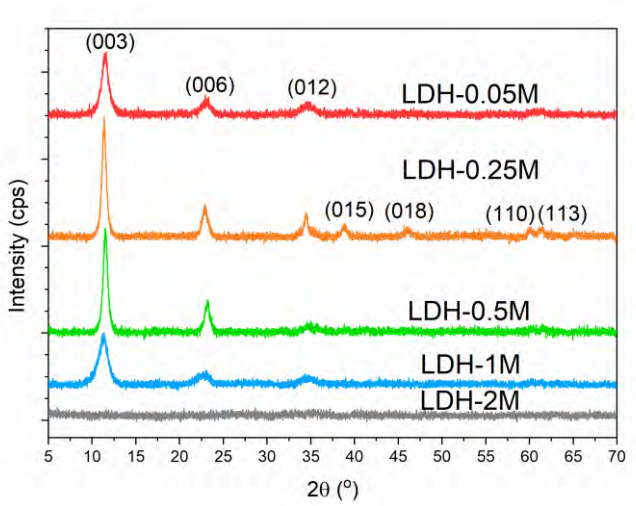

Figure 4.31 XRD diffractograms of NiFe-CO_3 LDHs prepared by urea hydrolysis at different metal concentrations.

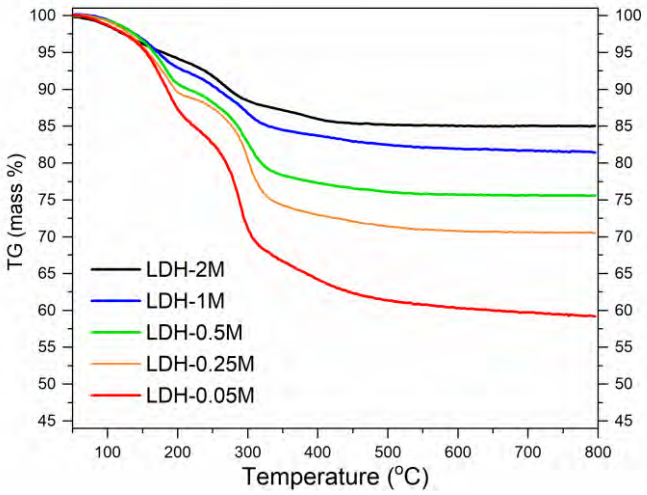

Figure 4.32 TG profiles of NiFe-CO_3 LDHs prepared by urea hydrolysis at different metal concentrations.

4.4.1.2 TGA

The thermal decomposition of Ni-Fe LDHs was analyzed by TGA (Fig. 4.32). The TG curves of all LDHs show common features for the decomposition of the layered structure material.[64] Initially, physisorbed water and water in the interlayer were removed at 150-250 °C. Then, dehydroxylation and decarbonation occurred simultaneously at temperature up to 600 °C. Above 600 °C, the sample mass remained unchanged, which implies a sufficient temperature for calcination.

Interestingly, the total weight loss of LDHs was reduced gradually from 41 wt.% to 15 wt.% when the metal concentration increased from 0.05 M to 2 M, which could be ascribed to a higher amount of water, hydroxyl, and anion in the interlayer.[147-148]

4.4.1.3 Elemental analysis

The elemental analysis via ICP-OES was carried out to verify the metal composition of the precursors. Indeed, LDHs precursors prepared at metal concentrations above 1 M had higher Fe content compared to the nominal value, i.e., Fe/Ni molar ratio of 0.25 (Table 4.9). Therefore, it can be concluded that 0.25 M was the most ideal metal concentration to prepare NiFe-CO_3 LDHs. The increase of Fe content must be the reason for the reduction in crystallinity and weight loss of NiFe-CO_3 LDHs.

Table 4.9 Actual Fe/Ni molar ratio from elemental analysis by ICP-OES.

Catalysts	Fe/Ni molar ratio
LDH-0.05M	0.36
LDH-0.25M	0.38
LDH-0.5M	0.78
LDH-1M	2.19
LDH-2M	3.35

4.4.1.4 XRD analysis of calcined LDHs

It was expected from TGA that the mixed metal oxides Ni and Fe would be obtained from LDHs precursors upon calcination at 600 ºC. The diffractograms of calcined LDHs are presented in Fig. 4.33. It confirmed that LDHs structures were completely decomposed since only the diffraction patterns of $NiFe_2O_4$ (JCPDS 00-054-0964) and NiO (JCPDS 01-089-5881) were identified. It can also be observed that the XRD pattern of the calcined LDH-2M mostly showed reflections of $NiFe_2O_4$ due to the highest Fe content among all samples.

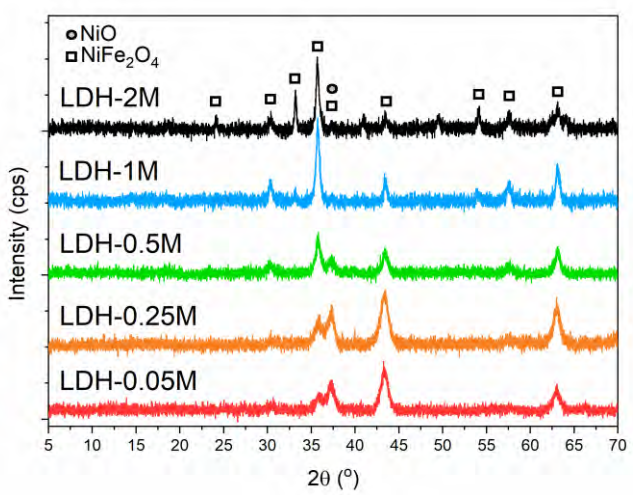

Figure 4.33 XRD diffractograms of the calcined NiFe-CO_3 LDHs prepared at different metal concentrations.

4.4.1.5 TPR analysis

The reducibility of calcined catalysts was investigated by H_2-TPR analysis (Fig. 4.34). With increasing metal concentrations, the main reduction temperature of the metal oxides was increased. It has been reported that pure NiO could be reduced at 340-410 ºC and Fe_2O_3 is reduced sequentially at 380, 620, and 715 ºC.[57, 109] In this study, the TPR peaks of calcined LDH-0.05M, LDH-0.25M and LDH-0.5M were

at 415, 430 and 485 °C, respectively. It is reasonable that the reduction temperature of Ni species would be increased due to the interaction with Fe species in the mixed oxides.[149] As for LDH-1M and LDH-2M samples, small reduction peaks were observed at 310-330 °C which could be attributed to the reduction of NiO, while the main peaks were recorded at high temperatures of 540-545 °C. It was in good agreement with the previous analysis that these two samples contained more iron oxides.

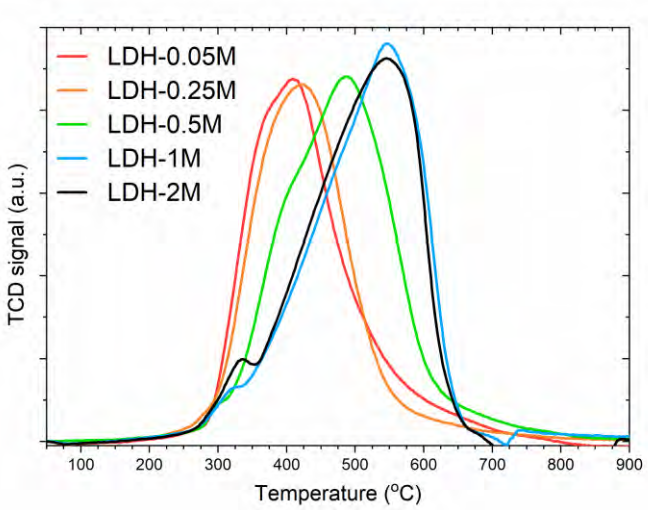

Figure 4.34 H_2-TPR profiles of calcined NiFe-CO_3 LDHs prepared at different metal concentrations.

4.4.2 Characterization of structured catalysts

4.4.2.1 Catalyst loadings

The NiFe-CO_3 LDHs layer was in-situ grown on the alumina-washcoated honeycomb ceramic substrate. The amount of deposited LDHs layers on the monoliths as well as catalyst loading are summarized in Table 4.10. Noted that the catalyst loading was calculated as the percentage of the catalyst mass after calcination on the total weight of

the final monolith. It was found that the highest amount of LDHs precursor could be deposited on monolith prepared at a metal concentration of 0.25 M. It is also the sample with the most crystalline LDHs structure. Thus, increasing metal concentrations could not increase the amount of in-situ grown LDHs precursors on washcoated substrate. As discussed in the XRD analysis, the formation of pure and high crystalline LDH structure was not favored at metal concentrations above 1 M.

Table 4.10 The mass of in-situ grown LDHs, catalyst loading and textural properties of the final calcined monolithic catalysts.

Structured catalysts	Mass of LDHs (mg)	Catalyst loading (wt. %)	BET specific surface area ($m^2/g_{\text{total COR}}$)	BJH pore volume (cm^3/g)
COR-0.05M	60.1	0.52	18.3	0.047
COR-0.25M	192.9	3.51	24.4	0.051
COR-0.5M	175.8	2.63	30.7	0.069
COR-1M	168.3	1.87	22.6	0.047
COR-2M	163.5	1.12	18.6	0.047

4.4.2.2 N_2 physisorption

The surface area and pore volume of final monoliths are also summarized in Table 4.10. Noted that the alumina-washcoated monoliths had a surface area of 18.3 m^2/g and pore volume of 0.064 cm^3/g (as reported in section 4.3.3.2, Table 4.8). Herein, the surface area was significantly improved after urea hydrolysis and calcination of monoliths prepared at 0.25-1 M. In contrast, the pore volume was reduced compared to that of the washcoated monoliths since it was occupied by LDHs layers.

4.4.2.3 SEM characterization

The morphology of catalytic layer deposited on cordierite monoliths upon urea hydrolysis at different metal concentrations was observed by

SEM. Numerous hexagonal platelets of LDHs were found on the exterior wall of the monolithic channels, in good agreement with literature.[138] Noted that, COR-0.05M and COR-0.5M in this section are COR-AluCC-0.05M and COR-AluCC-0.5M in previous section 4.3.

As shown in Fig. 4.35, the lateral size and thickness of these platelets on COR-0.25M and COR-1M were around 1 μm and 25±10 nm. The morphology of LDHs precursors on COR-0.05M was almost three-time smaller in lateral size (Fig. 4.27b), while the platelet dimensions of COR-0.25M, COR-0.5M and COR-1M (Fig. 4.35 and 4.27a) was similar.

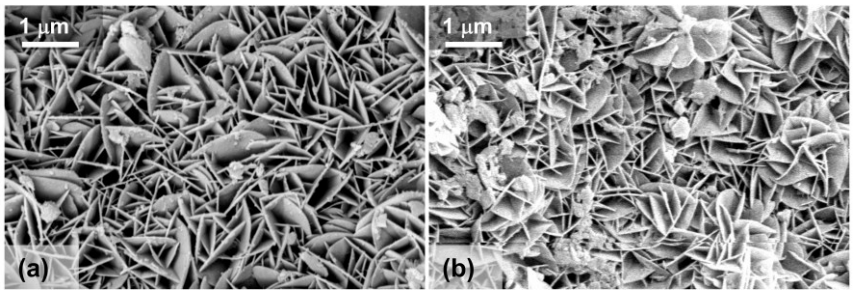

Figure 4.35 SEM images of in-situ grown NiFe-CO_3 LDHs on (a) COR-0.25M and (b) COR-1M monolith.

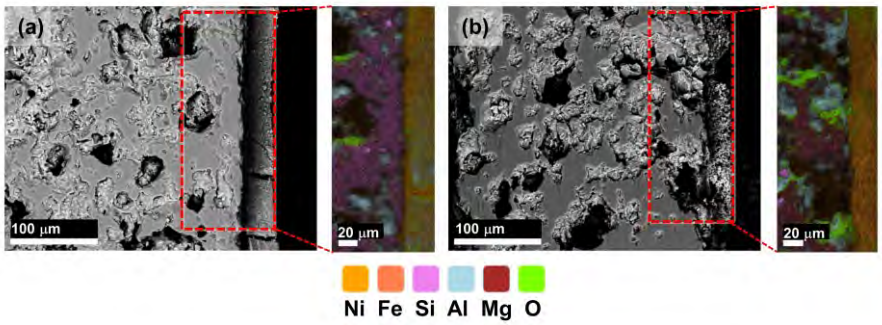

Figure 4.36 SEM and corresponding EDS elemental mapping images of the cross-sectional channel wall on (a) COR-0.25M and (b) COR-1M monolith.

The thickness of the catalytic layer was estimated using the cross-sectional SEM images of the channel wall. As shown in Fig. 4.36, the deposition of LDHs occurred on the porous exterior of the cordierite channel walls. The LDHs platelets were assumed to grow perpendicularly on the surface, resulting in a layer thickness of around 20-30 μm. Notably, the catalytic layer on COR-0.25M, COR-0.5M, and COR-1M had similar thicknesses (Fig. 4.36 and Fig. 4.28a). As for COR-0.05M, it was unable to measure the LDHs layer due to very low catalyst loading (Fig. 4.29). In addition, EDS elemental mapping was conducted and revealed a uniform spatial distribution of Ni and Fe on the layer, indicating that the metal ions were well dispersed on the monolithic surface.

4.4.3 CO_2 methanation activity tests

The temperature programmed reaction was carried out at 200-500 ºC for all monolithic catalysts. Due to kinetic limitations, high conversion of CO_2 could not be obtained at low temperature region of 200-250 ºC, even though CO_2 methanation is thermodynamically favored. The conversion was much improved at 300 ºC, especially for COR-0.25M monolith which achieved a CO_2 conversion of 70.1% (Fig. 4.37). COR-0.5M and COR-1M also exhibited good activity at 300 ºC with CO_2 conversion of 65.6% and 59.6%, respectively. The conversions peaked at 350 ºC and gradually decreased at elevated temperatures, following the thermodynamic equilibrium. On the other hand, COR-0.05M showed a poorer performance, and COR-2M presented the poorest activity.

In this study, CH_4 yield is reported together with the loading of catalysts (Fig. 4.38). The best performance of COR-0.25M amongst others was confirmed by the CH_4 yield at different reaction temperatures. This could be due to the highest catalyst loading of COR-0.25M with a thin and well-adhered layer on the honeycomb substrate. Interestingly, CO_2 conversion over the COR-2M catalyst was always increasing with temperature, distinct from the other catalysts as it did not follow the

thermodynamic curve for methanation. This could be explained by the high Fe content of COR-2M, which promoted the endothermic RWGS reaction and favors CO_2 conversion at high temperatures.[128] Indeed, the CH_4 selectivity was very low over the COR-2M monolith.

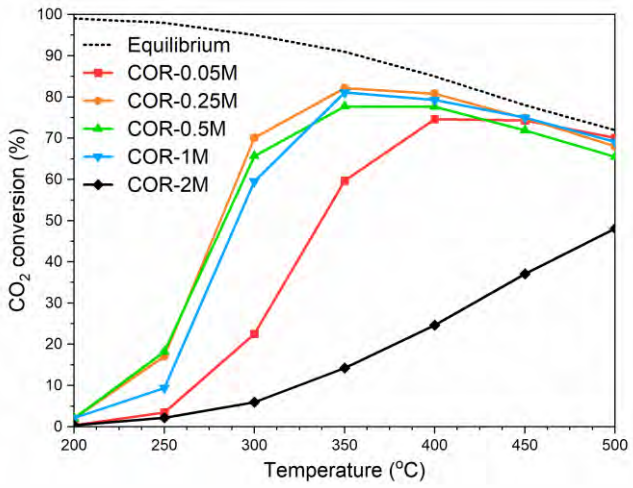

Figure 4.37 CO_2 conversion over structured catalysts in temperature programmed CO_2 methanation at atmospheric pressure, GHSV of 7,760 h^{-1}, $H_2/N_2/CO_2$ = 64/20/16 vol.%.

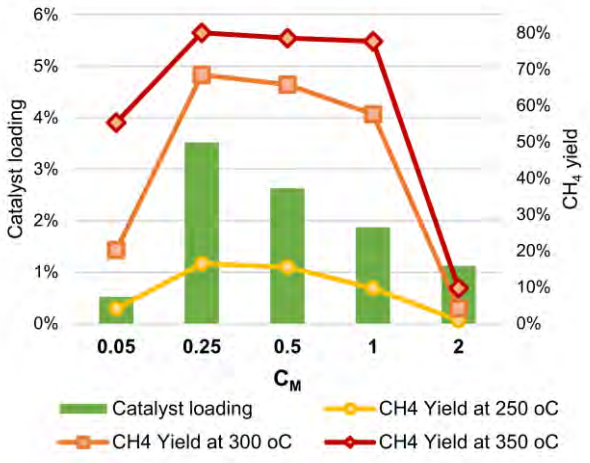

Figure 4.38 CH_4 yield obtained over structured catalysts at different reaction temperatures (200, 250 and 300 °C); CO_2 methanation reaction was at atmospheric pressure, GHSV of 7,760 h^{-1}, $H_2/N_2/CO_2$ = 64/20/16 vol.%.

4.4.4 Temperature profiles of structured reactor

4.4.4.1 Temperature profiles at increasing oven temperatures

The exothermic nature of the methanation reaction could be influenced by different catalytic activities of the monolithic catalysts. Thus, the temperature along the catalytic bed containing high and low activity catalysts (COR-0.25M and COR-0.05M, respectively) was measured by the multi-point thermocouple at the center of the bed. At first, the reaction was carried out on uniform catalytic beds containing three COR-0.25M monoliths (Uni-High bed) or three COR-0.05M monoliths (Uni-Low bed). Fig. 4.39 shows the temperature profile and the methane yield of the catalytic beds at steady state when T_{oven} was 200, 250 and 300 °C, respectively.

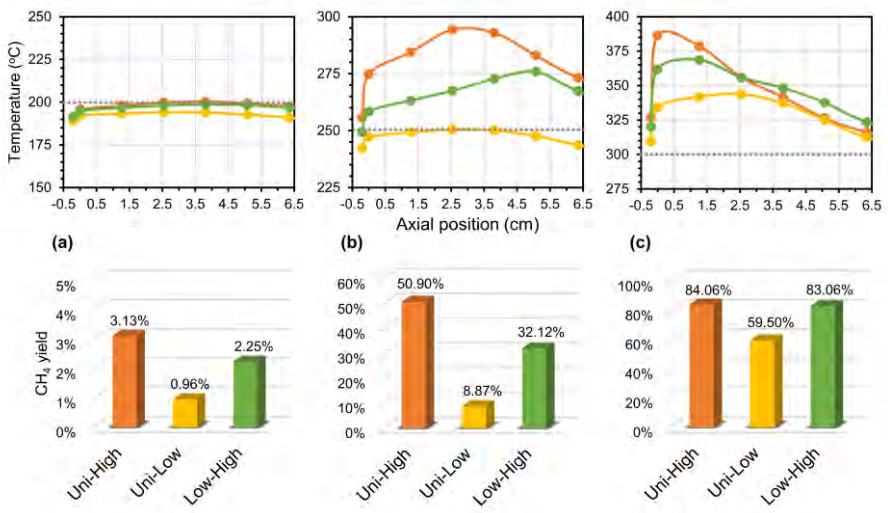

Figure 4.39 Temperature profiles of reactor (top) and methane yield (bottom) obtained from different catalytic beds in CO_2 methanation at T_{oven} of (a) 200 °C, (b) 250 °C, (c) 300 °C; The reaction was at atmospheric pressure, total gas rate of 500 mL/min, $H_2/N_2/CO_2$ = 64/20/16 vol.%.

At T_{oven} = 200 °C, the CH_4 yield on both monolithic beds was relatively low at less than 3.5% (Fig. 4.39a). As expected, no hot-spot formation

was observed from the axial temperature profiles. When T_{oven} was ramped up to 250 ºC (Fig. 4.39b), hot-spot appeared along the Uni-High bed with a maximum temperature increase (ΔT) of 42 ºC in the middle of the bed. The catalytic performance also improved with a CH_4 yield of 50.9%. In contrast, a CH_4 yield of only 8.9% was achieved on the Uni-Low bed, and there was obviously no hot-spot formation at this low conversion.

When T_{oven} was increased from 250 to 300 ºC, the hot-spot on Uni-High bed shifted from the center axial position to near the gas inlet region with a significant ΔT = 86 ºC, whereas the CH_4 yield increased to 84.1% (Fig. 4.39c). A CH_4 yield of 59.5% was achieved on the Uni-Low bed at T_{oven} = 300 ºC, and hot-spot was also observed with ΔT = 44 ºC. The thermal profile of catalytic beds could be resulted from the balance between the exothermic heat from methanation which increased exponentially with reaction temperature due to reaction rate acceleration, and heat transfer by conduction in the cordierite channel wall and by convection from the bed to the gas flow. The shift of hot-spot location at increasing T_{oven} has also been reported by Kosaka *et al.*[89] It could be due to the higher heat conductivity of the catalytic cordierite monolith bed compared to that of the flowing gas. Thus, heat transfer along the monolithic bed was faster than that between the catalytic bed and the gas. Subsequently, monolith at the near gas inlet was further heated and accelerated methanation reaction. Simultaneously, a large amount of exothermic reaction heat was released.

It was proposed that the excellent thermal conductivity of monolithic substrate could be utilized to boost up the performance of low activity catalysts in methanation.[89] Therefore, a monolithic bed with increasing catalytic activity was configured, i.e., Low-High bed consisting of two COR-0.05M and one COR-0.25M. Hot-spot was not observed at T_{oven} = 200 ºC (Fig. 4.39a) but was measured with ΔT = 26 ºC and a CH_4 yield of 32.1% at T_{oven} = 250 ºC. Notably, at T_{oven} = 300 ºC, the CH_4 yield of the Low-High bed was almost close to that of the Uni-High bed (83.1%

vs 84.1%) while a lower ΔT = 69 °C was recorded. Thus, although the Low-High bed contained less catalyst loading than the Uni-High bed, the CH_4 yield was almost similar at T_{oven} = 300 °C. As shown in Fig. 4.37, while COR-0.25M slowly dropped its performance at 350 °C and above, the CO_2 conversion over COR-0.05M still increased and reached a maximum at 400-450 °C. It seems that hot-spot generated in the reaction could be exploited to improve the overall performance of the Low-High bed. In terms of methane productivity when catalyst mass was taken into account, P_{CH4} was 0.9 mol/(g_{cat}.h) on Uni-High and 1.6 mol/(g_{cat}.h) on Low-High bed. Hence, it can be assumed that the Low-High bed packing strategy could enhance the catalytic efficiency of the monolithic reactor with a lower hot-spot temperature.

4.4.4.2 CFD simulations

The experimental results for all three catalytic beds were verified by a 3D CFD consisted of reaction kinetics, fluid dynamics, heat transfer and mass transport. The simulated temperature profiles at a gas inlet temperature of 250 °C along three catalytic beds (Fig. 4.40) showed similar patterns of hot-spot formation compared to the experimental results at T_{oven} = 250 °C (Fig. 4.39b). The simulation demonstrated that the highest temperature of 290 °C on Uni-High bed was at the middle of the bed (Fig. 4.40a), while on Low-High bed the maximum temperature T_{max} of 258 °C was detected at the third monolith COR-0.25M near the gas outlet (Fig. 4.40c). As expected, the temperature profile of the Uni-Low bed was quite flat without any hot-spot formation (Fig. 4.40b). Thus, the proposed bed packing strategy by combining catalysts with low and high activity appeared to be a promising approach to manage bed temperatures.

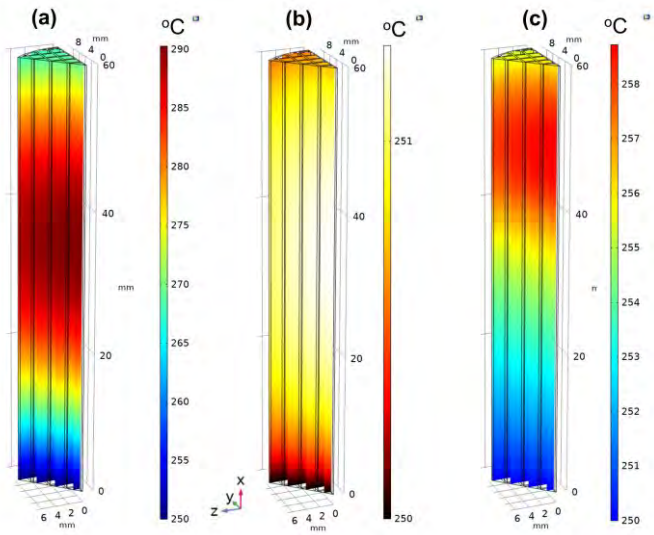

Figure 4.40 Simulated temperature profiles of monolithic reactor using (a) Uni-High, (b) Uni-Low and (c) Low-High bed at operating temperature of 250 °C, atmospheric pressure, total gas rate of 500 mL/min, $H_2/N_2/CO_2$ = 64/20/16 vol.%.

4.4.4.3 Temperature profiles at increasing gas rates

The effect of GHSV on the catalytic conversion and temperature profile of Uni-High and Low-High beds at T_{oven} = 250 °C was investigated (Fig. 4.41). For comparison, the CH_4 yield and temperature profile at the lowest gas rate of 500 mL/min were also included as Fig. 4.41a.

The hot-spot formation was more pronounced at higher gas rate of 1500 mL/min (corresponding to a GHSV of 7,760 h^{-1}). The Uni-High bed reached a T_{max} of 458 °C with a remarkable CH_4 yield of 80.4% (Fig. 4.41b). It is worth emphasizing that the ratio of the catalyst mass to volumetric gas rate was the same for the single-bed at 500 mL/min and Uni-High bed at 1500 mL/min, whereas the CH_4 yield was only 16.5% for the former (Fig. 4.38). Obviously, the hot-spot generated on the Uni-High bed had significantly boosted the overall CH_4 yield to 80.4%. Thus, while hot-spot formation is a big concern for many chemical

reactions,[90] it could also be utilized to boost the performance of exothermic monolithic reactors. As for the Low-High bed, it showed a lower T_{max} of 437 °C at a gas rate of 1500 mL/min while the CH_4 yield was only marginally lower at 77.6%, apparently due to the hot-spot formed on the reactor bed. The strategic Low-High packing was again demonstrated to be a promising alternative to the uniform Uni-High bed.

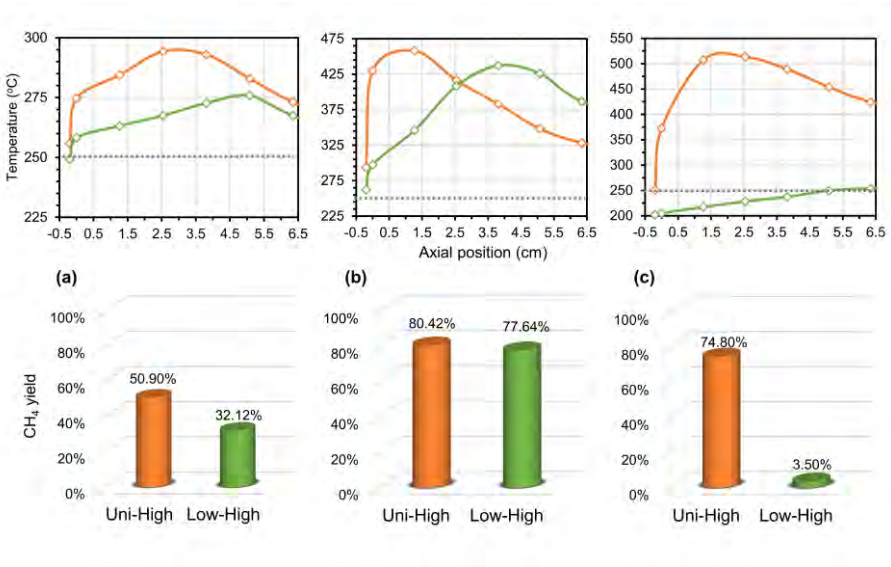

Figure 4.41 Temperature profiles of reactor (top) and methane yield (bottom) obtained from Uni-High and Low-High bed in CO_2 methanation at different gas rates of (a) 500 mL/min, (b) 1500 mL/min and (c) 3000 mL/min. The temperature of the oven was set at 250 °C. The reaction was at atmospheric pressure, $H_2/N_2/CO_2$ = 64/20/16 vol.%.

Lower CO_2 conversion and CH_4 yield are generally expected at higher GHSV at the same reaction temperature. Interestingly, the catalytic performance of both monolithic beds was significantly improved at a higher gas rate of 1500 mL/min compared to 500 mL/min. This could also be explained by the hot-spot observed in the reactor: the initial CO_2 conversion was probably lower at 1500 mL/min, but the amount of heat released and the heat transfer coefficient would be larger at higher rate, which increased the bed temperature thus further accelerated the reaction. Consequently, the monolithic bed was operated at a much

higher temperature at 1500 mL/min than that at 500 mL/min, as shown in Fig. 4.41a and Fig. 4.41b.

The reactor performance at 3000 mL/min was also studied (T_{oven} = 250 °C). For Uni-High bed, a higher T_{max} of 513 °C, corresponding to a ΔT of 263 °C could be observed, whereas the CH_4 yield decreased to 74.8%. Indeed, a larger amount of heat was released at 3000 mL/min which led to a higher temperature spike. However, at 450-500 °C, COR-0.25M exhibited a lower conversion of only 75-68% (Fig. 4.37). As for the Low-High bed, the CH_4 yield was merely 3.5%. The residence time at this condition could be too short for the two low-activity COR-0.05M catalytic beds, thus CO_2 was not reacted and no heat was released to form hot-spot (Fig. 4.41c). To sum up, at a very high gas flow of 3000 mL/min, extreme hot-spot formation was not favorable for the conversion on Uni-High bed while it was too harsh condition for Low-High bed to produce methane.

4.4.4.4 Long-term test

Long-term stability test was carried out on both Uni-High and Low-High beds at T_{oven} = 250 °C and a gas rate of 1500 mL/min. The T_{max} on Low-High bed was maintained at 440 °C during the 100-h long-term test. On Uni-High bed, the high hot-spot temperature was slightly decreased from 468 to 460 °C, which could be explained by the loss of activity during 100 h. Regardless, it was consistent with previous tests that Low-High bed had a lower hot-spot compared to that of Uni-High bed (Fig. 4.42). This could also explain the lower but more stable methane yield with a slight drop of 0.02%/h on the Low-High bed compared to a deactivation rate of 0.05%/h on the Uni-High bed. Nevertheless, both bed configurations have shown quite stable performance throughout 100 h of reaction. Therefore, CO_2 methanation could be effectively carried out on monolithic reactors at a very low operating temperature of 250 °C.

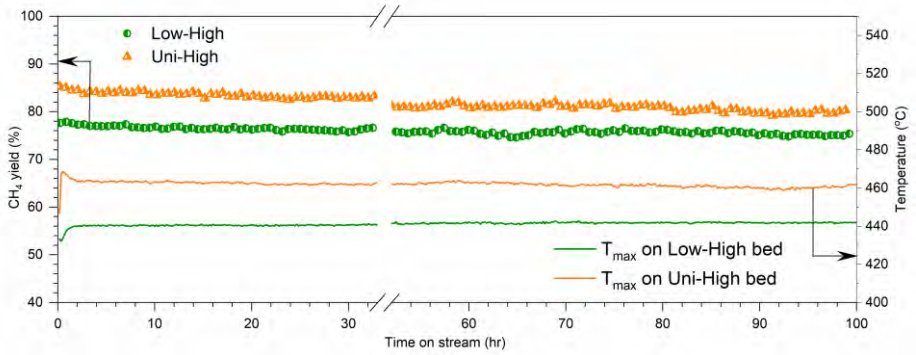

Figure 4.42 Methane yield and maximum temperature of the Low-High and Uni-High bed during long-term tests at T_{oven} = 250 ºC. The reaction was at atmospheric pressure, total gas rate of 1500 mL/min, $H_2/N_2/CO_2$ = 64/20/16 vol.%.

5 Concluding remarks

In this thesis, the rational design and synthesis of catalysts for CO_2 methanation have been focused on. Attempts to improve the reactor performance with less hot-spot formation at high gas flow rate for industrial application of monolithic catalysts have also been made.

Ni-Fe supported catalysts were prepared by rapid coprecipitation. Extensive characterizations revealed that small Ni-Fe alloy particles (6-7 nm) were formed upon reduction at 600 ^oC. The Ni-Fe alloy catalysts (with optimal Fe/Ni molar ratio of 0.25) could enhance the activity, selectivity towards CH_4, and stability in CO_2 methanation, particularly at low temperatures of 250-350 ^oC compared to monometallic Ni catalysts. The superior catalytic performance of Ni-Fe alloy catalysts could be explained by the lower energy barrier for CH_4 formation. At the same time, weak interaction with adsorbed *CO species maintained the free active sites and prolonged its catalytic stability. As CO_2 activation via hydrogenation to *HCOO was more preferred than its direct dissociation on both Ni and Ni-Fe alloy surfaces, the most energetically favorable pathway ($*CO_2 \rightarrow *HCOO \rightarrow *HCO \rightarrow *CH \rightarrow *CH_4$) was proposed for Ni-based catalysts in CO_2 methanation. Moreover, by increasing the total metal concentration, larger amount of catalyst mass per batch was obtained while its catalytic activity was maintained, demonstrating the high potential for large-scale production of Ni-Fe alloy supported catalysts for industrial applications.

A facile preparation method of structured catalysts for CO_2 methanation was developed. The thin layer of NiFe-CO_3 LDHs was successfully in-situ grown with excellent adherence to the washcoated cordierite monoliths via urea hydrolysis. Under CO_2 methanation reaction at high gas flow rate, the catalytic layer exhibited higher activity on Al_2O_3-washcoated than SiO_2-washcoated monolith. It could be due to Al_2O_3 was only washcoated on the exterior of the monolith and the diffusion

path for reactant gases was much shorter during methanation. A suitable high-concentration stock solution is also advantageous to achieve high catalyst loading on the ceramic monolith, thus high methane yield in CO_2 methanation. It was found that catalysts prepared by 0.25 M solution, i.e., COR-0.25M with the highest metal loading exhibited the best CO_2 conversion and CH_4 yield.

The formation of hot-spot during exothermic methanation reaction was observed on monolithic reactors and further verified by CFD simulations. Although a temperature spike of 86 ^oC was observed on the uniform-activity bed, a remarkable methane yield of 80.4% was achieved at low operating temperature of 250 ^oC. In contrast, the methane yield was merely 16.5% on the single COR-0.25M bed at this temperature. Therefore, controlled hot-spot formation was beneficial for the overall catalytic performance.

A strategic bed packing configuration was proposed by combining low and high activity monolith, i.e., Low-High bed. Amazingly, this bed achieved ~83% methane yield and the hot-spot formation was less severe compared to that of the uniform-activity bed at 300 ^oC. It is again confirmed that hot-spot formation could be exploited to achieve high methane yield on monolithic reactors at high gas rate and low temperature input. Utilizing hot-spot formation on a strategic bed packing emerges as a promising approach for industrial reactor designs, especially for the CO_2 methanation unit of the large-scale PtG process.

References

[1] IEA *CO2 Emissions Statistics*; International Energy Agency: **2018**.

[2] IEA *Energy Technology Perspectives 2020*; International Energy Agency: **2020**.

[3] *The European Power Sector in 2018. Up-to-date analysis on the electricity transition*; Agora Energiewende and Sandbag **2019**.

[4] M. Lehner *et al.*, *Power-to-gas: technology and business models*, Springer, **2014**.

[5] K. Ghaib *et al.*, *Renewable and Sustainable Energy Reviews* **2018**, *81*, 433-446.

[6] S. Rönsch *et al.*, *Fuel* **2016**, *166*, 276-296.

[7] C. Mebrahtu *et al.*, in *Studies in Surface Science and Catalysis, Vol. 178* (Eds.: S. Albonetti, S. Perathoner, E. A. Quadrelli), Elsevier, **2019**, pp. 85-103.

[8] IEA *Net Zero by 2050 A Roadmap for the Global Energy Sector*; International Energy Agency: **2021**.

[9] K. Hashimoto, *Materials Science and Engineering: A* **1994**, *179-180*, 27-30.

[10] S. Patel *A Review of Global Power-to-Gas Projects To Date*; POWER magazine: **2019**.

[11] M. Bailera *et al.*, *Renewable and Sustainable Energy Reviews* **2017**, *69*, 292-312.

[12] S. O., Audi Media Info - Technology and Innovation Communications, **2015**.

[13] P. Sabatier *et al.*, *Comptes Rendus Des Séances De L'Académie Des Sciences, Section VI – Chimie* **1902**, *134*, 514-516.

[14] C. Vogt *et al.*, *Nature Catalysis* **2019**, *2*, 188-197.

[15] G. A. Mills *et al.*, *Catalysis Reviews - Science and Engineering* **1974**, *8*, 159-210.

[16] J. Kopyscinski *et al.*, *Fuel* **2010**, *89*, 1763-1783.

[17] A. Muscatello *et al.*, in *50th AIAA Aerospace Sciences Meeting including the New Horizons Forum and Aerospace Exposition*, American Institute of Aeronautics and Astronautics, **2012**.

[18] M. Shima *et al.*, *Int. J. Microgravity Sci. Appl* **2013**, *30*, 86-93.

[19] J. Hu *et al.*, *Catalysis Today* **2007**, *125*, 103-110.

[20] J. Gao *et al.*, *RSC Advances* **2012**, *2*, 2358-2368.
[21] C. V. Miguel *et al.*, *Journal of Natural Gas Science and Engineering* **2015**, *22*, 1-8.
[22] K. Ghaib *et al.*, *ChemBioEng Reviews* **2016**, *3*, 266-275.
[23] B. Miao *et al.*, *Catalysis Science & Technology* **2016**, *6*, 4048-4058.
[24] E. Baraj *et al.*, *Chemical Papers* **2016**, *70*, 395-403.
[25] S. Kattel *et al.*, *Journal of the American Chemical Society* **2017**, *139*, 9739-9754.
[26] C. Vogt *et al.*, *Nature Communications* **2019**, *10*, 5330.
[27] C. Vogt *et al.*, *Nature Catalysis* **2018**, *1*, 127-134.
[28] A. Solis-Garcia *et al.*, *Journal of Nanoscience and Nanotechnology* **2019**, *19*, 3110-3123.
[29] J. H. Chiang *et al.*, *Industrial & Engineering Chemistry Product Research and Development* **1983**, *22*, 225-228.
[30] J. K. Kesavan *et al.*, *Journal of CO2 Utilization* **2018**, *23*, 200-211.
[31] F. Solymosi *et al.*, *Journal of the Chemical Society, Faraday Transactions 1: Physical Chemistry in Condensed Phases* **1981**, *77*, 1003-1012.
[32] X. Wang *et al.*, *Journal of Catalysis* **2016**, *343*, 185-195.
[33] A. Loder *et al.*, *Journal of Industrial and Engineering Chemistry* **2020**, *85*, 196-207.
[34] F. Koschany *et al.*, *Applied Catalysis B: Environmental* **2016**, *181*, 504-516.
[35] T. Kai *et al.*, *The Canadian Journal of Chemical Engineering* **1988**, *66*, 343-347.
[36] P. A. U. Aldana *et al.*, *Catalysis Today* **2013**, *215*, 201-207.
[37] J. Ashok *et al.*, *Catalysis Today* **2017**, *281*, 304-311.
[38] M. S. Duyar *et al.*, *Journal of CO2 Utilization* **2015**, *12*, 27-33.
[39] M. A. A. Aziz *et al.*, *Green Chemistry* **2015**, *17*, 2647-2663.
[40] P. Frontera *et al.*, *Catalysts* **2017**, *7*, 59.
[41] J. Gao *et al.*, *RSC Advances* **2015**, *5*, 22759-22776.
[42] C. Lv *et al.*, *Frontiers in Chemistry* **2020**, *8*.
[43] L. Shen *et al.*, *ACS Catalysis* **2020**, *10*, 14581-14591.
[44] C. d. Leitenburg *et al.*, *Journal of Catalysis* **1997**, *166*, 98-107.
[45] P. Panagiotopoulou, *Applied Catalysis A: General* **2017**, *542*, 63-70.

[46] G. D. Weatherbee *et al.*, *Journal of Catalysis* **1984**, *87*, 352-362.
[47] M. Albrecht *et al.*, *Applied Catalysis B: Environmental* **2017**, *204*, 119-126.
[48] A. I. Tsiotsias *et al.*, *Nanomaterials* **2021**, *11*, 28.
[49] R. Dębek *et al.*, *Renewable and Sustainable Energy Reviews* **2019**, *116*, 109427.
[50] J. K. Nørskov *et al.*, *Nature chemistry* **2009**, *1*, 37-46.
[51] M. P. Andersson *et al.*, *Journal of Catalysis* **2006**, *239*, 501-506.
[52] A. L. Kustov *et al.*, *Applied Catalysis A: General* **2007**, *320*, 98-104.
[53] J. Sehested *et al.*, *Topics in Catalysis* **2007**, *45*, 9-13.
[54] S. Hwang *et al.*, *Catalysis Letters* **2012**, *142*, 860-868.
[55] D. Pandey *et al.*, *Journal of Industrial and Engineering Chemistry* **2016**, *33*, 99-107.
[56] J. Ren *et al.*, *Fuel Processing Technology* **2015**, *137*, 204-211.
[57] D. Pandey *et al.*, *International Journal of Hydrogen Energy* **2018**, *43*, 4987-5000.
[58] B. Yan *et al.*, *Journal of Catalysis* **2019**, *374*, 60-71.
[59] B. Mutz *et al.*, *ACS Catalysis* **2017**, *7*, 6802-6814.
[60] C. Mebrahtu *et al.*, *Catalysis Science & Technology* **2018**, *8*, 1016-1027.
[61] T. Burger *et al.*, *Applied Catalysis A: General* **2018**, *558*, 44-54.
[62] J. Guo *et al.*, *Applied Catalysis A: General* **2004**, *273*, 75-82.
[63] W. Li *et al.*, *RSC Advances* **2018**, *8*, 7651-7669.
[64] F. Cavani *et al.*, *Catalysis Today* **1991**, *11*, 173-301.
[65] J. He *et al.*, in *Structure and Bonding* (Eds.: X. Duan, D. G. Evans), Springer, **2006**, pp. 89-119.
[66] G. Fan *et al.*, *Chemical Society Reviews* **2014**, *43*, 7040-7066.
[67] A. P. Tathod *et al.*, *Crystal Growth & Design* **2016**, *16*, 6709-6713.
[68] E. Tronconi *et al.*, *Current Opinion in Chemical Engineering* **2014**, *5*, 55-67.
[69] P. H. Ho *et al.*, in *Studies in Surface Science and Catalysis, Vol. 178* (Eds.: S. Albonetti, S. Perathoner, E. A. Quadrelli), Elsevier, **2019**, pp. 303-327.
[70] T. A. Nijhuis *et al.*, *Catalysis Reviews* **2001**, *43*, 345-380.
[71] H. Chen *et al.*, *Advanced Functional Materials* **2014**, *24*, 934-942.

[72] W. Li *et al.*, *ChemCatChem* **2016**, *8*, 2724-2733.
[73] H. Li *et al.*, *Chemical Communications* **2012**, *48*, 10645-10647.
[74] R. Chai *et al.*, *ACS Sustainable Chemistry & Engineering* **2017**, *5*, 4517-4522.
[75] H. Chen *et al.*, *Advanced Materials* **2006**, *18*, 3089-3093.
[76] X. Guo *et al.*, *Langmuir* **2009**, *25*, 9894-9897.
[77] Z. Lü *et al.*, *Chemical Engineering Science* **2008**, *63*, 4055-4062.
[78] T. Xue *et al.*, *Chemical Engineering Journal* **2020**, *384*, 123284.
[79] M. Adachi-Pagano *et al.*, *Journal of Materials Chemistry* **2003**, *13*, 1988-1993.
[80] M. Ogawa *et al.*, *Langmuir* **2002**, *18*, 4240-4242.
[81] J. Bremer *et al.*, *Reaction Chemistry & Engineering* **2019**, *4*, 1019-1037.
[82] A. Cybulski *et al.*, *Novel Concepts in Catalysis and Chemical Reactors* **2010**.
[83] F. Kapteijn *et al.*, *Catalysis Today* **2020**.
[84] D. Schlereth *et al.*, *Chemical Engineering & Technology* **2015**, *38*, 1845-1852.
[85] C. Fukuhara *et al.*, *Applied Catalysis A: General* **2017**, *532*, 12-18.
[86] S. Hwang *et al.*, *Chemical Engineering Science* **2004**, *59*, 4245-4260.
[87] S. Ratchahat *et al.*, *Journal of CO2 Utilization* **2018**, *24*, 210-219.
[88] F. Kosaka *et al.*, *International Journal of Hydrogen Energy* **2020**, *46*, 4116-4125.
[89] F. Kosaka *et al.*, *International Journal of Hydrogen Energy* **2020**, *45*, 12911-12920.
[90] W. Wang *et al.*, *ChemSusChem* **2020**, *13*, 5468-5479.
[91] J. Jenkins *et al.*, *Platinum Metals Review* **1989**, *33*, 118-127.
[92] S. Brunauer *et al.*, *Journal of the American Chemical Society* **1938**, *60*, 309-319.
[93] E. P. Barrett *et al.*, *Journal of the American Chemical Society* **1951**, *73*, 373-380.
[94] B. D. Cullity, *Elements of X-ray diffraction*, Addison-Wesley Pub. Co., **1956**.
[95] D. A. M. Monti *et al.*, *Journal of Catalysis* **1983**, *83*, 323-335.

[96] A. Gervasini, in *Calorimetry and Thermal Methods in Catalysis* (Ed.: A. Auroux), UK, **2013**.
[97] P. Marocco *et al.*, *Fuel* **2018**, *225*, 230-242.
[98] C. H. Bartholomew *Alloy catalysts with monolith supports for methanation of coal-derived gases*; **1975**.
[99] B. Delley, *The Journal of Chemical Physics* **1990**, *92*, 508-517.
[100] B. Delley, *Journal of Chemical Physics* **2000**, *113*, 7756-7764.
[101] J. P. Perdew *et al.*, *Physical Review Letters* **1996**, *77*, 3865-3868.
[102] M. V. Frash *et al.*, *The Journal of Physical Chemistry B* **1998**, *102*, 2232-2238.
[103] G. Tauer *et al.*, *Chemical Engineering & Technology* **2019**, *42*, 2401-2409.
[104] E. N. Fuller *et al.*, *Industrial & Engineering Chemistry* **1966**, *58*, 18-27.
[105] E. N. Fuller *et al.*, *The Journal of Physical Chemistry* **1969**, *73*, 3679-3685.
[106] T. Fuller, The Electrochemical Society, **2008**.
[107] K. Mette *et al.*, *ChemCatChem* **2014**, *6*, 100-104.
[108] K. S. Sing *et al.*, in *Handbook of Heterogeneous Catalysis*, **2008**.
[109] D. Beierlein *et al.*, *Applied Catalysis B: Environmental* **2019**, *247*, 200-219.
[110] M.-M. Millet *et al.*, *ACS Catalysis* **2019**, *9*, 8534-8546.
[111] S.-H. Kang *et al.*, *Korean Journal of Chemical Engineering* **2011**, *28*, 2282-2286.
[112] R. Brown *et al.*, *Applied Catalysis* **1982**, *3*, 177-186.
[113] X. Ge *et al.*, *Journal of Solid State Chemistry* **2001**, *161*, 38-44.
[114] S. M. Kim *et al.*, *Journal of the American Chemical Society* **2017**, *139*, 1937-1949.
[115] D. Pandey *et al.*, *Journal of Molecular Catalysis A: Chemical* **2014**, *382*, 23-30.
[116] S. A. Theofanidis *et al.*, *ACS Catalysis* **2015**, *5*, 3028-3039.
[117] L. He *et al.*, *Journal of Energy Chemistry* **2014**, *23*, 587-592.
[118] M. B. Jensen *et al.*, *Catalysis Today* **2012**, *197*, 38-49.
[119] J. I. Di Cosimo *et al.*, *Journal of Catalysis* **1998**, *178*, 499-510.
[120] F. Solymosi *et al.*, *Journal of the Chemical Society, Faraday Transactions 1: Physical Chemistry in Condensed Phases* **1981**, *77*, 2645-2657.
[121] G. Busca *et al.*, *Materials Chemistry* **1982**, *7*, 89-126.

[122] S. R. Tong *et al.*, *Atmos. Chem. Phys.* **2010**, *10*, 7561-7574.
[123] Y. Wang *et al.*, *International Journal of Hydrogen Energy* **2015**, *40*, 8864-8876.
[124] K. Ito *et al.*, *Canadian Journal of Chemistry* **1956**, *34*, 170-178.
[125] J. Raskó *et al.*, *Catalysis Letters* **2005**, *101*, 71-77.
[126] J. Coates, in *Encyclopedia of Analytical Chemistry*, Wiley, **2006**.
[127] D. H. Kim *et al.*, *Journal of Industrial and Engineering Chemistry* **2015**, *23*, 67-71.
[128] C.-S. Chen *et al.*, *Applied Catalysis A: General* **2004**, *257*, 97-106.
[129] E. B. Sterk, Master thesis, Utrecht University **2018**.
[130] W. Zhen *et al.*, *Journal of Catalysis* **2017**, *348*, 200-211.
[131] E. Vesselli *et al.*, *The Journal of Physical Chemistry Letters* **2010**, *1*, 402-406.
[132] M. Zhang *et al.*, *The Canadian Journal of Chemical Engineering* **2020**, *98*, 740-748.
[133] C. Mebrahtu *et al.*, *Catalysis Science & Technology* **2019**, *9*, 4023-4035.
[134] G. Giorgianni *et al.*, *Physical Chemistry Chemical Physics* **2020**.
[135] I. Delidovich *et al.*, *Journal of Catalysis* **2015**, *327*, 1-9.
[136] A. Y. Khodakov *et al.*, *Journal of Catalysis* **2002**, *206*, 230-241.
[137] D. Wu *et al.*, *Journal of Industrial and Engineering Chemistry* **2017**, *56*, 175-184.
[138] Y. Han *et al.*, *Solid State Sciences* **2009**, *11*, 2149-2155.
[139] J. A. Gursky *et al.*, *Journal of the American Chemical Society* **2006**, *128*, 8376-8377.
[140] C. Agrafiotis *et al.*, *Journal of the American Ceramic Society* **2000**, *83*, 1033-1038.
[141] D. Pandey *et al.*, *Chemical Engineering Communications* **2016**, *203*, 372-380.
[142] I. Wysocka *et al.*, *Catalysts* **2019**, *9*.
[143] Z. Chang *et al.*, *Journal of Solid State Chemistry* **2005**, *178*, 2766-2777.
[144] M. V. Bukhtiyarova, *Journal of Solid State Chemistry* **2019**, *269*, 494-506.
[145] V. Rives *et al.*, *Coordination Chemistry Reviews* **1999**, *181*, 61-120.
[146] N. J. Tro, *Chemistry A Molecular Approach*, Pearson, **2003**.

[147] H. Wang *et al.*, *Industrial & Engineering Chemistry Research* **2010**, *49*, 2759-2767.
[148] H. Wang *et al.*, *CrystEngComm* **2012**, *14*, 6843-6852.
[149] D. Shi *et al.*, *Catalysts* **2019**, *9*, 451.

Appendices

Appendix A – Paper I

Book chapter 9.

CO_2 Methanation

H. L. Huynh and Z. Yu

Chemical Valorization of Carbon Dioxide

(Royal Society of Chemistry)

(invited book chapter, to be submitted)

This paper is not included for copyright reasons.

Appendix B – Paper II

CO_2 Methanation on Hydrotalcite-Derived Catalysts and Structured Reactors: A Review

H. L. Huynh and Z. Yu

Energy Technology **2020**, *8*, 1901475

DOI: 10.1002/ente.201901475

Energy Technology
Generation, Conversion, Storage, Distribution
www.entechnol.de

CO_2 Methanation on Hydrotalcite-Derived Catalysts and Structured Reactors: A Review

*Huong Lan Huynh and Zhixin Yu**

CO_2 methanation reaction has attracted renewed interest since the power-to-gas (PtG) concept emerged as a promising alternative for CO_2 emission abatement using surplus renewable electricity. Although the reaction has been reported for more than a century, improvements in the catalytic system and reactor design remain challenging. Recently, hydrotalcite (HT) materials known for their facile synthesis and high performance are extensively used as precursors for supported catalysts in a wide range of reactions, including CO_2 hydrogenation to CH_4. Herein, a comprehensive overview on HT-derived catalysts applied for CO_2 methanation is provided. More importantly, new reactor concepts are extensively investigated, such as honeycomb and microchannel reactors, to overcome issues related to the high exothermic nature of the reaction. The latest achievements with respect to structured reactors are also comprehensively reviewed and thoroughly discussed.

1. Introduction

Society is struggling to meet the ambitious goals of reducing carbon emissions. In fact, in 2018, the global carbon emissions grew by 2.0%, the fastest growth since 2010.[1] Currently, electricity production and heat generation emit the largest amount of CO_2, accounting for 42% of global CO_2 emissions.[2] Regardless of the climate change controversy, our energy system is inevitably in transition from fossil fuel to renewable energy sources (RES) as one of the primary power sources. In Europe, a shift toward RES is observed by an increasing share of wind, solar, and biomass sources in the gross electricity production, from 20% in 2010 to 32% in 2018.[3,4] It is expected that half of the electricity in the European power sector will be generated by RES in 2030. However, RES is intermittent and unpredictable, resulting in a seasonal surplus of electricity that requires a flexible storage system. Power-to-gas (PtG) concept, a potential chemical energy storage system, is one of the promising solutions. The concept is to convert the excessive electrical power into a gaseous energy carrier, such as hydrogen (H_2) and/or methane (CH_4), via a two-step process: H_2 production by water electrolysis and H_2 conversion to CH_4 by methanation reaction with external CO_2 sources.[4,5] The existing well-established natural gas network in Europe is one of the advantages to distribute and store synthetic CH_4. Moreover, the large scale of CO_2 emissions can be recycled in this PtG process.

$$CO_2 + 4H_2 \leftrightarrow CH_4 + 2H_2O \quad \Delta H = -165.0\,\mathrm{kJ\,mol^{-1}} \tag{1}$$

CO_2 methanation, also called the Sabatier reaction (Equation (1)), was discovered in 1902.[6] Industrially, methanation was applied to remove traces of CO and CO_2 gases from the H_2-rich stream for ammonia plants, for instance. During the oil crisis in the 1970s, the reaction was further investigated for the production of synthetic natural gas (SNG).[5] However, only a few projects reached a commercial scale because of technical difficulties. Problems relating to reactor concept selection, cleaning reactant gases to avoid catalyst deactivation, process efficiency, and economical attractiveness, etc. have been challenging for the SNG projects. Recently, CO_2 methanation underwent a revival as it is an essential part of the PtG process that offers an alternative for renewable electricity storage and facilitates' industrial decarbonization. In addition, the reaction is also appealing for long-term space exploration missions by space agencies, such as the National Aeronautics and Space Administration (NASA), which has used the Sabatier reaction for Mars exploration.[7]

Depending on the catalyst used, typical operating conditions are temperatures of 200–550 °C and pressures of 1–100 bar.[8] In terms of thermodynamics, the exothermic Sabatier reaction is favored at high pressures and low temperatures.[9] Due to kinetic limitations, maximum CO_2 conversion and CH_4 production are only achieved at high temperatures and pressures. A comprehensive review on the kinetics of CO_2 methanation with kinetic models over Ni-, Ru-, and Cu-based catalysts has been reported.[10] However, operation at high pressures is not practically economical, whereas operation at low temperatures requires highly active catalysts. Hence, the primary research on CO_2 methanation focuses on the exploration of new active materials and reactor design with regard to the improvement of heat and mass transfer. Furthermore, the Sabatier reaction itself is a well-developed process, yet there are controversial arguments on the reaction mechanism, mainly due to uncertainties on the intermediates

H. L. Huynh, Prof. Z. Yu
Department of Energy and Petroleum Engineering
University of Stavanger
4036 Stavanger, Norway
E-mail: zhixin.yu@uis.no

The ORCID identification number(s) for the author(s) of this article can be found under https://doi.org/10.1002/ente.201901475.

DOI: 10.1002/ente.201901475

formed during the reaction.[10–13] CH_4 from CO_2 hydrogenation could be formed by the dissociation of CO_2 to CO, either via a direct C—O bond cleavage (carbide pathway) or via formate intermediate. In addition, CH_4 formation through carboxyl intermediate has also been reported.

Many metals in group VIII in the periodic table, e.g., Ni, Co, Fe, Ru, Rh, etc., are active for the methanation reaction.[11,14] Although noble metals like Ru showed excellent activity and selectivity, the Earth-abundant Ni-based catalysts have always been the first choice for industrial applications due to its availability and affordable price. However, Ni-based catalysts exhibited a poor catalytic activity below 350 °C.[13] Catalytic activity at low temperatures is dependent not only on the Ni active metal but also on various factors, e.g., supports, promoters, preparation conditions, reduction, activation, etc. Studies revealed that high dispersion of metallic active sites on suitable support greatly contributes to the activation and dissociation of H_2 molecules. Thus, oxide supports with a high surface area, like SiO_2, Al_2O_3, SiO_2–Al_2O_3, and zeolites, are commonly used to obtain highly dispersed Ni-based catalysts. Many other oxides have also been studied (e.g., CeO_2, α-Al_2O_3, TiO_2, MgO, CeO_2/ZrO_2, etc.) as promising supports.[15] As different materials with unique physiochemical properties can positively influence the catalytic properties, the combination of two or more compounds could be beneficial for catalysis development.

Moreover, surface basicity can be tuned to enhance the chemisorption and dissociation of CO_2 molecules. Alkaline Earth oxides, such as MgO, are usually used to strengthen the basicity of the catalytic surface. The combination of MgO and Al_2O_3, as anticipated, has been reported as the best support for CO_2 conversion reactions, such as dry reforming, due to its high basicity, large surface area, and pore volume.[16] Metal sintering and carbon deposition are other challenges of Ni-based catalysts in CO_2 methanation. Due to the exothermic feature of the reaction, hotspots possibly occur in the catalytic bed and can cause thermal agglomeration of metallic Ni active sites. Consequently, it reduces the stability of the catalysts. To address these problems, Ni active sites are often stabilized by well-defined crystalline structures (i.e., solid solution, spinel, perovskite, etc.), rigid mesoporous frameworks, or core–shell structures.[17]

A critical component of CO_2 methanation technology is to synthesize highly active and stable catalysts, based on the strategies discussed earlier. Much efforts from both academia and industry are focused on the development of the methanation catalysts and process technology. This is witnessed by the number of review papers dedicated to this process, which have covered general aspects of methanation,[9,13,17,18] reaction mechanism,[10,12,19] supported catalysts,[14,15] plasma-catalytic process,[20] etc. Among these, hydrotalcite (HT)-derived catalysts have emerged as promising catalytic material for CO_2 conversion reactions, particularly CO_2 methanation and CO_2 reforming of methane. A special review paper on HT-derived catalysts for CO_2 reforming of methane has been published.[21] To complement the aforementioned review, we first review the applications of HT-derived Ni-based catalysts for CO_2 methanation in this work, due to the specific features and performance of these catalyst materials. Furthermore, reactor design is another important focus for the commercialization of the Sabatier process. Heat management plays a key role to achieve high CO_2 conversion in this highly exothermic reaction.

Huong Lan Huynh received her B.Sc. degree in chemical engineering from Vietnam National University—Ho Chi Minh City University of Technology (Vietnam) in 2016. She obtained her M.Sc. degree in natural gas technology from the University of Stavanger (Norway) in 2018. Currently, she is a Ph.D. candidate at the same university. Her research interest is heterogeneous catalysis and chemical processes for CO_2 conversion.

Zhixin Yu obtained his B.Sc. degree in applied chemistry from University of Science and Technology of China (USTC) in 1998, M.Sc. degree in manufacturing management from Linköping University (Sweden) in 2001, and Ph.D. degree in chemical engineering from Norwegian University of Science and Technology (Norway) in 2005. He joined the University of Stavanger (Norway) as professor in Natural Gas Technology in 2013. His main research interests include nanomaterials and nanotechnology for petroleum and clean energy production, nanocatalysis, syngas and H_2 production, biogas production, CO_2 conversion and utilization, etc.

Structured catalysts and reactors are among the best solutions to address this challenge. In the second part of this Review, we will discuss in more detail the latest progress on structured catalysts and reactors, which has not been covered by other reviews.

2. HTs as Precursors for Supported Catalysts

HT-like materials are also called layered double hydroxides (LDHs), which have similar structures as natural magnesium–aluminum hydroxycarbonate. The general formula for LDH material is $[M_{1-x}^{2+}M_x^{3+}(OH)_2](A^{n-})_{x/n}\cdot mH_2O$, where M represents metals and A is the anion. The value of x (molar ratio of trivalent and divalent cations) is preferred to be in the range of 0.2–0.4 to obtain a pure LDH phase and avoid the formation of hydroxides and other compounds. Divalent cations can be Mg and/or other metals (e.g., Fe, Co, Cu, Ni, or Zn), whereas trivalent cations are Al and/or other metals (e.g., Cr, Ga, In, Mn, or Fe).[22] Because a wide range of cations and anions can be incorporated, HT-like precursors have drawn much attention as promising materials for heterogeneous catalyst design. As the cations in HT structures are well dispersed, the obtained mixed oxides upon thermal decomposition usually show a good distribution of metal active sites. Therefore, derivatives of HT-like precursors after calcination are often used as supported metal catalysts.[23] The phase transformations during calcination of the HT precursors and subsequent reduction of the mixed oxides are schematically shown in **Figure 1**. Another important feature of HT-derived catalysts is the tunable basic strength

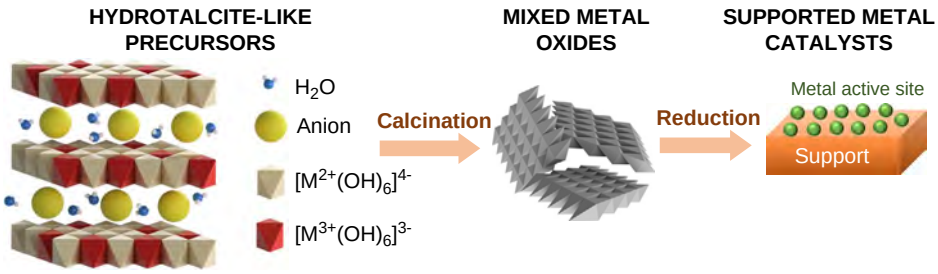

Figure 1. Preparation pathway of supported metal catalysts from HT-like precursors.

through judicious choices of metal cations and compositions, to achieve desirable activity and selectivity for specific catalytic reactions. Therefore, HT-derived catalysts have been extensively applied in many reactions, including hydrogenation and hydrodesulfurization, polymerizations, syngas production from steam reforming, dry reforming of methane, as well as the Sabatier reaction.[21,24]

2.1. Ni/Al_2O_3 Catalysts Derived from HT Materials

The main challenge in catalyst development for CO_2 methanation is to enhance the catalytic activity and stability for the Earth-abundant transition metal Ni. A higher CH_4 conversion can be achieved using high loading catalysts.[25] However, the catalyst may consequently possess low metal dispersion and is susceptible to sintering.[26] HT-derived catalysts can be an alternative solution because the calcined precursors have strong metal–support interaction and high dispersion of active metals, regardless of the metal loading. Regarding the application of HT-like materials for CO_2 methanation, Ni/Al_2O_3 HT-derived catalysts were first reported by Abelló et al.[27] Since then, there has been an increasing number of publications using Ni-based HT-derived catalysts for the Sabatier reaction, as shown in **Table 1**. In addition, different types of promoted catalysts were also included. The promoters could be a second metallic site (e.g., Fe and Co) or could be incorporated into the support structure (e.g., MgO, CeO_2, and La_2O_3). It was expected to enhance the basicity and/or improve Ni distribution for a better catalytic performance.

HT precursors are prepared by the conventional coprecipitation at constant pH, which is usually preferred at high pH (>8).[28] Aging or hydrothermal treatment is an additional step

Table 1. Summary of Ni-based HT-derived catalysts for CO_2 methanation.

HT-derived Catalysts	Ni loading [wt%]	$[M^2]^+/M^{3+}$	Reaction conditions			X_{CO2}[b)][%]	S_{CH4}[c)] [%]	Ref.
			T [°C]; P [bar][a)]	H_2:CO_2:standard gases ratio	Space velocity			
Ni/Al_2O_3	69.1	5	400; 10	4:1:1	268.8 L g_{cat}^{-1} h^{-1}	92.4	>99	[27]
Ni/Al_2O_3	75–76	3	300	10:2.5:87.5	20 000 h^{-1}	80–85	>97	[28]
Ni/Al_2O_3	78	3	350	72:18:10	75 L g_{cat}^{-1} h^{-1}	82.5	99.4	[29]
Ni/Al_2O_3	21.3–42.6	0.5–3	220	34.35:0.65:65	20 000 h^{-1}	–	–	[30]
Ni/Al_2O_3	–	2	275	4:1:1	≈107.5 L g_{cat}^{-1} h^{-1}	66	98.7	[31]
Ni/Al_2O_3	≈73	5	250	12:3:5	2400 h^{-1}	90	>99	[32]
Ni/Al_2O_3	75	3	350	40:10:50	30 000 h^{-1}	–	40	[33]
$Ni/MgAlO_x$	59	2	250	18.5:4.6:77	66 L g_{cat}^{-1} h^{-1}	20	18	[34]
$Ni/MgAlO_x$	10.3–42.5	3	250	12:3:5	12 000 h^{-1}	72	>99	[35]
$Ni/MgAlO_x$	17.2–57.8	2	250	12:3:5	2400 h^{-1}	97.9	97.5	[36]
$Ni/MgAlO_x$/SiC	12.5	5	400	4:1	60 L g_{cat}^{-1} h^{-1}	78.4	93.5	[37]
$Ni–Fe/Al_2O_3$	65–70	2	350	76:19:5	12 L g_{cat}^{-1} h^{-1}	96	>99	[38]
$Ni–Fe/MgAlO_x$	72.6	3	300	4:1	20 000 h^{-1}	83	97	[39]
$Ni–Fe/Al_2O_3$	39.6	≈1	250, 8	4:1:5	150 L g_{cat}^{-1} h^{-1}	≈45	>99	[40]
$Ni–Mn/Al_2O_3$	36.3	≈1	250, 8	4:1:5	150 L g_{cat}^{-1} h^{-1}	≈85	>99	[40]
$Ni–Fe–Mn/Al_2O_3$	35.6	≈1	250, 8	4:1:5	150 L g_{cat}^{-1} h^{-1}	≈80	>99	[41]
Ni–La/MgO	21	3	250	12:3:5	12 000 h^{-1}	56	>99	[42]
$Ni/CeO_2–Al_2O_3$	≈6	3.6	300	4:1	60 L g_{cat}^{-1} h^{-1}	≈75	>99	[43]
$NiCeZr/MgAlO_x$	20	3	375	4:1	20 000 h^{-1}	≈35	–	[44]

[a)]All reactions were run at atmospheric pressure; [b)]X_{CO2}—CO_2 conversion; [c)]S_{CH4}—selectivity of CH_4.

to achieve better crystallization, a higher surface area, and pore volume. With the aim to reduce the average particle size of Ni on Al_2O_3 support, Abelló et al. prepared Ni/Al_2O_3 HT precursors by coprecipitation at constant pH.[27] Although at high Ni loading (≈70 wt%), the Ni nanoparticles size in the range of 5–10 nm was achieved, demonstrating the advantage of using HT precursors. He et al. also reported a high-loading Ni/Al_2O_3 HT catalyst (78 wt%) with a very small Ni particle size in the range of 3–9 nm.[29] Despite different values of pH used during synthesis, HT-derived catalysts were successfully prepared with a homogeneous distribution of Ni on Al_2O_3 support.

In comparison with other conventional Ni/Al_2O_3 catalysts such as commercial catalysts and catalysts prepared by incipient wetness impregnation, Ni^{2+} surface species in HT-derived catalysts were harder to be reduced, reflecting a stronger metal–support interaction and a better metal dispersion.[28,29] The reducibility of Ni species was proportional to Al content, which could be explained by the formation of hardly reducible spinel $NiAl_2O_4$.[30] In fact, when only Ni and Al are incorporated in the LDH structure, it is called takovite and can be synthesized with Ni/Al molar ratios in the range of 1–5.6.[45] Gabrovska et al. found that this ratio could influence the crystallization degree of the precursors. A series of Ni/Al_2O_3 HT catalysts with varied Ni/Al molar ratios in the range of 0.5–3 was investigated.[30,31] The catalyst with a Ni/Al molar ratio of 2 exhibited the best performance in terms of CO_2 conversion and CH_4 selectivity. Notably, the catalyst maintained its activity during the 500 h long-term test at 275 °C. It is also noteworthy that a higher Ni/Al molar ratio did not significantly influence the catalytic performance of Ni/Al_2O_3 HT catalysts.[32] For instance, the CO_2 conversion of catalysts with a Ni/Al molar ratio of 3, 4, and 5 was 85–88%, whereas CH_4 selectivity was always ≈100% at 300 °C [gas hourly space velocity (GHSV) = 2400 h^{-1}, $H_2/CO_2 = 4$]. Moreover, mechanistic insights based on in situ Fourier transform infrared spectroscopy (FTIR) analysis during methanation reaction were provided.[31,32] Formate species as intermediates were detected, and the reaction mechanism via the formate pathway was proposed. In addition, the kinetic rate expression was important for the design of a full-scale methanation reactor. A kinetic study was also conducted for CO_2 methanation over Ni/Al_2O_3 HT catalysts, from the power law to the Langmuir–Hinshelwood approach.[33]

Overall, HT-derived catalysts exhibited better performance than conventional catalysts in CO_2 methanation. The Ni/Al_2O_3 HT catalyst (Ni/Al = 5, 70 wt% Ni) was able to maintain a high selectivity toward CH_4 (>99.7%) for 350 h of CO_2 methanation at harsh conditions (400 °C, 10 bar), even though the CO_2 conversion slowly decreased from 92.4% to 83.5%.[27] In fact, it was reported that Ni/Al_2O_3 HT-derived catalysts had better stability than conventionally impregnated catalysts, although slight deactivation was observed.[46] Abate et al. also concluded that Ni/Al_2O_3 HT-derived catalysts showed a more satisfactory stability and higher performance than commercial Ni/Al_2O_3 catalysts (at 300 °C and GHSV = 20 000 h^{-1}).[28]

2.2. Promoted Ni-Based HT-Derived Catalysts

The introduction of alkaline-Earth species to strengthen the surface basicity has been widely recognized as an effective way to improve catalytic activity and stability.[47] Studies on CO_2 methanation with promoted HT-derived Ni catalysts are also shown in Table 1. Liu et al. prepared the Ni nanocatalyst supported on Mg/Al mixed metal oxides derived from HT precursors.[36] Although the density of Ni nanoparticles increased as a result of a high Ni/Mg molar ratio, their average size remained the same at ≈2.5 nm. Compared with conventional Ni/Al_2O_3 and Ni/MgO catalysts, Ni/MgAl HT-derived catalysts showed better metal dispersion and significantly smaller particle size. Furthermore, the total basicity of the Ni/MgAl HT catalyst was enhanced, which was obviously due to the contribution of Mg species with medium-strong basic sites. As expected, Ni/MgAl HT catalysts (36.9 wt% Ni, (Ni+Mg)/Al = 2) exhibited an outstanding performance in CO_2 methanation, compared with Ni/Al_2O_3, Ni/MgO, and Ni/carbon nanotube (CNT) catalysts. The conversion of CO_2 reached 97.9% at 250 °C with diluted feed gases ($H_2/CO_2/Ar = 12/3/5$, GHSV = 2400 h^{-1}, 1 bar). The time-resolved diffuse reflectance infrared (IR) Fourier transform spectroscopy (DRIFTS) measurement was reported, suggesting that MgO could play an important role as an active site for CO_2 activation to form carbonate/hydrocarbonate species.

Bette et al. also prepared Ni/MgAl HT catalyst at the same (Ni + Mg)/Al molar ratio of 2 but at a higher Ni loading of 59 wt%.[34] In another work reported by Wierzbicki et al., the influence of Ni content of Ni/MgAl HT catalysts on the performance of CO_2 methanation was studied.[35] Apparently, the highest CO_2 conversion was achieved by the catalyst with the highest amount of Ni. The temperature-programmed reduction (TPR) study demonstrated that a large amount of Ni weakened the metal–support interaction and Ni species was easier to be reduced in Ni-rich catalysts. In contrast, the Ni-rich catalysts were found to have stronger basicity. The number of medium-strength basic sites increased steadily with the increase in Ni/Mg ratio when the M^{2+}/M^{3+} ratio was kept constant. Thus, the role of Mg was not clearly observed in this study, and Ni content was the dominating factor on the activity of Ni/MgAl HT catalyst. Nevertheless, Ni/MgAl HT-derived catalysts are considered as excellent alternatives for CO_2 methanation. An optimal tradeoff between H_2 activation (by Ni sites) and CO_2 activation (by basic sites of support) could be induced by a suitable composition of Ni, Mg, and Al. Hence, higher activity and stability could be achieved for CO_2 methanation, especially at low temperatures.

As mentioned, catalysts with good activity at low temperatures are highly desirable. An interesting concept was developed by Wang et al., who combined an HT-like structure with SiC substrate, known for high heat conductivity and superior thermal stability.[37] The Ni/MgAl–SiC catalysts exhibited better performance than Ni/MgAl HT catalysts, particularly at 275–300 °C, which could be ascribed to higher reducibility and a higher metallic surface area. A long-term test at 400 °C for 50 h showed that the Ni/MgAl–SiC catalysts had stable activity although slight deactivation still occurred, with CO_2 conversion dropping ≈1.5% over 50 h of reaction, which was assumed to be caused by mild metal sintering.[37] Another approach to increase the basic sites of support was reported by He et al., who fabricated the K–Ni/Al_2O_3 HT catalyst.[29] As expected, both the CO_2 conversion and CH_4 selectivity increased for the K-impregnated catalysts, which could be explained by the enhanced basicity from

the alkali metals. Comparisons in terms of enhancing the basicity between different types of alkali and alkaline Earth promoters are highly recommended.

A study on Ni–Fe/Al_2O_3 HT catalysts has been reported.[38] Fe was directly introduced into the HT structure during coprecipitation. The authors convinced that a certain amount of Fe addition could result in a catalytic system with a larger surface area, optimal particle size, and higher Ni dispersion. Using the Ni–Fe/Al_2O_3 HT catalyst (69 wt% Ni and 1.6 wt% Fe), the CO_2 conversion reached 80.8% at 219 °C but it was only 16.4% for the Ni/Al_2O_3 HT catalyst. Recent research suggested that Fe enhanced the adsorption of H_2 for CO_2 methanation,[48] whereas it is well known that the activity and selectivity of Fe catalysts are dependent on Fe loading and its oxidation state.[49] In fact, the bimetallic Ni–Fe catalyst was also considered as a promising candidate to substitute noble-metal catalysts in hydrogenation reactions.[50] Mebrahtu et al. studied the synergistic effect of bimetallic Ni–Fe alloys HT-derived catalysts for CO_2 methanation.[51] The addition of Fe increased the particle size, total basicity, and reducibility but reduced the surface area and total pore volume. It was found that Fe/Ni molar ratio of 0.1 was the best composition for Ni–Fe/MgAl HT catalyst (12 wt% Ni, $M^{2+}/M^{3+} = 3$). Both basicity and metal particle size were optimized at this ratio to accelerate the dissociation of H_2 from metallic sites and CO_x species from the support. The catalyst also exhibited a high stability in a 24 h long-term test without any observation of deactivation. However, the activity test was only conducted at 335 °C; thus, the challenge of CO_2 methanation at low temperatures was not pronounced. In another study, the authors further studied the deactivation of the bimetallic Ni–Fe catalysts during low-temperature CO_2 methanation.[39] They suggested that the formation of $Ni(OH)_2$ caused deactivation, which could be suppressed by doping Ni with Fe.

Apart from Fe, Mn has also been investigated as a promoter for CO_2 methanation, especially via HT-derived catalysts.[40] Mn as a promoter in Ni–Mn/Al HT catalysts appeared to improve the medium basic sites, which led to an increase in CO_2 adsorption. In contrast, the Fe promoter was assumed to strengthen the thermal stability of the catalysts. Hence, to increase the catalytic activity, a high amount of Mn addition was preferred, whereas a high amount of Fe was recommended to increase the stability. Indeed, the performance of Ni–Fe–Mn/Al HT-derived catalysts was significantly better than Ni/Al HT catalysts.[41]

Lanthanum has been shown to have a positive effect on CO_2 methanation. According to Wierzbicki et al., although La species existed as a separate phase and was not incorporated into the HT structure of Ni–La/MgAl HT catalyst (15 wt% Ni), La increased the total basicity due to its medium-strong basic sites.[42] Therefore, CO_2 adsorption capacity was enhanced. In this case, the catalyst with La loading of 2 wt% exhibited the highest CO_2 conversion and more significantly at a low temperature (<300 °C). The authors also studied the effect of different preparation methods of Ni–La/MgAl HT catalysts. Ion exchange using the La–ethylenediaminetetraacetic acid complex was reported as the most suitable method to dope La into the Ni/MgAl HT catalyst. The catalytic performance was very stable for the 24 h long-term test without any metal sintering or carbon deposition.

As mentioned earlier, Ce was one of the promising promoters to obtain highly active catalysts. Ni–Ce HT precursors were impregnated on γ-Al_2O_3 support by Xu et al.[43] Although the role of Ce addition was not addressed, this study revealed that the HT precursors that impregnated on Al_2O_3 support showed better catalytic performance than conventional catalysts. Interestingly, instead of using the traditional calcination method, the cold plasma technique was used to improve the catalytic properties. Moreover, cold plasma via dielectric barrier discharge (DBD) technology can also be implemented on the traditional fixed-bed reactor. Ni–Ce–Zr/Mg–Al HT catalysts presented the higher CO_2 conversion of ≈70% at 325 °C in CO_2 methanation using plasma, compared with the conventional reactor, where merely 5% of CO_2 conversion was achieved at similar conditions.[44]

3. Structured Catalysts and Reactors

Fixed-bed reactors, i.e., packed-bed reactors, are commonly used for CO_2 methanation due to their simplicity and cost effectiveness. The reactors provide more contact between the reactant gases and the catalyst granules/pellets. However, random maldistribution in the fixed-bed reactors causes nonuniform access of reactant gases to the catalytic surface, unexpected hotspot, and thermal runaways of exothermic reactions, which are the most challenging problems of the methanation process. The overall process performance, CH_4 yield, CH_4 selectivity, and the lifetime of the catalysts are consequently reduced. Therefore, different reactor concepts focusing on heat management have been proposed.[52] One of the most common reactor concepts with intensified heat transfer is structured reactors equipped with well-designed structured catalysts. The hydrodynamics in a structured reactor can be simplified as uniform laminar flow, enabling full access of reactant gases to the catalytic surface with a lower pressure drop and possibly diminishing mass transfer limitations.[53] Structured catalysts with high thermal conductivities could also increase the overall heat transfer coefficient, thus improving the heat transfer performance of the reactor.[54] For instance, based on modeling studies, Schlereth et al. concluded that honeycomb monolith reactors have superior performance in comparison with fixed-bed reactors in terms of heat transfer efficiency, although it was only applied on specific operating conditions of CO_2 methanation.[55]

In general, structured catalysts consist of a 3D-shaped support with a layer of catalytic material. The support materials are ceramic type (e.g., Al_2O_3, cordierite-Al_2O_3, MgO, SiO_2, SiC, etc.), metallic type (e.g., Al, Ni, Cu, Co, stainless steel, Inconel, FeCrAlloy, etc.), or carbon-type (e.g., activated carbon, reticulated vitreous carbon). Several 3D structural configurations are honeycomb, corrugated sheet, gauze, foam, fiber, wire packing, or periodic open-cellular structures.[56] Although the use of structured catalysts and reactors has been discussed in a previous study,[57] we present a more systematic and detailed review of the recent developments of conventional structured catalysts for CO_2 methanation, together with the latest innovative concepts of catalyst manufacturing. A summary of different configurations of structured catalysts and reactors applied for CO_2 methanation is shown in **Table 2**.

Table 2. Summary of structured catalysts and reactors for CO_2 methanation.

Structured catalyst types	Catalysts	Reactor type	Ref.
Cordierite honeycomb monolith (400 cpsi)[a)]	$Ru/\gamma\text{-}Al_2O_3$	Fixed bed	[58]
Aluminum honeycomb fin (45 × ∅18 mm, 100–200 cpsi)	Ni/CeO_2	Conventional flow type	[59,60]
Cordierite monolith (15×∅10 mm, 500 cpsi)	Ni/gadolinium-doped-ceria (GDC)	Fixed-bed quartz tubular	[61]
Cordierite honeycomb square channel (50 × 50 × 142 mm, 300 cpsi)	$Ni/\gamma\text{-}Al_2O_3$	Innovative single-stage lab scaled	[62]
Aluminum and stainless steel honeycomb (100 × ∅80 mm)	Ni/Al_2O_3	Multitube fixed bed (heat exchange by oil)	[63]
Ceramic honeycomb with square cell structure (100–300 cpsi)	Ni/CeO_2	Fixed-bed quartz tubular	[64]
SiC foam (150 × ∅20 mm)	Ru/TiO_2	Fixed bed	[65]
Ni foam (∅16 mm)	Ni/Al_2O_3	Fixed-bed quartz tubular	[66]
Sponge Ni	–	Fixed-bed quartz tubular	[67]
SiC, aluminum, and alumina open-cell foam	$Ni\text{-}Ru/CeO_2\text{–}ZrO_2\text{–}CNF$	PMR and double-walled reactor exchanger	[68–71]
Aluminum open-cell foam	Ni/Al_2O_3	Metallic foam reactor channel (heat exchange by oil)	[72]
Aluminum open-cell foam and SiC honeycomb monolith (150 cpsi)	$Ni/CeO_2\text{–}ZrO_2$	Fixed-bed quartz tubular	[73]
Spiral aluminum plate	Ni/CeO_2	Fixed-bed quartz tubular	[74]
FeCrAlloy plate	Ni/Al_2O_3	Plate reactor	[75,76]

[a)]cpsi—cells per square inch.

3.1. Honeycomb Monolith Catalysts and Reactors

One of the early studies using monolithic catalysts for methanation was conducted by Jarvi et al.[77] The authors reported that the monolithic-supported Ni catalyst was significantly more active and selective in CO methanation compared with catalysts in bead and pellet forms. Because of superior performance with a low-pressure drop at high space velocities, the honeycomb Ni-based catalysts were recommended as ideal catalysts for high throughput methanation. Despite those initial promising findings, the industrial applications of structured reactors were scarce and limited until the past decade, particularly for CO and CO_2 methanation. In recent years, there has been a considerable number of research using structured catalysts, particularly honeycomb monoliths for the synthesis of CH_4 from CO_2 and H_2.

The application of monoliths for CO_2 methanation was first introduced as a model for heat exchanger by Janke et al.[58] Although the reaction was conducted at low space velocity, the $Ru/\gamma\text{-}Al_2O_3$ monolith catalyst exhibited excellent activity at very low temperatures of CO_2 methanation (200–250 °C). Repeated tests on the spent monolith were also conducted and showed nearly the same activity as that of the fresh one. This is one of the earliest studies which proved the feasibility of wash-coated honeycomb monoliths for CO_2 methanation.

Recently, a honeycomb-structured catalyst with a high CO_2 methanation performance was reported by Fukuhara et al.[59] Among different support materials (i.e., Al_2O_3, ZrO_2, CeO_2, TiO_2, Y_2O_3, and MgO), CeO_2 was identified as the best catalyst with the highest activity in CO_2 methanation. The Ni/CeO_2 catalyst was subsequently wash coated on an Al substrate with different honeycomb-fin configurations. A temperature spike of ≈20 K from the set temperature was observed in the granular-type catalytic bed during reaction. In contrast, it was confirmed that the temperature of the honeycomb-type catalytic bed was constant and close to the set temperature. The advantage of structured reactors using monolith catalysts in terms of heat exchange and hotspots prevention was recognized.

The authors further investigated different stacking strategies of honeycomb monoliths and developed a multistacked design (**Figure 2**). For segment-type configuration, the optimum 15 mm-gap distance was found to boost the performance of catalysts.[60] Coated catalysts were placed alternating with static mixers which were considered as an advanced part to accelerate the mass transfer.[78] Even though hotspots were observed during reaction, the random flow channel and gap distance enhanced the methanation performance at low temperatures and high flow rate without pressure drop. The catalyst stability was maintained at a high CO_2 conversion of 92.7% with a slight decrease of 0.6% over 76 h at 300 °C and a highly undiluted flow of 3 L min^{-1}. The metallic honeycomb catalyst in multistacked design revealed an extremely promising concept for CO_2 methanation.

Cordierite, or magnesium iron aluminum cyclosilicate, is a common ceramic-type material used in monoliths manufacturing. Vita et al. used this type of substrate to enhance the activity of Ni-based catalysts (**Figure 3**a).[61] However, instead of using the conventional wash-coating method, the authors used solution combustion synthesis to prepare the structured catalysts. Solution combustion synthesis was suggested as a suitable procedure to deposit thin, adhesive, and uniform catalytic layers on the ceramic surface.[79] The monolith system showed better activity than the powder-type catalysts in terms of CH_4 productivity. A long-term reaction test was conducted at 400 °C and GHSV of 30 000 h^{-1}. During the reaction, the temperature at the center and outlet of the catalytic bed plunged up to 476 and 448 °C, respectively. Despite hotspot formation, the ceramic-type monolith still maintained its high activity with CO_2 conversion of 68–69% throughout 200 h of reaction.

Ahn et al. pointed out the knowledge gap in the influence of coating materials on the catalytic performance of honeycomb catalysts.[64] The authors used industrial ceramic honeycomb

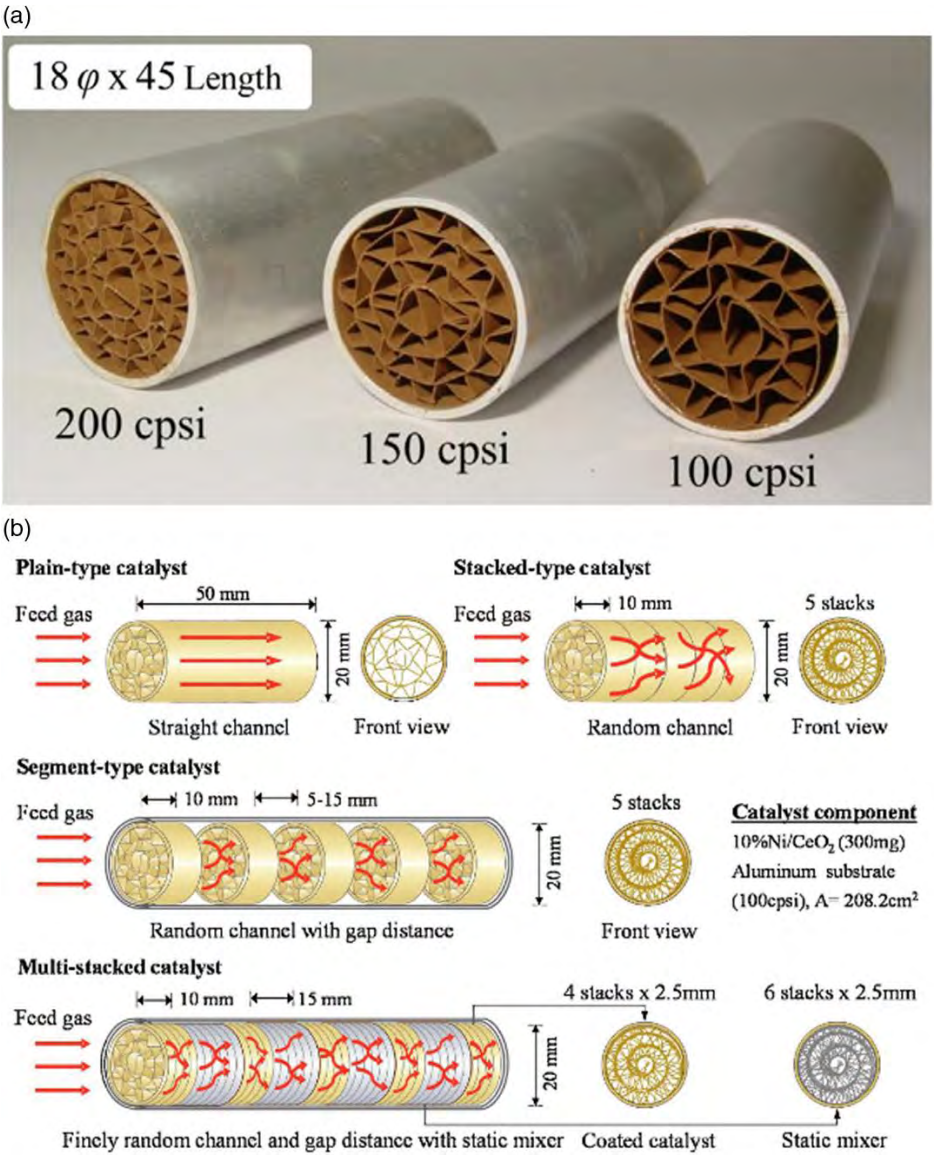

Figure 2. a) Overview of Al-honeycomb Ni-based catalysts with different cell density. Reproduced with permission.[59] Copyright 2017, Elsevier. b) Different configurations of the honeycomb catalysts: plain, stacked, segment and multi-stacked types. Reproduced with permission.[60] Copyright 2018, Elsevier.

support with various cell densities. Isopropanol was reported to be the most suitable coating liquid to achieve high CO_2 conversion, regardless of concentration. The excellent activity of Ni/CeO_2 powder-type catalyst was reconfirmed among Ni/Al_2O_3, Ni/Y_2O_3, and Ni/TiO_2 catalysts. The material was subsequently used to prepare honeycomb-type catalysts (Figure 3b). The square honeycomb catalyst at a higher cell density exhibited better performance, particularly at the low-temperature region, which could be ascribed to the higher surface area of the catalyst.

Many efforts have been dedicated to the innovation of the conventional fixed-bed reactors. A multibed reactor with up to four chambers per stage was proposed by Biegger et al.[62] The authors first tested two single-stage lab-scaled reactors using a square honeycomb $Ni/\gamma\text{-}Al_2O_3$ catalyst. CH_4 productivity achieved in the second reactor was significantly higher than the first reactor, as expected. Although heat management was not successfully achieved in this work, the possibility of enhanced CH_4 production via a multistage reactor system was revealed.

By mathematical modeling, a honeycomb reactor was simulated and upgraded to a semicommercial scale by Schollenberger et al.[63] The authors aimed to optimize the reaction path with a high reaction rate. The mathematical model was successfully developed and experimentally validated with commercial honeycomb Ni/Al_2O_3 catalysts. To obtain products with more than 95 vol% of CH_4, a reactor with two reaction zones was suggested. It was assumed that the high-temperature gas inlet was kinetically controlled and had a maximum possible rate, whereas the low-temperature gas outlet was controlled by thermodynamics and adjusted the necessary equilibrium composition. Based on the experimental temperature profiles and

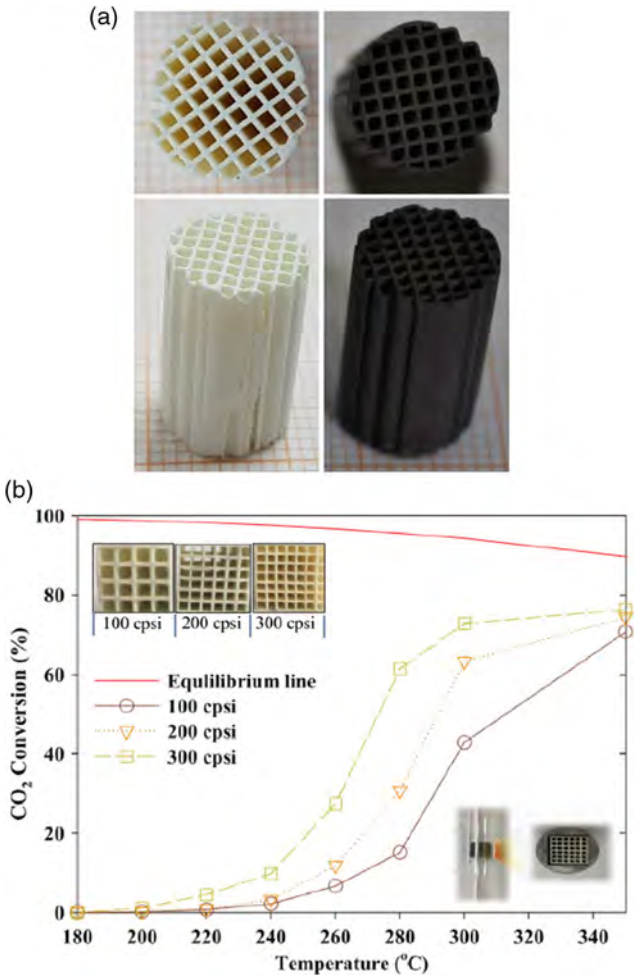

Figure 3. a) Photographs of uncoated (left) and coated (right) cordierite monoliths. Reproduced with permission.[61] Copyright 2018, Elsevier. b) CO_2 conversion in CO_2 methanation over 10 wt% Ni/CeO_2 honeycomb-type catalysts at different cell densities. The image of the honeycomb-type catalyst inside the quartz tube reactor is presented on the bottom right corner. Reproduced with permission.[64] Copyright 2019, Elsevier.

specific production rates, the combination of aluminum and steel honeycomb was found to be the most promising design.

3.2. Foam-Type Structured Catalysts and Reactors

As mentioned earlier, the Sabatier process is very appealing for aerospace exploration missions. Shima et al. reported Ru/TiO_2 on SiC foam catalysts for methanation reaction, which was a part of practical space systems called closed-loop air revitalization.[65] Later on, $Ni–Al_2O_3$ was embedded on Ni foam by the wet chemical etching method. While Ni foam could convert only 10% of CO_2 at 300 °C, a significantly high conversion of 91% could be achieved by $Ni–Al_2O_3$/Ni foam.[66] The improved heat transfer of foam-based catalysts was investigated by both experimental works and computational fluid dynamic (CFD) modeling. With an equivalent amount of reaction heat released from the catalytic surfaces at equal conversion, the foam-based catalytic bed generated a hotspot with ≈30 K temperature rise, whereas it was ≈155 K for the powder-packed bed. Hence, the exceptionally stable CO_2 methanation performance (CO_2 conversion of ≈90%, CH_4 selectivity of >99.9%) was observed during a 1200 h reaction over the foam-type catalyst at 320 °C. Ni foam was also reported as Ni sponge by Tada et al.[67]

Foam-based catalysts started to gain more attention in the application of small-sized structured reactors for the Sabatier reaction. A so-called platelet millireactor (PMR), with one single channel (**Figure 4**a), was used by Frey et al.[68] In their study, the central channel of the PMR contained β-SiC foam, which was impregnated with Ni–Ru-based catalysts. Based on specific CH_4 productivity, $Ni–Ru/CeO_2–ZrO_2$ powder catalysts showed superior performance to other catalysts. Interestingly, when carbon nanofibers (CNFs) were added to $CeO_2–ZrO_2$ support, the new foam-based catalysts ultimately exhibited better productivity. Moreover, for the first time, an in situ observation was conducted to study the reaction ignition and hotspot formation. The temperature on the foam surface during the methanation reaction was recorded by the IR camera (Figure 4b). The presence of the hotspot could be correlated with CH_4 and CO selectivity. Local hotspots were suspected to favor the reverse water gas shift (RWGS) reaction, which increased CO selectivity and reduced the CH_4 selectivity. However, the addition of CNFs allowing better heat transfer could be a good solution for the design of catalysts. Further investigation on the role of CNFs on foam catalysts is greatly appealing.[69]

Another study by Frey et al. revealed that SiC foam was a better support than Al and Al_2O_3 open-cell foam due to better anchoring strength.[70] Nevertheless, $Ni/CeO_2–ZrO_2$ coated on Al open-cell foam has been extensively tested.[71] A double-walled reactor exchanger was used for CO_2 methanation. Eight coated cylindrical foams (3 × ∅2 cm) were installed inside the reactor chamber. The foam had a central channel of 2 mm, allowing the insertion of a multipoint thermocouple, which can measure the temperature at six different positions. The experiments successfully proved that the hotspots are formed based on the temperature profiles along the reactor. More heat was released in the first one-third of the catalytic bed where a maximum temperature increase of 25 K was measured. Similarly, it was reported that at the higher set temperature, the Sabatier reaction released more exothermic heat, resulting in higher CH_4 productivity and CO_2 conversion. Subsequently, more severe hotspots were also suspected due to the high-temperature elevation.[66] Foam-structured materials were assumed to have excellent heat evacuation capacity, lower risk of thermal runaway, and premature catalyst deactivation, whereas the reactor exchanger was suggested to have advantages on heat convection. In this study, the heat transfer fluid was circulated outside the reactor tube at a maximum temperature of 320 °C. This could explain the temperature increase of only 25 K, when it could plunge up to 200–250 K in a powder-packed bed reactor under similar conditions.[80] The excellent heat transfer efficiency of the reactor exchanger can be useful for the development of the methanation reactor.

Bengaouer et al. evaluated the performance of the annular fixed bed, millistructured reactor channel, and open-cell foam reactor (i.e., metallic foam reactor channel).[72] The same commercial Ni/Al_2O_3 catalyst was used for comparison. Coated cellular Al open-foam pellets were stacked inside the foam

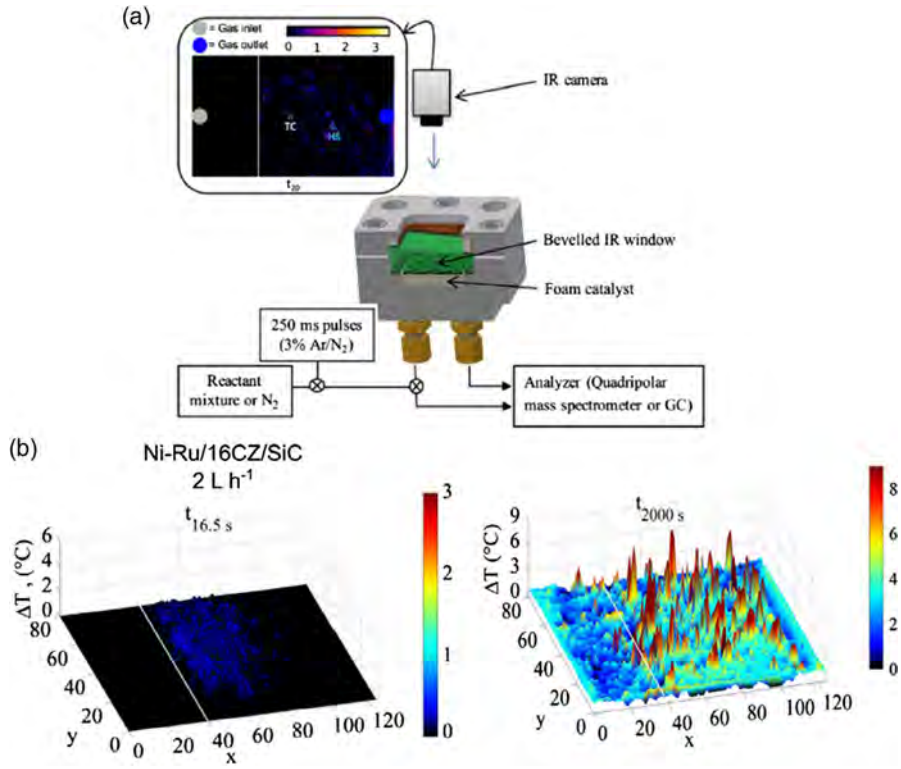

Figure 4. a) Simplified schematic of reaction set up, where foam-type catalyst was located inside a PMR equipped with an IR thermal camera; b) IR thermograph presenting ignition and stationary stage ($t_{16.5s}$ and t_{2000s}) of Ni–Ru/CeO_2–ZrO_2/SiC foam structured catalyst. Reproduced with permission.[69] Copyright 2019, Elsevier.

reactor. CH_4 yield, space–time yield, mass productivity, volumetric productivity, and temperature elevation were essential indicators for the reactor performance. Millistructured reactor channel exhibited the best volumetric productivity and space–time yield, although significantly the high-temperature elevation indicated poor heat management. In contrast, the metallic foam reactor showed excellent mass productivity and negligible hotspot formation, but the CH_4 yield was moderate. Thus, the authors proposed an alternative solution, such that two concepts could be combined for higher productivity and better thermal management.

As there are different configurations of structured catalysts, the comparison between monolith and foam type, for instance, is interestingly necessary. Ricca et al. tested the 5 wt% Ni/CeO_2–ZrO_2-supported catalysts in both powder and structured forms.[73] Based on adhesion tests, Al foam seemed to have less anchoring strength than SiC monolith. At 300 °C, the catalyst on SiC monolith achieved the highest CO_2 conversion and CH_4 selectivity. Undesirable hotspot formation was detected in all catalytic beds according to the thermal profiles. Although a temperature elevation of 100 K was measured, the heat dissipation on the SiC monolith bed was better than that of Al foam and powder bed.

3.3. Other Types of Structured Catalysts and Reactors

A spiral-type Ni/CeO_2 catalyst was prepared by Fukuhara et al.[74] The structured substrate was the Al plate, twisted to form the spiral shape, and subsequently wash coated by a slurry granular of Ni/CeO_2 catalyst. CO_2 conversion of 50% was obtained at a low temperature of ≈280 °C at GHSV of 80 L g_{cat}^{-1} h^{-1}, demonstrating the outstanding activity of the catalyst in CO_2 methanation. Moreover, an automethanation process (i.e., $CO_2 + 6H_2 + O_2 \rightarrow CH_4 + 4H_2O$) was also reported. The reaction readily occurred at room temperature, and ≈60% CO_2 was converted by the same catalytic system. An IR thermal image was recorded (**Figure 5**). The extremely exothermic heat released was clearly seen near the inlet of the reactor during reaction at room temperature. Despite a huge temperature spike of ≈300 K, the structured catalyst was able to maintain its stable activity during the 60 h test.

3.4. 3D Printing Structured Catalysts

In the past few years, an innovative technology developed from additive manufacturing, named 3D fiber deposition (3DFD), was used to produce macrostructured catalytic supports. 3DFD materials were constructed by the extrusion of a highly viscous paste consisting of metallic or ceramic mixtures through a thin nozzle. The so-called 3D printing catalysts provide better heat and mass transfer and lower pressure drops, for instance, similar to structured catalysts. However, the flexible design is the most significant feature.

Danaci et al. prepared stainless steel and copper support (3D-SS and 3D-Cu, respectively) using the extrusion method (**Figure 6**).[81,82] The support was then dip coated with

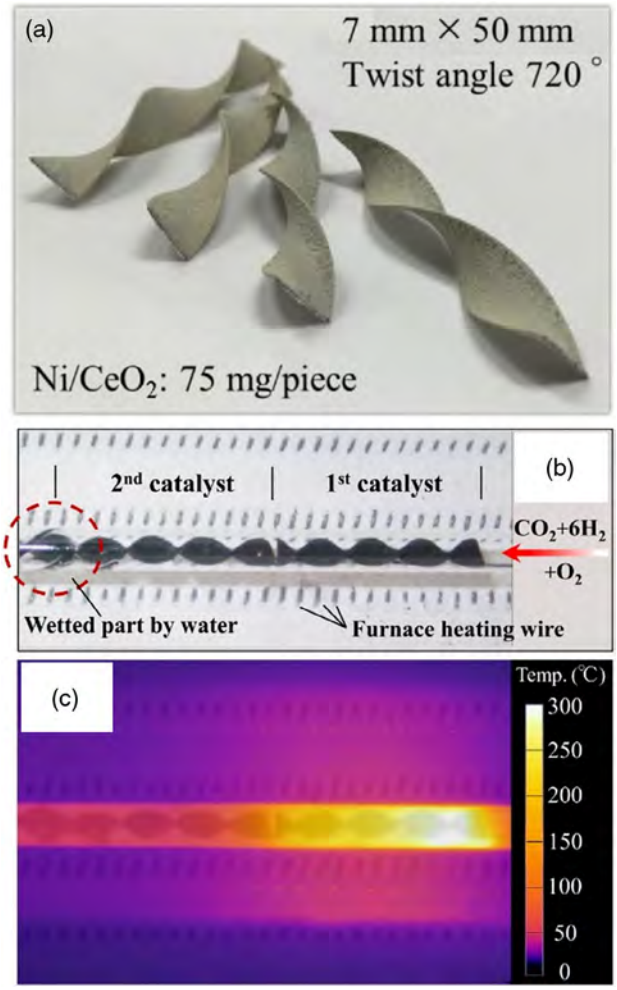

Figure 5. a,b) Coated spiral plate-type catalysts in the quartz reactor tube and c) snapshot of IR thermal image during the automethanation reaction at room temperature. Reproduced with permission.[74] Copyright 2019, The Chemical Society of Japan.

Ni/alumina suspension, dried, and sintered to form 3DFD structured catalysts. The challenge of homogeneous coating is addressed in this study, and optimal compositions for coating suspension were proposed. Indeed, the 3DFD catalysts showed better CO_2 conversion than the powder-type catalysts, even though only at high temperatures above 300 °C. Scaled-up experiments were investigated in a mini-pilot reactor with stacked 3DFD structured catalysts.[83] The authors successfully convinced the feasibility of CH_4 production using Ni/γ-Al_2O_3 catalysts on 3D-SS support. No hotspot formation was observed, which could be due to better heat transfer by the 3D catalytic network and/or by the circulated thermal oil.

The 3DFD method can be used to directly print out structured catalysts from the catalytic materials. Recently, Middelkoop et al. conducted 3D printing of Ni/Al_2O_3 structured catalysts in tetragonal shape.[84] A well-developed homogeneous ink was prepared and extruded through a nozzle of a syringe (**Figure 7**), whereas its position was computationally controlled.[85] The ink/paste consisted of catalytic materials in fine powder form and the binders.

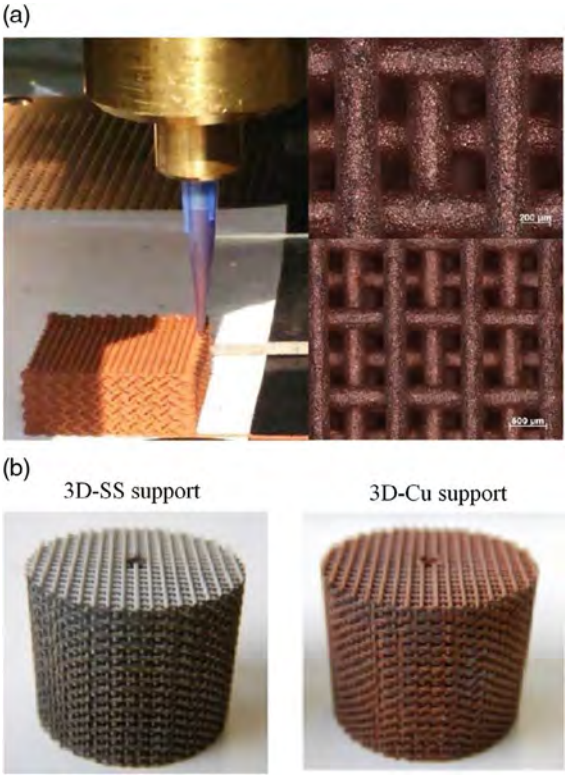

Figure 6. a) 3DFD manufactured by extrusion of copper supports and its optical microscope images. b) The 3D-printed supports made of stainless steel and copper. Reproduced with permission.[82] Copyright 2018, Elsevier.

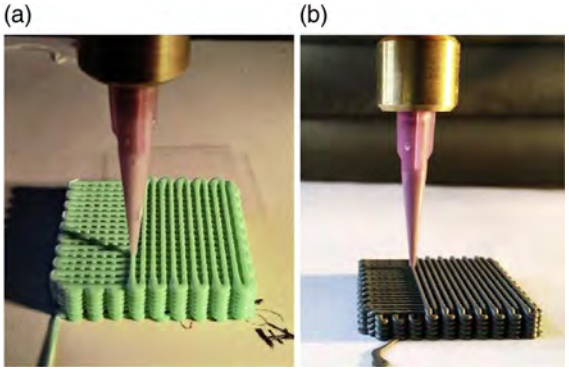

Figure 7. Tetragonal structured catalysts prepared by 3D printing. The catalytic phase in the printing ink/paste was a) as-prepared Ni alumina and b) commercial Ni alumina. Reproduced with permission.[84] Copyright 2019, Elsevier.

The binders were a mixture of polymer (e.g., methylcellulose), water, inorganic binders (e.g., colloidal silica and bentonite), and additives to achieve desired and reproducible rheological properties. The finished products were dried and subsequently heat treated at 500 °C to remove organic binders. The results showed that directly 3D printing Ni/Al_2O_3 catalyst exhibited better activity in CO_2 methanation, compared with the conventional impregnated catalysts.

3.5. Microchannel Reactors

The small volume and reduced dimension of the reaction zone are typical features of the microchannel reactor. In contrast, microchannel reactors can also be considered as structured reactors, because the catalytic materials are usually impregnated on a metallic plate installed inside the channel. The reactor enables more facile process control and thermal management for catalytic reactions at high temperatures.[86] Moreover, the improvement of hydrodynamics in the reaction zone can prevent the formation of hotspots and consequently the deactivation of catalysts. Nevertheless, microchannel reactors still have some drawbacks, e.g., a one-time-used system and limited scaling-up ability which prevent it from industrial applications. Many researchers have applied microchannel reactors for the development of the Sabatier process or PtG technology.

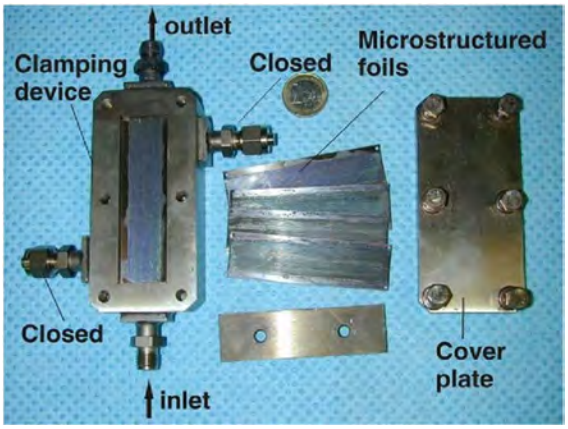

Figure 8. Microchannel reactor with clamping device and coated microstructured foils. Reproduced with permission.[87] Copyright 2005, Elsevier.

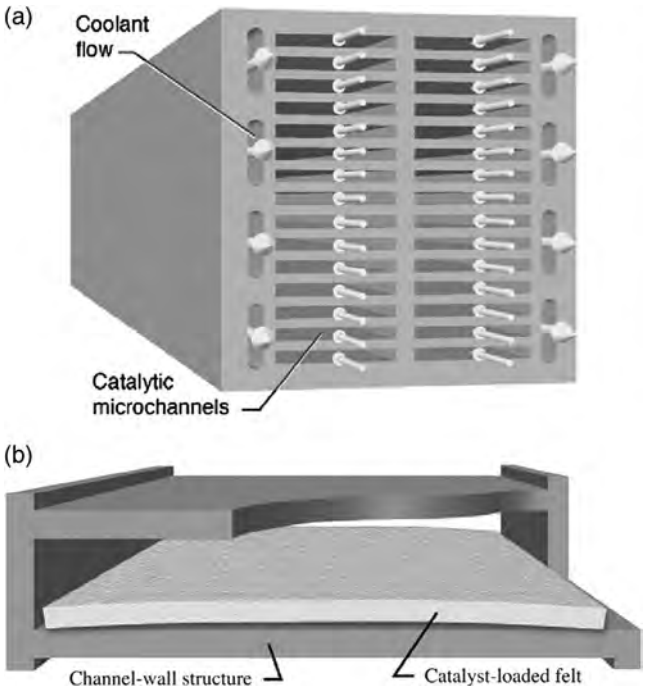

Figure 9. a) Illustration of a section of the microchannel reactor and b) a single channel with an interior coated metal felt. Reproduced with permission.[89] Copyright 2007, Elsevier.

Görke et al. first reported a highly selective methanation process using microchannel reactors coated with Ru/SiO_2 and Ru/Al_2O_3 catalysts.[87] The reactors consist of stainless steel foils with etched microchannels, which were coated with Al_2O_3 or SiO_2 gel (**Figure 8**). After calcination, Ru was impregnated on the coated foils. Although the work focused on CO methanation, CO_2 methanation was also tested at a temperature range of 100–380 °C with a highly diluted gas ($H_2/CO_2/N_2 = 25/4.5/70.5$). It was found that the Ru/SiO_2 catalyst exhibited good performance with high CH_4 yield at a low temperature of 170 °C. The temperature was assumed to be easily controlled with precision due to small dimensions and the enhanced heat transfer efficiency of the microreactor systems.

The microchannel designs were further investigated for applications such as propellant production on Mars or space habitat air revitalization. Prior to studying the microchannel reactor, Hu et al. evaluated many catalysts and supports in a packed-bed reactor.[88] The felts made of FeCrAlY intermetallic alloy were coated with 3 wt% Ru/TiO_2 catalyst and subsequently installed inside the single-channel reactor. The CO_2 conversion

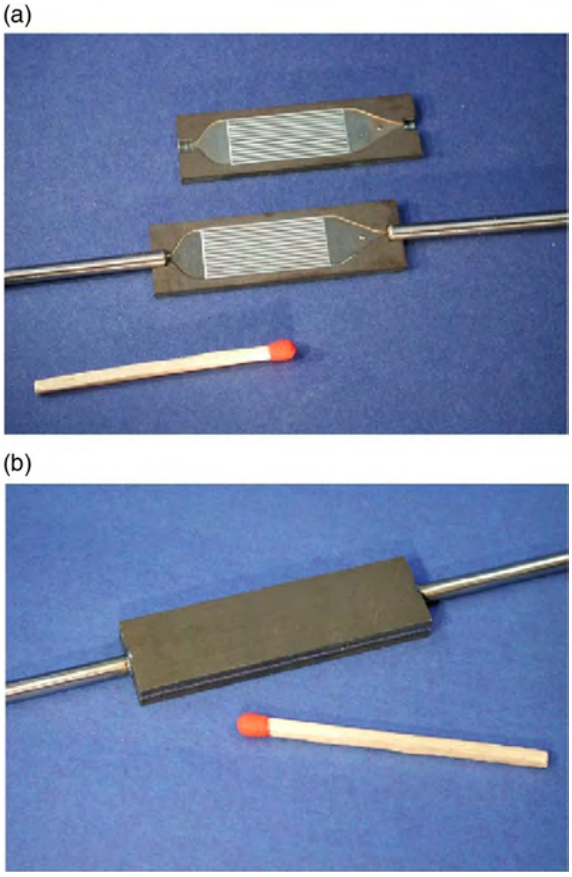

Figure 10. Sandwiched microchannel reactor: a) coated platelets with capillary and b) laser-welded reactor. Reproduced with permission.[90] Copyright 2007, Elsevier.

reached 78.6% at 365 °C (GHSV = 30 500 h^{-1}), even after the reactor was shut down and restarted during repeated tests.

Hu and coworkers continued the research on the challenging multichannel reactors. The microreactor with two parallel columns of 15 microchannels each was fabricated (**Figure 9**a).[89] More importantly, the felt was not directly bonded to the channel walls but separately inserted into the channels (Figure 9b). This method could overcome the disadvantageous "single-use" factor when applying microchannel reactors for any catalytic process. To avoid the initial temperature spike during the exothermic reaction, a short catalytic heat-exchanger section was designed, limiting the temperature increase up to 350 °C. Without this part, the initial temperature could increase up to 650 °C, potentially causing damage for catalysts.

Another microchannel reactor design was reported by Men et al. for both CO and CO_2 methanation.[90] The reactor had a sandwich design with two face-to-face microstructured platelets attached together. One pair of platelets with 14 channels containing coated catalysts was sealed by laser welding, together with the inlet and outlet capillaries (**Figure 10**). In this study, the Ni/CaO–Al_2O_3 catalyst was found to be the best catalytic system for CO_2 methanation at a low temperature of 200 °C. The designed microchannel reactor was considered as an excellent tool to investigate the reaction kinetics by tuning the feed compositions and reaction temperature.

Although the coated metallic substrate inside the microchannel was beneficial in terms of low-pressure drop, potential adhesion failure can occur, and catalytic layers could detach from the metallic substrate during the reaction due to differences in thermal expansion coefficients. An excellent metal–ceramic complex substrate with good stability was developed by Liu et al. (**Figure 11**).[91] The FeCrAlloy substrate was sprayed with a layer of Al_2O_3, heated to 1200 °C to ensure the embedding, further deposited with AlOOH sol, and subsequently impregnated with Ni ions. The results of the vibration test showed a minor weight loss, implying the potential of using metal–ceramics complex substrate in microchannel reactors for further process development.

Recently, Engelbrecht et al. developed a CFD model of microchannel reactors for CO_2 methanation.[92] The kinetic parameters of both Sabatier and RWGS reactions were estimated and validated by experimental data. The commercial Ru–Cs/Al_2O_3 catalysts were wash coated on 80 microchannels in the microreactor. The reactor (**Figure 12**) achieved 83.4% of CO_2 conversion at 400 °C and 5 bar with a high gas flow rate of 97.8 L g^{-1} h^{-1}. This high performance could be maintained for 150 h on stream, indicating an excellent stability of the catalytic system. The latest research on CO_2 methanation over Ni-based coated on the FeCrAlloy plate in a single-channel reactor (**Figure 13**a) was reported by Lalinde et al.[75,76] Different formulae of coating slurry and coating methods (i.e., brush coating, spin coating, and frame coating) were considered for the coating process optimization. For the first time, the thickness of the coating layer was measured by a profilometer. The nearly

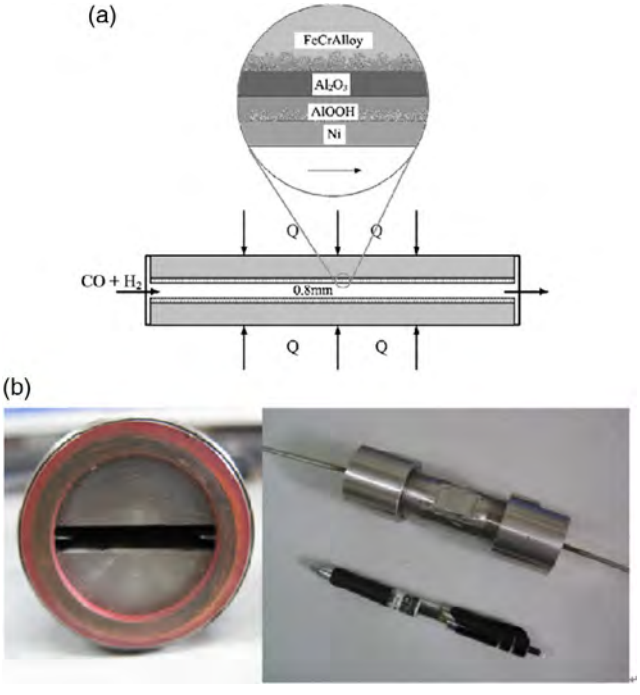

Figure 11. a) Schematic diagrams of metal–ceramics complex substrate with catalyst loading. b) Images of the microchannel reactor. Reproduced with permission.[91] Copyright 2012, Elsevier.

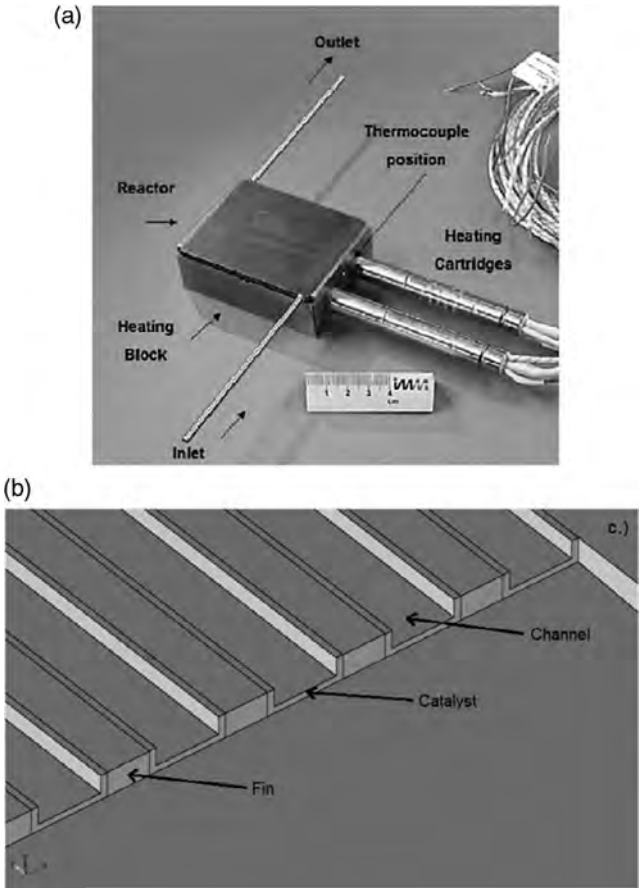

Figure 12. a) Reactor with laser-welded inlet/outlet tubes, heating block, and electric heater cartridges. Reproduced with permission.[93] Copyright 2015, Elsevier. b) Illustration of microchannels with the wash-coated catalyst. Reproduced with permission.[92] Copyright 2017, Elsevier.

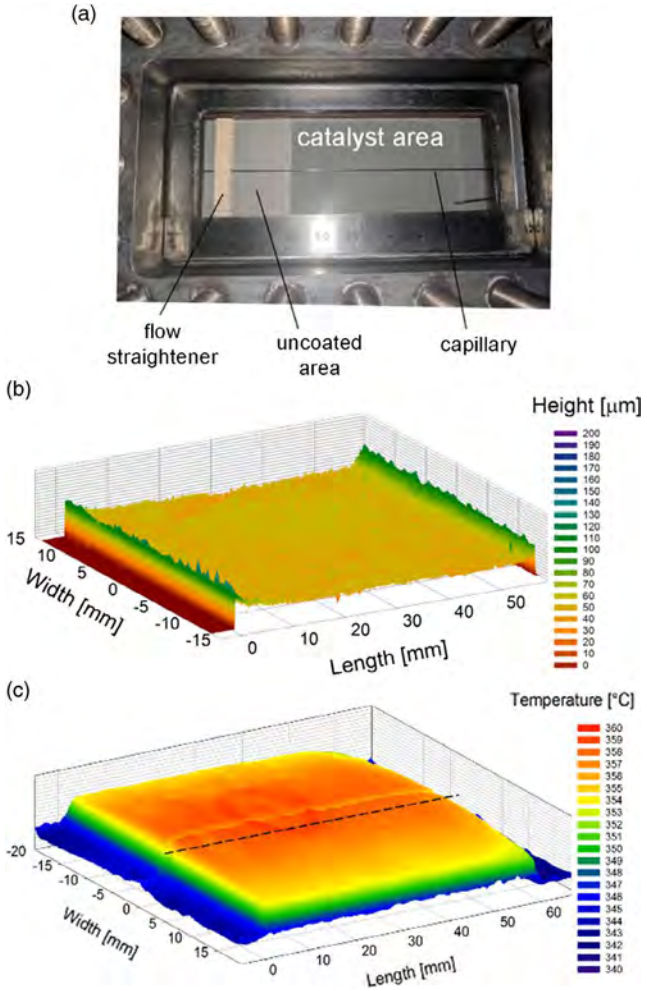

Figure 13. a) Catalytic plate reactor with the effective channel ($5 \times 40 \times 100$ mm). b) 3D catalyst height profile, measured by profilometer. c) 3D surface temperature profile during CO_2 methanation. Reproduced with permission.[75] Copyright 2019, Elsevier.

homogeneous coating layers with a thickness of 40–60 mm in a flat area were observed (Figure 13b). It was concluded that the catalytic mass was better distributed by the frame coating method. Moreover, a 3D surface temperature profile of the plate channel reactor during reaction was also recorded (Figure 13c). The temperature elevation was assumed to be negligible, and no hotspot formation was detected.

4. Summary and Outlook

Considerable efforts have been made in the development of the catalytic systems and reactors for the Sabatier process. Regarding the discovery of new material as heterogeneous catalysts for CO_2 methanation, this Review has focused on the potential of HT materials as precursors for supported catalysts. HT-derived catalysts can be prepared via a simple and highly reproducible coprecipitation method. The material offers strong metal–support interaction and high dispersion of active sites. Many studies have shown that HT-derived Ni-based catalysts exhibited better catalytic activity and stability than that of conventional catalysts. Moreover, to improve catalyticactivity and stability for low-temperature CO_2 methanation, the addition of promoters with different purposes (e.g., as second active site, improved basicity, enhanced CO_2 and H_2 adsorption, etc.) or further advanced treatment (e.g., cold plasma technology) is feasible to be applied for HT-derived catalysts.

The implementation of laboratory research into industrial practice is usually conducted on structured catalysts and reactors as it provides better heat and mass transfer, enhanced hydrodynamics, etc. Structured catalysts have been intensively studied for CO_2 methanation in terms of different materials, configurations, and preparation methods. High CO_2 conversion and CH_4 yield at low temperatures could be achieved using structured catalysts. The structural reactor–exchanger concept with excellent efficiency in heat management is highly recommended to prevent hotspots' formation.

The latest catalytic preparations using additive manufacturing technology, such as 3D printing, have also been applied to obtain structured catalysts for the Sabatier reaction. Although, in an early stage, the application of 3D printing is promising for the future of chemical engineering and catalysis manufacturing. It enables a feasible fabrication of complex and geometrically customized catalytic design. Furthermore, both structured catalysts and structured reactors can be produced by this technology. New opportunities have arisen for researchers, unleashing the boundary of human creativity, especially for energy environmental applications such as the production of CH_4 via renewable H_2 and CO_2.

Acknowledgements

The authors would like to thank the Norwegian Ministry of Education and Research and Valide AS through the Plogen Program for financial support.

Conflict of Interest

The authors declare no conflict of interest.

Keywords

CO_2 methanation, hydrotalcite-derived catalysts, Sabatier reaction, structured catalysts, structured reactors

Received: December 20, 2019
Revised: February 27, 2020
Published online:

[1] B. P. p.l.c, BP Statistical Review of World Energy 2019 (accessed: March 2020).
[2] I. E. Agency, CO_2 Emissions Statistics 2018, www.iea.org/statistics/co2emissions (accessed: March 2020).
[3] A. E. a. Sandbag, The European Power Sector in 2018. Up-to-date analysis on the electricity transition 2019 (accessed: December 2018).
[4] K. Ghaib, F.-Z. Ben-Fares, *Renew. Sustainable Energy Rev.* **2018**, *81*, 433.

[5] S. Rönsch, J. Schneider, S. Matthischke, M. Schlüter, M. Götz, J. Lefebvre, P. Prabhakaran, S. Bajohr, *Fuel* **2016**, *166*, 276.
[6] P. Sabatier, J.-B. Senderens, *Comptes Rendus Des Séances De L'Académie Des Sciences, Section VI Chimie* **1902**, *134*, 514.
[7] A. Muscatello, E. Santiago-Maldonado, in 50th AIAA Aerospace Sciences Meeting including the New Horizons Forum and Aerospace Exposition, American Institute of Aeronautics and Astronautics, Reston, VA **2012**.
[8] T. Schaaf, J. Grünig, M. R. Schuster, T. Rothenfluh, A. Orth, *Energy Sustainability Soc.* **2014**, *4*, 2.
[9] K. Ghaib, K. Nitz, F.-Z. Ben-Fares, *ChemBioEng Rev.* **2016**, *3*, 266.
[10] K. Jalama, *Catal. Rev. Sci. Eng.* **2017**, *59*, 95.
[11] G. A. Mills, F. W. Steffgen, *Catal. Rev. Sci. Eng.* **1974**, *8*, 159.
[12] B. Miao, S. S. K. Ma, X. Wang, H. Su, S. H. Chan, *Catal. Sci. Technol.* **2016**, *6*, 4048.
[13] C. Vogt, M. Monai, G. J. Kramer, B. M. Weckhuysen, *Nat. Catal.* **2019**, *2*, 188.
[14] P. Frontera, A. Macario, M. Ferraro, P. Antonucci, *Catalysts* **2017**, *7*, 59.
[15] M. A. A. Aziz, A. A. Jalil, S. Triwahyono, A. Ahmad, *Green Chem.* **2015**, *17*, 2647.
[16] J. Guo, H. Lou, H. Zhao, D. Chai, X. Zheng, *Appl. Catal. A* **2004**, *273*, 75.
[17] W. Li, H. Wang, X. Jiang, J. Zhu, Z. Liu, X. Guo, C. Song, *RSC Adv.* **2018**, *8*, 7651.
[18] a) M. Younas, L. Loong Kong, M. J. K. Bashir, H. Nadeem, A. Shehzad, S. Sethupathi, *Energy Fuels* **2016**, *30*, 8815; b) J. Gao, Y. Wang, Y. Ping, D. Hu, G. Xu, F. Gu, F. Su, *RSC Adv.* **2012**, *2*, 2358.
[19] E. Baraj, S. Vagaský, T. Hlinčík, K. Ciahotný, V. Tekáč, *Chem. Pap.* **2016**, *70*, 395.
[20] R. Dębek, F. Azzolina-Jury, A. Travert, F. Maugé, *Renew. Sustainable Energy Rev.* **2019**, *116*, 109427.
[21] R. Debek, M. Motak, T. Grzybek, M. Galvez, P. Da Costa, *Catalysts* **2017**, *7*, 32.
[22] a) F. Cavani, F. Trifirò, A. Vaccari, *Catal. Today* **1991**, *11*, 173; b) J. He, M. Wei, B. Li, Y. Kang, D. G. Evans, X. Duan, *Structure and Bonding*, Springer, Berlin, Heidelberg **2006**, pp. 89–119.
[23] G. Fan, F. Li, D. G. Evans, X. Duan, *Chem. Soc. Rev.* **2014**, *43*, 7040.
[24] Z. P. Xu, J. Zhang, M. O. Adebajo, H. Zhang, C. Zhou, *Appl. Clay Sci.* **2011**, *53*, 139.
[25] A. L. Hausberger, C. B. Knight, K. Atwood, *Methanation of Synthesis Gas*, Vol. *146*, American Chemical Society, Washington D.C. **1975**, pp. 47–70.
[26] C. H. Bartholomew, *Appl. Catal. A* **2001**, *212*, 17.
[27] S. Abelló, C. Berrueco, D. Montané, *Fuel* **2013**, *113*, 598.
[28] S. Abate, K. Barbera, E. Giglio, F. Deorsola, S. Bensaid, S. Perathoner, R. Pirone, G. Centi, *Ind. Eng. Chem. Res.* **2016**, *55*, 8299.
[29] L. He, Q. Lin, Y. Liu, Y. Huang, *J. Energy Chem.* **2014**, *23*, 587.
[30] M. Gabrovska, R. Edreva-Kardjieva, D. Crişan, P. Tzvetkov, M. Shopska, I. Shtereva, *React Kinet. Mech. Catal.* **2012**, *105*, 79.
[31] S. Abelló, C. Berrueco, F. Gispert-Guirado, D. Montané, *Catal. Sci. Technol.* **2016**, *6*, 2305.
[32] X. Guo, Z. Peng, M. Hu, C. Zuo, A. Traitangwong, V. Meeyoo, C. Li, S. Zhang, *Ind. Eng. Chem. Res.* **2018**, *57*, 9102.
[33] P. Marocco, E. Alexandru Morosanu, E. Giglio, D. Ferrero, C. Asmelash, A. Lanzini, S. Abate, S. Bensaid, S. Perathoner, M. Santarelli, R. Pirone, G. Centi, *Fuel* **2018**, *225*, 230.
[34] N. Bette, J. Thielemann, M. Schreiner, F. Mertens, *ChemCatChem* **2016**, *8*, 2903.
[35] D. Wierzbicki, R. Baran, R. Dębek, M. Motak, T. Grzybek, M. E. Gálvez, P. Da Costa, *Int. J. Hydrogen Energy* **2017**, *42*, 23548.
[36] J. Liu, W. Bing, X. Xue, F. Wang, B. Wang, S. He, Y. Zhang, M. Wei, *Catal. Sci. Technol.* **2016**, *6*, 3976.
[37] Y. Wang, Y. Xu, Q. Liu, J. Sun, S. Ji, Z.-j. Wang, *J. Chem. Technol. Biotechnol.* **2019**.
[38] X. Wang, T. Zhen, C. Yu, *Appl. Petrochem. Res.* **2016**, *6*, 217.
[39] C. Mebrahtu, S. Perathoner, G. Giorgianni, S. Chen, G. Centi, F. Krebs, R. Palkovits, S. Abate, *Catal. Sci. Technol.* **2019**, *9*, 4023.
[40] T. Burger, F. Koschany, O. Thomys, K. Köhler, O. Hinrichsen, *Appl. Catal. A* **2018**, *558*, 44.
[41] T. Burger, F. Koschany, A. Wenng, O. Thomys, K. Köhler, O. Hinrichsen, *Catal. Sci. Technol.* **2018**, *8*, 5920.
[42] D. Wierzbicki, M. Motak, T. Grzybek, M. E. Gálvez, P. Da Costa, *Catal. Today* **2018**, *307*, 205.
[43] Y. Xu, Y. Chen, J. Li, J. Zhou, M. Song, X. Zhang, Y. Yin, *Int. J. Hydrogen Energy* **2017**, *42*, 13085.
[44] M. Nizio, R. Benrabbah, M. Krzak, R. Debek, M. Motak, S. Cavadias, M. E. Gálvez, P. Da Costa, *Catal. Commun.* **2016**, *83*, 14.
[45] M. K. Titulaer, J. B. H. Jansen, J. W. Geus, *Clays Clay Miner.* **1994**, *42*, 249.
[46] S. Ewald, M. Kolbeck, T. Kratky, M. Wolf, O. Hinrichsen, *Appl. Catal. A* **2019**, *570*, 376.
[47] a) M. Guo, G. Lu, *RSC Adv.* **2014**, *4*, 58171; b) Q. Pan, J. Peng, T. Sun, S. Wang, S. Wang, *Catal. Commun.* **2014**, *45*, 74.
[48] R. Merkache, I. Fechete, M. Maamache, M. Bernard, P. Turek, K. Al-Dalama, F. Garin, *Appl. Catal., A* **2015**, *504*, 672.
[49] a) T. Yoshida, K. Nishizawa, M. Tabata, H. Abe, T. Kodama, M. Tsuji, Y. Tamaura, *J. Mater. Sci.* **1993**, *28*, 1220-; b) M. Tsuji, T. Kodama, T. Yoshida, Y. Kitayama, Y. Tamaura, *J. Catal.* **1996**, *164*, 315.
[50] D. Shi, R. Wojcieszak, S. Paul, E. Marceau, *Catalysts* **2019**, *9*, 451.
[51] C. Mebrahtu, F. Krebs, S. Perathoner, S. Abate, G. Centi, R. Palkovits, *Catal. Sci. Technol.* **2018**, *8*, 1016.
[52] J. Bremer, K. Sundmacher, *React. Chem. Eng.* **2019**, *4*, 1019.
[53] a) A. Cybulski, J. A. Moulijn, *Novel Concepts Catal. Chem. React.* **2010**; b) E. Tronconi, G. Groppi, C. G. Visconti, *Curr. Opin. Chem. Eng.* **2014**, *5*, 55.
[54] T. Boger, A. K. Heibel, *Chem. Eng. Sci.* **2005**, *60*, 1823.
[55] D. Schlereth, P. J. Donaubauer, O. Hinrichsen, *Chem. Eng. Technol.* **2015**, *38*, 1845.
[56] P. H. Ho, M. Ambrosetti, G. Groppi, E. Tronconi, R. Palkovits, G. Fornasari, A. Vaccari, P. Benito, *Studies in Surface Science and Catalysis*, Vol. *178*, Elsevier, Netherlands **2019**, pp. 303–327.
[57] C. J. Navarro, A. M. Centeno, H. O. Laguna, A. J. Odriozola, *Catalysts* **2018**, *8*, 578.
[58] C. Janke, M. S. Duyar, M. Hoskins, R. Farrauto, *Appl. Catal. B.* **2014**, *152–153*, 184.
[59] C. Fukuhara, K. Hayakawa, Y. Suzuki, W. Kawasaki, R. Watanabe, *Appl. Catal. A* **2017**, *532*, 12.
[60] S. Ratchahat, M. Sudoh, Y. Suzuki, W. Kawasaki, R. Watanabe, C. Fukuhara, *J. CO2. Util.* **2018**, *24*, 210.
[61] A. Vita, C. Italiano, L. Pino, P. Frontera, M. Ferraro, V. Antonucci, *Appl. Catal. B.* **2018**, *226*, 384.
[62] P. Biegger, F. Kirchbacher, R. A. Medved, M. Miltner, M. Lehner, M. Harasek, *Energies* **2018**, *11*, 1679.
[63] D. Schollenberger, S. Bajohr, M. Gruber, R. Reimert, T. Kolb, *Chem. Ing. Tech.* **2018**, *90*, 696.
[64] J. Y. Ahn, S. W. Chang, S. M. Lee, S. S. Kim, W. J. Chung, J. C. Lee, Y. J. Cho, K. S. Shin, D. H. Moon, D. D. Nguyen, *Fuel* **2019**, *250*, 277.
[65] M. Shima, Y. Sakurai, M. Sone, A. Ohnishi, T. Yoneda, T. Abe, *Int. J. Microgravity Sci. Appl.* **2013**, *30*, 86.
[66] Y. Li, Q. Zhang, R. Chai, G. Zhao, Y. Liu, Y. Lu, F. Cao, *AlChE J.* **2015**, *61*, 4323.
[67] S. Tada, S. Ikeda, N. Shimoda, T. Honma, M. Takahashi, A. Nariyuki, S. Satokawa, *Int. J. Hydrogen Energy* **2017**, *42*, 30126.
[68] M. Frey, D. Édouard, A.-C. Roger, *C. R. Chim.* **2015**, *18*, 283.
[69] M. Frey, T. Romero, A.-C. Roger, D. Edouard, *Chem. Eng. Sci.* **2019**, *195*, 271.
[70] M. Frey, T. Romero, A.-C. Roger, D. Edouard, *Catal. Today* **2016**, *273*, 83.

[71] M. Frey, A. Bengaouer, G. Geffraye, D. Edouard, A.-C. Roger, *Energy Technol.* **2017**, *5*, 2078.
[72] A. Bengaouer, J. Ducamp, I. Champon, R. Try, *Can. J. Chem. Eng.* **2018**, *96*, 1937.
[73] A. Ricca, L. Truda, V. Palma, *Chem. Eng. J.* **2019**, *377*, 120461.
[74] C. Fukuhara, S. Ratchahat, A. Kamiyama, M. Sudoh, R. Watanabe, *Chem. Lett.* **2019**, *48*, 441.
[75] J. A. H. Lalinde, J. Jiang, G. Jai, J. Kopyscinski, *Chem. Eng. J.* **2019**, *357*, 435.
[76] J. A. H. Lalinde, K. Kofler, X. Huang, J. Kopyscinski, *Catalysts* **2018**, *8*, 86.
[77] G. A. Jarvi, K. B. Mayo, C. H. Bartholomew, *Chem. Eng. Commun.* **1980**, *4*, 325.
[78] J. G. Khinast, A. Bauer, D. Bolz, A. Panarello, *Chem. Eng. Sci.* **2003**, *58*, 1063.
[79] S. Specchia, C. Galletti, V. Specchia, *Studies in Surface Science and Catalysis*, Vol. *175*, Elsevier, Netherlands **2010**, pp. 59–67.
[80] J. Ducamp, A. Bengaouer, P. Baurens, *Can. J. Chem. Eng.* **2017**, *95*, 241.
[81] S. Danaci, L. Protasova, J. Lefevere, L. Bedel, R. Guilet, P. Marty, *Catal. Today* **2016**, *273*, 234.
[82] S. Danaci, L. Protasova, F. Snijkers, W. Bouwen, A. Bengaouer, P. Marty, *Chem. Eng. Process* **2018**, *127*, 168.
[83] S. Danaci, L. Protasova, V. Middelkoop, N. Ray, M. Jouve, A. Bengaouer, P. Marty, *React. Chem. Eng.* **2019**, *4*, 1318.
[84] V. Middelkoop, A. Vamvakeros, D. de Wit, S. D. M. Jacques, S. Danaci, C. Jacquot, Y. de Vos, D. Matras, S. W. T. Price, A. M. Beale, *J. CO2. Util.* **2019**, *33*, 478.
[85] V. Middelkoop, K. Coenen, J. Schalck, M. Van Sint Annaland, F. Gallucci, *Chem. Eng. J.* **2019**, *357*, 309.
[86] V. Gokhale Sagar, K. Tayal Rajiv, K. Jayaraman Valadi, D. Kulkarni Bhaskar, *Int. J. Chem. React. Eng.* **2005**, *3*.
[87] O. Görke, P. Pfeifer, K. Schubert, *Catal. Today* **2005**, *110*, 132.
[88] J. Hu, K. P. Brooks, J. D. Holladay, D. T. Howe, T. M. Simon, *Catal. Today* **2007**, *125*, 103.
[89] K. P. Brooks, J. Hu, H. Zhu, R. J. Kee, *Chem. Eng. Sci.* **2007**, *62*, 1161.
[90] Y. Men, G. Kolb, R. Zapf, V. Hessel, H. Löwe, *Catal. Today* **2007**, *125*, 81.
[91] Z. Liu, B. Chu, X. Zhai, Y. Jin, Y. Cheng, *Fuel* **2012**, *95*, 599.
[92] N. Engelbrecht, S. Chiuta, R. C. Everson, H. W. J. P. Neomagus, D. G. Bessarabov, *Chem. Eng. J.* **2017**, *313*, 847.
[93] S. Chiuta, R. C. Everson, H. W. J. P. Neomagus, D. G. Bessarabov, *Int. J. Hydrogen Energy* **2015**, *40*, 2921.

Appendix C – Paper III

Promoting effect of Fe on supported Ni catalysts in CO_2 methanation by in situ DRIFTS and DFT study

H. L. Huynh, J. Zhu, G. Zhang, Y. Shen, W. M. Tucho, Y. Ding, and Z. Yu

Journal of Catalysis **2020**, *392*, 266-277

DOI: 10.1016/j.jcat.2020.10.018

Journal of Catalysis 392 (2020) 266–277

Contents lists available at ScienceDirect

Journal of Catalysis

journal homepage: www.elsevier.com/locate/jcat

Promoting effect of Fe on supported Ni catalysts in CO_2 methanation by *in situ* DRIFTS and DFT study

Huong Lan Huynh [a], Jie Zhu [b], Guanghui Zhang [b], Yongli Shen [d,*], Wakshum Mekonnen Tucho [c], Yi Ding [d], Zhixin Yu [a,*]

[a] Department of Energy and Petroleum Engineering, University of Stavanger, 4036 Stavanger, Norway
[b] State Key Laboratory of Fine Chemicals, PSU-DUT Joint Center for Energy Research, School of Chemical Engineering, Dalian University of Technology, Dalian 116024, China
[c] Department of Mechanical and Structural Engineering and Materials Science, University of Stavanger, 4036 Stavanger, Norway
[d] Tianjin Key Laboratory of Advanced Functional Porous Materials, Institute for New Energy Materials & Low-Carbon Technologies, School of Materials Science and Engineering, Tianjin University of Technology, Tianjin 300384, China

ARTICLE INFO

Article history:
Received 14 August 2020
Revised 12 October 2020
Accepted 13 October 2020
Available online 29 October 2020

Keywords:
CO_2 methanation
NiFe
In situ XRD
In situ DRIFTS
DFT calculation
Reaction mechanism

ABSTRACT

Bimetallic NiFe catalysts have emerged as a promising alternative to the traditional Ni catalysts for CO_2 methanation. However, the promoting effect of Fe on the bimetallic catalysts remains ambiguous. In this study, a series of NiFe catalysts derived from hydrotalcite precursors were investigated. *In situ* x-ray diffraction (XRD) analysis revealed that small NiFe alloy particles were formed and remained stable during reaction. When Fe/Ni = 0.25, the alloy catalysts exhibited the highest CO_2 conversion, CH_4 selectivity and stability in CO_2 methanation at low temperature of 250–350 °C. The *in situ* diffuse reflectance infrared Fourier transform spectroscopy (DRIFTS) study indicated that the formate pathway was the most plausible reaction scheme on both Ni and NiFe alloy catalysts, while a moderate addition of Fe facilitated the activation of CO_2 via hydrogenation to *HCOO. Density functional theory (DFT) calculations further demonstrated that the overall energy barrier for CH_4 formation was lower on the alloy surface.

1. Introduction

Chemical conversion of CO_2 into valuable products has been attractive to chemists ever since the advent of catalysis [1]. The discovery of CO_2 methanation (Sabatier reaction, Eq. (1)) in 1902, which converts CO_2 and H_2 into CH_4, has been crucial for the development of CO_2 conversion processes [2]. The potential for CO_2 mitigation and renewable energy storage has been demonstrated in the emerging Power-to-Gas (PtG) technology. In this concept, the synthetic or substitute natural gas (SNG) produced via the Sabatier process is considered as a promising chemical energy carrier for the surplus electricity produced from intermittent renewables such as wind and solar power [3–5].

$$CO_2 + 4H_2 \leftrightarrow CH_4 + 2H_2O \quad \Delta H^{\circ}_{298K} = -165 \text{ kJ mol}^{-1} \qquad (1)$$

$$CO_2 + H_2 \leftrightarrow CO + H_2O \quad \Delta H^{\circ}_{298K} = 41 \text{ kJ mol}^{-1} \qquad (2)$$

The molecular transformation of CO_2 is challenging since the molecule is well-known for its thermodynamic stability. Metal catalysts are therefore crucial to activate the closed-shell molecule [6]. At atmospheric pressure, CO_2 methanation and the reverse water–gas shift reaction (RWGS, Eq. (2)) occur simultaneously on group VIII metals. Although noble metals (e.g., Ru, Rh) are highly active, Ni-based catalysts are prominently exploited as methanation catalysts due to cost effectiveness. Considerable efforts have been devoted to improving the activity and stability of Ni-based catalysts at low temperatures (<350 °C) [7,8].

The addition of Fe to Ni has been reported as a promising strategy to achieve better catalytic performance and stability of methanation catalyst. It was first predicted by theoretical modeling, i.e., density functional theory (DFT) simulations. Based on the calculated energies, NiFe and Ni_3Fe showed excellent activity compare to Ni and Fe, close to that of the best catalysts (i.e., Ru and Co) [9,10]. Experimental investigations have also verified that NiFe catalysts exhibited higher activity than their individual constituent in CO_2 hydrogenation (H_2/CO_2 = 91/9) at 250 °C [11]. The bimetallic NiFe catalytic system is very attractive because cheap Fe will further contribute to the cost-effectiveness of the Ni-based methanation catalysts.

Studies on NiFe catalysts for CO_2 methanation have been reported on different catalytic supports, i.e., Al_2O_3 [12], TiO_2, SiO_2, Nb_2O_5, and ZrO_2 [13,14], while unsupported NiFe catalysts were also investigated [15]. The optimal composition of Fe in

* Corresponding authors.
E-mail addresses: ylshen@tjut.edu.cn (Y. Shen), zhixin.yu@uis.no (Z. Yu).

https://doi.org/10.1016/j.jcat.2020.10.018
0021-9517/

Ni-based catalysts to achieve the promoting effect appears to be dependent on the support type and metal loading. Importantly, the amount of Fe addition plays a crucial role since a small amount of Fe boosted the production of CH_4 while large amount of Fe promoted the formation of CO via RWGS reaction [16]. NiFe catalysts prepared from layered double hydroxides (LDH) materials were also studied [17,18]. Overall, most of these studies have confirmed the superiority of NiFe alloy catalysts in CO_2 methanation compared to monometallic Ni catalysts. Regardless of metal loading or type of supports, the optimal Fe content has been reported with a Fe/Ni molar ratio up to 1/3. Besides, the Ni_3Fe/Al_2O_3 catalysts showed a more stable performance compared to commercial Ni methanation catalysts [19]. Based on kinetic measurements, Mutz *et al.* assumed the effect of Fe could be due to the synergetic effect of NiFe alloy [19]. While the CO dissociation energy was used as a descriptor for CO and CO_2 methanation activity [9,17], the binding energy of adsorbed CO was proposed as the key descriptor for CO_2 hydrogenation to CH_4 (H_2/CO_2 = 2) [16]. An improvement in CO_2 uptake capacity on alloy surfaces corresponding to the promoted CH_4 production has also been speculated [20]. Nevertheless, there is no consensus on the promotional effect of Fe on Ni, while the mechanism of CO_2 methanation on NiFe alloy catalysts is not clearly understood.

Insights at the atomic scale of active intermediates and key elementary reaction steps are essential to unravel the reaction mechanism of catalytic reaction. In this work, we attempted to understand the role of Fe and the reaction mechanism by *in situ* X-ray diffraction (XRD) and *in situ* diffuse reflectance infrared Fourier transform spectroscopy (DRIFTS) study combined with DFT simulations. To the best of our knowledge, this is the first combined experimental and theoretical study on NiFe alloy catalysts for the Sabatier reaction. We prepared a series of NiFe on (Mg,Al)O_x supported catalysts derived from hydrotalcite (HT) precursors in order to study the impact of Fe content on the physicochemical properties and catalytic performance in CO_2 methanation. The formation of NiFe alloy upon reduction, as well as the structural changes during reaction was investigated by *in situ* XRD analysis.

2. Experimental

2.1. Catalyst synthesis

A series of NiFe/(Mg,Al)O_x catalysts were prepared by calcination of HT precursors. The precursors were synthesized by rapid coprecipitation reported in our previous work [21]. In a typical synthesis, a metal nitrate solution (1 M) containing a calculated amount of Ni$(NO_3)_2{\cdot}6H_2O$, Fe$(NO_3)_3{\cdot}9H_2O$, Mg$(NO_3)_2{\cdot}6H_2O$ and Al$(NO_3)_3{\cdot}9H_2O$ were quickly injected to a base solution of NaOH and Na_2CO_3 under vigorous stirring at 60 °C. The mixture was aged at 85 °C for 18 h. The calcination of the as-prepared precursors was conducted at 600 °C for 6 h in flowing synthetic air. In all the catalysts, the (Ni + Mg)/(Al + Fe) molar ratio was fixed at 3 and the Ni loading was kept constant at 20 wt%. The calcined catalysts were denoted as NiFe-*x*, where *x* is the Fe/Ni molar ratio that varies from 0 to 0.5 (Table 1).

2.2. Catalyst characterization

The elemental compositions of the calcined catalysts were analyzed by inductively coupled plasma optical emission spectrometry (ICP-OES) using OPTIMA 4300 DV (PerkinElmer) instrument. The dried samples were dissolved in a mixture of HCl and HNO_3 at a ratio of 3 and further diluted for analysis.

Crystallographic information of the as-prepared and calcined catalysts was determined by X-ray diffraction. The *ex situ* XRD patterns were recorded on D8 Advance (Bruker) micro-diffractometer using CuKα radiation source with a step interval of 1° min^{-1}.

Nitrogen physisorption was performed in a Tristar 3000 (Micromeritics) instrument at −196 °C. Prior to analysis, all samples were degassed at 150 °C under vacuum overnight. The specific surface area of the catalysts was calculated using Brunauer-Emmett-Teller (BET) method, while the pore volume and pore size distributions were evaluated using Barrett-Joyner-Halenda (BJH) models.

Temperature-programmed reduction (TPR) of the calcined catalysts and temperature-programmed desorption (TPD) of the reduced catalysts were performed on AutoChem II 2920 (Micromeritics). In a typical measurement, 100 mg of calcined sample was used to obtain reliable data [22]. The calcined catalysts were degassed, then the analysis was carried out by heating the sample from 50 °C to 950 °C at a heating rate of 10 K min^{-1} in 10 vol% H_2/Ar (50 mL min^{-1}). Subsequently, the sample was purged with He flow at 600 °C for 30 min and cooled down to 50 °C. Thereafter, the sample was exposed to a flow of 6 vol% CO_2/Ar (50 mL min^{-1}) for 1 h, followed by purging in He for another 1 h to remove weakly adsorbed CO_2. Finally, CO_2-TPD data were recorded by heating the sample to 800 °C at a heating rate of 10 K min^{-1} in flowing He.

Hydrogen chemisorption analysis was conducted in ASAP 2020 Plus (Micromeritics) instrument at 35 °C. In a typical experiment, 200 mg of calcined catalyst was reduced in H_2 flow at 600 °C for 4 h with a heating rate of 5 K min^{-1} and cooled down to 35 °C in flowing He. It was assumed that the chemisorption of H_2 occurred only on Ni atom with a dissociative mechanism because Fe is known to be inactive in H_2 chemisorption.

The morphology and particle size of the reduced-passivated and spent catalysts were revealed by transmission electron microscopy (TEM) analysis using JEM-2100 Plus (JEOL) microscope operating at 200 kV. The calcined catalysts were reduced in 50 vol% H_2/N_2 (100 mL min^{-1}, STP) at 600 °C for 4 h (heating rate of 5 K min^{-1}) in a fixed-bed reactor. The sample was cooled down in a flowing N_2 to room temperature before being passivated by adding synthetic air to the gas mixture. The oxygen content was adjusted to 0.1 vol% and slowly increased to 1 vol%.

2.3. CO_2 methanation tests

The catalytic performance was evaluated on a stainless-steel tubular fixed-bed reactor as reported in our previous work [21]. In a typical experiment, 60 mg of calcined catalyst (200–355 μm) was diluted with 600 mg of SiC (ca. 355 μm). The catalyst was reduced using 50 vol% H_2/N_2 (100 mL min^{-1}, STP) at 600 °C for 4 h (heating rate of 5 K min^{-1}). The temperature-dependent activity tests were carried out at a temperature interval of 200–450 °C at a heating rate of 1 K min^{-1}. The condition was held for 1 h at each temperature to obtain a stable CO_2 conversion. The total flow rate of reactant gases ($H_2/CO_2/N_2$ vol.% = 64/16/20) was 270 mL min^{-1} (STP), which corresponding to a weight hourly space velocity (WHSV) of 43,200 mL_{CO2} $g_{cat}^{-1}h^{-1}$ or a gas hourly space velocity (GHSV) of 34,000 h^{-1}.

For long-term stability evaluation, the catalysts were tested at 300 °C for more than 60 h of time on stream (TOS). Moreover, a blank test was conducted to confirm the inert nature of SiC in the stainless-steel reactor under reaction condition. The conversion of CO_2 and product selectivity were defined following Eq. (3) and Eq. (4), where F^{in} and F^{out} are the molar flow rates (mol h^{-1}).

$$X_{CO2}(\%) = \frac{F_{CO2}^{in} - F_{CO2}^{out}}{F_{CO2}^{in}} \times 100 \quad (3)$$

$$S_i(\%) = \frac{F_i^{out}}{F_{CO2}^{in} - F_{CO2}^{out}} \times 100 \quad (4)$$

Table 1
Elemental compositions and textural properties of calcined catalysts.

Catalyst	Nominal Fe/Ni molar ratio	ICP-OES analysis			N_2 physisorption of calcined catalyst		
		Ni [wt %]	Fe [wt %]	Fe/Ni molar ratio	BET Specific surface area [m^2 g^{-1}]	BJH Pore volume [cm^3 g^{-1}]	BJH Average pore size [nm]
NiFe-0	0	19.85	0	0	227.8	0.73	10.1
NiFe-0.1	0.1	19.84	1.87	0.1	240.0	0.77	11.0
NiFe-0.25	0.25	19.62	4.70	0.25	232.6	0.70	9.7
NiFe-0.33	0.33	18.83	6.39	0.36	247.3	0.72	9.7
NiFe-0.5	0.5	19.50	9.45	0.51	197.4	0.68	10.5

2.4. In situ XRD study

In situ XRD diffractograms were collected on a SmartLab 9 kW (Rigaku) diffractometer equipped with an XRK900 reactor chamber and a 1D/Dtex detector to improve the signal-to-noise ratio. The diffractometer was operated at 45 kV and 200 mA using CuKα radiation source. About 50 mg of calcined catalyst was loaded in the sample holder and heated up to 600 °C at a heating rate of 10 K min^{-1} under a flow of pure H_2 (30 mL min^{-1}) for reduction at atmospheric pressure. The diffractograms were subsequently recorded at 100–600 °C at a scanning speed of 8° min^{-1} (hold for 5 min at each temperature). When the temperature reached 600 °C, the data were collected every 15 min for 90 min. The *in situ* XRD measurement was also conducted under reaction conditions. A gas mixture of $CO_2/H_2/N_2$ = 17/69/14 (30 mL min^{-1}) was introduced after cooling the reduced sample down to 200 °C. The XRD diffractograms were continuously recorded at elevated temperatures.

2.5. In situ DRIFTS study

In situ DRIFTS was conducted on a Nicolet iS 50 (Thermo Scientific) FTIR spectrometer equipped with a mercury cadmium telluride detector cooled by liquid N_2. Prior to measurement, the calcined catalysts were reduced in 30% H_2/N_2 flow at 600 °C for 90 min (heating rate of 10 K min^{-1}). Thereafter, the sample was cooled down to 200 °C followed by N_2 purging for 10 min. For CO_2 adsorption study, a flow of CO_2/N_2 at a ratio of 1/5 (6 mL min^{-1}) was introduced. For CO_2 methanation study, a gas mixture of $CO_2/H_2/N_2$ at a ratio of 1/4/5 was used. The *in situ* DRIFTS spectra were continuously collected at elevated temperatures.

2.6. DFT calculations

Spin-unrestricted calculations were performed using DFT-D scheme provided by DMol3 code [23,24]. The exchange–correlation functional was expressed using the generalized gradient approximation (GGA)-Perdew, Burke, and Ernzerhof (PBE) functional [25]. The Ni(1 1 1) and Ni4Fe(1 1 1) alloy were modeled using five-layered slab of (3 × 3) surface unit cell. In the Ni4Fe catalyst, Ni atoms were replaced with Fe atoms with a Fe/Ni ratio of ¼, representing NiFe-0.25 catalyst. A vacuum region was set to be 30 Å between repeated slabs. In our calculations, the atoms in the bottom two layers were fixed at their bulk position and those in the top three layers together with the adsorbates are allowed to relax. Double numerical plus polarization (DNP) basis set was used throughout the calculation. The convergence criteria were set to be 1×10^{-5} Ha, 0.001 Ha $Å^{-1}$, and 0.005 Å for energy, force, and displacement convergence, respectively. A self-consistent field (SCF) density convergence with a threshold value of 1×10^{-5} Ha was specified. K-points were sampled using the 4 × 4 × 1 Monkhorst-Pack mesh for Ni and NiFe alloys.

All the transition states (TS) were determined using the linear synchronous transit (LST) and quadratic synchronous transit (QST) methods. The TS structures were confirmed by using a local minimum search (after a small distortion of each TS in the reaction coordinate direction) to reach the reactants and products [26]. The desorption energy (E_{des}) of adsorbed species was calculated with Eq. (5), where E_{ads} and E_{surf} are the total energies of the isolated adsorbates in vacuum and the clean surface, respectively. E_{ads_surf} is the total energy of the adsorbed system.

$$E_{des} = E_{surf} + E_{ads} - E_{ads_{surf}} \quad (5)$$

3. Results and discussion

3.1. Physicochemical properties

XRD diffractograms of the as-prepared HT precursors show the characteristic diffractions of pure HT with layered structures in rhombohedral 3R symmetry (**Figure S1**). Based on calculated lattice parameters (**Table S1**), it is confirmed that pure crystalline Ni-Fe-Mg-Al HT precursors were successfully synthesized via the rapid coprecipitation method. After calcination at 600 °C, the precursors fully decomposed into mixed metal oxides (Fig. 1). The diffraction patterns of bimetallic NiFe catalysts were similar to monometallic NiFe-0 catalyst and were dominated by the reflections of not only NiO (JCPDS 01–089-5881) but also MgO (JCPDS 03–065-0476) and Al_2O_3 (JCPDS 01–073-1512). It has been reported that at a moderate calcination temperature of 600 °C, only

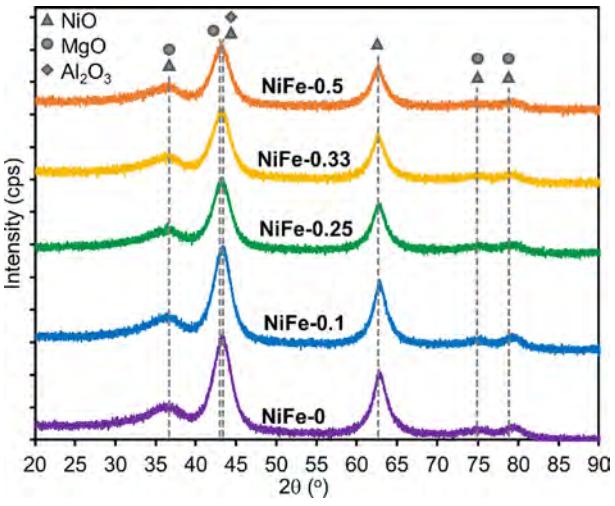

Fig. 1. XRD diffractograms of the calcined catalysts.

the rock-salt-type phase (NiO or MgO) was observed while crystalline spinels (e.g., $MgAl_2O_4$) would be formed at above 800 °C [27]. Therefore, it is assumed that the support was in the mixed oxide phase $(Mg,Al)O_x$. Notably, the increase of Fe resulted in poorer crystallinity with slightly smaller crystallite sizes of the oxide catalysts, as can be seen by the reduced intensity of the diffraction lines (Fig. 1).

Elemental analysis by ICP-OES of the calcined catalysts reveals the actual metal loading and Fe/Ni molar ratio, which was close to the nominal values (Table 1). It could be assumed that Ni and Fe ions were successfully precipitated.

The N_2 physisorption analysis of calcined catalysts shows that all isotherms were type IV with hysteresis loop at high P/P_o range (**Figure S2**), attributed to mesoporous materials according to IUPAC classification [28]. The pore size distribution of calcined catalysts (**Figure S3**) further confirmed that the calcined catalysts had mesopores in the range of 10–15 nm. In general, all HT-derived catalysts had a relatively high surface area of 200–250 $m^2\ g^{-1}$ and a large pore volume of 0.7–0.8 $cm^3\ g^{-1}$ (Table 1). Interestingly, the increase of Fe content did not significantly affect the mesoporous texture of the catalysts.

3.2. Temperature programmed reduction and in situ XRD study

The reduction behavior of calcined catalysts was investigated by H_2-TPR analysis (Fig. 2). For the monometallic NiFe-0 catalyst, only a single reduction peak at 810 °C was observed, corresponding to the reduction of NiO to metallic Ni. In fact, the reduction temperature of pure NiO is at 290–340 °C [29]. Other types of Ni^{2+} cations such as NiO aggregates or freely bounded NiO were not depicted. It has been suggested that Ni was embedded in the $MgO\text{-}Al_2O_3$ structure, thus it was harder to be reduced [29,30]. For bimetallic NiFe catalysts, the sequential reduction of Fe_2O_3 was not observed due to low Fe content [31,32], and only small peaks at 350–400 °C were observed in Fe-rich catalysts. This could be ascribed to the partial reduction of Fe_2O_3 to Fe_3O_4 [19,33], whereas the reduction of Fe_3O_4 to Fe and NiO to Ni was overlapped at higher temperatures [31,32]. The main reduction peaks of Ni species shifted to lower temperatures with increasing Fe content. Therefore, it can be suggested that Fe enhanced the reducibility of the NiFe alloy catalysts.

The *in situ* XRD diffractograms of NiFe-0, NiFe-0.25, and NiFe-0.5 catalysts during reduction are shown in Fig. 3. For the monometallic catalyst, the diffraction line associated with metallic

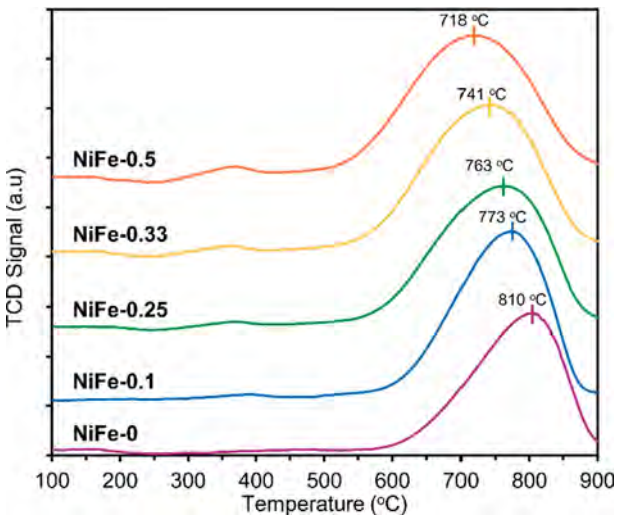

Fig. 2. H_2-TPR profiles of the calcined catalysts.

Ni(200) was detected at 2θ of 51.4° (JCPDS 03–065-2865) after the sample reached 600 °C for 15 min. The intensity of this line gradually increased during 90 min of reduction, indicating the growth of Ni particle from 5.3 nm to 9.1 nm (**Table S2**). Besides, the mixed oxides phases $(Mg,Al)O_x$ remained unchanged, demonstrating their irreducible nature. As for the NiFe-0.25 and NiFe-0.5 catalysts, the characteristic peak shifted to a lower angle of 50.85° and 50.75°, respectively. Correspondingly, the d-spacing obtained from the (200) reflection was in a linear correlation with the molar ratio of Ni/(Ni + Fe) (Figure S4) [34]. The lattice parameter appeared to be increased with increasing Fe content. The shift in peak position could confirm the formation of Ni-rich NiFe fcc alloy upon reduction of NiFe-0.25 and NiFe-0.5 catalysts at 600 °C [19,34–36]. Moreover, the alloy crystals were smaller in size (5–6 nm) than Ni crystals (9 nm) (**Table S2**).

3.3. Metal surface area and basicity of the reduced catalysts

The maximum Ni surface area of 5.52 $m^2\ g^{-1}$ was obtained from NiFe-0 catalyst based on H_2 chemisorption analysis. With increasing Fe content, the Ni surface area dramatically dropped to 0.1 $m^2\ g^{-1}$ for NiFe-0.5 catalyst although the Ni loading was kept constant at 20 wt% (Table 2). These results further confirmed the formation of NiFe alloy which is inactive in H_2 chemisorption [34].

CO_2-TPD analysis showed that the alloy catalysts exhibited stronger basicity than monometallic catalyst, due to the larger integrated area of the desorption profiles (**Figure S5**). It reveals that Fe addition could enhance the total basicity of the catalysts. However, the impact of different basic types (i.e., weak, medium, and strong) on the catalytic activity in CO_2 methanation remains disputable [37,38].

3.4. CO_2 methanation activity tests

3.4.1. Temperature-programmed reaction study

The catalytic behavior of different NiFe catalysts was firstly studied in temperature-programmed reaction at atmospheric pressure. It shows that NiFe alloy catalysts were more active than monometallic Ni catalysts in CO_2 methanation at low temperatures, particularly at 260–290 °C (Fig. 4**.a**). NiFe-0.25 achieved the highest CO_2 conversion of 53% at 270 °C. As the temperature increased to 450 °C, a decline of activity for all catalysts was observed.

During CO_2 methanation, the simultaneous RWGS reaction led to a competition between CO and CH_4 formation. At 250 °C, the highest CH_4 selectivity was obtained from the NiFe-0 catalyst (Fig. 4**.b**). However, at 270–400 °C, NiFe alloy catalysts exhibited better CH_4 selectivity, particularly for NiFe-0.25 with S_{CH4} greater than 97%. At a higher temperature of 400–450 °C, a decrease of S_{CH4} was observed because the endothermic RWGS reaction was favored. Moreover, the addition of too large amount of Fe facilitated the formation of CO for NiFe-0.33 and NiFe-0.5. It has been reported that although $Fe/(Mg,Al)O_x$ catalysts had very low activity in CO_2 methanation, the CO selectivity was very high (~100%) [17]. Fe-rich Ni/ZrO_2 catalysts have also been found to significantly promote the RWGS reaction rather than CO_2 methanation [16]. Hence, it could be concluded that a high CH_4 yield could only be achieved over a suitable composition of Ni and Fe, particularly the NiFe-0.25 catalyst in the low-temperature region.

3.4.2. Long-term activity test

The best performing NiFe-0.25 catalyst was tested in CO_2 methanation under high GHSV condition for more than 100 h of TOS at 300 °C. The formation rate of CH_4 was higher over NiFe-0.25 alloy catalyst compared to the monometallic NiFe-0 catalyst

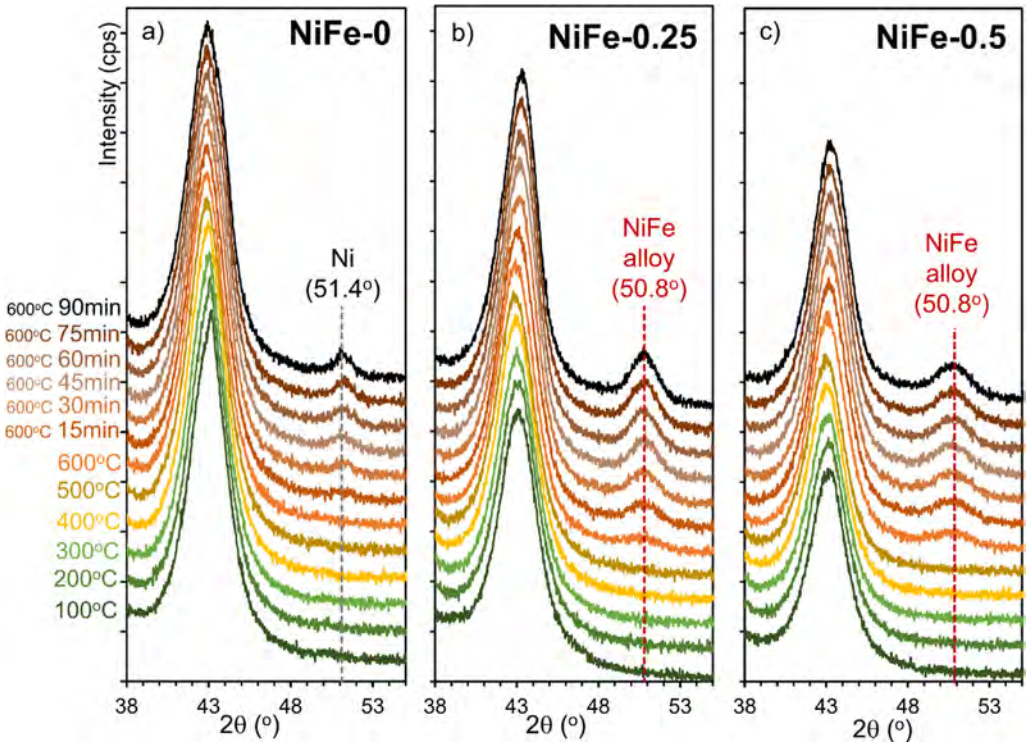

Fig. 3. *In situ* XRD diffractograms of (a) NiFe-0, (b) NiFe-0.25, and (c) NiFe-0.5 catalysts during reduction in pure H_2 at increasing temperatures and time.

Table 2
H_2 chemisorption uptake and Ni surface area of reduced catalysts.

Samples	H_2 chemisorption uptake [μmol g_{cat}^{-1}]	Metal surface area [m^2 g^{-1}]
NiFe-0	70.6	5.52
NiFe-0.1	50.1	3.91
NiFe-0.25	29.4	2.30
NiFe-0.33	16.4	1.28
NiFe-0.5	1.3	0.10

(Fig. 5). A slight decline in CO_2 conversion with 0.18% h^{-1} for NiFe-0 and 0.08% h^{-1} for NiFe-0.25 was observed. Both catalysts exhibited high stability and the deactivation rate was low compared to those reported in literature [19].

3.4.3. Catalyst deactivation study

The TEM images of NiFe-0 and NiFe-0.25 reduced-passivated catalysts show that metallic particles (Ni and NiFe alloy) were well dispersed on the support (Fig. 6.**a** and Fig. 6.**b**). The average particle sizes were close at 6.7 ± 1.8 nm and 6.1 ± 1.5 nm. The TEM images of catalysts after long-term tests were also examined (Fig. 6.**c** and Fig. 6.**d**). The average particle sizes of the spent catalysts remained constant at 6.7 ± 1.4 nm and 6.1 ± 2.2 nm for NiFe-0 and NiFe-0.25, respectively. Since carbonaceous species were not observed, carbon formation, as well as metal sintering, are not the reason for the degradation of methanation activity.

In situ XRD analysis was further used to study the phase changes during CO_2 methanation at increasing temperatures. In addition to previously identified mixed oxides and Ni or NiFe

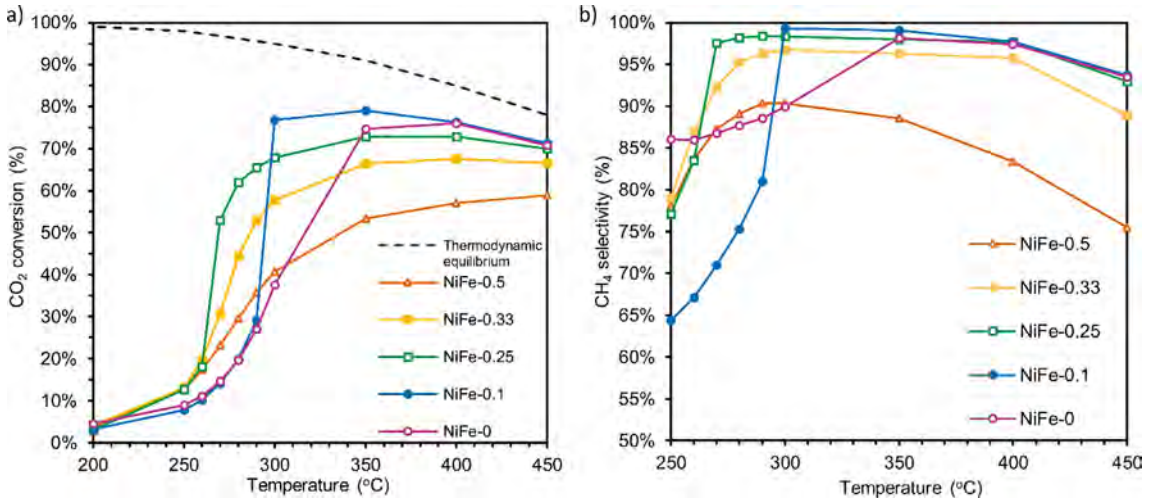

Fig. 4. (a) CO_2 conversion and (b) CH_4 selectivity as a function of reaction temperature in CO_2 methanation ($H_2/CO_2/N_2$ vol.% = 64/16/20, WHSV = 43,200 mL_{CO2} g_{cat}^{-1} h^{-1}).

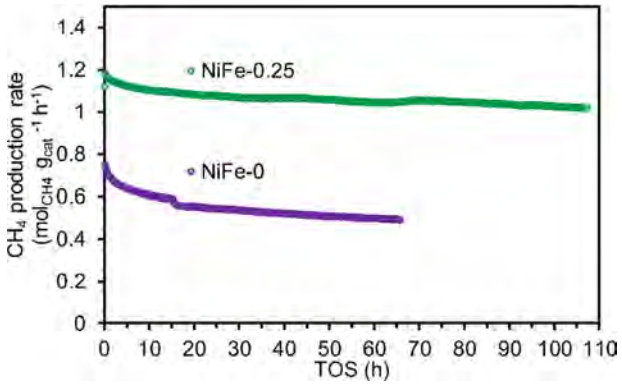

Fig. 5. Methane production rate over NiFe-0.25 and NiFe-0 catalysts during long-term test at 300 °C ($H_2/CO_2/N_2$ vol.% = 64/16/20, WHSV = 43,200 mL_{CO2} $g_{cat}^{-1}h^{-1}$).

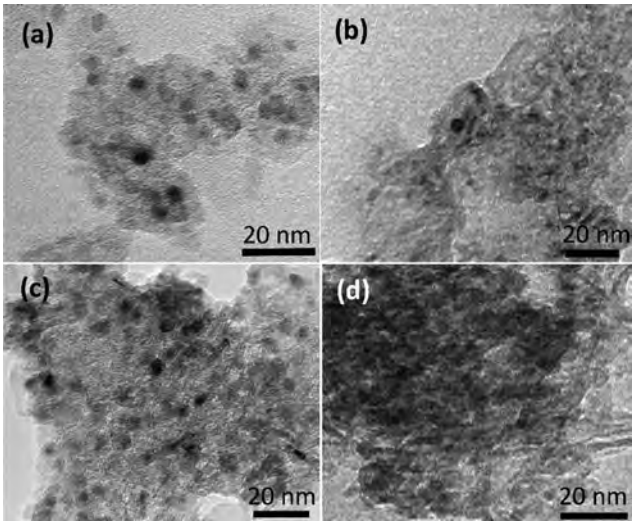

Fig. 6. TEM images of (a) reduced-passivated NiFe-0, (b) reduced-passivated NiFe-0.25, (c) spent NiFe-0 and (d) spent NiFe-0.25 catalysts after the long-term stability test.

phases, no carbon formation was observed in the *in situ* XRD diffractograms (**Figure S6**). The crystallite size of Ni and NiFe alloy particles were almost unchanged during reaction at 200–350 °C. NiFe-0 catalyst maintained its metal crystallite size of approximately 9 nm, whereas NiFe alloy crystallite size was stable in the range of 5–6 nm under reaction conditions at increasing temperatures (**Table S2**).

Furthermore, time-resolved *in situ* DRIFTS spectra during CO_2 methanation were also recorded at 300 °C for 180 min over NiFe-0 catalysts (**Figure S7**). While the intensity of vibration bands attributed to gaseous CH_4 species gradually reduced, linearly adsorbed *CO species on Ni was not detected during reaction. As a result, the presence of nickel carbonyl could not be confirmed [39]. Overall, metal sintering, carbon, and nickel carbonyl formation were likely not the reasons for catalyst deactivation on both Ni and NiFe alloy catalysts.

3.5. In situ DRIFTS study

3.5.1. In situ DRIFTS of CO_2 adsorption

To identify the surface species on catalysts during CO_2 adsorption, the sample was *in situ* reduced before exposure to CO_2 at increasing temperatures. The *in situ* DRIFTS spectra over NiFe-0 catalyst show intense IR bands of gaseous linearly adsorbed $*CO_2$ at 2350 cm^{-1}, as well as the surface *OH species at 3600–3700 cm^{-1} (Fig. 7**.a**). It is worth noting that $*OH^-$ could be produced during the reduction of catalysts [40]. The IR bands at 1223, 1395–1405 and 1668 cm^{-1} are characteristic of surface $*CO_2$ species, namely bicarbonate $*HCO_3^-$ (1220 and 1650 cm^{-1}) and monodentate carbonate $*CO_3$ (1360–1400 cm^{-1}). As the temperature increases, the intensity of $*HCO_3$ bands at 1223 and 1668 cm^{-1} gradually decreased, while the band of $*CO_3$ species only slightly reduced. Monodentate $*CO_3$ species were assumed to adsorb on strong basic sites of the catalyst, more stable and harder to remove at high temperatures. As for Ni-based on (Mg, Al)O_x catalysts, it is anticipated that surface *OH species possibly provided weak basic sites to produce $*HCO_3$, whereas *O species with strong basic site facilitated the formation of monodentate $*CO_3$ [41].

In addition, similar surface species were detected over the NiFe-0.25 catalyst (Fig. 7**.b**). Nevertheless, the most significant difference was the transition of $*HCO_3$ vibration bands to formate-related bands over NiFe alloy catalysts, but not on NiFe-0 catalyst. The IR bands at 1605 cm^{-1} were ascribed to *HCOO species [42–44]. The formate species started to appear at 290 °C, while the band intensity of HCO_3^- was decreased. Likewise, the *HCOO species on NiFe-0.5 was detected at an even lower temperature of 250 °C (**Figure S8**). It is suggested that NiFe alloy provided a synergistic effect in the transformation of $*HCO_3$ to formate species.

Moreover, linearly adsorbed *CO species on Ni surface (small IR bands at 2035 cm^{-1}) were detected at 200 °C but disappeared at higher temperatures of 250–350 °C. On the other hand, both linear and gaseous *CO species were found on the alloy catalysts (IR bands at 2210 cm^{-1}), especially on the Fe-rich NiFe-0.5 catalyst (**Figure S8**). As the Fe content increased, a larger amount of gaseous *CO on the alloy surface was observed. This observation is in good agreement with previous reports that the binding energy of *CO was weaker on NiFe alloy compared to Ni surface, thus *CO was desorbed easier [16,45]. It can be speculated that the activation of $*CO_2$ via direct dissociation was promoted on NiFe alloy surface compared to that on Ni surface. A DFT study has also reported that CO_2 activation by decomposition to *CO and *O was easier on Ni_3Fe surface than monometallic Ni surface [34].

3.5.2. In situ DRIFTS of CO_2 methanation

In situ DRIFTS spectra of NiFe-0 and NiFe-0.25 catalysts during CO_2 methanation (H_2/CO_2 = 4) are presented in Fig. 8. The C-H stretching vibrations of $*CH_4$ were observed at 3015 and 1305 cm^{-1}. The $*CH_4$ vibration on NiFe-0.25 appeared at low temperature of 200 °C, while the band intensity was always higher than on NiFe-0 at the same temperature. This further proves that the NiFe-0.25 catalyst performed higher activity in CO_2 methanation, in accordance with the temperature-dependent activity test results. Similar to the *in situ* DRIFTS spectra during CO_2 adsorption, $*CO_3$, $*HCO_3$, gaseous $*CO_2$, and *OH species were all detected.

As the temperature increased, a transition from $*HCO_3$ (1665 cm^{-1}) to *HCOO (1605 cm^{-1}) was observed over both catalysts. Small bands at 2855 cm^{-1} were attributed to the C-H stretching vibration from *HCOO species [46]. For NiFe-0, the peak of $*HCO_3$ (at 1665 and 1223 cm^{-1}) decreased and disappeared at 300 °C, accompanied by the increase in intensity of *HCOO (at 1605 and 2855 cm^{-1}). For NiFe-0.25 catalyst, the disappearance of $*HCO_3$ readily occurred at 280 °C. Moreover, the IR bands at 2735 cm^{-1} could also be assigned to aldehyde hydrogen (formyl) *HCO species [47,48].

Therefore, a formate pathway is highly plausible for CO_2 methanation of over Ni and NiFe alloy catalysts on (Mg,Al)O_x support. The addition of Fe to Ni-based catalysts would not interfere with this pathway since similar surface species were observed. The transition of $*HCO_3$ to *HCOO observed on both catalytic surfaces was

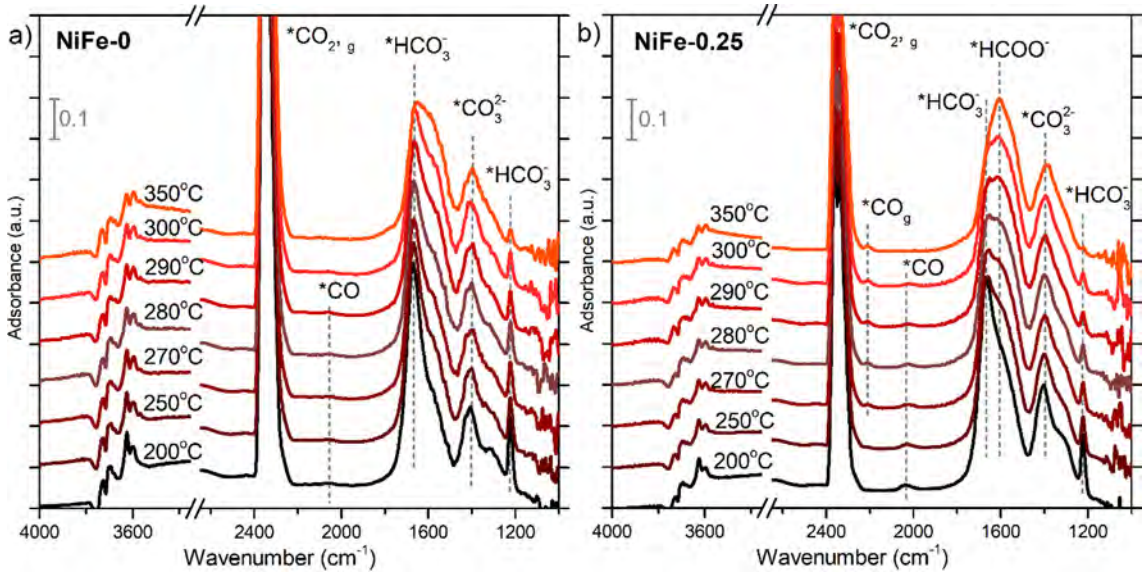

Fig. 7. *In situ* DRIFTS spectra of (a) NiFe-0 and (b) NiFe-0.25 catalysts under CO_2 adsorption condition (CO_2/N_2 vol.% = 1/5) at increasing temperatures.

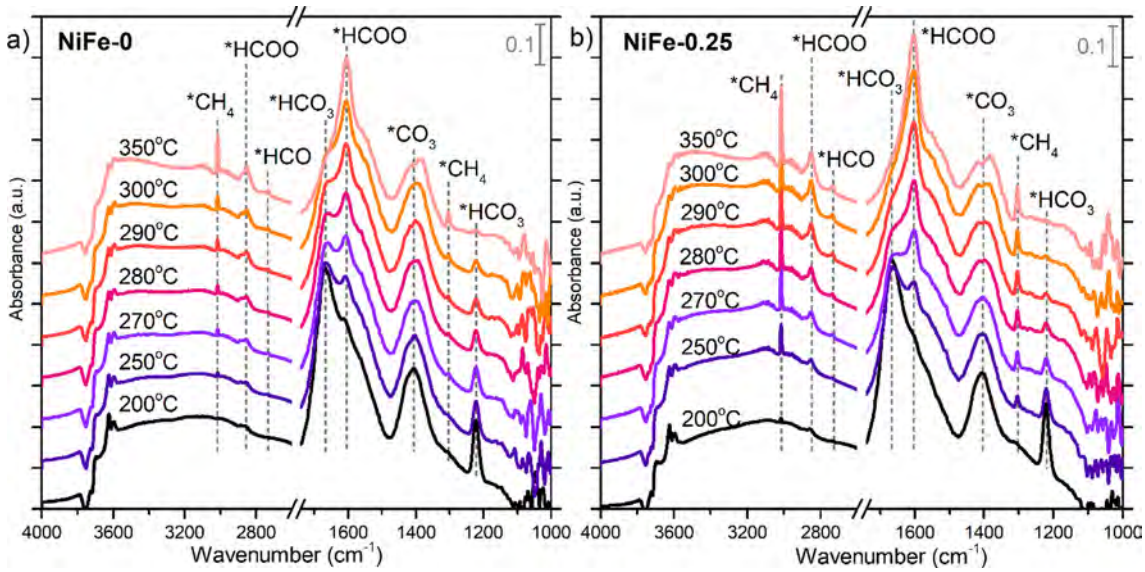

Fig. 8. *In situ* DRIFTS spectra of (a) NiFe-0 and (b) NiFe-0.25 catalysts under CO_2 methanation condition ($CO_2/H_2/N_2$ vol.% = 1/4/5) at increasing temperatures.

assumed to follow the decomposition $*HCO_3 \leftrightarrow *HCOO+*O$. It is also possible that CO_2 was directly hydrogenated $*CO_2+*H \leftrightarrow *HCOO$ at elevated temperature, thus $*HCO_3$ formation was bypassed. *HCOO and *HCO could be the key intermediates in the reaction pathway of CO_2 methanation, while the RWGS could occur via direct CO_2 dissociation since gaseous CO species was found on Fe-rich (NiFe-0.5) catalyst during CO_2 adsorption and methanation (**Figure S8 and S9**). Based on the relative intensity of *in situ* DRIFTS spectra, it further revealed that NiFe alloy could accelerate the formation of *HCOO and *HCO intermediates compared to the monometallic (NiFe-0) catalyst (**Figure S10**). *HCOO formation rate would be promoted by increasing Fe content (NiFe-0.5 > NiFe-0.25 > NiFe-0). However, the production rate of *HCO and CH_4 did not follow this trend (NiFe-0.25 > NiFe-0.5 > NiFe-0). Moreover, because Fe-based catalysts are active for the RWGS reaction [49,50], tuning Fe content is therefore of great importance to achieve the best performance of NiFe alloy catalysts for CO_2 methanation. The transformation of $*HCOO \rightarrow *HCO \rightarrow *CH_4$ could be the key to decipher the promoting effect of Fe in the NiFe alloy catalysts.

3.6. DFT simulations

To further unravel the reaction mechanisms and the higher activity of NiFe alloy compared to monometallic Ni catalysts in CO_2 methanation, DFT calculations were performed on the Ni (111) and Ni4Fe(111) (representing NiFe-0 and NiFe-0.25 catalysts, respectively, as shown in **Figure S11**). Energetics of elementary reactions and the desorption energy of adsorbed species are presented in **Table S3** and **Table S4**, together with the stable geometries of reaction intermediates and its coordinates (**Figure S12 and S13** and **Table S5**).

3.6.1. H_2 dissociation and diffusion

The dissociation of H_2 and diffusion of *H atom on the surface of catalyst directly determine whether the catalyst can provide

enough *H atom for CO_2 methanation. Our calculation shows that the activation energy (E_a) for the dissociation of H_2 on Ni(1 1 1) and Ni4Fe(1 1 1) was estimated to be 1.6, 2.3 (H_2 adsorbed on Fe), and 4.7 (H_2 adsorbed on Ni) kcal mol^{-1}, respectively (Fig. 9.**a**). This implies that H_2 dissociation was facile on these two catalysts. The reaction energy (ΔE) for H_2 dissociation was between −19.2 to −30 kcal mol^{-1}, thus it can be speculated that the formed *H atoms were relatively stable on both catalysts. The diffusion barriers for *H atom on Ni(1 1 1) and Ni4Fe(1 1 1) were estimated to be 12.0 and 16.0 kcal mol^{-1}, respectively (Fig. 9.**b**). This indicates that the diffusion of *H atoms was relatively easy on both catalysts, suggesting the sufficient availability of *H atoms for CO_2 methanation.

3.6.2. CO_2 methanation on Ni and NiFe alloy surface

Based on the *in situ* DRIFTS observation and literature data [51], possible pathways for CO_2 hydrogenation to CH_4 and CO are proposed in Fig. 10. The initial step of CO_2 hydrogenation could occur on either O-terminal to produce *COOH (carboxyl pathway) or C-terminal to produce *HCOO (formate pathway). In the carboxyl pathway, *COOH was dissociated into *CO and *OH, which could be further hydrogenated to produce water or to yield *HCO intermediates. In the formate pathway, *HCOO could directly dissociate to *HCO and *O. The direct dissociation of CO_2 to *CO and *O is also possible. The C-O bond of $*CO_2$ could split to form adsorbed *CO and *O, which underwent hydrogenation to either *HCO+*O following the formate pathway or *CO+*OH following the carboxyl pathway. It is noteworthy that *COH can also be formed from *CO hydrogenation. However, it was not included in our study because *HCO (also written as *CHO) formation was more favorable [52]. It could be assumed that *HCO is the key intermediate in the initial hydrogenation of CO_2, in agreement with literature and the *in situ* DRIFTS study [16,53].

*HCO intermediate can transform to *CHOH, $*H_2CO$, or *CH as intermediates, which could be further hydrogenated to CH_4. It was reported that *HCO dissociation (*HCO↔*CH+*O) was the most favorable pathway amongst others [16,52]. As illustrated in Fig. 10, *CH species underwent sequential hydrogenation reactions to $*CH_2$, $*CH_3$ and eventually $*CH_4$. Likewise, surface *O removal was carried out by two steps of hydrogenation to water. Finally, $*H_2O$ and $*CH_4$ desorbed as gaseous products. Beside CO_2 methanation, the RWGS reaction can occur simultaneously and its mechanism can also be understood by DFT calculations. The side reaction could follow either carboxyl pathway or direct CO_2 dissociation pathway since the dissociated *CO species (cyan route in Fig. 10) could desorb as a gaseous product while surface *O and *OH were removed as water.

The energy diagram of *HCO formation via COOH route with a partial contribution from direct CO_2 dissociation is presented in Fig. 11. On Ni surface, the energy barrier for *COOH formation from $*CO_2$ was calculated to be 12.3 kcal mol^{-1}, while it required 23.9 kcal mol^{-1} for the splitting of *CO and *O. In contrast, *COOH formation had a higher energy barrier (E_a = 20 kcal mol^{-1}) than that of $*CO_2$ direct dissociation on Ni4Fe surface (E_a = 16.3 kcal mo l^{-1}). Therefore, the NiFe alloy surface promoted the dissociation of $*CO_2$, consistent with Kim *et al.* [34] and the *in situ* CO_2 adsorption study.

However, the subsequent hydrogenation of *O at (*CO+*O) state was difficult on both surfaces (E_a of 31.1 and 37.6 kcal mol^{-1} for Ni and Ni4Fe, respectively). Therefore, $*CO_2$→*CO→*HCO transformation can occur easier via the COOH pathway rather than via the direct dissociation. *CO+*H↔*HCO was the rate-determining step (RDS) for the formation of *HCO via COOH route. The activation energy of this reaction was 37.7 kcal mol^{-1} on Ni and 39.5 kcal mol^{-1} on Ni4Fe catalysts. Notably, the hydrogenation of *CO was much less favorable compared to the reverse reaction on both surfaces. The *HCO intermediate was not stable and preferred to decompose back to *CO since the energy barrier of *HCO formation was much higher than its dissociation. It suggests that the RWGS reaction has likely occurred following the COOH pathway. However, the desorption energy of *CO was calculated to be 59.7 kcal mol^{-1} on Ni and 58.1 kcal mol^{-1} on Ni4Fe surface. Hence, CO desorption was very difficult due to the strong binding of *CO to the metallic surfaces. While steadily adsorbed *CO would not contribute to the production of CH_4 via *HCO, it would occupy the active sites, consequently, cause catalytic deactivation during reaction. In our study, *CO was formed and desorbed easier on NiFe alloy compared to the Ni surface in both experimental and theoretical studies. This could explain the more stable performance of NiFe-0.25 compared to NiFe-0 catalyst in the long-term test.

Fig. 12 illustrates the energy diagram of *HCO formation via HCOO route and direct CO_2 dissociation pathway. In the dissociation pathway, the hydrogenation of *CO to *HCO had a very high energy barrier for both Ni (E_a = 38.6 kcal mol^{-1}) and Ni4Fe catalysts (E_a = 39.3 kcal mol^{-1}). Indeed, *CO hydrogenation was rather difficult via either COOH or direct dissociation pathway with E_a of roughly 38–40 kcal mol^{-1}. It is also noticeable that the reaction was not facilitated on Ni4Fe alloy surface. In contrast, $*CO_2$ was more likely to be hydrogenated to *HCOO with a moderate E_a of 15.2–16.0 kcal mol^{-1} on both surfaces. For the C-O bond cleavage of *HCOO to *HCO, an energy barrier of 32.3 kcal mol^{-1} was needed to overcome for monometallic Ni, but it required only 8.5 kcal mol^{-1} for Ni4Fe alloy. Therefore, the transformation of $*CO_2$→*HCOO→

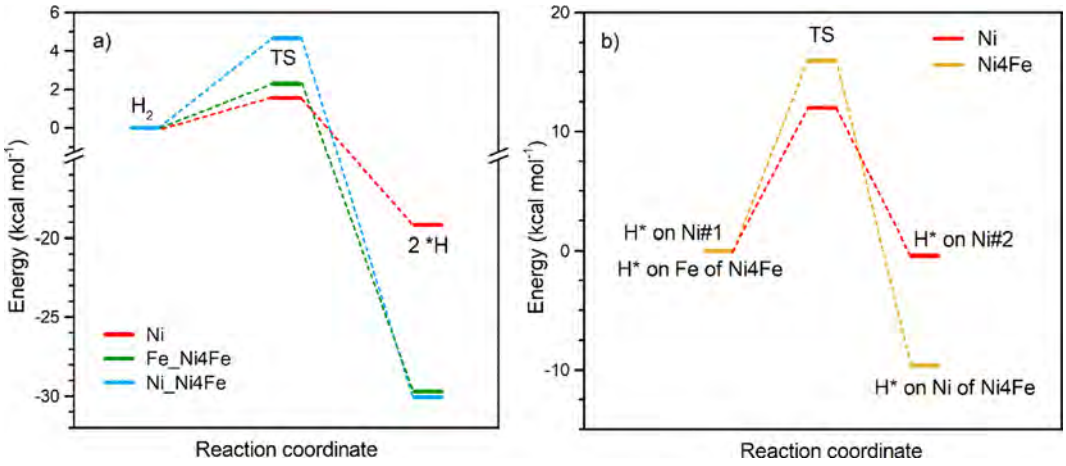

Fig. 9. (a) H_2 dissociation pathway and (b) *H diffusion pathway on Ni and Ni4Fe surface.

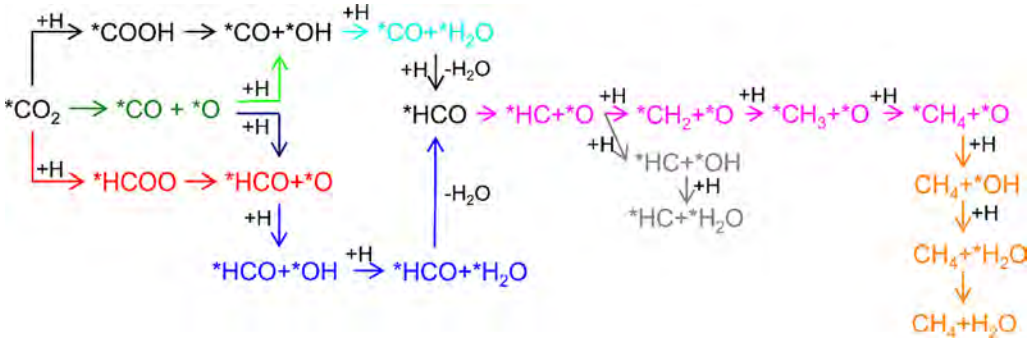

Fig. 10. Plausible reaction schemes of CO_2 methanation.

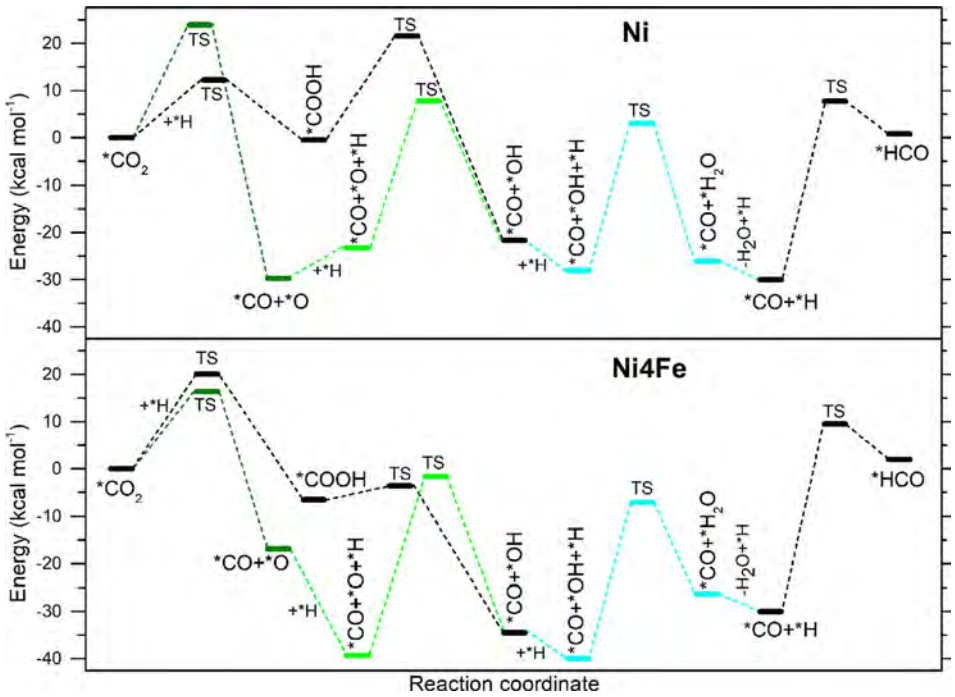

Fig. 11. Energy diagram for the formation of *HCO via COOH pathway and CO_2 direct dissociation pathway on Ni(1 1 1) and Ni4Fe(1 1 1).

*HCO was more facile than that of $*CO_2 \rightarrow *CO \rightarrow *HCO$ regardless of the catalytic systems, and *HCO was formed much easier on Ni4Fe alloy surface than on Ni surface. *HCOO appeared to be more stable on Ni surface and could be detected experimentally [6], while Ni4Fe alloy was more active to produce *HCO. This could explain the higher formation rate of *HCOO and *HCO observed in the *in situ* DRIFTS study.

Fig. 13 illustrates the energy diagram of $*HCO \rightarrow *CH_4$ transformation for both catalyst surfaces. It shows that the decomposition of *HCO occurred with a moderate E_a of 23.5 kcal mol^{-1} on Ni surface and 22.6 kcal mol^{-1} on Ni4Fe surface. Alloy surface promoted the formation of *CH and *O better than Ni surface. When (*CH+*O) reacted with *H, either $*CH_2$ or *OH could be formed. While *CH further yielded $*CH_4$ (Fig. 13), water could also be produced (**Figure S14**, gray pathway). *CH and $*CH_3$ were other stable adsorbed species on the metal surfaces. *CH could easily overcome small barriers of approximately 15 kcal mol^{-1} to form $*CH_2$ and $*CH_3$, while the formation of $*CH_4$ from $*CH_3$ required very high activation energy of 26.2–26.9 kcal mol^{-1} on both surfaces, which could be assumed to be the RDS of $*HCO \rightarrow *CH_4$ transformation.

Finally, $*CH_4$ was desorbed to gaseous CH_4 as product with a desorption energy of 8.27 and 19.14 kcal mol^{-1} from Ni and Ni4Fe surface, respectively. Indeed, $*CH_4$ was more strongly bound on Ni4Fe alloy surface than on Ni surface. According to Young, reactions with a barrier of 21 kcal mol^{-1} or less can readily occur at room temperature [54]. Accordingly, CH_4 could easily desorb from both catalytic surfaces. The energy diagram for water produced from *O at ($*CH_4$+*O) state is also presented in **Figure S14** (orange pathway). The removal of *O by two steps hydrogenation is crucial because not only the active sites would be free from occupied *O, but $*H_2O$ would also be produced as a product from both RWGS and CO_2 methanation. The formation of $*H_2O$ via $*OH+*H \leftrightarrow *H_2O$ required significantly high activation energy compared to the formation of $*CH_4$, which agreed with Zhang *et al.* [55]. However, $*H_2O$ could also be formed via $*OH+*OH \leftrightarrow *H_2O+*O$ at very low activation energy of 3.4 kcal mol^{-1} and 1.2 kcal mol^{-1} on Ni and Ni4Fe surface, respectively.

Microkinetic modeling on Ni(1 1 1) surface reported that $HCO^* \leftrightarrow CH^*+O^*$ was the main RDS for CO_2 methanation [56]. As mentioned above, the decomposition of *HCO was better facilitated on Ni4Fe than on Ni surface due to a lower energy barrier. Accord-

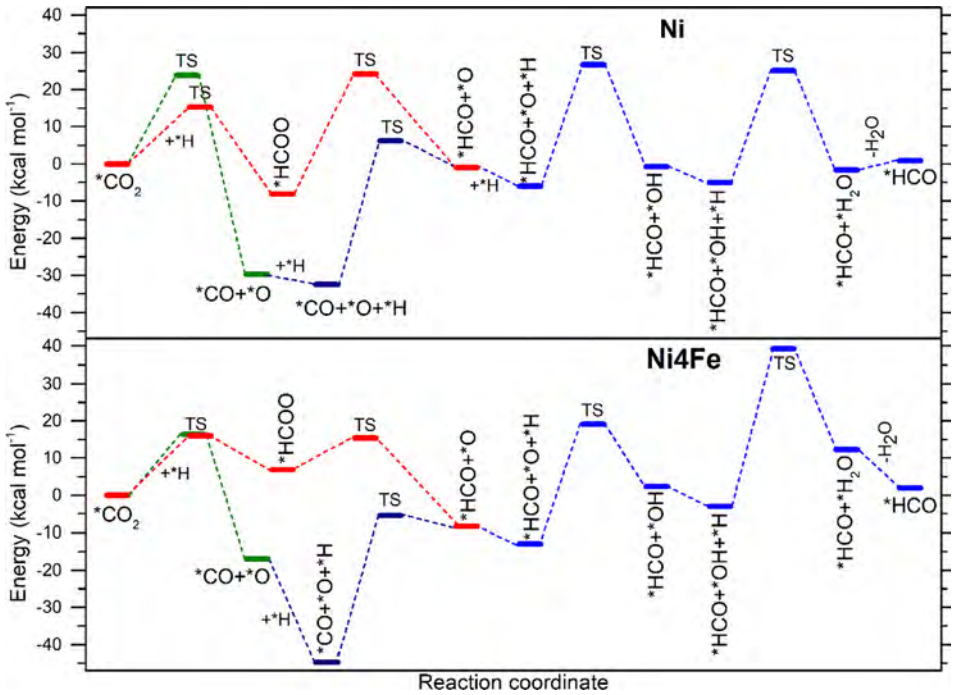

Fig. 12. Energy diagram for the formation of *HCO via HCOO pathway and CO_2 direct dissociation pathway on Ni(1 1 1) and Ni4Fe(1 1 1).

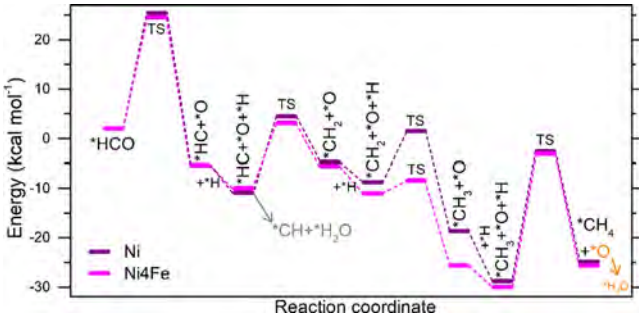

Fig. 13. Energy diagram for the formation of $*CH_4$ from *HCO on Ni(1 1 1) and Ni4Fe (1 1 1).

ing to our DFT calculations, *HCO formation via *HCOO was the most energetically favorable pathway, especially on Ni4Fe alloy surface. Fe alloying with Ni at a certain molar ratio could result in an effective catalytic system that reduced the energy barrier for $*CO_2$ hydrogenation. The alloy surface further facilitated the dissociation of *HCO to *CH, thus accelerated the $*CH_4$ formation.

On the other hand, the desorption of *CO was easier on Ni4Fe than on Ni surface. While stably adsorbed *CO could block available sites on the surface, *O and $*H_2O$ were also possible to occupy the Ni and NiFe active sites. The removal of *O via two-step hydrogenation to water is important. It was recently proposed that Fe could hinder Ni hydroxylation thus catalyst deactivation since it could be the preferential site for water production [57,58]. However, our DFT results showed similar energy is required for·H_2O formation and desorption on both Ni and alloy surfaces. Further studies on the deactivation mechanism of Ni and NiFe alloy are highly recommended.

4. Conclusions

Bimetallic NiFe on $(Mg,Al)O_x$ support catalysts were derived from HT precursors prepared by rapid coprecipitation method. Extensive characterizations verified that small NiFe alloy particles (6–7 nm) were formed upon reduction at 600 °C. The NiFe alloy catalysts could enhance the activity, selectivity towards CH_4, and stability in CO_2 methanation, particularly at low temperatures of 250–350 °C compared to monometallic Ni catalysts. However, the amount of Fe addition significantly influenced the catalytic behavior in which an optimal Fe/Ni molar ratio of 0.25 would obtain the highest CH_4 yield. Both *in situ* DRIFTS observation and DFT calculations showed that CO_2 activation via hydrogenation to *HCOO was more preferred than its direct dissociation on both Ni and NiFe alloy surfaces. $*CO_2 \rightarrow *HCOO \rightarrow *HCO \rightarrow *CH \rightarrow *CH_4$ transformation was considered as the most energetically favorable pathway for CO_2 methanation. The superior catalytic performance of NiFe-0.25 alloy catalysts could be explained by the lower energy barrier for CH_4 formation. At the same time, weak interaction with adsorbed *CO species maintained the free active sites and prolonged the catalytic stability. Our study has provided additional insights into the formate pathway and the promoting effect of Fe for Ni-based catalysts in CO_2 methanation. The NiFe alloy catalyst is a plausible industrial catalyst because it improved the efficiency and lowered the cost of traditional Ni-based catalysts, which are important factors for the development of the PtG process.

Declaration of Competing Interest

The authors declared that there is no conflict of interest.

Acknowledgments

This research has received funding from the Norwegian Ministry of Education and Research and the Plogen program from Valide AS (Norway). JZ and GZ would like to acknowledge the National Natural Science Foundation of China (21902019) and the Fundamental Research Funds for Central Universities (DUT20RC(5)002).

Appendix A. Supplementary data

Supplementary data to this article can be found online at https://doi.org/10.1016/j.jcat.2020.10.018.

References

[1] J. Artz, T.E. Müller, K. Thenert, J. Kleinekorte, R. Meys, A. Sternberg, A. Bardow, W. Leitner, Sustainable Conversion of Carbon Dioxide: An Integrated Review of Catalysis and Life Cycle Assessment, Chem. Rev. 118 (2018) 434–504.

[2] P. Sabatier, J.-B. Senderens, Nouvelles syntheses du methane, Comptes Rendus Des Séances De L'Académie Des Sciences, Section VI –, Chimie 134 (1902) 514–516.

[3] C. Vogt, M. Monai, G.J. Kramer, B.M. Weckhuysen, The renaissance of the Sabatier reaction and its applications on Earth and in space, Nat. Catal. 2 (2019) 188–197.

[4] M. Bailera, P. Lisbona, L.M. Romeo, S. Espatolero, Power to Gas projects review: Lab, pilot and demo plants for storing renewable energy and CO2, Renew. Sustain. Energy Rev. 69 (2017) 292–312.

[5] S. Rönsch, J. Schneider, S. Matthischke, M. Schlüter, M. Götz, J. Lefebvre, P. Prabhakaran, S. Bajohr, Review on methanation – From fundamentals to current projects, Fuel 166 (2016) 276–296.

[6] E. Vesselli, M. Rizzi, L. De Rogatis, X. Ding, A. Baraldi, G. Comelli, L. Savio, L. Vattuone, M. Rocca, P. Fornasiero, A. Baldereschi, M. Peressi, Hydrogen-Assisted Transformation of CO2 on Nickel: The Role of Formate and Carbon Monoxide, The Journal of Physical Chemistry Letters 1 (2010) 402–406.

[7] M.A.A. Aziz, A.A. Jalil, S. Triwahyono, A. Ahmad, CO2 methanation over heterogeneous catalysts: recent progress and future prospects, Green Chem. 17 (2015) 2647–2663.

[8] M. Younas, L. Loong Kong, M.J.K. Bashir, H. Nadeem, A. Shehzad, S. Sethupathi, Recent Advancements, Fundamental Challenges, and Opportunities in Catalytic Methanation of CO2, Energy Fuels 30 (2016) 8815–8831.

[9] M.P. Andersson, T. Bligaard, A. Kustov, K.E. Larsen, J. Greeley, T. Johannessen, C. H. Christensen, J.K. Nørskov, Toward computational screening in heterogeneous catalysis: Pareto-optimal methanation catalysts, J. Catal. 239 (2006) 501–506.

[10] A.L. Kustov, A.M. Frey, K.E. Larsen, T. Johannessen, J.K. Nørskov, C.H. Christensen, CO methanation over supported bimetallic Ni–Fe catalysts: From computational studies towards catalyst optimization, Appl. Catal. A 320 (2007) 98–104.

[11] J. Sehested, K.E. Larsen, A.L. Kustov, A.M. Frey, T. Johannessen, T. Bligaard, M.P. Andersson, J.K. Nørskov, C.H. Christensen, Discovery of technical methanation catalysts based on computational screening, Top. Catal. 45 (2007) 9–13.

[12] S. Hwang, U.G. Hong, J. Lee, J.H. Baik, D.J. Koh, H. Lim, I.K. Song, Methanation of Carbon Dioxide Over Mesoporous Nickel–M–Alumina (M = Fe, Zr, Ni, Y, and Mg) Xerogel Catalysts: Effect of Second Metal, Catal. Lett. 142 (2012) 860–868.

[13] D. Pandey, G. Deo, Effect of support on the catalytic activity of supported Ni–Fe catalysts for the CO2 methanation reaction, J. Ind. Eng. Chem. 33 (2016) 99–107.

[14] J. Ren, X. Qin, J.-Z. Yang, Z.-F. Qin, H.-L. Guo, J.-Y. Lin, Z. Li, Methanation of carbon dioxide over Ni–M/ZrO2 (M=Fe Co, Cu) catalysts: Effect of addition of a second metal, Fuel Process. Technol. 137 (2015) 204–211.

[15] D. Pandey, K. Ray, R. Bhardwaj, S. Bojja, K.V.R. Chary, G. Deo, Promotion of unsupported nickel catalyst using iron for CO2 methanation, Int. J. Hydrogen Energy 43 (2018) 4987–5000.

[16] B. Yan, B. Zhao, S. Kattel, Q. Wu, S. Yao, D. Su, J.G. Chen, Tuning CO2 hydrogenation selectivity via metal-oxide interfacial sites, J. Catal. 374 (2019) 60–71.

[17] C. Mebrahtu, F. Krebs, S. Perathoner, S. Abate, G. Centi, R. Palkovits, Hydrotalcite based Ni–Fe/(Mg, Al)Ox catalysts for CO2 methanation – tailoring Fe content for improved CO dissociation, basicity, and particle size, Catal. Sci. Technol. 8 (2018) 1016–1027.

[18] T. Burger, F. Koschany, A. Wenng, O. Thomys, K. Köhler, O. Hinrichsen, Simultaneous activity and stability increase of co-precipitated Ni–Al CO2 methanation catalysts by synergistic effects of Fe and Mn promoters, Catal. Sci. Technol. 8 (2018) 5920–5932.

[19] B. Mutz, M. Belimov, W. Wang, P. Sprenger, M.-A. Serrer, D. Wang, P. Pfeifer, W. Kleist, J.-D. Grunwaldt, Potential of an Alumina-Supported Ni3Fe Catalyst in the Methanation of CO2: Impact of Alloy Formation on Activity and Stability, ACS Catal. 7 (2017) 6802–6814.

[20] T. Burger, F. Koschany, O. Thomys, K. Köhler, O. Hinrichsen, CO2 methanation over Fe- and Mn-promoted co-precipitated Ni-Al catalysts: Synthesis, characterization and catalysis study, Appl. Catal. A 558 (2018) 44–54.

[21] H.L. Huynh, W.M. Tucho, X. Yu, Z. Yu, Synthetic natural gas production from CO2 and renewable H2: Towards large-scale production of Ni–Fe alloy catalysts for commercialization, J. Cleaner Prod. 121720 (2020).

[22] D.A.M. Monti, A. Baiker, Temperature-programmed reduction. Parametric sensitivity and estimation of kinetic parameters, J. Catal. 83 (1983) 323–335.

[23] B. Delley, An all-electron numerical method for solving the local density functional for polyatomic molecules, J. Chem. Phys. 92 (1990) 508–517.

[24] B. Delley, From molecules to solids with the DMol3 approach, J. Chem. Phys. 113 (2000) 7756–7764.

[25] J.P. Perdew, K. Burke, M. Ernzerhof, Generalized Gradient Approximation Made Simple, Phys. Rev. Lett. 77 (1996) 3865–3868.

[26] M.V. Frash, V.B. Kazansky, A.M. Rigby, R.A. van Santen, Cracking of Hydrocarbons on Zeolite Catalysts: Density Functional and Hartree−Fock Calculations on the Mechanism of the β-Scission Reaction, J. Phys. Chem. B 102 (1998) 2232–2238.

[27] K. Mette, S. Kühl, H. Düdder, K. Kähler, A. Tarasov, M. Muhler, M. Behrens, Stable Performance of Ni Catalysts in the Dry Reforming of Methane at High Temperatures for the Efficient Conversion of CO2 into Syngas, ChemCatChem 6 (2014) 100–104.

[28] K.S. Sing, D.H. Everett, R.A. Haul, L. Moscou, R.A. Pierotti, R. J., T. Siemieniewska, Reporting Physisorption Data for Gas/Solid Systems, in: Handbook of Heterogeneous Catalysis, 2008.

[29] D. Beierlein, D. Häussermann, M. Pfeifer, T. Schwarz, K. Stöwe, Y. Traa, E. Klemm, Is the CO2 methanation on highly loaded Ni-Al2O3 catalysts really structure-sensitive?, Appl. Catal. B 247 (2019) 200–219.

[30] M.-M. Millet, A.V. Tarasov, F. Girgsdies, G. Algara-Siller, R. Schlögl, E. Frei, Highly Dispersed Ni0/NixMg1−xO Catalysts Derived from Solid Solutions: How Metal and Support Control the CO2 Hydrogenation, ACS Catal. 9 (2019) 8534–8546.

[31] S.-H. Kang, J.-H. Ryu, J.-H. Kim, S.-J. Seo, Y.-D. Yoo, P.S. Sai Prasad, H.-J. Lim, C.-D. Byun, Co-methanation of CO and CO2 on the NiX-Fe1−X/Al2O3 catalysts; effect of Fe contents, Korean J. Chem. Eng. 28 (2011) 2282–2286.

[32] R. Brown, M.E. Cooper, D.A. Whan, Temperature programmed reduction of alumina-supported iron, cobalt and nickel bimetallic catalysts, Applied Catalysis 3 (1982) 177–186.

[33] X. Ge, M. Li, J. Shen, The Reduction of Mg–Fe–O and Mg–Fe–Al–O Complex Oxides Studied by Temperature-Programmed Reduction Combined with in Situ Mössbauer Spectroscopy, J. Solid State Chem. 161 (2001) 38–44.

[34] S.M. Kim, P.M. Abdala, T. Margossian, D. Hosseini, L. Foppa, A. Armutlulu, W. van Beek, A. Comas-Vives, C. Copéret, C. Müller, Cooperativity and Dynamics Increase the Performance of NiFe Dry Reforming Catalysts, J. Am. Chem. Soc. 139 (2017) 1937–1949.

[35] D. Pandey, G. Deo, Promotional effects in alumina and silica supported bimetallic Ni–Fe catalysts during CO2 hydrogenation, J. Mol. Catal. A: Chem. 382 (2014) 23–30.

[36] S.A. Theofanidis, V.V. Galvita, H. Poelman, G.B. Marin, Enhanced Carbon-Resistant Dry Reforming Fe-Ni Catalyst: Role of Fe, ACS Catal. 5 (2015) 3028–3039.

[37] L. He, Q. Lin, Y. Liu, Y. Huang, Unique catalysis of Ni-Al hydrotalcite derived catalyst in CO2 methanation: cooperative effect between Ni nanoparticles and a basic support, Journal of Energy Chemistry 23 (2014) 587–592.

[38] P.A.U. Aldana, F. Ocampo, K. Kobl, B. Louis, F. Thibault-Starzyk, M. Daturi, P. Bazin, S. Thomas, A.C. Roger, Catalytic CO2 valorization into CH4 on Ni-based ceria-zirconia, Reaction mechanism by operando IR spectroscopy, Catalysis Today 215 (2013) 201–207.

[39] M.B. Jensen, S. Morandi, F. Prinetto, A.O. Sjåstad, U. Olsbye, G. Ghiotti, FT-IR characterization of supported Ni-catalysts: Influence of different supports on the metal phase properties, Catal. Today 197 (2012) 38–49.

[40] K. Hadjiivanov, Chapter Two - Identification and Characterization of Surface Hydroxyl Groups by Infrared Spectroscopy, in: F.C. Jentoft (Ed.), Advances in Catalysis, Academic Press, 2014, pp. 99–318.

[41] J.I. Di Cosimo, V.K. Díez, M. Xu, E. Iglesia, C.R. Apesteguía, Structure and Surface and Catalytic Properties of Mg-Al Basic Oxides, J. Catal. 178 (1998) 499–510.

[42] F. Solymosi, A. Erdöhelyi, T. Bánsági, Infrared study of the surface interaction between H2 and CO2 over rhodium on various supports, J. Chem. Soc., Faraday Trans. 1 F 77 (1981) 2645–2657.

[43] G. Busca, V. Lorenzelli, Infrared spectroscopic identification of species arising from reactive adsorption of carbon oxides on metal oxide surfaces, Materials Chemistry 7 (1982) 89–126.

[44] S.R. Tong, L.Y. Wu, M.F. Ge, W.G. Wang, Z.F. Pu, Heterogeneous chemistry of monocarboxylic acids on alpha-Al2O3 at different relative humidities, Atmos. Chem. Phys. 10 (2010) 7561–7574.

[45] Y. Wang, Y. Su, M. Zhu, L. Kang, Mechanism of CO methanation on the Ni4/γ-Al2O3 and Ni3Fe/γ-Al2O3 catalysts: A density functional theory study, Int. J. Hydrogen Energy 40 (2015) 8864–8876.

[46] K. Ito, H.J. Bernstein, The Vibrational Spectra Of The Formate, Acetate, And Oxalate Ions, Can. J. Chem. 34 (1956) 170–178.

[47] J. Raskó, J. Kiss, Adsorption and surface reactions of acetaldehyde on alumina-supported noble metal catalysts, Catal. Lett. 101 (2005) 71–77.

[48] J. Coates, Interpretation of Infrared Spectra, A Practical Approach, in: Encyclopedia of Analytical Chemistry, Wiley, 2006.

[49] D.H. Kim, S.W. Han, H.S. Yoon, Y.D. Kim, Reverse water gas shift reaction catalyzed by Fe nanoparticles with high catalytic activity and stability, J. Ind. Eng. Chem. 23 (2015) 67–71.

[50] C.-S. Chen, W.-H. Cheng, S.-S. Lin, Study of iron-promoted Cu/SiO2 catalyst on high temperature reverse water gas shift reaction, Appl. Catal. A 257 (2004) 97–106.

[51] S. Kattel, P. Liu, J.G. Chen, Tuning Selectivity of CO2 Hydrogenation Reactions at the Metal/Oxide Interface, J. Am. Chem. Soc. 139 (2017) 9739–9754.

[52] E.B. Sterk, CO2 methanation over Ni and its structure sensitivity. A computational study, Inorganic Chemistry and Catalysis, Utrecht University, 2018.

[53] W. Zhen, F. Gao, B. Tian, P. Ding, Y. Deng, Z. Li, H. Gao, G. Lu, Enhancing activity for carbon dioxide methanation by encapsulating (111) facet Ni particle in metal–organic frameworks at low temperature, J. Catal. 348 (2017) 200–211.

[54] D. Young, Finding Transition Structures, in: Computational Chemistry: A Practical Guide for Applying Techniques to Real World Problems, John Wiley & Sons, Inc., 2002, pp. 145-158.
[55] M. Zhang, B. Zijlstra, I.A.W. Filot, F. Li, H. Wang, J. Li, E.J.M. Hensen, A theoretical study of the reverse water-gas shift reaction on Ni(111) and Ni (311) surfaces, The Canadian Journal of Chemical Engineering 98 (2020) 740–748.
[56] C. Vogt, M. Monai, E.B. Sterk, J. Palle, A.E.M. Melcherts, B. Zijlstra, E. Groeneveld, P.H. Berben, J.M. Boereboom, E.J.M. Hensen, F. Meirer, I.A.W. Filot, B.M. Weckhuysen, Understanding carbon dioxide activation and carbon–carbon coupling over nickel, Nat. Commun. 10 (2019) 5330.
[57] C. Mebrahtu, S. Perathoner, G. Giorgianni, S. Chen, G. Centi, F. Krebs, R. Palkovits, S. Abate, Deactivation mechanism of hydrotalcite-derived Ni–AlOx catalysts during low-temperature CO2 methanation via Ni-hydroxide formation and the role of Fe in limiting this effect, Catal. Sci. Technol. 9 (2019) 4023–4035.
[58] G. Giorgianni, C. Mebrahtu, M.E. Schuster, A.I. Large, G. Held, P. Ferrer, F. Venturini, D. Grinter, R. Palkovits, S. Perathoner, G. Centi, S. Abate, R. Arrigo, Elucidating the mechanism of the CO2 methanation reaction over Ni–Fe hydrotalcite-derived catalysts via surface-sensitive in situ XPS and NEXAFS, PCCP (2020).

Supporting information

Promoting effect of Fe on Ni supported catalysts in CO_2 methanation by *in situ* DRIFTS and DFT study

Huong Lan Huynh[1], Jie Zhu[2], Guanghui Zhang[2], Yongli Shen[4,], Wakshum Mekonnen Tucho[3], Yi Ding[4], Zhixin Yu[1,]**

[1]Department of Energy and Petroleum Engineering, University of Stavanger, 4036 Stavanger, Norway

[2]State Key Laboratory of Fine Chemicals, PSU-DUT Joint Center for Energy Research, School of Chemical Engineering, Dalian University of Technology, Dalian 116024, China

[3]Department of Mechanical and Structural Engineering and Materials Science, University of Stavanger, 4036 Stavanger, Norway

[4]Tianjin Key Laboratory of Advanced Functional Porous Materials, Institute for New Energy Materials & Low-Carbon Technologies, School of Materials Science and Engineering, Tianjin University of Technology, Tianjin 300384, China

*zhixin.yu@uis.no

*ylshen@tjut.edu.cn

Figure S1. XRD diffractograms of HT precursors.

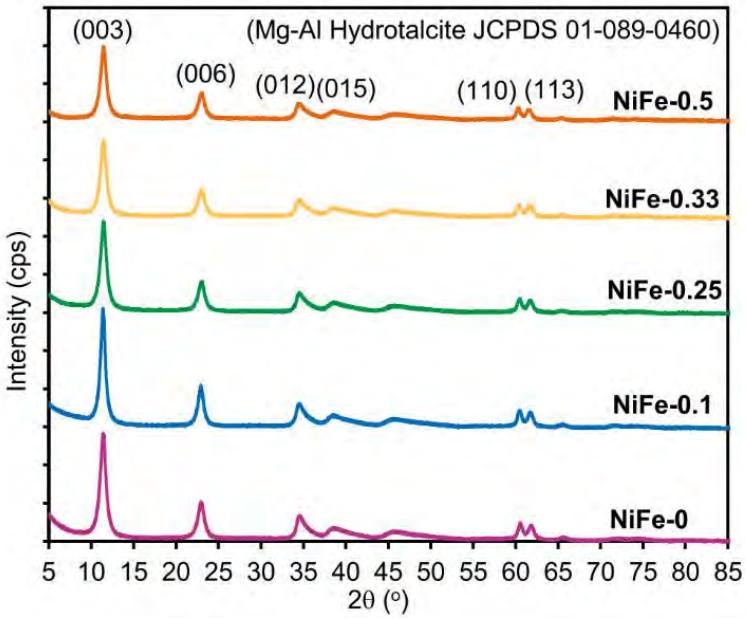

Table S1. Lattice parameters of HT precursors.

Samples	*d*(003) [Å]	*d*(110) [Å]	Lattice cell parameter *a* [Å]*	Lattice cell parameter *c* [Å]*
$Mg_{0.75}Al_{0.25}CO_3(OH)_{0.125}\bullet 0.71H_2O$[1]	-	-	3.07	23.31
NiFe-0	7.742	1.528	3.056	23.226
NiFe-0.1	7.756	1.530	3.060	23.268
NiFe-0.25	7.715	1.530	3.060	23.145
NiFe-0.33	7.709	1.531	3.062	23.127
NiFe-0.5	7.702	1.534	3.068	23.106

*a=2×*d*(110) and c=3×*d*(003)

1. Delidovich, I.; Palkovits, R., Structure–performance correlations of the hydrotalcite catalysts for the isomerization of glucose into fructose. *J. Catal.* **2015,** *327*, 1-9.

Figure S2. N_2 physisorption isotherms of the calcined catalysts.

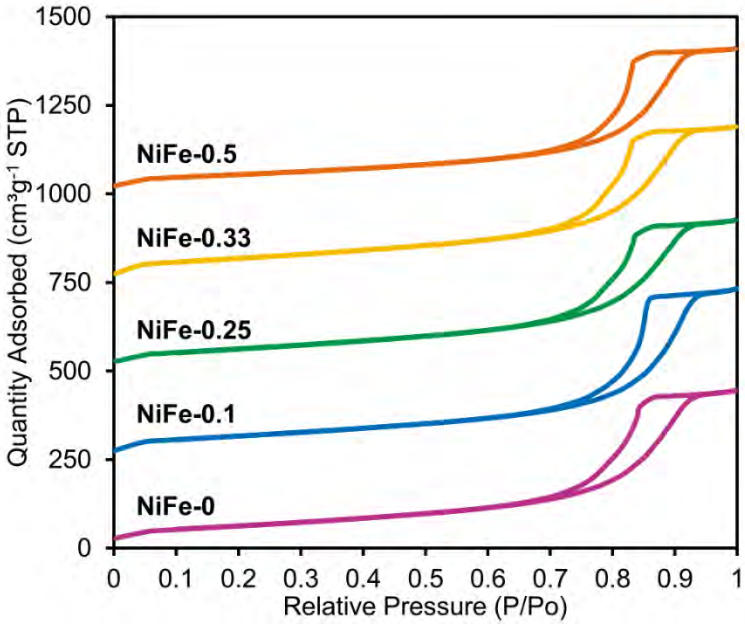

Figure S3. BJH pore size distribution of the calcined catalysts.

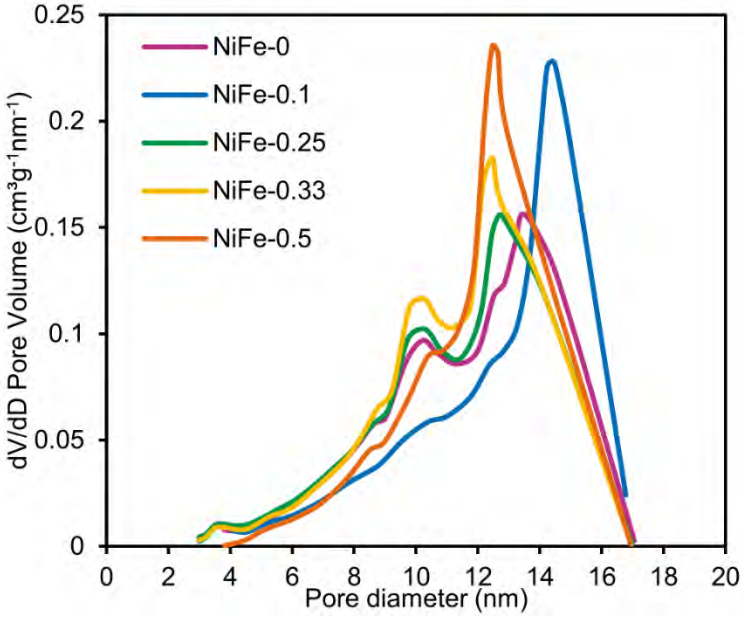

Table S2. Crystallite size of Ni and NiFe alloy particles during reduction and reaction based on *in situ* XRD analysis.

Crystallite size (nm)	NiFe-0 *	NiFe-0.25 **	NiFe-0.5 **
Under reduction condition			
600 °C – 15 min	5.3	4.7	4.2
600 °C – 30 min	7.9	5.2	4.2
600 °C – 45 min	7.4	6.3	4.2
600 °C – 60 min	7.9	6.1	4.4
600 °C – 75 min	9.1	5.6	4.6
600 °C – 90 min	9.1	5.8	4.6
Under reaction condition			
200 °C	8.9	5.8	4.5
250 °C	9.2	5.8	4.6
270 °C	9.2	5.8	4.5
280 °C	9.2	6.0	4.6
290 °C	9.1	5.8	4.6
300 °C	9.0	5.8	4.6
350 °C	9.3	5.8	4.8

*calculated from Scherrer equation, based on Ni (200) plane at $2\theta = 51.4^{o}$; **calculated based on Ni_3Fe (200) plane at $2\theta = 50.8^{o}$.

Figure S4. The relationship between the d-spacing of fcc NiFe (200) and the molar ratio of Ni/(Ni+Fe). The dashed line illustrates a linear correlation.

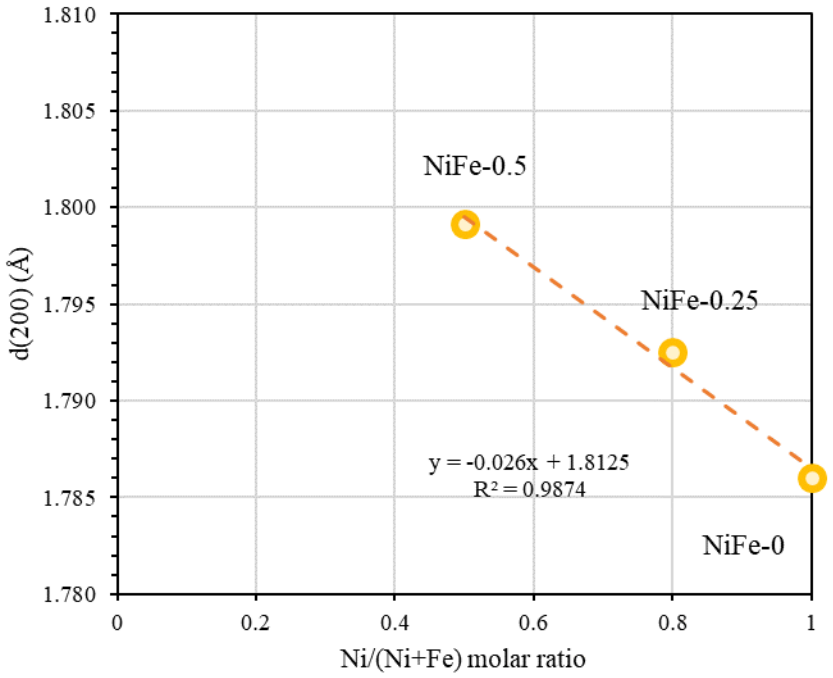

Figure S5. CO_2-TPD profiles of the calcined catalysts.

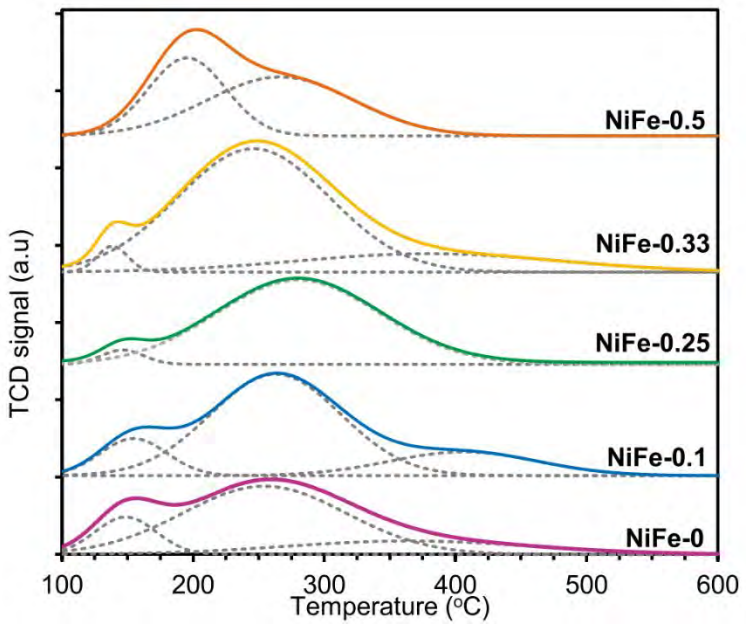

Figure S6. *In situ* XRD diffractograms of a) NiFe-0, b) NiFe-0.25 and c) NiFe-0.5 catalysts during CO_2 methanation ($H_2/CO_2/N_2$ vol% = 79/16/14, 30 mL min^{-1}) at increasing temperatures.

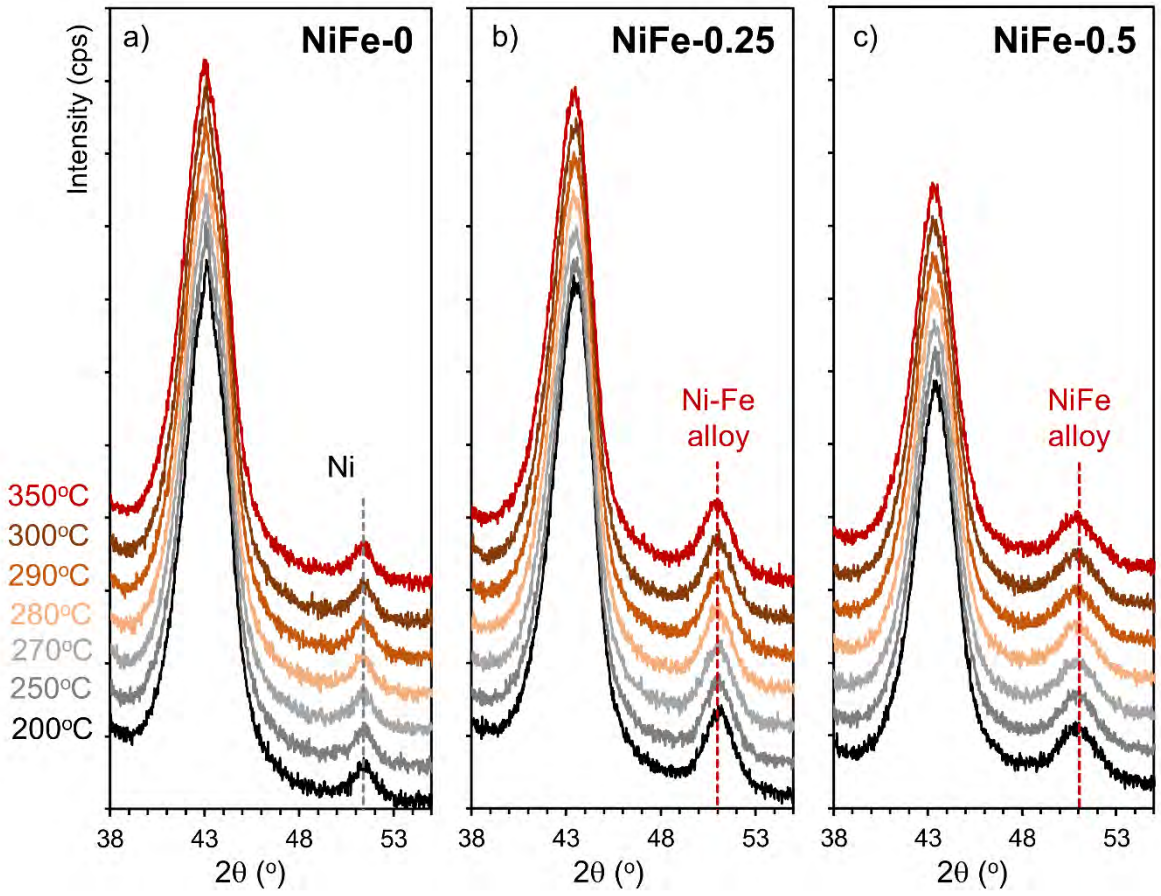

Figure S7. Time-resolved *in situ* DRIFTS spectra for NiFe-0 catalyst under CO_2 methanation condition at 300 °C for 180 min. The spectra were recorded every 1 min of reaction.

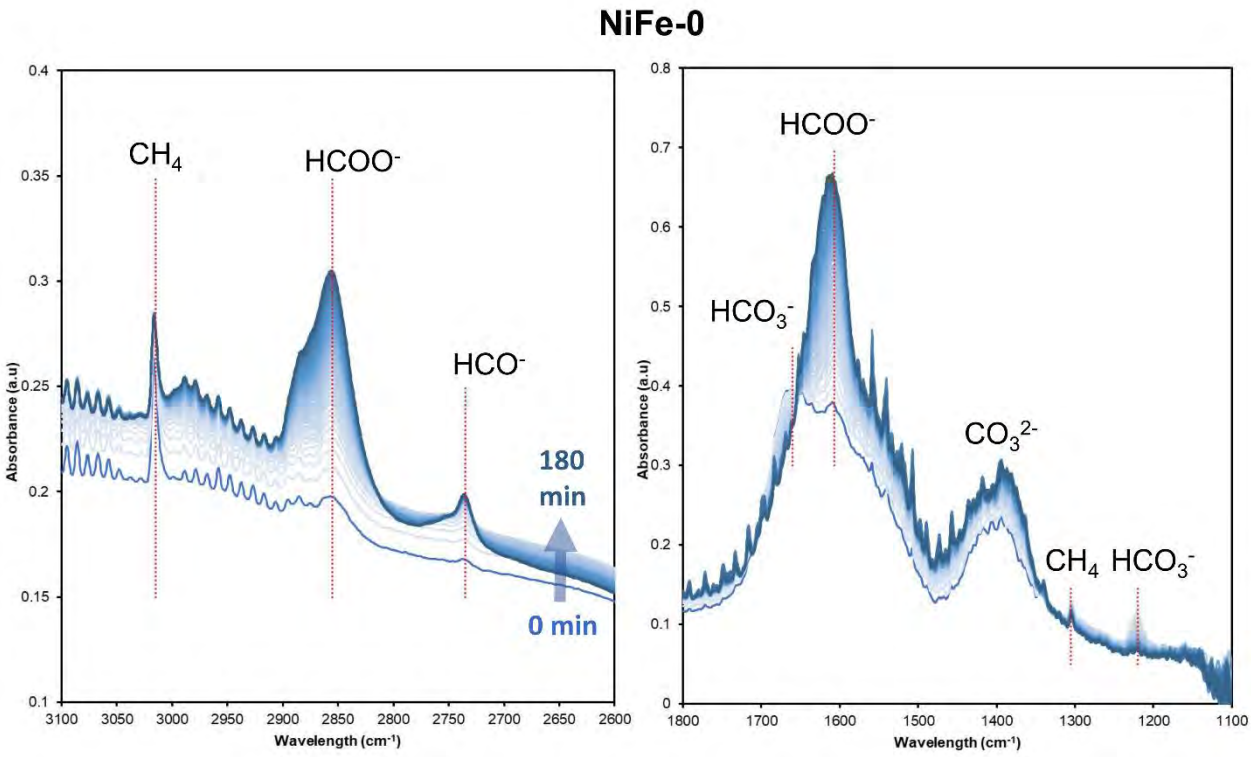

Figure S8. *In situ* DRIFTS spectra for NiFe-0.5 catalyst under CO_2 adsorption condition with increasing temperatures.

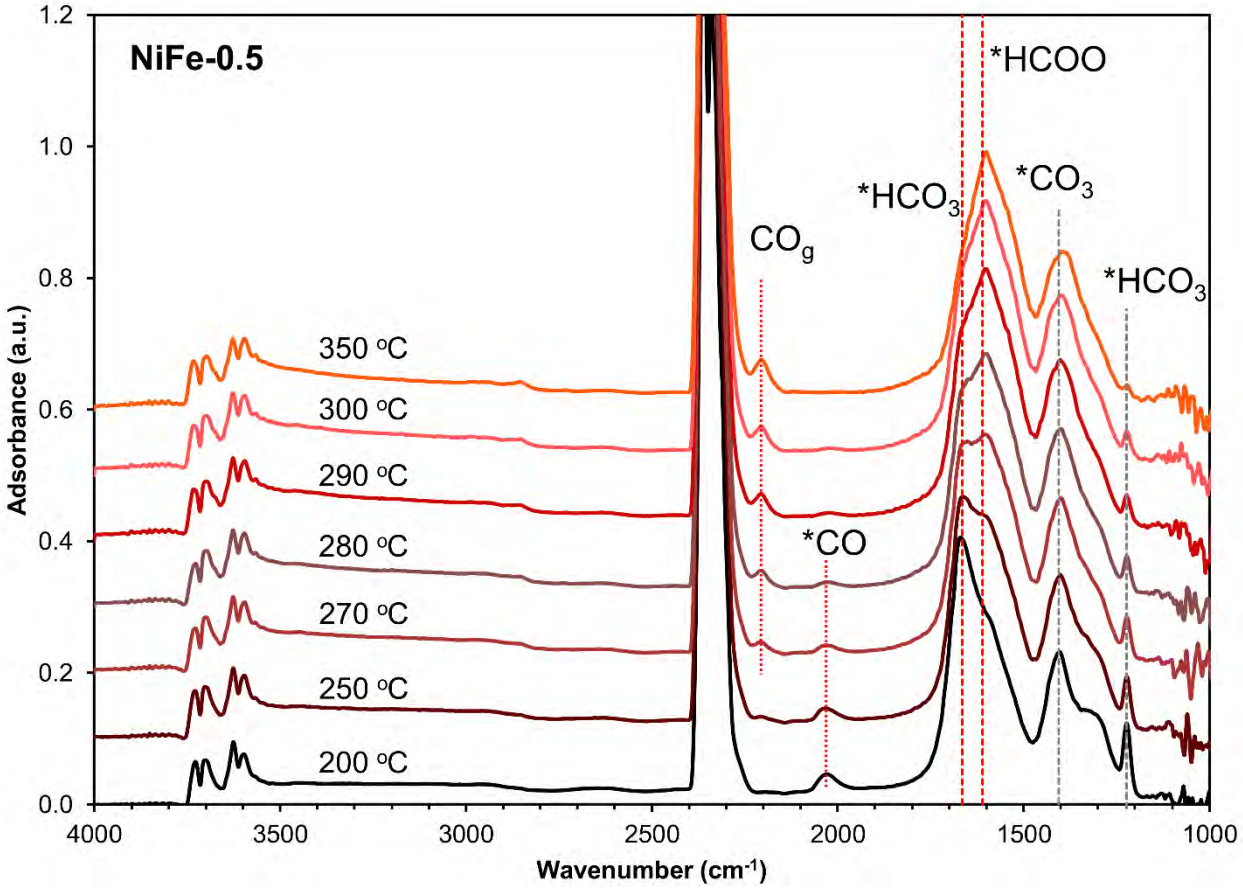

Figure S9. *In situ* DRIFTS spectra for NiFe-0.5 catalyst under CO_2 methanation condition at increasing temperatures.

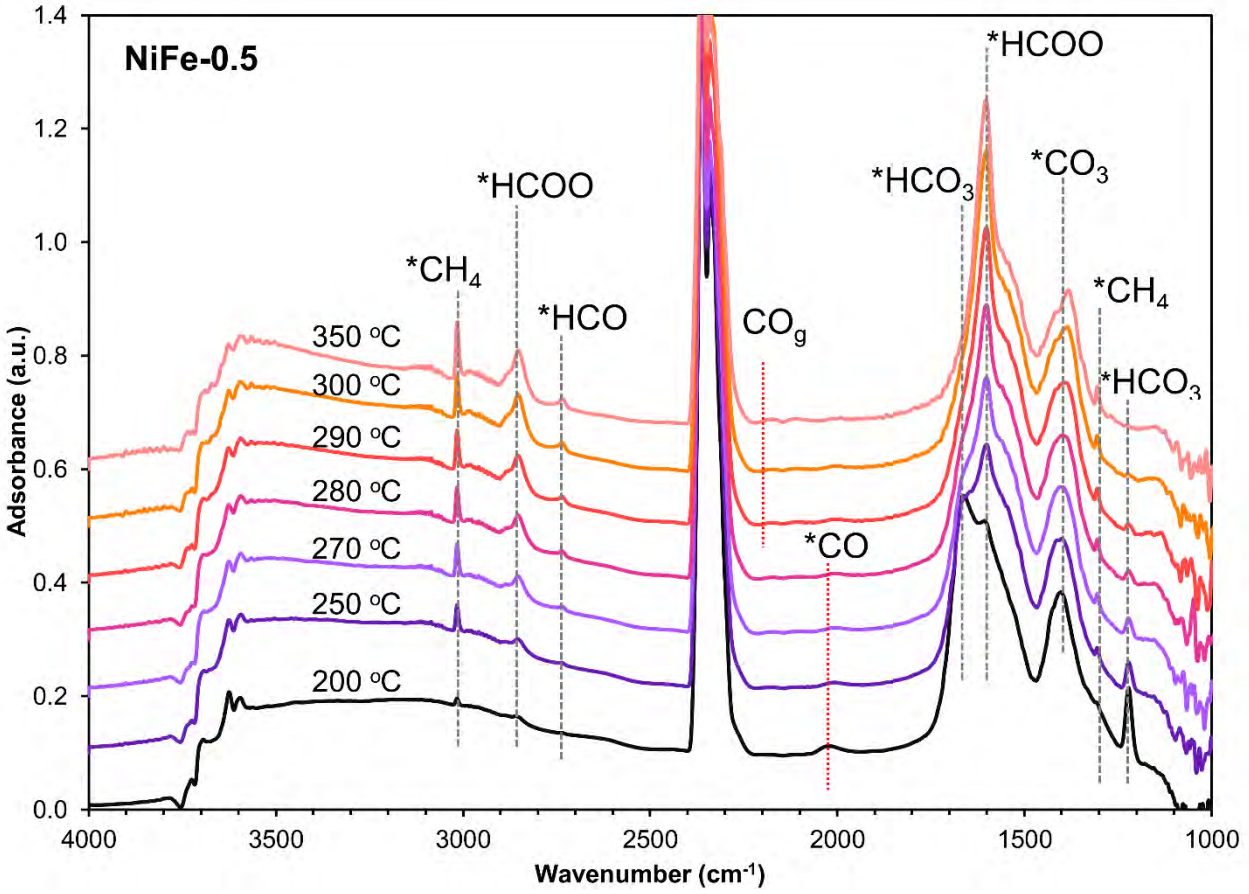

Figure S10. Formation rate of adsorbed species formate HCOO, formyl HCO and gaseous CH_4 from *in situ* DRIFTS spectra over NiFe-0, NiFe-0.25 and NiFe-0.5 under CO_2 methanation condition.

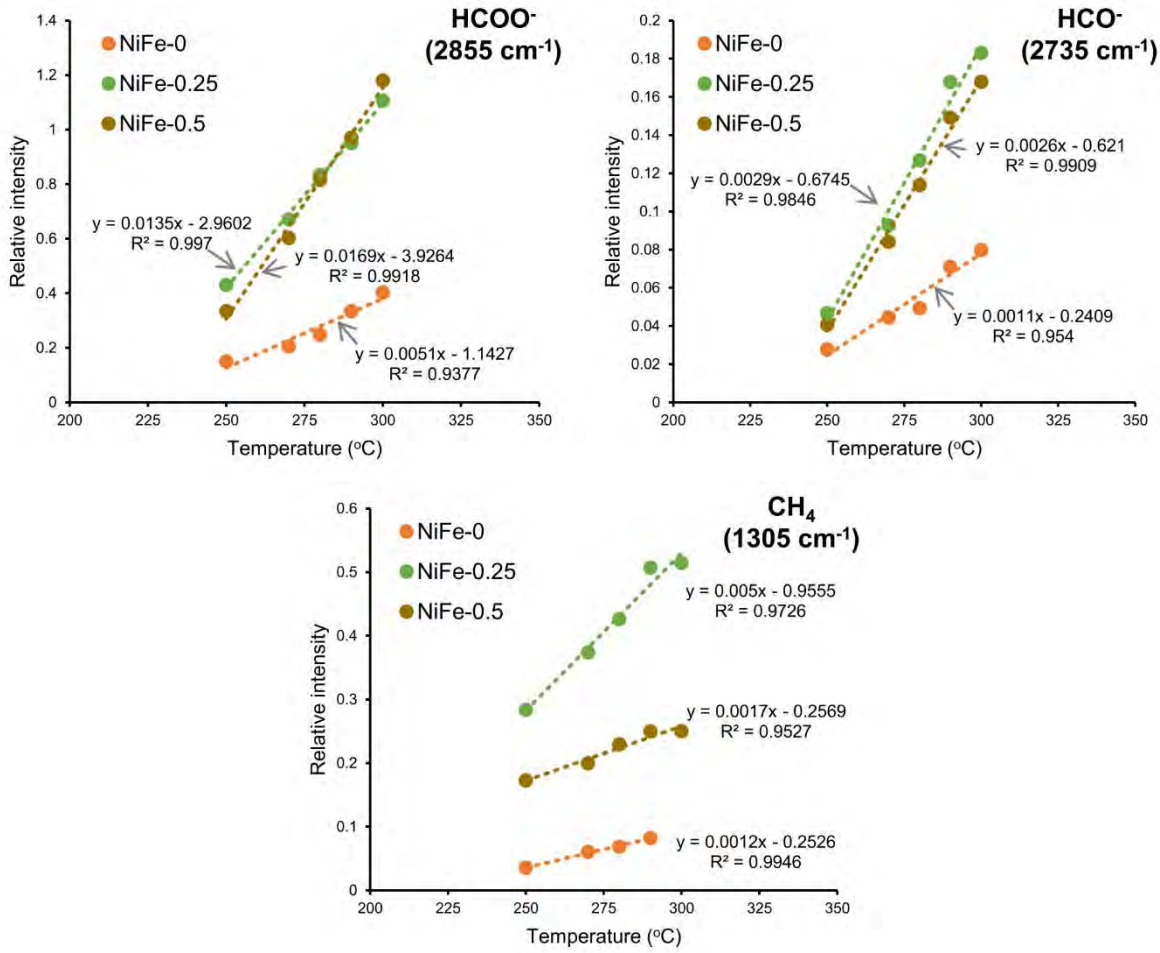

Figure S11. Original structures of Ni (left) and Ni4Fe (right) catalysts.

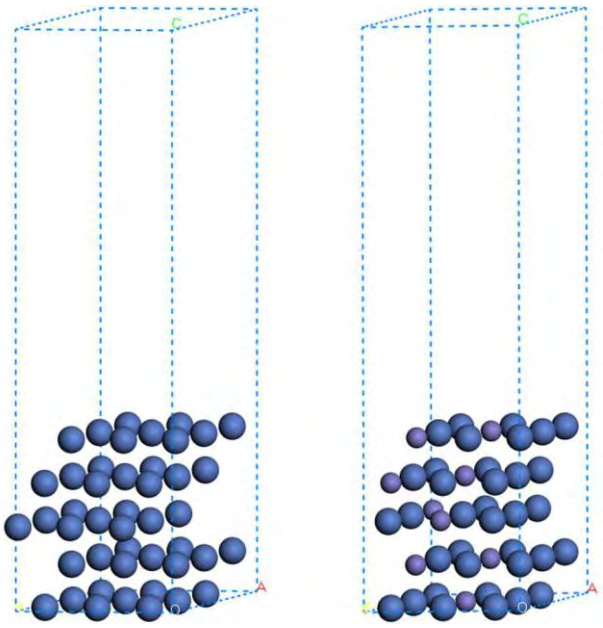

Figure S12. Stable geometrical structures of Ni(111) reaction intermediates.

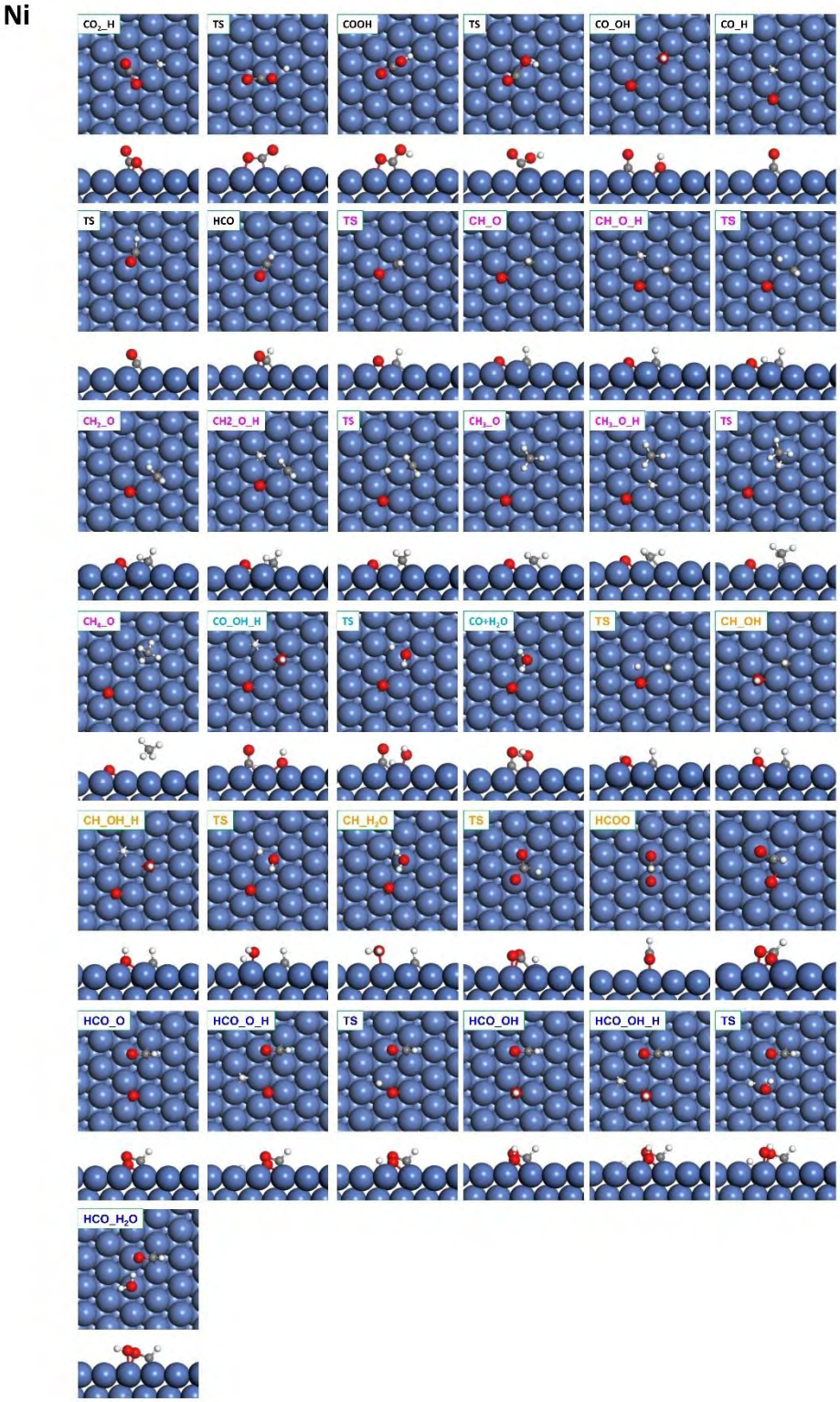

Figure S13. Stable geometrical structures of Ni4Fe(111) reaction intermediates.

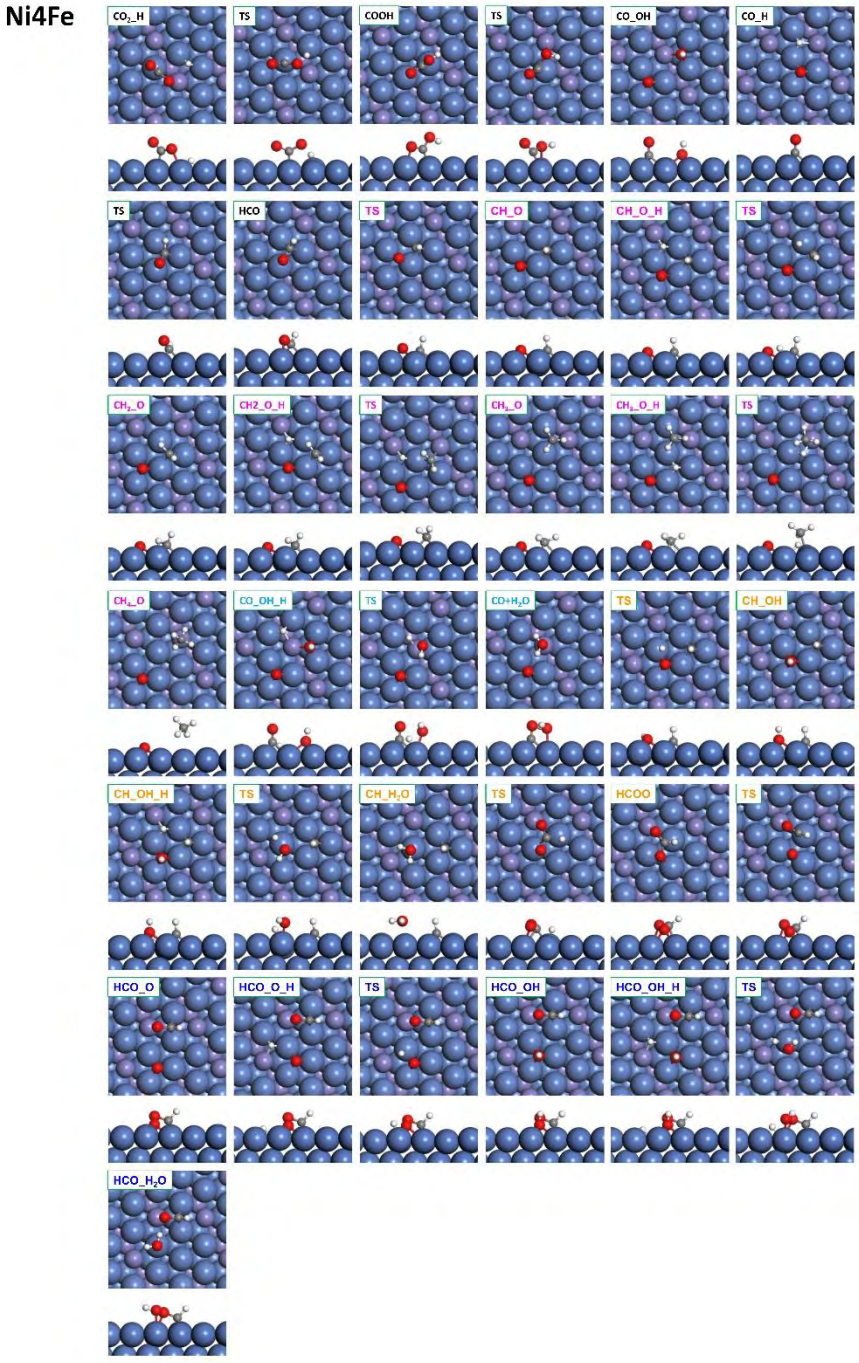

Table S3. Energetics of CO_2 hydrogenation elementary steps on Ni(111) and Ni4Fe(111).

No.	Elementary reactions	Ni(111)		Ni4Fe(111)	
		E_a [kcal mol^{-1}]	**ΔE** [kcal mol^{-1}]	**E_a** [kcal mol^{-1}]	**ΔE** [kcal mol^{-1}]
1	$*CO_2+*H \leftrightarrow *COOH$	12.3	-0.5	20.0	-6.5
2	$*COOH \leftrightarrow *CO+*OH$	22.0	-21.2	2.9	-28.0
4	$*CO+*OH+*H \leftrightarrow *CO+*H_2O$	31.1	2.0	32.9	13.8
5	$*CO+*H \leftrightarrow *HCO$	37.7	30.8	39.5	32.0
6	$*CO_2 \leftrightarrow *CO+*O$	23.9	-29.7	16.3	-16.9
7	$*CO+*O+*H \leftrightarrow *CO+*OH$	31.1	1.6	37.6	4.8
8	$*CO+*O+*H \leftrightarrow *HCO+*O$	38.6	31.5	39.3	36.5
9	$*CO_2+*H \leftrightarrow *HCOO$	15.2	-8.1	16.0	6.9
10	$*HCOO \leftrightarrow *HCO+*O$	32.3	7.1	8.5	-15.1
11	$*HCO+*O+*H \leftrightarrow *HCO+*OH$	32.7	5.2	32.1	15.3
12	$*HCO+*OH+*H \leftrightarrow *HCO+*H_2O$	30.1	3.3	42.3	15.3
13	$*HCO \leftrightarrow *HC+*O$	23.5	-7.4	22.6	-7.4
14	$*HC+*O+*H \leftrightarrow *CH+*OH$	32.5	6.8	29.8	4.1
15	$*HC+*OH+*H \leftrightarrow *CH+*H_2O$	32.7	1.6	28.9	-0.5
16	$*HC+*O+*H \leftrightarrow *CH_2+*O$	15.3	6.1	13.1	4.5
17	$*CH_2+*O+*H \leftrightarrow *CH_3+*O$	10.3	-9.8	2.6	-14.7
18	$*CH_3+*O \leftrightarrow *CH_4+*O$	26.2	3.9	26.9	4.3
19	$*O+*H \leftrightarrow *OH$	32.6	6.7	31.9	5.6
20	$*OH+*H \leftrightarrow *H_2O$	33.8	4.7	35.0	15.1
21	$*OH+*OH \leftrightarrow *H_2O+*O$	3.4	-10.4	1.2	-11.7
22	*OH diffusion	15.7	0.0	15.4	0.0
23	$*O+*H \leftrightarrow *OH$ (on clean surface)	32.6	6.6	34.1	7.6

Table S4. Desorption energy E_{des} (kcal mol^{-1}) of the adsorbed species on Ni(111) and Ni4Fe(111) surface.

Species	**Ni(111)**	**Ni4Fe(111)**
*CH_4	8.3	19.1
*CO	59.7	58.1
*H_2O from *H_2O+*CO	20.99	23.51
*H_2O from *H_2O+*HCO	20.50	18.56
*H_2O from *H_2O+*CH	14.83	13.10
*H_2O (orange pathway in Fig. S14)	14.77	13.09
*H_2O from *H_2O+*O	20.6	19.8

Figure S14. Energy diagram for the removal of *O via water formation at (*CH+*O) and (*O) states on Ni(111) and Ni4Fe(111).

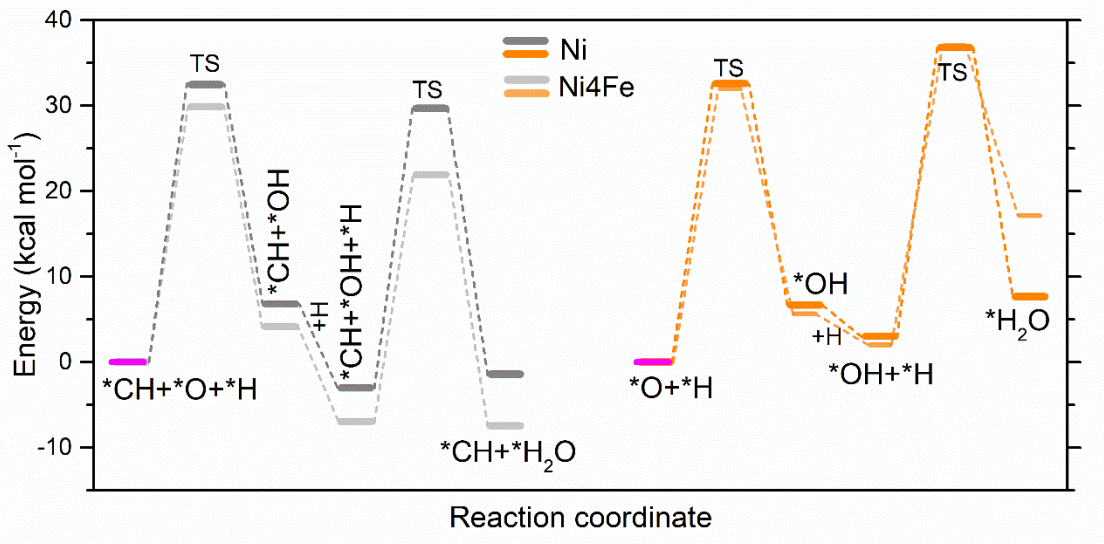

Table S5. *XYZ* coordination of intermediate species on Ni4Fe(111) and Ni(111).

Ni4Fe_CO_2_H				Ni4Fe _COOH				Ni4Fe_CO_OH			
Ni	1.29866	0.62816	2.07070	Ni	1.29866	0.62816	2.07070	Ni	1.29866	0.62816	2.07070
Ni	6.28049	2.06795	4.08652	Ni	6.27672	2.06763	4.08821	Ni	6.26984	2.06556	4.10200
Ni	1.30722	0.58265	8.08554	Ni	1.30932	0.61411	8.16320	Ni	1.29399	0.61787	8.09229
Ni	0.05274	1.34132	0.09651	Ni	0.05274	1.34132	0.09651	Ni	0.05274	1.34132	0.09651
Ni	0.05648	1.34560	6.09757	Ni	0.06249	1.33103	6.11192	Ni	0.04276	1.34035	6.09391
Ni	3.79044	0.62816	2.07070	Ni	3.79044	0.62816	2.07070	Ni	3.79044	0.62816	2.07070
Ni	1.29683	2.06530	4.09469	Ni	1.29519	2.06634	4.10116	Ni	1.29085	2.06569	4.09778
Ni	3.81885	0.59631	8.09877	Ni	3.81855	0.61275	8.10158	Ni	3.78143	0.65024	8.16208
Ni	2.54451	1.34132	0.09651	Ni	2.54451	1.34132	0.09651	Ni	2.54451	1.34132	0.09651
Ni	2.54541	1.35880	6.12796	Ni	2.54388	1.35188	6.13246	Ni	2.54246	1.35239	6.12374
Ni	6.28221	0.62816	2.07070	Ni	6.28221	0.62816	2.07070	Ni	6.28221	0.62816	2.07070
Ni	3.78906	2.06621	4.09047	Ni	3.78779	2.06672	4.10735	Ni	3.78603	2.06472	4.10059
Ni	6.30625	0.60764	8.09258	Ni	6.31036	0.62033	8.10411	Ni	6.32374	0.62512	8.14773
Ni	5.03629	1.34132	0.09651	Ni	5.03629	1.34132	0.09651	Ni	5.03629	1.34132	0.09651
Ni	5.04451	1.34029	6.08097	Ni	5.04305	1.34255	6.10714	Ni	5.02141	1.33472	6.11867
Ni	0.05278	2.78610	2.07070	Ni	0.05278	2.78610	2.07070	Ni	0.05278	2.78610	2.07070
Ni	5.03491	4.21825	4.09215	Ni	5.03240	4.22363	4.08793	Ni	5.02769	4.21728	4.09356
Ni	0.06149	2.75263	8.17446	Ni	0.06276	2.77671	8.13900	Ni	0.06070	2.74169	8.17389
Ni	-1.19315	3.49927	0.09651	Ni	-1.19315	3.49927	0.09651	Ni	-1.19315	3.49927	0.09651
Ni	-1.19068	3.49499	6.10854	Ni	-1.19468	3.50024	6.10686	Ni	-1.20089	3.50037	6.12683
Fe	2.54455	2.78610	2.07070	Fe	2.54455	2.78610	2.07070	Fe	2.54455	2.78610	2.07070
Fe	0.07124	4.21191	4.10453	Fe	0.05913	4.21942	4.09412	Fe	0.05438	4.22065	4.12142
Fe	2.58739	2.76564	8.34920	Fe	2.58772	2.78189	8.19894	Fe	2.56877	2.77665	8.17192
Fe	1.29863	3.49927	0.09651	Fe	1.29863	3.49927	0.09651	Fe	1.29863	3.49927	0.09651
Fe	1.32300	3.48191	6.19380	Fe	1.29964	3.50231	6.13190	Fe	1.28928	3.51027	6.14737
Ni	5.03633	2.78610	2.07070	Ni	5.03633	2.78610	2.07070	Ni	5.03633	2.78610	2.07070
Ni	2.54485	4.22046	4.09637	Ni	2.54354	4.22428	4.09440	Ni	2.53928	4.22570	4.09834
Ni	5.07284	2.77128	8.10158	Ni	5.04847	2.77309	8.11818	Ni	5.05905	2.77069	8.16348
Ni	3.79040	3.49927	0.09651	Ni	3.79040	3.49927	0.09651	Ni	3.79040	3.49927	0.09651
Ni	3.78046	3.49409	6.13021	Ni	3.78693	3.49687	6.12486	Ni	3.78562	3.49538	6.11895
Fe	-1.19315	4.94411	2.07070	Fe	-1.19315	4.94411	2.07070	Fe	-1.19315	4.94411	2.07070
Fe	3.78109	6.38578	4.05895	Fe	3.77930	6.38707	4.06148	Fe	3.77538	6.38338	4.07161
Fe	-1.15637	4.91899	8.16489	Fe	-1.15955	4.91426	8.15335	Fe	-1.22170	4.91459	8.25128
Ni	-2.43904	5.65721	0.09651	Ni	-2.43904	5.65721	0.09651	Ni	-2.43904	5.65721	0.09651
Fe	-2.43051	5.65125	6.08491	Fe	-2.43182	5.65533	6.10854	Fe	-2.42446	5.64283	6.12149
Ni	1.29863	4.94411	2.07070	Ni	1.29863	4.94411	2.07070	Ni	1.29863	4.94411	2.07070
Ni	-1.18836	6.38312	4.09328	Ni	-1.19461	6.39005	4.09356	Ni	-1.19539	6.38714	4.09834
Ni	1.32845	4.94838	8.09792	Ni	1.31788	4.93342	8.12550	Ni	1.36348	4.92048	8.19106
Ni	0.05274	5.65721	0.09651	Ni	0.05274	5.65721	0.09651	Ni	0.05274	5.65721	0.09651
Ni	0.05237	5.65928	6.10404	Ni	0.05528	5.65436	6.09588	Ni	0.04179	5.65973	6.13978
Ni	3.79040	4.94411	2.07070	Ni	3.79040	4.94411	2.07070	Ni	3.79040	4.94411	2.07070
Ni	1.29537	6.38215	4.08456	Ni	1.29575	6.38604	4.08793	Ni	1.29205	6.38235	4.10847
Ni	3.80711	4.94145	8.10439	Ni	3.80109	4.94074	8.12550	Ni	3.80868	4.93019	8.11537
Ni	2.54451	5.65721	0.09651	Ni	2.54451	5.65721	0.09651	Ni	2.54451	5.65721	0.09651
Ni	2.55113	5.65882	6.09138	Ni	2.55532	5.66219	6.10629	Ni	2.53110	5.65442	6.13359
C	0.59407	2.80462	10.03581	C	0.33770	2.77969	10.00513	C	6.22708	2.01092	15.11646
O	1.87285	2.80870	10.19366	O	1.74633	2.76189	10.28905	O	6.23564	1.99765	16.31487
O	-0.33688	2.80779	10.81580	O	-0.43283	2.81808	10.93792	O	0.10335	5.67948	9.55098
H	4.12074	1.87341	9.07713	H	1.89924	2.79018	11.26179	H	0.21675	5.74771	10.51275

Ni4Fe_CO_H_2O				Ni4Fe_HCO				Ni4Fe_HCOO			
Ni	1.29866	0.62816	2.07070	Ni	1.29866	0.62816	2.07070	Ni	1.29866	0.62816	2.07070
Ni	6.27339	2.07080	4.10678	Ni	6.27429	2.06601	4.10341	Ni	6.27422	2.07054	4.10144
Ni	1.30382	0.61275	8.12015	Ni	1.30891	0.60693	8.12522	Ni	1.30023	0.60693	8.12156
Ni	0.05274	1.34132	0.09651	Ni	0.05274	1.34132	0.09651	Ni	0.05274	1.34132	0.09651
Ni	0.05375	1.33440	6.10489	Ni	0.04511	1.33912	6.12486	Ni	0.05764	1.33763	6.09785
Ni	3.79044	0.62816	2.07070	Ni	3.79044	0.62816	2.07070	Ni	3.79044	0.62816	2.07070
Ni	1.29209	2.06394	4.09412	Ni	1.29037	2.06316	4.10059	Ni	1.29414	2.06400	4.09328
Ni	3.78375	0.61722	8.10946	Ni	3.78068	0.61217	8.11255	Ni	3.77878	0.61340	8.10355
Ni	2.54451	1.34132	0.09651	Ni	2.54451	1.34132	0.09651	Ni	2.54451	1.34132	0.09651
Ni	2.54059	1.34993	6.11530	Ni	2.53838	1.34728	6.11952	Ni	2.55431	1.36204	6.12092
Ni	6.28221	0.62816	2.07070	Ni	6.28221	0.62816	2.07070	Ni	6.28221	0.62816	2.07070
Ni	3.78543	2.06627	4.09862	Ni	3.78696	2.06595	4.10650	Ni	3.79014	2.06899	4.10453
Ni	6.29354	0.60699	8.18628	Ni	6.28464	0.54549	8.19162	Ni	6.30333	0.59327	8.09454
Ni	5.03629	1.34132	0.09651	Ni	5.03629	1.34132	0.09651	Ni	5.03629	1.34132	0.09651
Ni	5.04231	1.33504	6.10517	Ni	5.04313	1.34100	6.12683	Ni	5.03846	1.35259	6.12402
Ni	0.05278	2.78610	2.07070	Ni	0.05278	2.78610	2.07070	Ni	0.05278	2.78610	2.07070
Ni	5.02560	4.22402	4.10059	Ni	5.02496	4.22136	4.09609	Ni	5.02795	4.22175	4.10369
Ni	0.05633	2.75160	8.17783	Ni	0.01988	2.76759	8.20907	Ni	0.08713	2.75781	8.11762
Ni	-1.19315	3.49927	0.09651	Ni	-1.19315	3.49927	0.09651	Ni	-1.19315	3.49927	0.09651
Ni	-1.19408	3.49959	6.12852	Ni	-1.19905	3.48593	6.11108	Ni	-1.21001	3.49428	6.13893
Fe	2.54455	2.78610	2.07070	Fe	2.54455	2.78610	2.07070	Fe	2.54455	2.78610	2.07070
Fe	0.05371	4.22078	4.11523	Fe	0.05536	4.21858	4.10960	Fe	0.05823	4.21592	4.11776
Fe	2.56077	2.76681	8.17361	Fe	2.55591	2.75684	8.17024	Fe	2.52833	2.77289	8.29292
Fe	1.29863	3.49927	0.09651	Fe	1.29863	3.49927	0.09651	Fe	1.29863	3.49927	0.09651
Fe	1.30259	3.50043	6.13162	Fe	1.30023	3.49881	6.13640	Fe	1.30573	3.49434	6.14625
Ni	5.03633	2.78610	2.07070	Ni	5.03633	2.78610	2.07070	Ni	5.03633	2.78610	2.07070
Ni	2.53992	4.22512	4.09356	Ni	2.53894	4.22939	4.10088	Ni	2.54358	4.22292	4.10144
Ni	5.04418	2.75684	8.15167	Ni	5.06716	2.78863	8.19022	Ni	5.07561	2.73088	8.21329
Ni	3.79040	3.49927	0.09651	Ni	3.79040	3.49927	0.09651	Ni	3.79040	3.49927	0.09651
Ni	3.78782	3.49324	6.12064	Ni	3.78651	3.49214	6.12711	Ni	3.78779	3.48800	6.15188
Fe	-1.19315	4.94411	2.07070	Fe	-1.19315	4.94411	2.07070	Fe	-1.19315	4.94411	2.07070
Fe	3.77261	6.38701	4.07077	Fe	3.77149	6.38765	4.07189	Fe	3.77605	6.38765	4.06289
Fe	-1.16601	4.94113	8.30586	Fe	-1.16956	4.94417	8.16827	Fe	-1.17184	4.92753	8.18093
Ni	-2.43904	5.65721	0.09651	Ni	-2.43904	5.65721	0.09651	Ni	-2.43904	5.65721	0.09651
Fe	-2.41810	5.63986	6.14400	Fe	-2.43896	5.64801	6.11755	Fe	-2.43866	5.65267	6.12318
Ni	1.29863	4.94411	2.07070	Ni	1.29863	4.94411	2.07070	Ni	1.29863	4.94411	2.07070
Ni	-1.19995	6.38455	4.10059	Ni	-1.20010	6.38519	4.09440	Ni	-1.19988	6.38675	4.09581
Ni	1.31888	4.92158	8.13197	Ni	1.30221	4.89905	8.13197	Ni	1.29078	4.96275	8.12325
Ni	0.05274	5.65721	0.09651	Ni	0.05274	5.65721	0.09651	Ni	0.05274	5.65721	0.09651
Ni	0.04829	5.65662	6.13274	Ni	0.05360	5.65999	6.10826	Ni	0.04665	5.66517	6.10292
Ni	3.79040	4.94411	2.07070	Ni	3.79040	4.94411	2.07070	Ni	3.79040	4.94411	2.07070
Ni	1.28794	6.38196	4.10538	Ni	1.29160	6.38584	4.10453	Ni	1.29067	6.38720	4.09609
Ni	3.77926	4.92857	8.12859	Ni	3.79377	4.90669	8.13197	Ni	3.77650	4.93608	8.10524
Ni	2.54451	5.65721	0.09651	Ni	2.54451	5.65721	0.09651	Ni	2.54451	5.65721	0.09651
Ni	2.55251	5.66174	6.11473	Ni	2.54825	5.66964	6.13387	Ni	2.54668	5.65708	6.09307
C	6.22764	1.99933	9.46685	C	-1.24592	2.39197	9.69449	C	3.94937	2.78850	10.79610
O	-1.22967	2.14409	10.67370	O	6.26166	1.15034	10.05804	O	5.05961	2.77348	10.18213
O	-1.30610	4.95304	16.06359	H	-1.24275	3.11905	10.53048	O	2.78735	2.79944	10.27695
H	-1.30319	4.01316	16.37790					H	3.99840	2.78837	11.89884
H	-2.20536	5.29350	16.24171								

Ni4Fe_HCO_O				Ni4Fe_HCO_OH				Ni4Fe_HCO_H_2O			
Ni	1.29866	0.62816	2.07070	Ni	1.29866	0.62816	2.07070	Ni	1.29866	0.62816	2.07070
Ni	6.27665	2.06349	4.10059	Ni	6.27242	2.06174	4.09919	Ni	6.26913	2.06264	4.10003
Ni	1.28741	0.62059	8.13253	Ni	1.27732	0.60285	8.11227	Ni	1.26682	0.59722	8.11509
Ni	0.05274	1.34132	0.09651	Ni	0.05274	1.34132	0.09651	Ni	0.05274	1.34132	0.09651
Ni	0.04145	1.33420	6.13105	Ni	0.03655	1.32909	6.12064	Ni	0.04866	1.33815	6.09841
Ni	3.79044	0.62816	2.07070	Ni	3.79044	0.62816	2.07070	Ni	3.79044	0.62816	2.07070
Ni	1.29130	2.06077	4.10482	Ni	1.29003	2.06375	4.10678	Ni	1.29377	2.06129	4.10172
Ni	3.79085	0.55183	8.12325	Ni	3.74207	0.64266	8.15645	Ni	3.79739	0.58828	8.20738
Ni	2.54451	1.34132	0.09651	Ni	2.54451	1.34132	0.09651	Ni	2.54451	1.34132	0.09651
Ni	2.54620	1.35602	6.15919	Ni	2.55038	1.35317	6.15272	Ni	2.55147	1.35375	6.15807
Ni	6.28221	0.62816	2.07070	Ni	6.28221	0.62816	2.07070	Ni	6.28221	0.62816	2.07070
Ni	3.78334	2.06705	4.10847	Ni	3.78360	2.06375	4.10847	Ni	3.78622	2.06310	4.11101
Ni	6.28588	0.64227	8.19218	Ni	6.32210	0.63781	8.15926	Ni	6.29156	0.60913	8.10833
Ni	5.03629	1.34132	0.09651	Ni	5.03629	1.34132	0.09651	Ni	5.03629	1.34132	0.09651
Ni	5.03307	1.34119	6.10573	Ni	5.03218	1.33873	6.11924	Ni	5.02452	1.33919	6.14203
Ni	0.05278	2.78610	2.07070	Ni	0.05278	2.78610	2.07070	Ni	0.05278	2.78610	2.07070
Ni	5.02564	4.22292	4.09694	Ni	5.02485	4.21948	4.09412	Ni	5.02463	4.22052	4.09469
Ni	0.08653	2.76765	8.13169	Ni	0.04616	2.75095	8.11509	Ni	0.03674	2.74888	8.12437
Ni	-1.19315	3.49927	0.09651	Ni	-1.19315	3.49927	0.09651	Ni	-1.19315	3.49927	0.09651
Ni	-1.19741	3.49680	6.09166	Ni	-1.20204	3.49176	6.08800	Ni	-1.20952	3.49046	6.09335
Fe	2.54455	2.78610	2.07070	Fe	2.54455	2.78610	2.07070	Fe	2.54455	2.78610	2.07070
Fe	0.06294	4.21722	4.10847	Fe	0.06507	4.21677	4.11438	Fe	0.06096	4.21845	4.11410
Fe	2.56672	2.77166	8.35285	Fe	2.48213	2.72201	8.30249	Fe	2.47806	2.74111	8.26956
Fe	1.29863	3.49927	0.09651	Fe	1.29863	3.49927	0.09651	Fe	1.29863	3.49927	0.09651
Fe	1.30763	3.48975	6.14597	Fe	1.30666	3.49933	6.16116	Fe	1.30023	3.49557	6.14147
Ni	5.03633	2.78610	2.07070	Ni	5.03633	2.78610	2.07070	Ni	5.03633	2.78610	2.07070
Ni	2.54167	4.22829	4.10059	Ni	2.54044	4.22693	4.10425	Ni	2.54175	4.22725	4.10116
Ni	5.08634	2.84514	8.11030	Ni	5.04963	2.81692	8.14913	Ni	5.03603	2.80539	8.17361
Ni	3.79040	3.49927	0.09651	Ni	3.79040	3.49927	0.09651	Ni	3.79040	3.49927	0.09651
Ni	3.76913	3.49182	6.13331	Ni	3.77130	3.49441	6.12486	Ni	3.77440	3.49706	6.12908
Fe	-1.19315	4.94411	2.07070	Fe	-1.19315	4.94411	2.07070	Fe	-1.19315	4.94411	2.07070
Fe	3.77493	6.38830	4.06880	Fe	3.77078	6.38785	4.06880	Fe	3.77171	6.38610	4.06430
Fe	-1.15850	4.91608	8.17868	Fe	-1.17446	4.91756	8.11424	Fe	-1.16882	4.91245	8.11480
Ni	-2.43904	5.65721	0.09651	Ni	-2.43904	5.65721	0.09651	Ni	-2.43904	5.65721	0.09651
Fe	-2.43257	5.65326	6.11755	Fe	-2.44076	5.65539	6.09138	Fe	-2.44143	5.65487	6.09841
Ni	1.29863	4.94411	2.07070	Ni	1.29863	4.94411	2.07070	Ni	1.29863	4.94411	2.07070
Ni	-1.19872	6.39160	4.10059	Ni	-1.19805	6.38940	4.09750	Ni	-1.19692	6.38798	4.09947
Ni	1.33496	4.88494	8.09708	Ni	1.30046	4.88500	8.15420	Ni	1.31062	4.91970	8.10918
Ni	0.05274	5.65721	0.09651	Ni	0.05274	5.65721	0.09651	Ni	0.05274	5.65721	0.09651
Ni	0.04698	5.66730	6.10348	Ni	0.05648	5.66497	6.10657	Ni	0.04990	5.67702	6.11924
Ni	3.79040	4.94411	2.07070	Ni	3.79040	4.94411	2.07070	Ni	3.79040	4.94411	2.07070
Ni	1.29235	6.38260	4.09694	Ni	1.28973	6.38338	4.09440	Ni	1.28880	6.38539	4.09919
Ni	3.79870	4.97324	8.11115	Ni	3.83002	4.92093	8.17164	Ni	3.79930	4.93090	8.20710
Ni	2.54451	5.65721	0.09651	Ni	2.54451	5.65721	0.09651	Ni	2.54451	5.65721	0.09651
Ni	2.54440	5.67423	6.11839	Ni	2.54635	5.65572	6.12458	Ni	2.55218	5.65416	6.12064
C	4.62219	2.25136	10.09574	C	4.27413	3.73686	9.65706	C	4.21026	3.72669	9.66241
H	5.38091	2.74085	10.72351	H	4.94965	4.09635	10.45844	H	4.89306	4.05867	10.46970
O	3.39843	2.69631	10.14611	O	3.18011	3.16275	10.10193	O	3.12132	3.11336	10.13316
O	4.88813	0.98617	9.75330	O	1.29089	6.39601	9.47191	O	3.81709	0.55546	10.32535
				H	1.30113	6.46230	10.43987	H	-0.67439	6.45932	10.56762
								H	3.50921	1.49139	10.50487

Ni4Fe_CH_O				Ni4Fe_CH_OH				Ni4Fe_CH_H_2O			
Ni	1.29866	0.62816	2.07070	Ni	1.29866	0.62816	2.07070	Ni	1.29866	0.62816	2.07070
Ni	6.27493	2.06530	4.11945	Ni	6.27317	2.06329	4.10904	Ni	6.27291	2.06478	4.11101
Ni	1.34116	0.60350	8.13197	Ni	1.30449	0.59100	8.12690	Ni	1.30020	0.59482	8.12268
Ni	0.05274	1.34132	0.09651	Ni	0.05274	1.34132	0.09651	Ni	0.05274	1.34132	0.09651
Ni	0.03498	1.33673	6.15441	Ni	0.03812	1.33090	6.13865	Ni	0.03670	1.33220	6.13246
Ni	3.79044	0.62816	2.07070	Ni	3.79044	0.62816	2.07070	Ni	3.79044	0.62816	2.07070
Ni	1.29261	2.06666	4.11298	Ni	1.28730	2.05993	4.10763	Ni	1.28861	2.05947	4.10538
Ni	3.85585	0.62894	8.32275	Ni	3.73321	0.63612	8.18825	Ni	3.72481	0.63904	8.22961
Ni	2.54451	1.34132	0.09651	Ni	2.54451	1.34132	0.09651	Ni	2.54451	1.34132	0.09651
Ni	2.55890	1.33297	6.14934	Ni	2.55322	1.33414	6.13668	Ni	2.55356	1.33537	6.13556
Ni	6.28221	0.62816	2.07070	Ni	6.28221	0.62816	2.07070	Ni	6.28221	0.62816	2.07070
Ni	3.79066	2.06614	4.12001	Ni	3.78584	2.06258	4.10650	Ni	3.78752	2.06174	4.10847
Ni	6.41931	0.58220	8.23524	Ni	6.32396	0.66642	8.31177	Ni	6.34187	0.64784	8.29967
Ni	5.03629	1.34132	0.09651	Ni	5.03629	1.34132	0.09651	Ni	5.03629	1.34132	0.09651
Ni	5.03506	1.33492	6.15694	Ni	5.03763	1.33291	6.13753	Ni	5.03905	1.33252	6.14315
Ni	0.05278	2.78610	2.07070	Ni	0.05278	2.78610	2.07070	Ni	0.05278	2.78610	2.07070
Ni	5.02952	4.22279	4.09891	Ni	5.02369	4.22136	4.09075	Ni	5.02381	4.22143	4.09075
Ni	0.07046	2.73438	8.28392	Ni	0.09288	2.75872	8.16517	Ni	0.08085	2.77011	8.14097
Ni	-1.19315	3.49927	0.09651	Ni	-1.19315	3.49927	0.09651	Ni	-1.19315	3.49927	0.09651
Ni	-1.19177	3.49130	6.12515	Ni	-1.19248	3.49201	6.09870	Ni	-1.20507	3.49428	6.10770
Fe	2.54455	2.78610	2.07070	Fe	2.54455	2.78610	2.07070	Fe	2.54455	2.78610	2.07070
Fe	0.05678	4.22466	4.11720	Fe	0.05379	4.22194	4.10791	Fe	0.05132	4.22259	4.10960
Fe	2.55763	2.76629	8.15701	Fe	2.56051	2.75380	8.13647	Fe	2.52104	2.77490	8.11424
Fe	1.29863	3.49927	0.09651	Fe	1.29863	3.49927	0.09651	Fe	1.29863	3.49927	0.09651
Fe	1.29638	3.51519	6.15525	Fe	1.31403	3.50911	6.10545	Fe	1.30939	3.51415	6.09250
Ni	5.03633	2.78610	2.07070	Ni	5.03633	2.78610	2.07070	Ni	5.03633	2.78610	2.07070
Ni	2.53786	4.23528	4.09750	Ni	2.53760	4.23120	4.08484	Ni	2.53917	4.22926	4.08315
Ni	5.00497	2.84106	8.14322	Ni	5.02721	2.81679	8.15842	Ni	5.03633	2.81044	8.21301
Ni	3.79040	3.49927	0.09651	Ni	3.79040	3.49927	0.09651	Ni	3.79040	3.49927	0.09651
Ni	3.78771	3.49875	6.12008	Ni	3.77997	3.49816	6.10348	Ni	3.78438	3.49454	6.10714
Fe	-1.19315	4.94411	2.07070	Fe	-1.19315	4.94411	2.07070	Fe	-1.19315	4.94411	2.07070
Fe	3.77283	6.39633	4.09018	Fe	3.77130	6.38824	4.07583	Fe	3.77108	6.38875	4.07246
Fe	-1.16381	4.94029	8.20175	Fe	-1.19397	4.91640	8.18037	Fe	-1.19715	4.92786	8.17558
Ni	-2.43904	5.65721	0.09651	Ni	-2.43904	5.65721	0.09651	Ni	-2.43904	5.65721	0.09651
Fe	-2.42794	5.64743	6.11811	Fe	-2.43235	5.64730	6.11305	Fe	-2.43537	5.64983	6.10939
Ni	1.29863	4.94411	2.07070	Ni	1.29863	4.94411	2.07070	Ni	1.29863	4.94411	2.07070
Ni	-1.19517	6.39063	4.10088	Ni	-1.20006	6.38707	4.09750	Ni	-1.19958	6.38623	4.09666
Ni	1.32102	4.90520	8.15420	Ni	1.32513	4.84888	8.13788	Ni	1.31814	4.85412	8.12803
Ni	0.05274	5.65721	0.09651	Ni	0.05274	5.65721	0.09651	Ni	0.05274	5.65721	0.09651
Ni	0.05592	5.67320	6.15919	Ni	0.05532	5.65636	6.12149	Ni	0.05210	5.66841	6.13077
Ni	3.79040	4.94411	2.07070	Ni	3.79040	4.94411	2.07070	Ni	3.79040	4.94411	2.07070
Ni	1.29014	6.38914	4.11804	Ni	1.28966	6.38649	4.10819	Ni	1.28895	6.38552	4.11016
Ni	3.79679	4.90753	8.13900	Ni	3.79855	4.93025	8.10890	Ni	3.80038	4.93342	8.10017
Ni	2.54451	5.65721	0.09651	Ni	2.54451	5.65721	0.09651	Ni	2.54451	5.65721	0.09651
Ni	2.54926	5.67074	6.14428	Ni	2.54179	5.66841	6.12965	Ni	2.54216	5.66543	6.12318
C	6.05840	2.10006	9.38525	C	-1.18108	2.25712	9.35120	C	-1.11129	2.21705	9.36302
O	5.17485	0.50924	9.60923	H	-1.26080	2.24268	10.44662	H	-1.17188	2.15833	10.45732
H	-1.20193	2.27382	10.45985	O	1.19883	6.24096	9.50540	O	1.25901	6.20185	9.51215
				H	1.19049	6.21771	10.47504	H	1.31586	6.11582	10.47673
								H	3.80012	2.11929	9.10105

Ni4Fe_CH_2_O				Ni4Fe_CH_3_O				Ni4Fe_CH_4_O			
Ni	1.29866	0.62816	2.07070	Ni	1.29866	0.62816	2.07070	Ni	1.29866	0.62816	2.07070
Ni	6.27145	2.06575	4.10847	Ni	6.27152	2.06420	4.10313	Ni	6.27380	2.06349	4.10031
Ni	1.29422	0.61761	8.11227	Ni	1.30094	0.63820	8.10355	Ni	1.29773	0.62356	8.11255
Ni	0.05274	1.34132	0.09651	Ni	0.05274	1.34132	0.09651	Ni	0.05274	1.34132	0.09651
Ni	0.03555	1.33886	6.13471	Ni	0.04496	1.33200	6.11586	Ni	0.04354	1.33873	6.12515
Ni	3.79044	0.62816	2.07070	Ni	3.79044	0.62816	2.07070	Ni	3.79044	0.62816	2.07070
Ni	1.28446	2.06239	4.09722	Ni	1.28996	2.06608	4.09469	Ni	1.29044	2.06653	4.10088
Ni	3.73052	0.62952	8.18571	Ni	3.76185	0.62978	8.20035	Ni	3.76775	0.64389	8.20457
Ni	2.54451	1.34132	0.09651	Ni	2.54451	1.34132	0.09651	Ni	2.54451	1.34132	0.09651
Ni	2.54336	1.34489	6.12177	Ni	2.54803	1.34171	6.12008	Ni	2.54354	1.34819	6.13753
Ni	6.28221	0.62816	2.07070	Ni	6.28221	0.62816	2.07070	Ni	6.28221	0.62816	2.07070
Ni	3.78711	2.06452	4.10622	Ni	3.78756	2.06349	4.10285	Ni	3.78521	2.06459	4.10341
Ni	6.31073	0.64894	8.33372	Ni	6.32329	0.63561	8.18881	Ni	6.32438	0.64189	8.19078
Ni	5.03629	1.34132	0.09651	Ni	5.03629	1.34132	0.09651	Ni	5.03629	1.34132	0.09651
Ni	5.03928	1.33407	6.13640	Ni	5.03532	1.34573	6.13359	Ni	5.03345	1.33459	6.11333
Ni	0.05278	2.78610	2.07070	Ni	0.05278	2.78610	2.07070	Ni	0.05278	2.78610	2.07070
Ni	5.02388	4.22324	4.09215	Ni	5.02601	4.22227	4.09018	Ni	5.02810	4.21864	4.09047
Ni	0.06537	2.78940	8.13366	Ni	0.08215	2.75943	8.10524	Ni	0.06605	2.76312	8.12268
Ni	-1.19315	3.49927	0.09651	Ni	-1.19315	3.49927	0.09651	Ni	-1.19315	3.49927	0.09651
Ni	-1.19902	3.49739	6.10686	Ni	-1.20137	3.49551	6.10460	Ni	-1.20130	3.50224	6.10742
Fe	2.54455	2.78610	2.07070	Fe	2.54455	2.78610	2.07070	Fe	2.54455	2.78610	2.07070
Fe	0.05296	4.22311	4.10763	Fe	0.05547	4.22382	4.11185	Fe	0.05820	4.22453	4.11663
Fe	2.54160	2.77529	8.12015	Fe	2.53984	2.75878	8.12522	Fe	2.55995	2.77315	8.18346
Fe	1.29863	3.49927	0.09651	Fe	1.29863	3.49927	0.09651	Fe	1.29863	3.49927	0.09651
Fe	1.30958	3.50529	6.09898	Fe	1.29549	3.50936	6.13105	Fe	1.29283	3.50788	6.15103
Ni	5.03633	2.78610	2.07070	Ni	5.03633	2.78610	2.07070	Ni	5.03633	2.78610	2.07070
Ni	2.54339	4.22894	4.09412	Ni	2.54025	4.23166	4.10116	Ni	2.53969	4.23017	4.10144
Ni	5.02276	2.83122	8.17277	Ni	5.04746	2.79309	8.13703	Ni	5.04040	2.79821	8.08976
Ni	3.79040	3.49927	0.09651	Ni	3.79040	3.49927	0.09651	Ni	3.79040	3.49927	0.09651
Ni	3.79324	3.49460	6.12430	Ni	3.77904	3.49719	6.10911	Ni	3.77302	3.49765	6.11305
Fe	-1.19315	4.94411	2.07070	Fe	-1.19315	4.94411	2.07070	Fe	-1.19315	4.94411	2.07070
Fe	3.76917	6.38934	4.07583	Fe	3.76869	6.38655	4.07640	Fe	3.77287	6.38746	4.07611
Fe	-1.20376	4.94346	8.17896	Fe	-1.19042	4.91543	8.15476	Fe	-1.20750	4.90267	8.16067
Ni	-2.43904	5.65721	0.09651	Ni	-2.43904	5.65721	0.09651	Ni	-2.43904	5.65721	0.09651
Fe	-2.43563	5.65857	6.10798	Fe	-2.43575	5.65229	6.11361	Fe	-2.43395	5.65552	6.11276
Ni	1.29863	4.94411	2.07070	Ni	1.29863	4.94411	2.07070	Ni	1.29863	4.94411	2.07070
Ni	-1.19939	6.38888	4.09497	Ni	-1.19861	6.38584	4.09778	Ni	-1.19236	6.38966	4.10144
Ni	1.31799	4.88856	8.18234	Ni	1.29508	4.89005	8.24959	Ni	1.31257	4.89821	8.24987
Ni	0.05274	5.65721	0.09651	Ni	0.05274	5.65721	0.09651	Ni	0.05274	5.65721	0.09651
Ni	0.05222	5.65954	6.11276	Ni	0.05255	5.66400	6.12515	Ni	0.04799	5.66387	6.14034
Ni	3.79040	4.94411	2.07070	Ni	3.79040	4.94411	2.07070	Ni	3.79040	4.94411	2.07070
Ni	1.29149	6.38668	4.10791	Ni	1.29018	6.38468	4.10763	Ni	1.29040	6.38493	4.10031
Ni	3.80169	4.94786	8.10974	Ni	3.81649	4.93103	8.15138	Ni	3.81522	4.92779	8.10608
Ni	2.54451	5.65721	0.09651	Ni	2.54451	5.65721	0.09651	Ni	2.54451	5.65721	0.09651
Ni	2.54093	5.66860	6.13021	Ni	2.54537	5.65403	6.14428	Ni	2.53050	5.66297	6.12740
C	-1.11597	2.22708	9.48570	O	1.30932	6.40047	9.32869	O	1.30805	6.40436	9.33347
O	1.19169	6.30809	9.33713	C	5.02493	4.19022	9.72854	C	-1.17158	4.88047	11.17259
H	-0.57362	2.08945	10.43171	H	-1.56068	4.67149	10.20126	H	-0.16162	4.91679	11.59945
H	5.30413	2.53433	9.86163	H	4.14047	4.69590	10.17565	H	-1.93534	4.86105	11.96215
				H	5.01558	3.13977	10.11431	H	-1.27411	3.96642	10.56256
								H	-1.32487	5.78416	10.55833

Ni4Fe_CO_O				Ni_CO_2_H				Ni _COOH			
Ni	1.29866	0.62816	2.07070	Ni	1.29866	0.62816	2.07070	Ni	1.29866	0.62816	2.07070
Ni	6.27549	2.06899	4.10285	Ni	-1.19214	2.07585	4.06824	Ni	-1.19427	2.07307	4.07668
Ni	1.31122	0.58660	8.10524	Ni	1.32012	0.61897	8.13225	Ni	1.32987	0.63651	8.05487
Ni	0.05274	1.34132	0.09651	Ni	0.05274	1.34132	0.09651	Ni	0.05274	1.34132	0.09651
Ni	0.04807	1.35201	6.12430	Ni	0.05868	1.36431	6.06915	Ni	0.04638	1.36398	6.07506
Ni	3.79044	0.62816	2.07070	Ni	3.79044	0.62816	2.07070	Ni	3.79044	0.62816	2.07070
Ni	1.29040	2.06439	4.10144	Ni	1.30169	2.07177	4.07414	Ni	1.29840	2.07669	4.07611
Ni	3.78782	0.60952	8.10073	Ni	3.83559	0.62505	8.04249	Ni	3.78394	0.64499	8.07035
Ni	2.54451	1.34132	0.09651	Ni	2.54451	1.34132	0.09651	Ni	2.54451	1.34132	0.09651
Ni	2.54066	1.35343	6.11839	Ni	2.54160	1.36256	6.08744	Ni	2.54313	1.36638	6.06915
Ni	6.28221	0.62816	2.07070	Ni	6.28221	0.62816	2.07070	Ni	6.28221	0.62816	2.07070
Ni	3.78494	2.06737	4.09947	Ni	3.78786	2.07242	4.07837	Ni	3.79044	2.07559	4.07386
Ni	6.28311	0.61612	8.15307	Ni	6.28857	0.63904	8.05965	Ni	6.27833	0.62259	8.16883
Ni	5.03629	1.34132	0.09651	Ni	5.03629	1.34132	0.09651	Ni	5.03629	1.34132	0.09651
Ni	5.03756	1.34003	6.09532	Ni	5.04474	1.36243	6.06437	Ni	5.04776	1.35770	6.08744
Ni	0.05278	2.78610	2.07070	Ni	0.05278	2.78610	2.07070	Ni	0.05278	2.78610	2.07070
Ni	5.02665	4.22026	4.09919	Ni	5.02399	4.23897	4.07077	Ni	-2.44307	4.23463	4.06852
Ni	0.03850	2.75593	8.29799	Ni	0.01155	2.81595	8.07288	Ni	0.05379	2.81025	8.12212
Ni	-1.19315	3.49927	0.09651	Ni	-1.19315	3.49927	0.09651	Ni	-1.19315	3.49927	0.09651
Ni	-1.18736	3.49027	6.12655	Ni	-1.20470	3.52885	6.04973	Ni	-1.18952	3.51448	6.06859
Fe	2.54455	2.78610	2.07070	Ni	2.54455	2.78610	2.07070	Ni	2.54455	2.78610	2.07070
Fe	0.05457	4.21916	4.11298	Ni	0.05162	4.23179	4.07105	Ni	0.05289	4.23191	4.07527
Fe	2.61127	2.73360	8.23355	Ni	2.57382	2.77840	8.16320	Ni	2.54044	2.81226	8.07091
Fe	1.29863	3.49927	0.09651	Ni	1.29863	3.49927	0.09651	Ni	1.29863	3.49927	0.09651
Fe	1.30225	3.49946	6.15075	Ni	1.29937	3.51157	6.07140	Ni	1.28827	3.51797	6.07590
Ni	5.03633	2.78610	2.07070	Ni	5.03633	2.78610	2.07070	Ni	5.03633	2.78610	2.07070
Ni	2.53951	4.22583	4.10172	Ni	2.54534	4.23075	4.07386	Ni	2.54829	4.23612	4.07133
Ni	5.05397	2.75697	8.15870	Ni	5.05460	2.79368	8.06753	Ni	5.00908	2.83356	8.05206
Ni	3.79040	3.49927	0.09651	Ni	3.79040	3.49927	0.09651	Ni	3.79040	3.49927	0.09651
Ni	3.78607	3.48994	6.13105	Ni	3.77384	3.50800	6.09870	Ni	3.78775	3.51979	6.07028
Fe	-1.19315	4.94411	2.07070	Ni	-1.19315	4.94411	2.07070	Ni	-1.19315	4.94411	2.07070
Fe	3.77239	6.38882	4.07246	Ni	-3.68175	6.38927	4.07443	Ni	-3.68814	6.38791	4.07527
Fe	-1.20163	4.94676	8.18093	Ni	-1.17738	4.94993	8.05909	Ni	3.78726	6.38791	4.07527
Ni	-2.43904	5.65721	0.09651	Ni	-2.43904	5.65721	0.09651	Ni	-1.19154	4.96605	8.06950
Fe	-2.43773	5.65222	6.10601	Ni	-2.43945	5.69754	6.09841	Ni	-2.43904	5.65721	0.09651
Ni	1.29863	4.94411	2.07070	Ni	1.29863	4.94411	2.07070	Ni	-2.44393	5.67825	6.07309
Ni	-1.19775	6.38565	4.09581	Ni	-1.19644	6.38817	4.07471	Ni	1.29863	4.94411	2.07070
Ni	1.30408	4.96301	8.21498	Ni	1.29960	4.96677	8.07738	Ni	-1.19292	6.39011	4.07105
Ni	0.05274	5.65721	0.09651	Ni	0.05274	5.65721	0.09651	Ni	1.29171	4.95673	8.07344
Ni	0.06119	5.65992	6.12036	Ni	0.05887	5.66976	6.06521	Ni	0.05274	5.65721	0.09651
Ni	3.79040	4.94411	2.07070	Ni	3.79040	4.94411	2.07070	Ni	0.05483	5.67598	6.07281
Ni	1.29063	6.38131	4.10003	Ni	1.29859	6.38992	4.06936	Ni	3.79040	4.94411	2.07070
Ni	3.81395	4.93893	8.10946	Ni	3.81324	4.96450	8.07513	Ni	1.30035	6.39063	4.07696
Ni	2.54451	5.65721	0.09651	Ni	2.54451	5.65721	0.09651	Ni	3.78965	4.95654	8.07485
Ni	2.53857	5.66180	6.12346	Ni	2.54586	5.67456	6.06802	Ni	2.54451	5.65721	0.09651
C	6.12676	1.95343	9.53157	C	0.49895	2.43684	9.86782	Ni	2.54037	5.69236	6.09982
O	6.11439	1.92372	10.72097	O	1.61637	1.71785	9.80226	C	-0.31756	2.29719	9.86191
O	1.41636	3.50561	9.37146	O	-0.10989	2.83388	10.83437	O	0.04638	3.04227	10.92132
				H	2.58245	4.30436	8.96261	O	6.54849	1.22117	10.10587
								H	0.50194	3.82717	10.54483

Ni_CO_OH				Ni_CO_H_2O				Ni_HCO			
Ni	1.29866	0.62816	2.07070	Ni	1.29866	0.62816	2.07070	Ni	1.29866	0.62816	2.07070
Ni	-1.19532	2.07566	4.07499	Ni	-1.19397	2.07514	4.07668	Ni	-1.19311	2.07378	4.07330
Ni	1.28973	0.65464	8.03658	Ni	1.30722	0.65412	8.04474	Ni	1.31223	0.65231	8.05571
Ni	0.05274	1.34132	0.09651	Ni	0.05274	1.34132	0.09651	Ni	0.05274	1.34132	0.09651
Ni	0.05061	1.36444	6.05086	Ni	0.04878	1.36023	6.06071	Ni	0.04261	1.36327	6.08125
Ni	3.79044	0.62816	2.07070	Ni	3.79044	0.62816	2.07070	Ni	3.79044	0.62816	2.07070
Ni	1.30038	2.07702	4.07246	Ni	1.29934	2.07533	4.06992	Ni	1.29762	2.07546	4.07611
Ni	3.77149	0.67341	8.11115	Ni	3.77829	0.65153	8.05797	Ni	3.77627	0.65257	8.05515
Ni	2.54451	1.34132	0.09651	Ni	2.54451	1.34132	0.09651	Ni	2.54451	1.34132	0.09651
Ni	2.55483	1.36178	6.07478	Ni	2.54646	1.36359	6.06409	Ni	2.54448	1.36470	6.06859
Ni	6.28221	0.62816	2.07070	Ni	6.28221	0.62816	2.07070	Ni	6.28221	0.62816	2.07070
Ni	3.79040	2.07501	4.07133	Ni	3.79029	2.07495	4.06852	Ni	3.79100	2.07553	4.07611
Ni	6.30853	0.65833	8.10186	Ni	6.28685	0.63852	8.14322	Ni	6.28221	0.58336	8.14041
Ni	5.03629	1.34132	0.09651	Ni	5.03629	1.34132	0.09651	Ni	5.03629	1.34132	0.09651
Ni	5.02803	1.35952	6.07759	Ni	5.03879	1.35809	6.06521	Ni	5.04593	1.36321	6.07928
Ni	0.05278	2.78610	2.07070	Ni	0.05278	2.78610	2.07070	Ni	0.05278	2.78610	2.07070
Ni	-2.43941	4.23191	4.07189	Ni	-2.43810	4.23172	4.07499	Ni	-2.44079	4.23211	4.07161
Ni	0.05461	2.77568	8.10327	Ni	0.06182	2.78908	8.09933	Ni	0.02344	2.82074	8.13619
Ni	-1.19315	3.49927	0.09651	Ni	-1.19315	3.49927	0.09651	Ni	-1.19315	3.49927	0.09651
Ni	-1.19476	3.52963	6.07844	Ni	-1.19259	3.52963	6.08603	Ni	-1.19311	3.51694	6.06549
Ni	2.54455	2.78610	2.07070	Ni	2.54455	2.78610	2.07070	Ni	2.54455	2.78610	2.07070
Ni	0.05390	4.22991	4.07668	Ni	0.05214	4.23217	4.07668	Ni	0.05416	4.23243	4.07105
Ni	2.54949	2.80772	8.05684	Ni	2.54676	2.80908	8.06584	Ni	2.54380	2.80669	8.06922
Ni	1.29863	3.49927	0.09651	Ni	1.29863	3.49927	0.09651	Ni	1.29863	3.49927	0.09651
Ni	1.29777	3.52820	6.08491	Ni	1.29803	3.51856	6.06971	Ni	1.29343	3.51448	6.07731
Ni	5.03633	2.78610	2.07070	Ni	5.03633	2.78610	2.07070	Ni	5.03633	2.78610	2.07070
Ni	2.54298	4.23353	4.06739	Ni	2.54436	4.23256	4.06373	Ni	2.54407	4.23515	4.07021
Ni	5.03569	2.80248	8.11002	Ni	5.03035	2.78817	8.09933	Ni	5.06544	2.82074	8.13394
Ni	3.79040	3.49927	0.09651	Ni	3.79040	3.49927	0.09651	Ni	3.79040	3.49927	0.09651
Ni	3.79395	3.51784	6.06746	Ni	3.79302	3.51726	6.06662	Ni	3.79481	3.51428	6.07731
Ni	-1.19315	4.94411	2.07070	Ni	-1.19315	4.94411	2.07070	Ni	-1.19315	4.94411	2.07070
Ni	-3.68627	6.38791	4.07274	Ni	-3.68496	6.38694	4.07499	Ni	-3.68784	6.39011	4.07499
Ni	-1.22996	4.95997	8.11509	Ni	-1.19322	4.98295	8.17277	Ni	-1.19337	4.99991	8.04615
Ni	-2.43904	5.65721	0.09651	Ni	-2.43904	5.65721	0.09651	Ni	-2.43904	5.65721	0.09651
Ni	-2.43418	5.66886	6.07562	Ni	-2.43033	5.66879	6.08350	Ni	-2.44502	5.67818	6.06493
Ni	1.29863	4.94411	2.07070	Ni	1.29863	4.94411	2.07070	Ni	1.29863	4.94411	2.07070
Ni	-1.19494	6.39115	4.07302	Ni	-1.19259	6.38824	4.07330	Ni	-1.19349	6.39057	4.06908
Ni	1.33238	4.94119	8.12240	Ni	1.31175	4.95841	8.06359	Ni	1.28715	4.94106	8.06838
Ni	0.05274	5.65721	0.09651	Ni	0.05274	5.65721	0.09651	Ni	0.05274	5.65721	0.09651
Ni	0.05532	5.67721	6.06915	Ni	0.04298	5.66698	6.09279	Ni	0.05838	5.67838	6.06493
Ni	3.79040	4.94411	2.07070	Ni	3.79040	4.94411	2.07070	Ni	3.79040	4.94411	2.07070
Ni	1.30109	6.39024	4.07640	Ni	1.29702	6.38681	4.07640	Ni	1.30109	6.38998	4.07443
Ni	3.79171	4.95906	8.05740	Ni	3.77896	4.95952	8.05177	Ni	3.80038	4.94158	8.06866
Ni	2.54451	5.65721	0.09651	Ni	2.54451	5.65721	0.09651	Ni	2.54451	5.65721	0.09651
Ni	2.53696	5.67430	6.08491	Ni	2.54291	5.68291	6.07421	Ni	2.54429	5.68271	6.09166
C	-1.20055	2.09469	15.04724	C	-1.19162	2.06562	9.39369	C	-1.20563	2.43250	9.62274
O	-1.20918	2.10485	16.24846	O	-1.19431	2.22126	10.60110	O	6.27732	1.19586	10.00120
O	0.06249	5.67514	9.45559	O	-1.27508	5.05636	15.92178	H	-1.20272	3.18062	10.44297
H	0.09217	5.67747	10.42721	H	-1.25258	4.12387	16.24790				
				H	-2.17983	5.37630	16.10580				

Ni_HCOO				Ni_HCO_O				Ni_HCO_OH			
Ni	1.29866	0.62816	2.07070	Ni	1.29866	0.62816	2.07070	Ni	1.29866	0.62816	2.07070
Ni	-1.19420	2.07397	4.07049	Ni	-1.19356	2.07197	4.07330	Ni	-1.19266	2.07236	4.07189
Ni	1.27287	0.64279	8.04587	Ni	1.28061	0.63431	8.05121	Ni	1.27852	0.62926	8.05712
Ni	0.05274	1.34132	0.09651	Ni	0.05274	1.34132	0.09651	Ni	0.05274	1.34132	0.09651
Ni	0.05091	1.36366	6.06240	Ni	0.04029	1.35628	6.07872	Ni	0.03547	1.35246	6.08519
Ni	3.79044	0.62816	2.07070	Ni	3.79044	0.62816	2.07070	Ni	3.79044	0.62816	2.07070
Ni	1.30173	2.07495	4.07808	Ni	1.29788	2.07488	4.07133	Ni	1.29784	2.07443	4.07949
Ni	3.80199	0.63871	8.16123	Ni	3.75964	0.64965	8.12184	Ni	3.74618	0.65613	8.09286
Ni	2.54451	1.34132	0.09651	Ni	2.54451	1.34132	0.09651	Ni	2.54451	1.34132	0.09651
Ni	2.55700	1.36670	6.10067	Ni	2.54848	1.36890	6.09335	Ni	2.55255	1.36547	6.10151
Ni	6.28221	0.62816	2.07070	Ni	6.28221	0.62816	2.07070	Ni	6.28221	0.62816	2.07070
Ni	3.78962	2.07430	4.07696	Ni	3.78850	2.07210	4.07921	Ni	3.78764	2.07229	4.07893
Ni	6.28943	0.65568	8.06078	Ni	6.30658	0.66195	8.15279	Ni	6.31899	0.66921	8.12296
Ni	5.03629	1.34132	0.09651	Ni	5.03629	1.34132	0.09651	Ni	5.03629	1.34132	0.09651
Ni	5.02377	1.35589	6.08125	Ni	5.03550	1.36871	6.08153	Ni	5.03554	1.36748	6.08041
Ni	0.05278	2.78610	2.07070	Ni	0.05278	2.78610	2.07070	Ni	0.05278	2.78610	2.07070
Ni	-2.44109	4.23159	4.07105	Ni	-2.43956	4.23269	4.06852	Ni	-2.43982	4.23224	4.06795
Ni	0.03738	2.81420	8.06078	Ni	0.02919	2.80144	8.05065	Ni	0.02504	2.80177	8.05768
Ni	-1.19315	3.49927	0.09651	Ni	-1.19315	3.49927	0.09651	Ni	-1.19315	3.49927	0.09651
Ni	-1.19349	3.52108	6.06409	Ni	-1.19244	3.51927	6.05199	Ni	-1.19277	3.51895	6.05058
Ni	2.54455	2.78610	2.07070	Ni	2.54455	2.78610	2.07070	Ni	2.54455	2.78610	2.07070
Ni	0.05379	4.23230	4.07583	Ni	0.05835	4.23347	4.07049	Ni	0.05887	4.23256	4.06964
Ni	2.53521	2.82482	8.16602	Ni	2.49103	2.77251	8.13281	Ni	2.48923	2.76875	8.14238
Ni	1.29863	3.49927	0.09651	Ni	1.29863	3.49927	0.09651	Ni	1.29863	3.49927	0.09651
Ni	1.31092	3.51228	6.08857	Ni	1.30704	3.51901	6.09504	Ni	1.30730	3.52244	6.10179
Ni	5.03633	2.78610	2.07070	Ni	5.03633	2.78610	2.07070	Ni	5.03633	2.78610	2.07070
Ni	2.54283	4.23185	4.07218	Ni	2.54070	4.23321	4.07921	Ni	2.54081	4.23211	4.07865
Ni	5.05292	2.82637	8.04587	Ni	5.03648	2.85848	8.10918	Ni	5.03528	2.85214	8.10383
Ni	3.79040	3.49927	0.09651	Ni	3.79040	3.49927	0.09651	Ni	3.79040	3.49927	0.09651
Ni	3.77343	3.51545	6.08209	Ni	3.78491	3.52043	6.06465	Ni	3.78480	3.52011	6.06634
Ni	-1.19315	4.94411	2.07070	Ni	-1.19315	4.94411	2.07070	Ni	-1.19315	4.94411	2.07070
Ni	-3.68552	6.39050	4.06655	Ni	-3.68788	6.39238	4.07358	Ni	-3.68732	6.39245	4.07246
Ni	-1.20361	4.96133	8.06134	Ni	-1.19831	4.96431	8.02223	Ni	-1.19449	4.96599	8.01829
Ni	-2.43904	5.65721	0.09651	Ni	-2.43904	5.65721	0.09651	Ni	-2.43904	5.65721	0.09651
Ni	-2.43934	5.67792	6.06240	Ni	-2.44233	5.68103	6.05396	Ni	-2.44277	5.68051	6.05227
Ni	1.29863	4.94411	2.07070	Ni	1.29863	4.94411	2.07070	Ni	1.29863	4.94411	2.07070
Ni	-1.19106	6.39102	4.07865	Ni	-1.19098	6.39452	4.07161	Ni	-1.19121	6.39491	4.07105
Ni	1.29975	4.97039	8.05712	Ni	1.28614	4.93310	8.12634	Ni	1.28446	4.91569	8.09905
Ni	0.05274	5.65721	0.09651	Ni	0.05274	5.65721	0.09651	Ni	0.05274	5.65721	0.09651
Ni	0.05345	5.69016	6.08800	Ni	0.06059	5.68245	6.06127	Ni	0.06246	5.68297	6.06015
Ni	3.79040	4.94411	2.07070	Ni	3.79040	4.94411	2.07070	Ni	3.79040	4.94411	2.07070
Ni	1.29650	6.39044	4.07330	Ni	1.29971	6.39212	4.06964	Ni	1.30020	6.39232	4.06852
Ni	3.79369	4.98295	8.05937	Ni	3.83342	4.93757	8.11283	Ni	3.82651	4.93724	8.10749
Ni	2.54451	5.65721	0.09651	Ni	2.54451	5.65721	0.09651	Ni	2.54451	5.65721	0.09651
Ni	2.54328	5.67967	6.06409	Ni	2.54597	5.67643	6.08294	Ni	2.54549	5.67650	6.08209
C	3.17559	1.72730	10.68777	C	4.13947	3.71750	9.61289	C	4.14440	3.71789	9.60276
H	3.17794	1.72840	11.79473	H	4.78011	4.08755	10.44015	H	4.79760	4.08794	10.42243
O	2.60159	2.71385	10.12922	O	3.06633	3.09957	9.97503	O	3.07172	3.10138	9.99501
O	3.74802	0.74087	10.12782	O	1.29351	6.39950	9.25244	O	1.29309	6.40229	9.42577
								H	1.28577	6.41174	10.39682

Ni_HCO_H_2O				Ni_CH_O				Ni_CH_OH			
Ni	1.29866	0.62816	2.07070	Ni	1.29866	0.62816	2.07070	Ni	1.29866	0.62816	2.07070
Ni	-1.19677	2.07326	4.07218	Ni	-1.19446	2.07093	4.07977	Ni	-1.19363	2.07119	4.07837
Ni	1.26850	0.63341	8.05177	Ni	1.30767	0.64130	8.06162	Ni	1.30917	0.63457	8.06500
Ni	0.05274	1.34132	0.09651	Ni	0.05274	1.34132	0.09651	Ni	0.05274	1.34132	0.09651
Ni	0.04739	1.36405	6.06183	Ni	0.03760	1.35291	6.09166	Ni	0.03517	1.35013	6.09447
Ni	3.79044	0.62816	2.07070	Ni	3.79044	0.62816	2.07070	Ni	3.79044	0.62816	2.07070
Ni	1.30117	2.07346	4.07752	Ni	1.29556	2.07242	4.07189	Ni	1.29646	2.07164	4.08033
Ni	3.80401	0.62253	8.13844	Ni	3.74656	0.65548	8.15842	Ni	3.72649	0.65632	8.13028
Ni	2.54451	1.34132	0.09651	Ni	2.54451	1.34132	0.09651	Ni	2.54451	1.34132	0.09651
Ni	2.55532	1.36806	6.10404	Ni	2.55266	1.35751	6.08350	Ni	2.55913	1.35227	6.08969
Ni	6.28221	0.62816	2.07070	Ni	6.28221	0.62816	2.07070	Ni	6.28221	0.62816	2.07070
Ni	3.79078	2.07320	4.08090	Ni	3.78876	2.07346	4.07611	Ni	3.78962	2.07352	4.07668
Ni	6.29171	0.65186	8.07035	Ni	6.29350	0.68565	8.29179	Ni	6.32296	0.69536	8.26788
Ni	5.03629	1.34132	0.09651	Ni	5.03629	1.34132	0.09651	Ni	5.03629	1.34132	0.09651
Ni	5.02646	1.36392	6.10038	Ni	5.03588	1.36042	6.08941	Ni	5.03749	1.35855	6.09447
Ni	0.05278	2.78610	2.07070	Ni	0.05278	2.78610	2.07070	Ni	0.05278	2.78610	2.07070
Ni	-2.44019	4.23302	4.06992	Ni	-2.44038	4.23295	4.06767	Ni	-2.44064	4.23237	4.06655
Ni	0.01921	2.80552	8.05881	Ni	0.09412	2.81575	8.08413	Ni	0.09027	2.81452	8.09342
Ni	-1.19315	3.49927	0.09651	Ni	-1.19315	3.49927	0.09651	Ni	-1.19315	3.49927	0.09651
Ni	-1.20070	3.51830	6.05677	Ni	-1.18833	3.52212	6.05424	Ni	-1.18892	3.52134	6.05199
Ni	2.54455	2.78610	2.07070	Ni	2.54455	2.78610	2.07070	Ni	2.54455	2.78610	2.07070
Ni	0.05517	4.23405	4.06936	Ni	0.05678	4.23243	4.07302	Ni	0.05715	4.23140	4.07161
Ni	2.47989	2.78830	8.13563	Ni	2.55595	2.80585	8.04446	Ni	2.56074	2.80287	8.05206
Ni	1.29863	3.49927	0.09651	Ni	1.29863	3.49927	0.09651	Ni	1.29863	3.49927	0.09651
Ni	1.30401	3.51299	6.07984	Ni	1.30917	3.52568	6.06183	Ni	1.30853	3.52898	6.06746
Ni	5.03633	2.78610	2.07070	Ni	5.03633	2.78610	2.07070	Ni	5.03633	2.78610	2.07070
Ni	2.54306	4.23366	4.07499	Ni	2.54373	4.23897	4.05726	Ni	2.54362	4.23852	4.05726
Ni	5.02448	2.84987	8.13056	Ni	5.02732	2.84702	8.10833	Ni	5.02197	2.84450	8.10580
Ni	3.79040	3.49927	0.09651	Ni	3.79040	3.49927	0.09651	Ni	3.79040	3.49927	0.09651
Ni	3.78651	3.52361	6.06999	Ni	3.78592	3.52400	6.05621	Ni	3.78640	3.52406	6.05564
Ni	-1.19315	4.94411	2.07070	Ni	-1.19315	4.94411	2.07070	Ni	-1.19315	4.94411	2.07070
Ni	-3.68687	6.39102	4.06824	Ni	-3.68769	6.39128	4.07780	Ni	-3.68747	6.39180	4.07668
Ni	-1.18354	4.97020	8.02589	Ni	-1.22148	4.96910	8.05656	Ni	-1.22167	4.97084	8.04812
Ni	-2.43904	5.65721	0.09651	Ni	-2.43904	5.65721	0.09651	Ni	-2.43904	5.65721	0.09651
Ni	-2.44322	5.68051	6.05621	Ni	-2.44019	5.67993	6.06521	Ni	-2.44120	5.67792	6.06212
Ni	1.29863	4.94411	2.07070	Ni	1.29863	4.94411	2.07070	Ni	1.29863	4.94411	2.07070
Ni	-1.18922	6.39419	4.07330	Ni	-1.19266	6.39238	4.07471	Ni	-1.19292	6.39245	4.07330
Ni	1.29403	4.96592	8.04924	Ni	1.31141	4.89762	8.11030	Ni	1.30603	4.87756	8.08470
Ni	0.05274	5.65721	0.09651	Ni	0.05274	5.65721	0.09651	Ni	0.05274	5.65721	0.09651
Ni	0.05730	5.68789	6.07140	Ni	0.05771	5.67786	6.07281	Ni	0.05939	5.67702	6.07281
Ni	3.79040	4.94411	2.07070	Ni	3.79040	4.94411	2.07070	Ni	3.79040	4.94411	2.07070
Ni	1.29866	6.39342	4.07274	Ni	1.29900	6.39257	4.07696	Ni	1.29904	6.39316	4.07696
Ni	3.80715	4.95874	8.13478	Ni	3.80917	4.96262	8.04755	Ni	3.80120	4.96424	8.04502
Ni	2.54451	5.65721	0.09651	Ni	2.54451	5.65721	0.09651	Ni	2.54451	5.65721	0.09651
Ni	2.55147	5.67702	6.07759	Ni	2.53857	5.68912	6.08491	Ni	2.53644	5.68906	6.08519
C	4.09820	3.75039	9.60219	C	-1.15480	2.29227	9.27692	C	-1.16437	2.29098	9.28029
H	4.77054	4.09363	10.41736	H	-1.21950	2.30801	10.37572	H	-1.22548	2.29700	10.38078
O	3.01808	3.12592	10.03299	O	1.20556	6.28614	9.28114	O	1.21430	6.25572	9.45419
O	3.72656	0.58369	15.86944					H	1.19861	6.17686	10.42158
H	-0.73592	6.42514	16.03742								
H	3.35253	1.49825	16.03264								

Ni_CH_H_2O				Ni_CH_2_O				Ni_CH_3_O			
Ni	1.29866	0.62816	2.07070	Ni	1.29866	0.62816	2.07070	Ni	1.29866	0.62816	2.07070
Ni	-1.19648	2.07287	4.07865	Ni	-1.19599	2.07190	4.07724	Ni	-1.19498	2.07197	4.07499
Ni	1.30367	0.64059	8.05374	Ni	1.30008	0.65056	8.04727	Ni	1.29765	0.66862	8.03939
Ni	0.05274	1.34132	0.09651	Ni	0.05274	1.34132	0.09651	Ni	0.05274	1.34132	0.09651
Ni	0.05012	1.36761	6.06662	Ni	0.03203	1.35699	6.08913	Ni	0.04268	1.35641	6.07309
Ni	3.79044	0.62816	2.07070	Ni	3.79044	0.62816	2.07070	Ni	3.79044	0.62816	2.07070
Ni	1.30087	2.07410	4.07443	Ni	1.29328	2.07378	4.06992	Ni	1.29825	2.07462	4.06570
Ni	3.77377	0.64486	8.15392	Ni	3.72970	0.66202	8.13394	Ni	3.76020	0.66461	8.13844
Ni	2.54451	1.34132	0.09651	Ni	2.54451	1.34132	0.09651	Ni	2.54451	1.34132	0.09651
Ni	2.55393	1.36101	6.08688	Ni	2.54691	1.36165	6.07421	Ni	2.55311	1.35634	6.07337
Ni	6.28221	0.62816	2.07070	Ni	6.28221	0.62816	2.07070	Ni	6.28221	0.62816	2.07070
Ni	3.79085	2.07475	4.07752	Ni	3.79059	2.07326	4.07808	Ni	3.79126	2.07197	4.07499
Ni	6.29526	0.63548	8.13141	Ni	6.30169	0.68015	8.29376	Ni	6.31077	0.66441	8.13957
Ni	5.03629	1.34132	0.09651	Ni	5.03629	1.34132	0.09651	Ni	5.03629	1.34132	0.09651
Ni	5.02851	1.35906	6.09447	Ni	5.03857	1.35693	6.09419	Ni	5.03577	1.36515	6.08828
Ni	0.05278	2.78610	2.07070	Ni	0.05278	2.78610	2.07070	Ni	0.05278	2.78610	2.07070
Ni	-2.44019	4.23159	4.07189	Ni	-2.44057	4.23276	4.06852	Ni	-2.43978	4.23230	4.06683
Ni	0.06754	2.81828	8.14970	Ni	0.06298	2.84197	8.06190	Ni	0.06818	2.79775	8.03967
Ni	-1.19315	3.49927	0.09651	Ni	-1.19315	3.49927	0.09651	Ni	-1.19315	3.49927	0.09651
Ni	-1.19031	3.51920	6.06746	Ni	-1.19210	3.52218	6.05592	Ni	-1.19408	3.51966	6.06268
Ni	2.54455	2.78610	2.07070	Ni	2.54455	2.78610	2.07070	Ni	2.54455	2.78610	2.07070
Ni	0.05379	4.23295	4.07527	Ni	0.05782	4.23204	4.07218	Ni	0.05360	4.23405	4.07555
Ni	2.54253	2.82274	8.06162	Ni	2.53558	2.81122	8.04249	Ni	2.52706	2.79763	8.03967
Ni	1.29863	3.49927	0.09651	Ni	1.29863	3.49927	0.09651	Ni	1.29863	3.49927	0.09651
Ni	1.29937	3.51765	6.06465	Ni	1.30565	3.52658	6.06380	Ni	1.29799	3.52924	6.07421
Ni	5.03633	2.78610	2.07070	Ni	5.03633	2.78610	2.07070	Ni	5.03633	2.78610	2.07070
Ni	2.54511	4.23373	4.05670	Ni	2.55012	4.23438	4.06570	Ni	2.54253	4.23405	4.07583
Ni	5.03685	2.82469	8.13000	Ni	5.01637	2.85977	8.10411	Ni	5.03547	2.82682	8.07879
Ni	3.79040	3.49927	0.09651	Ni	3.79040	3.49927	0.09651	Ni	3.79040	3.49927	0.09651
Ni	3.79029	3.52264	6.07056	Ni	3.79780	3.51597	6.07787	Ni	3.78992	3.51966	6.06296
Ni	-1.19315	4.94411	2.07070	Ni	-1.19315	4.94411	2.07070	Ni	-1.19315	4.94411	2.07070
Ni	-3.68563	6.39070	4.07049	Ni	-3.68937	6.39277	4.07555	Ni	-3.68806	6.39024	4.07471
Ni	-1.19976	4.97887	8.05206	Ni	-1.22754	4.98541	8.04277	Ni	-1.21038	4.95621	8.07485
Ni	-2.43904	5.65721	0.09651	Ni	-2.43904	5.65721	0.09651	Ni	-2.43904	5.65721	0.09651
Ni	-2.44229	5.67747	6.06634	Ni	-2.44397	5.68362	6.05789	Ni	-2.43978	5.67883	6.06127
Ni	1.29863	4.94411	2.07070	Ni	1.29863	4.94411	2.07070	Ni	1.29863	4.94411	2.07070
Ni	-1.19206	6.39147	4.07471	Ni	-1.19319	6.39316	4.07049	Ni	-1.19102	6.39018	4.07443
Ni	1.31160	4.95673	8.04390	Ni	1.30233	4.91077	8.11086	Ni	1.29773	4.92870	8.13985
Ni	0.05274	5.65721	0.09651	Ni	0.05274	5.65721	0.09651	Ni	0.05274	5.65721	0.09651
Ni	0.05610	5.68543	6.08153	Ni	0.05479	5.68122	6.06380	Ni	0.05050	5.67624	6.08744
Ni	3.79040	4.94411	2.07070	Ni	3.79040	4.94411	2.07070	Ni	3.79040	4.94411	2.07070
Ni	1.29851	6.39186	4.07752	Ni	1.30102	6.39089	4.07752	Ni	1.29818	6.39050	4.07471
Ni	3.79048	4.96819	8.07232	Ni	3.80214	4.97428	8.04755	Ni	3.80625	4.95550	8.07625
Ni	2.54451	5.65721	0.09651	Ni	2.54451	5.65721	0.09651	Ni	2.54451	5.65721	0.09651
Ni	2.54750	5.67831	6.06549	Ni	2.53894	5.68912	6.08660	Ni	2.54567	5.67630	6.08800
C	-1.19573	2.07961	9.27270	C	-1.10180	2.26651	9.41085	O	1.29721	6.40138	9.27073
H	6.22286	2.05229	10.37262	O	1.19464	6.31217	9.27073	C	-2.43934	4.24616	9.61908
O	3.61208	0.33813	15.99437	H	-0.53696	2.14894	10.34899	H	-1.54565	4.76834	10.03749
H	0.36861	5.96348	15.97580	H	5.33220	2.60613	9.79635	H	4.14077	4.76374	10.04115
H	2.67081	0.05956	15.96483					H	5.03902	3.21959	10.05635

Ni_CH_4_O				Ni_CO_O			
Ni	1.29866	0.62816	2.07070	Ni	1.29866	0.62816	2.07070
Ni	-1.19334	2.07223	4.07640	Ni	-1.19595	2.07715	4.07105
Ni	1.29788	0.64286	8.08667	Ni	1.29010	0.65192	8.10130
Ni	0.05274	1.34132	0.09651	Ni	0.05274	1.34132	0.09651
Ni	0.05248	1.35822	6.08181	Ni	0.05237	1.36411	6.05396
Ni	3.79044	0.62816	2.07070	Ni	3.79044	0.62816	2.07070
Ni	1.29855	2.07216	4.07640	Ni	1.30035	2.07579	4.07386
Ni	3.78969	0.64292	8.08667	Ni	3.79795	0.61541	8.04840
Ni	2.54451	1.34132	0.09651	Ni	2.54451	1.34132	0.09651
Ni	2.54429	1.35816	6.08181	Ni	2.54137	1.37434	6.08209
Ni	6.28221	0.62816	2.07070	Ni	6.28221	0.62816	2.07070
Ni	3.79029	2.07223	4.07640	Ni	3.78995	2.07423	4.07724
Ni	6.28150	0.64286	8.08667	Ni	6.26782	0.64182	8.04924
Ni	5.03629	1.34132	0.09651	Ni	5.03629	1.34132	0.09651
Ni	5.03603	1.35822	6.08181	Ni	5.03760	1.37246	6.07450
Ni	0.05278	2.78610	2.07070	Ni	0.05278	2.78610	2.07070
Ni	-2.43919	4.23010	4.07640	Ni	-2.43896	4.23373	4.07049
Ni	0.05195	2.80086	8.08667	Ni	0.05270	2.79724	8.09764
Ni	-1.19315	3.49927	0.09651	Ni	-1.19315	3.49927	0.09651
Ni	-1.19341	3.51616	6.08181	Ni	-1.19588	3.51370	6.08125
Ni	2.54455	2.78610	2.07070	Ni	2.54455	2.78610	2.07070
Ni	0.05263	4.23017	4.07640	Ni	0.05237	4.23036	4.07274
Ni	2.54373	2.80086	8.08667	Ni	2.52011	2.79180	8.23439
Ni	1.29863	3.49927	0.09651	Ni	1.29863	3.49927	0.09651
Ni	1.29836	3.51616	6.08153	Ni	1.30790	3.51325	6.08238
Ni	5.03633	2.78610	2.07070	Ni	5.03633	2.78610	2.07070
Ni	2.54440	4.23017	4.07640	Ni	2.54395	4.23250	4.07611
Ni	5.03558	2.80086	8.08667	Ni	5.06843	2.78643	8.14182
Ni	3.79040	3.49927	0.09651	Ni	3.79040	3.49927	0.09651
Ni	3.79014	3.51616	6.08181	Ni	3.78696	3.51985	6.07281
Ni	-1.19315	4.94411	2.07070	Ni	-1.19315	4.94411	2.07070
Ni	-3.68507	6.38817	4.07640	Ni	-3.68429	6.38785	4.07077
Ni	-1.19393	4.95880	8.08667	Ni	-1.16504	4.98243	8.04727
Ni	-2.43904	5.65721	0.09651	Ni	-2.43904	5.65721	0.09651
Ni	-2.43937	5.67410	6.08181	Ni	-2.44707	5.68084	6.08266
Ni	1.29863	4.94411	2.07070	Ni	1.29863	4.94411	2.07070
Ni	-1.19334	6.38811	4.07640	Ni	-1.19554	6.39141	4.07386
Ni	1.29788	4.95887	8.08667	Ni	1.27418	4.99085	8.04474
Ni	0.05274	5.65721	0.09651	Ni	0.05274	5.65721	0.09651
Ni	0.05248	5.67410	6.08181	Ni	0.05076	5.67708	6.05142
Ni	3.79040	4.94411	2.07070	Ni	3.79040	4.94411	2.07070
Ni	1.29851	6.38811	4.07640	Ni	1.29919	6.39109	4.06936
Ni	3.78969	4.95880	8.08667	Ni	3.78932	4.99972	8.14210
Ni	2.54451	5.65721	0.09651	Ni	2.54451	5.65721	0.09651
Ni	2.54421	5.67417	6.08181	Ni	2.55505	5.67572	6.07421
O	1.30805	6.40436	9.33347	C	1.15446	2.00231	9.46713
C	-1.17158	4.88047	11.17259	O	1.10651	1.98062	10.65682
H	-0.16162	4.91679	11.59945	O	3.86796	3.56951	9.28958
H	-1.93534	4.86105	11.96215				
H	-1.27411	3.96642	10.56256				
H	-1.32487	5.78416	10.55833				

Appendix D – Paper IV

Synthetic natural gas production from CO_2 and renewable H_2: Towards large-scale production of Ni-Fe alloy catalysts for commercialization

H. L. Huynh, W. M. Tucho, X. Yu, and Z. Yu

Journal of Cleaner Production **2020**, 121720

DOI: 10.1016/j.jclepro.2020.121720

Journal of Cleaner Production 264 (2020) 121720

Contents lists available at ScienceDirect

Journal of Cleaner Production

journal homepage: www.elsevier.com/locate/jclepro

Synthetic natural gas production from CO_2 and renewable H_2: Towards large-scale production of Ni–Fe alloy catalysts for commercialization

Huong Lan Huynh [a], Wakshum Mekonnen Tucho [b], Xinhai Yu [c], Zhixin Yu [a, *]

[a] Department of Energy and Petroleum Engineering, University of Stavanger, 4036, Stavanger, Norway
[b] Department of Mechanical and Structural Engineering and Material Science, University of Stavanger, 4036, Stavanger, Norway
[c] State Key Laboratory of Bioreactor Engineering, East China University of Science and Technology, 200237, Shanghai, China

ARTICLE INFO

Article history:
Received 18 January 2020
Received in revised form
9 March 2020
Accepted 13 April 2020
Available online 20 April 2020

Handling editor: Bin Chen

Keywords:
Power-to-Gas
CO_2 methanation
Ni–Fe alloy Catalyst
Hydrotalcite precursors
Space-time yield

ABSTRACT

Synthetic natural gas (SNG) is one of the promising energy carriers for the excessive electricity generated from variable renewable energy sources. SNG production from renewable H_2 and CO_2 via catalytic CO_2 methanation has gained much attention since CO_2 emissions could be simultaneously reduced. In this study, Ni–Fe/(Mg,Al)O_x alloy catalysts for CO_2 methanation were prepared via hydrotalcite precursors using a rapid coprecipitation method. The effect of total metal concentration on the physicochemical properties and catalytic behavior was investigated. Upon calcination, the catalysts showed high specific surface area of above 230 $m^2\ g^{-1}$. Small particle sizes of about 5 nm were obtained for all catalysts, even though the produced catalyst amount was increased by 10 times. The catalysts exhibited excellent space-time yield under very high gas space velocity (34,000 h^{-1}), irrespective of the metal concentration. The CO_2 conversions reached 73–79% at 300 °C and CH_4 selectivities were at 93–95%. Therefore, we demonstrated the potential of large-scale production of earth-abundant Ni–Fe based catalysts for CO_2 methanation and the Power-to-Gas technology.

1. Introduction

Fossil fuels including coal, oil, and natural gas have been our primary energy sources to supply the rising needs of heating, cooling, lighting, transportation, and other energy demands. However, fossil fuels are not replenished, and its combustion releases a massive amount of greenhouse gas CO_2 into the atmosphere, which is partially responsible for global warming and climate change (Rashid et al., 2019, 2020). Hence, the development of a sustainable low-carbon economy is urgently needed for our future energy system (Song, 2006). In recent years, the shift towards renewable energy sources (RES), like wind and solar energy, has substantially occurred. In the European power sector, for instance, RES are expected to contribute half of the total gross electricity generation in 2030 (Agora Energiewende and Sandbag, 2019). Clean energy produced from RES is practically unlimited but highly dependent on weather conditions. Consequently, the mismatch between energy supply and demand necessitates the development of large-scale and flexible energy storage technologies for the transformation of surplus electricity.

Synthetic or substitute natural gas (SNG), an effective energy carrier with high heating value, is one of the promising chemical compounds for energy storage (Rönsch et al., 2016). With the existing infrastructure including pipeline networks, storage facilities, and filling stations, SNG can be distributed and stored without additional expenses. This is an advantage of using SNG as energy carrier compared to hydrogen, for instance. Traditionally, SNG is produced from coke oven gas, or syngas from coal or wood, or biomass (Kopyscinski et al., 2010). Since the 1970s, considerable efforts have been devoted to the application of CO and CO_2 methanation reactions for the production of SNG.

$$CO_2 + 4H_2 \leftrightarrow CH_4 + 2H_2O \quad (1)$$

CO_2 methanation (Eq. (1)), known as the Sabatier reaction, has gained renewed attention due to the emerging Power-to-Gas concept. On the one hand, this technology can converge the value chains of both gas and electricity sectors into one energy system,

* Corresponding author.
E-mail address: zhixin.yu@uis.no (Z. Yu).

https://doi.org/10.1016/j.jclepro.2020.121720

Abbreviations

GHSV	Gas Hourly Space Velocity
HT	Hydrotalcite
LDH	Layered Double Hydroxides
RES	Renewable Energy Sources
RWGS	Reverse Water Gas Shift
SEM	Scanning Electron Microscopy
S_i	Product Selectivity
SMSI	Strong Metal-Support Interaction
SNG	Synthetic Natural Gas
STP	Standard Temperature and Pressure
STY	Space Time Yield
TEM	Transmission Electron Microscopy
TOS	Time On Stream
TPD	Temperature-Programmed Desorption
TPR	Temperature-Programmed Reduction
WHSV	Weight Hourly Space Velocity
X_{CO2}	CO_2 Conversion
XRD	X-Ray Diffraction

allowing flexible handling and storage of surplus renewable electricity. On the other hand, the process also tackles greenhouse gases emission by large-scale recycling of CO_2. Hydrogen (H_2) is produced via water electrolysis using renewable electricity, which further reacts with CO_2 (e.g., directly captured from the air) to form methane (CH_4). The produced SNG, also called renewable natural gas, can be used in natural gas end-use appliances, such as mobility and residential heating or being injected into the existing gas grid (Bailera et al., 2017).

Catalytic CO_2 methanation was discovered for more than a century by (Sabatier and Senderens, 1902). Although the reaction is thermodynamically favorable at low temperatures and elevated pressures, high activation energy is required to overcome the thermodynamic barrier of extremely stable CO_2 molecules (Vogt et al., 2019). Many different metals such as Ni, Co, Fe, Cu, Ru, Rh, Ir, Pd, and Pt have been exploited. Despite the fact that noble metals (i.e., Ru, Rh) are highly active and produce exclusively CH_4, Ni-based catalysts have always been the first choice for industrial catalysts due to its availability and affordable price (Aziz et al., 2015; Ghaib and Ben-Fares, 2018).

Rational design and synthesis of new catalytic materials play an important role in the enhancement of industrial process efficiency. Recently, by taking advantage of molecular simulations such as density functional theory, not only the kinetics of methanation reaction can be described but preliminary screening of new catalytic models can also be performed (Nørskov et al., 2009). According to the Pareto-optimal set, when both the catalytic activity and price of the catalysts were under consideration, nickel-iron (Ni_3Fe) alloys were found to be a promising candidate to substitute the noble-metal catalysts (e.g., Ru) with higher activity than each individual constituent in methanation (Andersson et al., 2006). Moreover, the Ni–Fe alloy catalysts are relatively cheaper than pure Ni catalysts. Many experimental studies have been carried out and confirmed the superiority of Ni–Fe alloy catalysts. It has also shown that the optimal compositions of Ni and Fe depend on the supports and metal loadings (Kustov et al., 2007). Ni–Fe alloys on Al_2O_3 were found to be less active than on $MgAl_2O_4$ for CO hydrogenation to CH_4 at 225 °C. Moreover, at a low metal loading of 2.5 wt%, the 75Ni25Fe alloy catalyst exhibited the highest conversion. Meanwhile, the 50Ni50Fe alloy catalyst performed better at a higher metal loading of 10 wt%. Different supports, namely Al_2O_3, ZrO_2, TiO_2, SiO_2, and Nb_2O_5 were investigated for CO_2 hydrogenation to CH_4 at 250 °C ($H_2/CO_2 = 24/1$). The Ni_3Fe alloy on Al_2O_3 support emerged as the best catalyst with the highest activity at total metal loading of both 10 wt% and 15 wt% (Pandey and Deo, 2016; Ray and Deo, 2017). In another study, unsupported Ni–Fe catalysts were also studied. It revealed that Ni–Fe alloy with Fe/Ni molar ratio of approximately 0.1 performed better than Ni_3Fe and monometallic catalysts (Pandey et al., 2018). Recently, it has been reported that the Fe/Ni molar ratio of 0.1 was the optimal composition of Ni–Fe/(Mg,Al)O_x catalysts for CO_2 methanation at 335 °C (Mebrahtu et al., 2018). It would be interesting to investigate the performance of Ni–Fe catalysts derived from HTs for CO_2 methanation over a wide temperature range for practical applications.

In the methanation unit of Power-to-Gas pilot plants, Ni-based catalysts are commonly used (Bailera et al., 2017). Besides the activity and selectivity, the main concern of Ni-based catalysts for industrial applications is catalyst deactivation, possibly due to metal sintering and/or carbon formation. CO_2 methanation is a highly exothermic reaction (Eq. (1), $\Delta H = -165.0$ kJ mol^{-1}). Thus, hotspots could possibly occur in the catalyst bed and cause thermal agglomeration of Ni active sites, which consequently reduced the catalysts' stability. To address these problems, it was recommended that well-defined crystalline structures like solid solution, spinel, perovskite, rigid mesoporous frameworks, or core-shell structures could be used to synthesize highly dispersed and stable Ni active sites. Reinforcing strong metal-support interaction (SMSI) was also suggested due to their ability to enhance not only the activity but also the stability of heterogeneous catalysts (Li et al., 2019). On the other hand, lowering CO_2 activation energy by enhanced chemisorption and dissociation of CO_2 could be achieved on the catalytic surfaces with strong basicity. The combination of alkaline oxides MgO and Al_2O_3 has been reported as the best catalytic support for CO_2 conversion reactions, due to its strong basicity and good thermal stability (Fan, M.-T. et al., 2014). Interestingly, the Lewis basic (Mg,Al)O_x mixed oxide can be derived from hydrotalcite-like materials (Bette et al., 2016).

Hydrotalcite (HT) materials, also called layered double hydroxides (LDH), have gained much attention for the synthesis of supported catalysts. The general formula for HT-like material is $[M^{2+}_{1-x}M^{3+}_x(OH)_2](A^{n-})_{x/n} \bullet mH_2O$, where M represents metals, and A is anion (Cavani et al., 1991). HT-like precursors offer access to well-dispersed and homogeneous metallic sites with SMSI after thermal decomposition and activation (i.e., calcination and reduction, respectively). Upon reduction, small and thermally stable metal nanoparticles were formed from the mixed metal oxides. Another compelling interest of this material is driven by its compositional flexibility with a wide choice of metal cations (Fan, G. et al., 2014). Conventionally, HT-like precursors are synthesized by coprecipitation method. The coprecipitation between the mixed salt solutions and the base solution was carried out by a slow addition rate (i.e., dropwise addition in several hours), leading to slow nucleation and simultaneous agglomeration (Othman et al., 2009). Recently, rapid coprecipitation for HT synthesis has been reported, where mixed salt solutions were quickly injected into a base solution within minutes (Tathod and Gazit, 2016). The nucleation rate was high with relatively slow crystal growth. Upon calcination, the obtained catalysts have small and uniform particle sizes as well as narrow pore size distribution, which are important features of catalysts prepared from HT precursors with rapid coprecipitation. This method was also considered as a highly efficient and facile procedure for HTs synthesis since it was fast and simple. Unfortunately, only small quantities of catalysts were produced from the original reported work, which focused on the fundamentals of nucleation and growth of HT crystals.

In this study, Ni–Fe/(Mg,Al)O_x HT-derived catalysts were prepared by rapid coprecipitation with Ni loading of 20 wt% and Fe loading of 2 wt%, corresponding to a Fe/Ni molar ratio of 0.1. The catalysts have been maintained at a Ni loading of 20 wt%, which is close to the loading of commercial Ni catalysts. The HT precursors with high purity and crystallinity were successfully synthesized in large quantities by rapid coprecipitation, which is more facile, energy-efficient and environmental-friendly compared to the conventional method. The catalysts were tested in CO_2 methanation in the temperature range of 200–450 °C and at a high space velocity of 34,000 h^{-1}. All Ni–Fe catalysts showed excellent activity, selectivity and high stability in CO_2 methanation. Moreover, we confirmed that large-scale production of HT-derived catalysts for the commercial application of CO_2 methanation was possible without interfering with the catalytic activity and stability. To the best of our knowledge, this is the first study to explore the upscale potential of Ni–Fe alloy catalysts via rapid coprecipitation for CO_2 methanation at industrial relevant conditions.

2. Experimental

2.1. Catalyst preparation

All reagents were analytical grade (Merck Millipore) and used as received without purification. The procedure was adapted from (Tathod and Gazit, 2016). In a typical preparation, mixed salt solutions consisting of $Ni(NO_3)_2.6H_2O$, $Fe(NO_3)_3.9H_2O$, $Mg(NO_3)_2.6H_2O$ and $Al(NO_3)_3.9H_2O$ with total metal concentration of 0.25M, 1M and 2.5M were used. 100 mL of the mixed salt solution was rapidly injected by a syringe into a 500 mL base solution containing a sufficient amount of NaOH and Na_2CO_3 under vigorous stirring at 60 °C. The suspension was then aged under flowing N_2 at 85 °C for 18 h. Subsequently, the gel-like mass was filtered, washed until the pH of the filtrate was neutral, and dried at 90 °C overnight. The dried precursors were calcined at 600 °C for 6 h in flowing synthetic air (heating rate of 5 K min^{-1}). In all catalysts, the Ni and Fe loading were kept constant at 20 wt% and 2 wt%, respectively, which corresponding to a Fe/Ni molar ratio of 0.1. The ratio between divalent and trivalent cations was fixed at 3. The catalysts were denoted as NiFe-*x*M, where *x* is the total metal concentration used during preparation.

The calcined samples were reduced and passivated for further characterization. The calcined catalysts were reduced at 600 °C for 4 h (heating rate of 5 K min^{-1}) under 50 vol% H_2/N_2 with a total flow of 100 mL min^{-1} (STP). Upon reduction, the samples were cooled down to room temperature in flowing N_2 (total flow of 50 mL min^{-1}, STP). Thereafter, synthetic air was added to adjust the oxygen content in the gas mixture to 0.1 vol% and then 1 vol% to passivate the catalysts.

2.2. Catalyst characterization

X-ray diffraction (XRD) patterns were recorded on a Bruker D8 Advance micro-diffractometer using CuKα radiation source in the 2θ range of 5-90° at a step interval of 1° min^{-1}. The *d*-spacing was calculated based on Bragg's law (Cullity, 1956). The average crystallite size *d* was calculated by the Scherrer equation (Eq. (2) (Cullity, 1956),), where K_F is the shape factor (0.9), λ is the wavelength of CuKα (1.5406 Å), θ is the diffraction angle of the peak and β represents the full width at half maximum of the peak (in radians).

$$d = \frac{K_F \times \lambda}{\beta \times cos\theta} \quad (2)$$

The N_2 adsorption-desorption isotherms were determined at −196 °C using Micromeritics Tristar 3000 instrument. Prior to measurement, the sample (~120 mg) was degassed overnight at 150 °C under vacuum. The surface area was calculated by the BET method in the pressure range of $0.05 < P/P_o < 0.3$. The pore volume and pore size distribution were calculated from the desorption branch of the isotherms by the BJH method.

Temperature programmed reduction (TPR) of the calcined catalysts and temperature-programmed desorption (TPD) of the reduced catalysts were carried out by Micromeritics Autochem II ASAP 2020 instrument equipped with a thermal conductivity detector (TCD). The calcined sample (~100 mg) was first degassed at 200 °C for 30 min and then reduced using 10 vol% H_2/Ar from 50 °C to 950 °C at a heating rate of 10 K min^{-1}. Subsequently, TPD measurement was conducted on the reduced sample by degassing at 600 °C in He for 30 min. A flow of 6 vol% CO_2/Ar was then introduced for 1 h. Weakly adsorbed CO_2 was desorbed by He flow for 1 h. The CO_2-TPD was recorded by heating up the sample to 800 °C under He flow at a heating rate of 10 K min^{-1}. The same equipment was also used to measure TPR data of reduced catalysts in order to determine the reduction degree (Eq. (3)) (Marocco et al., 2018).

$$Reduction\ degree\ f\ (\%) = \frac{TPR\ peak\ area\ of\ calcined\ sample - TPR\ peak\ area\ of\ reduced\ sample}{TPR\ peak\ area\ of\ calcined\ sample} \times 100 \quad (3)$$

H_2 chemisorption analysis was performed at 35 °C on Micromeritics ASAP 2020 Plus instrument. Calcined samples (~200 mg) were degassed in He flow at 200 °C for 2 h, reduced in H_2 flow at 600 °C for 4 h (heating rate of 5 K min^{-1}), and cooled down to 35 °C prior to measurement. The chemisorption of H_2 was assumed to occur only on Ni atom with an adsorption stoichiometry of one hydrogen atom per nickel atom. The dispersion of Ni active sites was calculated by Eq. (4) (Bartholomew, 1975), where n_{H2} is the mol of H_2 uptake in chemisorption study, w_{Ni} is weight percentage, *f* is the reduction degree and M_{Ni} is the molar mass of Ni.

$$Ni\ dispersion\ (\%) = \frac{number\ of\ Ni\ at\ surface}{total\ number\ of\ Ni} = \frac{2 \times n_{H2} \times M_{Ni}}{w_{Ni} \times f/100} \times 100 \quad (4)$$

The morphology of the precursors was examined using Gemini Supra 35VP (ZEISS) Scanning Electron Microscopy (SEM). The dried powder samples were spread on carbon tape and coated with Pd plasma to inhibit charging. Further analyses were performed using JEM-2100F (JEOL) Transmission Electron Microscopy (TEM) working at 200 kV. The reduced-passivated powder samples were dissolved in ethanol, assisted by ultrasonic dispersion. A drop of the suspension was deposited on a holey carbon-coated copper grid.

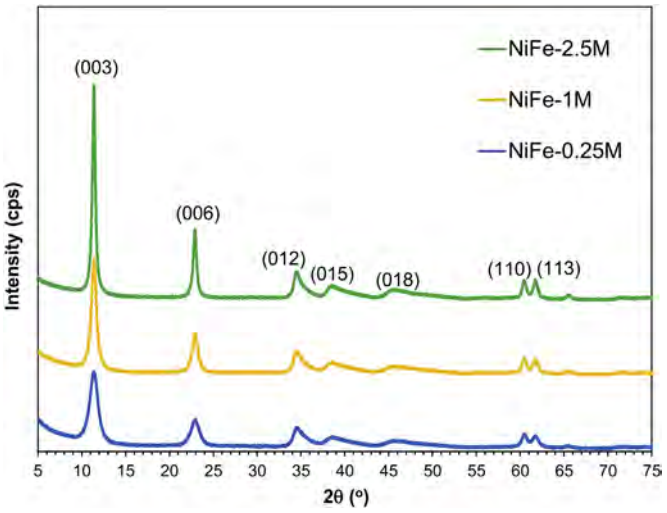

Fig. 1. XRD patterns of HT precursors.

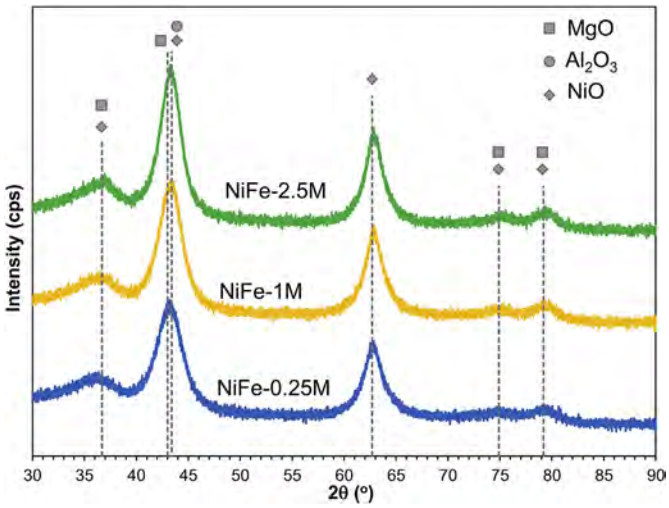

Fig. 2. XRD patterns of calcined catalysts.

2.3. Activity tests

CO_2 methanation was conducted in a stainless steel fixed-bed reactor (inner diameter of 4.5 mm) heated by an electric oven at atmospheric pressure. The temperature was controlled by a K-type thermocouple installed in the bottom of the catalyst bed. The flow rate of reactant gases was regulated by calibrated mass flow controllers (Alicat). In a typical experiment, 60 mg of calcined catalysts (pressed and sieved into particles of 300–355 μm) was diluted with 600 mg of silicon carbide (SiC, grit 45, particle size of 355 μm) and placed on the quartz wool, located above the thermocouple. Prior to reaction, the catalyst was reduced at 600 °C for 4 h in 50 vol% H_2/N_2 with a total flow of 100 mL min^{-1} (STP). Thereafter, the reactor was cooled down in pure N_2 flow for 1 h. Residual H_2 from reduction was purged out from the reactor. Subsequently, the reactant gases of $H_2/N_2/CO_2$ in a ratio of 64/20/16 (i.e., $H_2/CO_2 = 4/1$) was introduced at 270 mL min^{-1} (STP), corresponding to a weight hourly space velocity (WHSV) of 270 L g_{cat}^{-1} h^{-1} or a gas hourly space velocity (GHSV) of 34,000 h^{-1} with regards to the catalytic bed length of 3 cm. The CO_2 methanation tests were run at 200–450 °C at ambient pressure and were maintained at steady state for 1 h at each temperature. Water formed during the reaction was condensed by a cold trap operating at 1 °C. The outgases were analyzed using an online gas chromatograph (Agilent 7890A). A blank test was conducted, and no significant conversion was found over SiC powder in the stainless steel reactor.

The CO_2 conversion (X_{CO2}), CH_4 and CO selectivity (S_i) and space-time yield (STY) of CH_4 were defined in Eqs. (5)–(7), where F^{in} and F^{out} are the molar flow rates (mol h^{-1}), V^{in} is the volumetric flow rates (cm^3 h^{-1}) and V_R is the volume of the catalytic bed (cm^3).

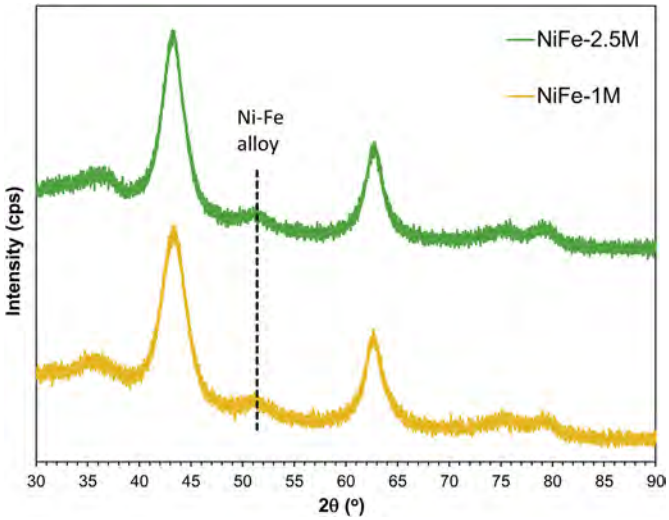

Fig. 3. XRD patterns of reduced-passivated catalysts.

$$X_{CO2}\,(\%) = \frac{F_{CO2}^{in} - F_{CO2}^{out}}{F_{CO2}^{in}} \times 100 \quad (5)$$

$$S_i(\%) = \frac{F_i^{out}}{F_{CO2}^{in} - F_{CO2}^{out}} \times 100 \quad (6)$$

Table 1
Physicochemical properties of as-prepared HT precursors.

Precursors	Lattice cell parameter a (Å) *	Lattice cell parameter c (Å) *	Crystallite size (nm)	Mass obtained per batch (g)	BET surface area (m^2 g^{-1})	BJH pore volume (cm^3 g^{-1})
NiFe-0.25M	3.06	23.31	7.9	1.90	218.8	0.45
NiFe-1M	3.06	23.29	12.8	7.66	158.8	0.46
NiFe-2.5M	3.06	23.29	22.0	18.77	114.4	0.30
Reference (Delidovich and Palkovits, 2015)	3.07	23.81	5.8	–	118	0.40

*$a = 2 \times d(110)$ and $c = 3 \times d(003)$.

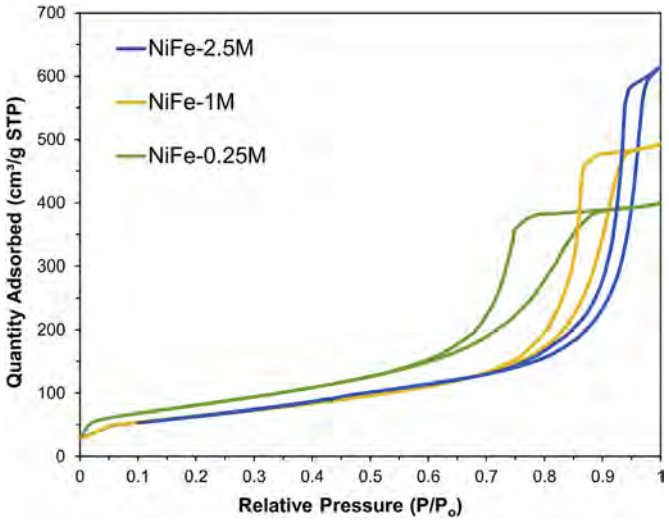

Fig. 4. N_2 physisorption isotherms of calcined catalysts.

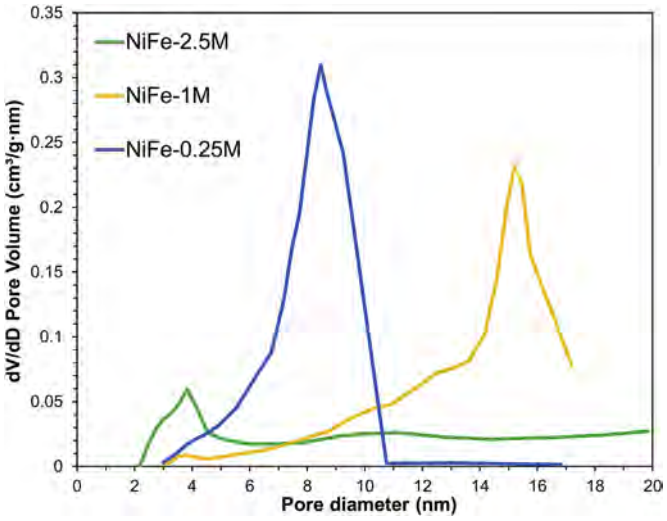

Fig. 5. BJH pore size distribution of calcined catalysts.

$$STY_{CH4}(h^{-1}) = \frac{X_{CO2} \times S_{CH4} \times V_{CO2}^{in}}{1000 \times V_R} \quad (7)$$

The stability tests were conducted at 350 °C for 12 h and at 300 °C for 65 h using the same procedure and condition.

3. Results and discussion

3.1. Catalysts characterization

The presence of hydrotalcite in the as-prepared precursors was confirmed by XRD analysis (Fig. 1). The XRD patterns of the precursors show common features of LDH structures (MgAl-HT JCPDS 01-089-0460) with symmetric and sharp reflections of the basal (003), (006), (012) planes at 2θ of 11.4°, 22.9°, and 34.5°, respectively. Broader and smaller peaks at 2θ of 38.5°, 45.6°, 60.5°, and 61.8° could be ascribed to the nonbasal (015), (018), (110) and (113) planes, respectively. No other phases were identifiable in the XRD diffractograms. Thus, it can be inferred that HT precursors with high purity and crystallinity were successfully synthesized by rapid coprecipitation, regardless of metal concentrations.

It was reported that HT materials have layered structures in rhombohedral 3R symmetry and the parameters of a unit cell, *a* and *c*, could be derived from *d* (110) and *d* (003) spacing (Cavani et al., 1991). The thickness of one layer consisting of a brucite-like sheet and one interlayer could be estimated based on the *d*-spacing of the (003) plane. Meanwhile, the average cation-cation distance in the brucite-like layer could be correlated to the *d*-spacing of the (110) plane. The lattice parameters of as-prepared precursors are summarized in Table 1. Interestingly, there was no significant difference

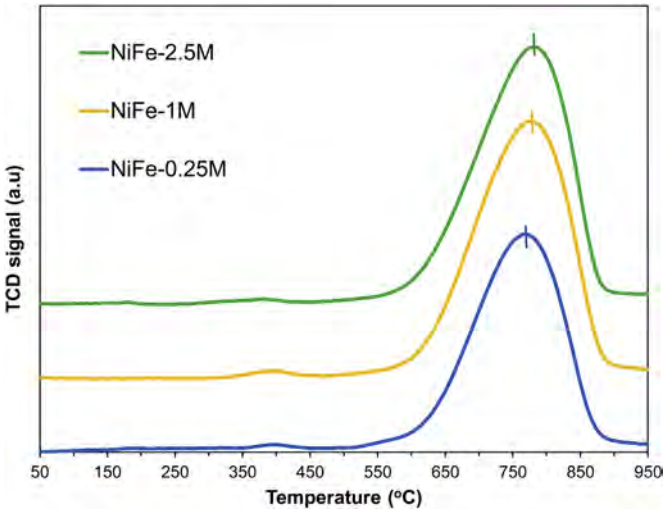

Fig. 6. H_2-TPR profiles of calcined catalysts.

in the lattice parameters between precursors prepared at different concentrations. Moreover, the unit cells of all precursors were slightly smaller than that of the reference material, $Mg_{0.75}Al_{0.25}CO_3(OH)_{0.125}\bullet\ 0.71H_2O$ (Delidovich and Palkovits, 2015). This could be due to the substitution of smaller Ni^{2+} ion for larger Mg^{2+} ion (i.e., radii of 0.69 Å and 0.72 Å, respectively) in the layered structures. Thus, Ni (and Fe) cations were assumed to incorporate well into the HT structures. The crystallite size of the precursors was calculated from the (003) reflection using Scherrer's

Table 2
Physicochemical properties of calcined catalysts.

Catalysts	Oxide crystallite size (nm)	BET surface area (m^2 g^{-1})	BJH pore volume (cm^3 g^{-1})	Ni surface area (m^2 g^{-1})	Reduction degree	Ni Dispersion	Ni–Fe crystallite size (nm)
NiFe-0.25M	4.6	294.7	0.68	3.38	66%	4.07%	–
NiFe-1M	4.9	240.6	0.77	3.91	69%	4.48%	4.8
NiFe-2.5M	5.1	231.4	0.45	4.00	68%	4.68%	5.1

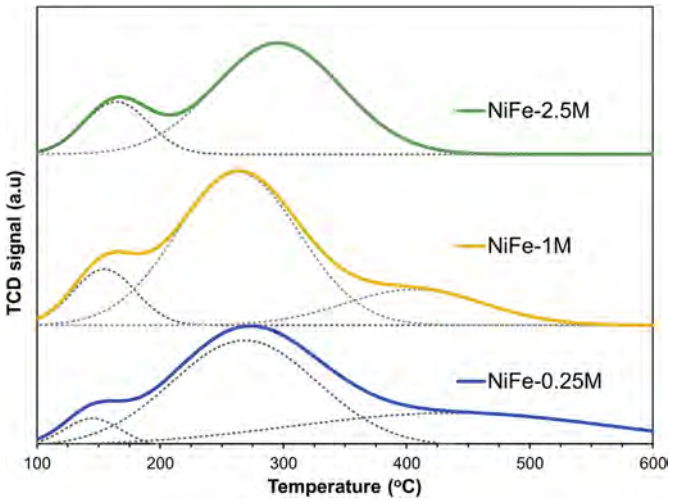

Fig. 7. CO_2-TPD profiles of reduced catalysts.

equation (Table 1). The crystallite size was larger than that of the reference material. As the metal concentration increased, larger crystals were obtained. Furthermore, it can be seen that a significantly larger amount of catalyst mass was obtained by increasing the total metal concentration during coprecipitation (Table 1).

Upon calcination, the HT structures were completely decomposed since only diffraction patterns of oxide phases were detected (Fig. 2). It was reported that only the rock-salt-type phase (NiO or MgO) was observed when Ni–Mg–Al HT precursors were calcined at a moderate calcination temperature of 600 °C. When the calcination temperature increased to 800 °C and above, the crystalline spinel phase such as $MgAl_2O_4$ was detected (Mette et al., 2014). In this study, the main reflection peaks could be attributed to not only NiO (JCPDS 01-089-5881) but also MgO (JCPDS 03-065-0476) and Al_2O_3 (JCPDS 01-073-1512). However, it is difficult to distinguish these phases due to overlapped diffraction patterns.

The XRD patterns of reduced-passivated catalysts are shown in Fig. 3. The formation of Ni–Fe alloy was confirmed by the representative peak of Ni_3Fe (200) at 2θ of 51.2° (JCPDS 03-065-3244). Diffraction peaks of MgO and Al_2O_3 were still apparent in the

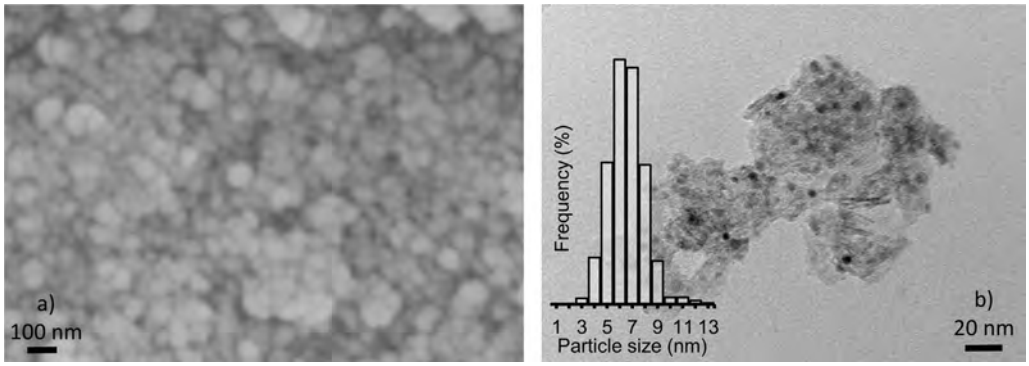

Fig. 8. a) SEM images of NiFe-1M HT precursors; b) TEM bright-field images of reduced-passivated NiFe-1M catalyst. The inset in (b) is the particle size distribution.

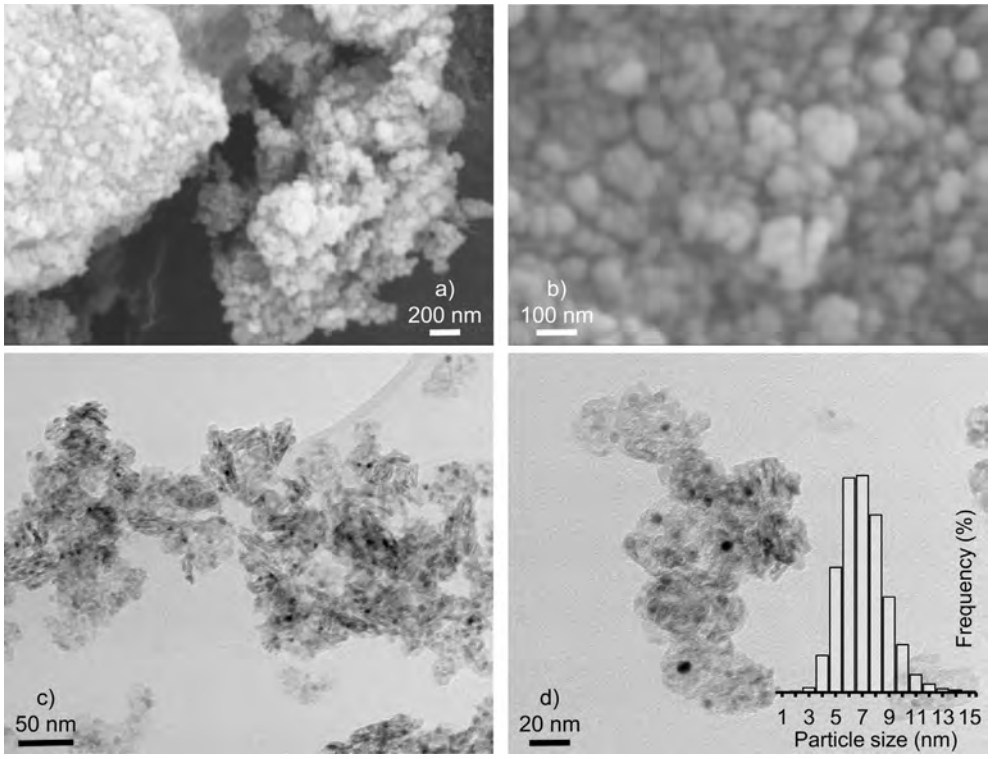

Fig. 9. a-b) SEM images of NiFe-2.5M HT precursors; c-d) TEM bright-field images of reduced-passivated NiFe-2.5M catalyst. The inset in (d) is the particle size distribution.

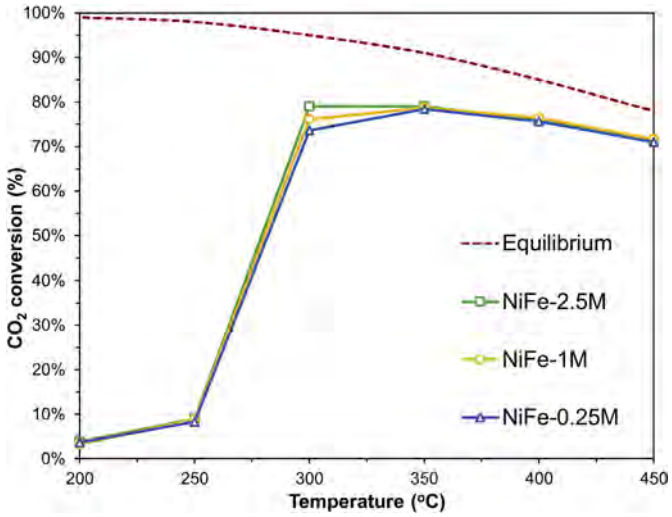

Fig. 10. CO_2 conversion *vs* temperature of different Ni–Fe/(Mg,Al)O_x catalysts in CO_2 methanation; the dashed line is the thermodynamic equilibrium.

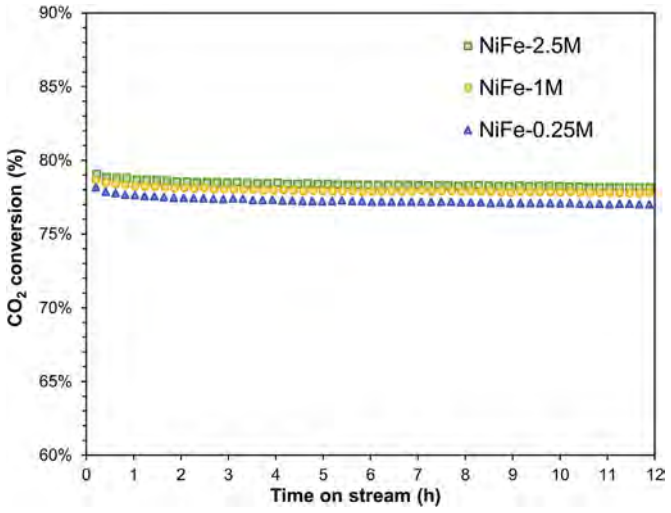

Fig. 12. CO_2 conversion of different Ni–Fe/(Mg,Al)O_x catalysts in CO_2 methanation at 350 °C.

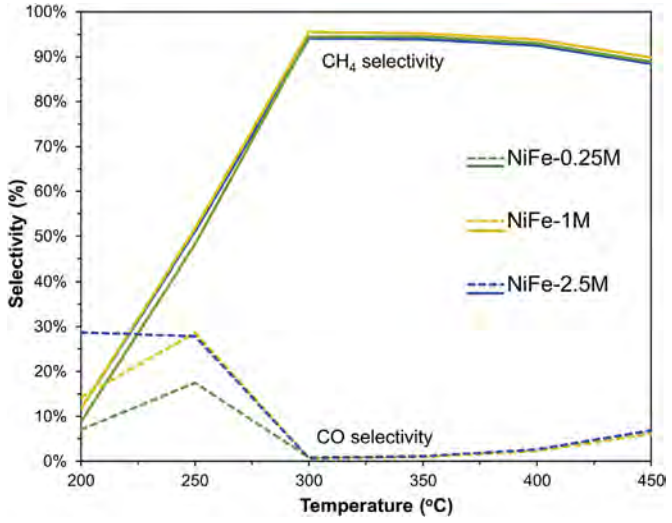

Fig. 11. CH_4 and CO selectivity *vs* temperature of different Ni–Fe/(Mg,Al)O_x catalysts in CO_2 methanation.

reduced-passivated samples. The calculated crystallite size of Ni–Fe alloy was close to the oxide crystallite size of the calcined catalysts of ca. 5 nm (Table 2), which are further independent of the total metal concentration during preparation.

The textural properties of calcined catalysts are summarized in Table 2. The N_2 adsorption-desorption isotherms show a type IV isotherm with hysteresis at high P/P_o range, which is characteristic of mesoporous materials (Fig. 4). Compared to the textural properties of as-prepared precursors (Table 1), the calcined catalysts had higher surface area and pore volume. Upon calcination at 600 °C, the layered structures collapsed, resulting in higher surface area and larger pore channels. However, with increasing metal concentration, the surface area and pore volume decreased. Nevertheless, all calcined catalysts exhibited a high surface area (230–300 $m^2\ g^{-1}$) and pore volume (0.4–0.8 $cm^3\ g^{-1}$) compared to conventional catalysts (Mebrahtu et al., 2018). Catalysts prepared by the rapid coprecipitation method also possessed a uniform pore structure according to their pore size distribution (Fig. 5). The pore size of the calcined NiFe-0.25M catalyst was 8–10 nm, while the pore size of the calcined NiFe-1M catalyst was larger at 14–16 nm. Interestingly, the structure of the calcined NiFe-2.5M catalyst consisted of significantly small pores of ~4 nm. It is worth mentioning that this tunable pore dimension by different metal concentrations in this study can be employed in other reactions such as Fischer-Tropsch synthesis (Khodakov et al., 2002).

To study the reducibility of different catalysts, TPR analysis was conducted. All H_2-TPR profiles exhibit one intense peak at a high temperature range of 760–800 °C (Fig. 6), ascribed to the reduction of NiO species to metallic Ni. This is to be compared with the reduction peak of pure NiO at 290–340 °C (Beierlein et al., 2019). The reduction of iron oxide species was negligible by small peaks at ~400 °C due to low Fe content in the catalysts. A fine distribution of NiO was assumed, resulting in stronger interaction and thus a higher reduction temperature (Guo et al., 2004; Rostrup-Nielsen, 1984). For catalysts prepared at higher metal concentrations, the reduction peaks slightly shifted to higher temperatures. However, it can be assumed that the reducibility of all three catalysts was similar, regardless of the total metal concentration during preparation.

CO_2-TPD has been carried out to study the surface basicity. The desorption profiles (Fig. 7) show three peaks corresponding to weak, medium and strong basic sites (Di Cosimo et al., 1998). The NiFe-1M catalyst possessed the highest total basicity among the others since its integrated area under the desorption line was the largest, which is expected to perform better catalytic activity. However, the impact of different basic types (weak, medium, and strong) on the catalytic activity in CO_2 methanation remains ambiguous. The strong basic site was suggested to be the dominant factor by (He et al., 2014) while (Aldana et al., 2013) convinced that the weak basic site was more responsible for the improvement of catalytic activity.

The Ni surface area was calculated from the adsorbed amount of H_2 based on the chemisorption study. H_2 was assumed to adsorb only on Ni atoms and not Fe atoms. For the determination of metal dispersion, the reduction degree was calculated (Table 2), reconfirmed the similar reducibility of all catalysts. Moreover, as the metal concentration increased, the Ni–Fe alloy catalysts exhibited slightly higher Ni surface area and better Ni dispersion.

The SEM characterization revealed an agglomerated morphology of NiFe-1M (Fig. 8a) and NiFe-2.5M HT precursors (Fig. 9ab). Spherical agglomerates were observed for both

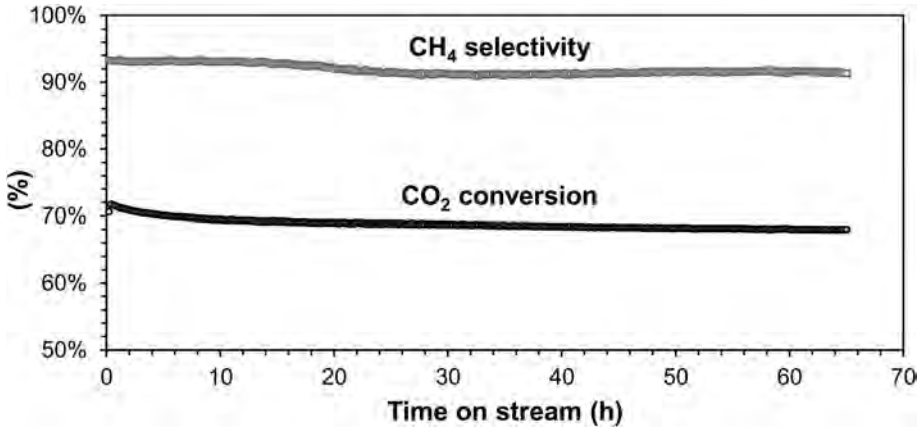

Fig. 13. CO_2 conversion and CH_4 selectivity during a long-term test of NiFe-1M catalyst in CO_2 methanation at 300 °C.

Table 3
Specific methane production rate of our catalysts and different catalytic systems for CO_2 methanation ($H_2/CO_2 = 4$) reported in the literature.

Catalysts	Ni wt%	Preparation method	T (°C)	Space velocity of CO_2	Specific CH_4 productivity ($mol_{CH4}\ g_{Ni}^{-1}\ h^{-1}$)	STY (h^{-1})
Ni–Fe/(Mg,Al)O_x HT	20	Coprecipitation	300	5440 h^{-1} or 43.2 $L.g_{cat}^{-1}.h^{-1}$	7.01	3954
(NiFe-1M)			350		7.22	4076
Ni–Fe/(Mg,Al)O_x HT	12	Coprecipitation	335	2115 h^{-1}	0.47	–
Mebrahtu et al. (2018)						
Ni(Al)O_x HT [a]	69.1	Coprecipitation	400	44.8 $L.g_{cat}^{-1}.h^{-1}$	2.65	–
Abelló et al. (2013)						
Ni/(Mg,Al)O_x HT	17.2	Coprecipitation	300	360 h^{-1}	0.02	332
Liu et al. (2016)						
Ni/Al_2O_3 [b] (Bengaouer et al., 2018)	14–17	Commercial catalyst	250	526 h^{-1}	0.187	437
Ni/Al_2O_3 HT (Abate et al., 2016)	76	Coprecipitation	300	750 h^{-1}	–	487.5
Ni/ZrO_2 (Jia et al., 2019)	8.68	Impregnation	300	9600 h^{-1}	1.27	2845
Ni/TiO_2 (Zhou et al., 2016)	10	Impregnation	350	12,000 h^{-1}	6.39	3600
Ni/La_2O_3 (Song et al., 2010)	10	Impregnation	350	5100 h^{-1}	1.88	4131
Ni–Ce/USY zeolite (Graça et al., 2014)	14	Impregnation	400	7036 h^{-1}	2.92	4570
Ni/CeO_2–ZrO_2 (Aldana et al., 2013)	5	Pseudo sol-gel	350	7052 h^{-1}	2.55	5581

[a] Reaction at 10 bar.
[b] Reaction at 4 bar, the desirable temperature was 250 °C but the actual temperature inside the reactor was 400–540 °C.

precursors. TEM images of the reduced-passivated catalysts show the highly dispersed Ni–Fe round-shaped particles (dark color) on the support (Figs. 8b and 9cd). The average particle size from the TEM images was obtained by measuring about 750–800 particles for each sample using ImageJ software. Notably, the increase in total metal concentration did not significantly affect the average size of Ni–Fe alloy particles, which was approximately 6.0 ± 1.4 nm for NiFe-1M and 6.5 ± 1.7 nm for the NiFe-2.5M catalyst. These results are also close to the crystallite size obtained from the XRD study.

3.2. Catalytic activity

The activity of Ni–Fe/(Mg,Al)O_x catalysts for CO_2 methanation was studied in the temperature range of 200–450 °C at a stoichiometric H_2/CO_2 ratio of 4. A high GHSV of 34,000 h^{-1} was used. Although CO_2 methanation was thermodynamically favored at low temperatures, kinetic limitation prevents the reaction to readily occur. As expected, poor performance at 200–250 °C is observed for all catalysts (Fig. 10). From 250 °C to 300 °C, CO_2 conversions plunged up from approximately 10% to 73–79%. The conversions slightly declined at 350–450 °C because of the thermodynamics of methanation reaction (Gao et al., 2012).

The CH_4 selectivity reached 93–95% at 300–450 °C for all catalysts (Fig. 11). The production of CH_4 was not significant at low temperatures of 200–250 °C. Meanwhile, a small amount of CO was also formed, probably from the reverse water gas shift reaction (RWGS, $CO_2 + H_2 \leftrightarrow CO + H_2O$). The selectivity of CO increased at 400–450 °C because CO production via RWGS was thermodynamically favored at high temperatures. Overall, the activity of all three catalysts were not significantly different. By increasing the total metal concentration during preparation (up to 10 times higher), a larger amount of catalyst mass was obtained but their catalytic performance remained unchanged. This demonstrates the feasibility of large-scale preparation of catalysts by our proposed method in this study.

The stability of all catalysts at a fixed temperature of 350 °C is presented in Fig. 12. All catalysts exhibited satisfactory stability and good performance during 12 h time on stream (TOS) despite slight deactivation. CO_2 conversions of ca. 78% are in line with the result of the temperature-dependent activity tests (Fig. 10). A long-term test of NiFe-1M catalysts was also carried out at 300 °C (Fig. 13). The initial CO_2 conversion was 71.78% and reduced to 68.09% after 65 h TOS, corresponding to a deactivation rate of only 0.057% h^{-1} (Mutz et al., 2017). reported a deactivation rate of 0.12% h^{-1} of 20 wt% Ni/Al_2O_3 commercial catalysts in CO_2 methanation at 358 °C, 6 bar, and WHSV of 80.5 $L_{CO2}\ g_{cat}\ h^{-1}$. Under the same condition but at 305 °C, the prepared 17 wt% Ni_3Fe/Al_2O_3 catalysts showed a deactivation of 0.3% h^{-1}. Thus, our Ni–Fe/(Mg,Al)O_x can be assumed to have better stability than the commercial and other alumina supported catalysts.

The specific productivity of methane ($mol_{CH4}\ g_{Ni}^{-1}\ h^{-1}$) and

space-time yield (STY, the number of molecules produced per unit volume of reactor per unit time) of different catalysts in CO_2 methanation tested at high space velocity of CO_2 are summarized in Table 3. Overall, our Ni−Fe/(Mg,Al)O_x catalysts showed the highest specific methane productivity compared to the commercial catalyst, Ni/Al_2O_3 HT catalyst and other catalytic systems in literature. Although our space-time yield was slightly lower than La- and Ce-promoted catalysts, the price and availability of Ni−Fe/(Mg,Al)O_x catalyst is more attractive for the development of commercial catalysts for CO_2 methanation (U.S. Geological Survey, 2019).

4. Conclusions

Ni−Fe/(Mg,Al)O_x HT-derived catalysts were successfully prepared by rapid coprecipitation. The method was reproducible, energy-efficient and environmental-friendly for supported catalysts preparation compared to conventional synthesis. Overall, the prepared catalysts exhibited almost similar physicochemical properties, such as reducibility and particle sizes. Moreover, insignificant differences in catalytic performance were obtained for all Ni−Fe/(Mg,Al)O_x catalysts in CO_2 methanation. Thus, by increasing the total metal concentration, larger amount of catalyst mass per batch was obtained while the catalytic activity was maintained. It revealed a great opportunity for a mass production of highly active Ni−Fe/(Mg,Al)O_x HT-derived catalysts. The scaled-up catalysts performed significantly high conversion of CO_2 (up to 79%) and CH_4 selectivity (up to 95%) at 300 °C under relevant industrial conditions (high GHSV of 34,000 h^{-1}, $H_2/CO_2 = 4$). The specific rate of methane production and space-time yield was higher than many reported catalytic systems in literature. Ni−Fe/(Mg,Al)O_x HT-derived catalysts with outstanding performance and high potential for large-scale production emerge as a promising candidate for the commercialization of CO_2 methanation process to produce SNG from renewable H_2 and CO_2.

Declaration of competing interest

The authors declare that they have no known competing financial interests or personal relationships that could have appeared to influence the work reported in this paper.

CRediT authorship contribution statement

Huong Lan Huynh: Investigation, Validation, Writing - original draft, Visualization. **Wakshum Mekonnen Tucho:** Investigation, Resources, Writing - review & editing. **Xinhai Yu:** Resources, Supervision. **Zhixin Yu:** Methodology, Writing - review & editing, Supervision, Project administration.

Acknowledgments

The authors would like to thank the Norwegian Ministry of Education and Research and Valide AS through the Plogen Program for financial support.

References

Abate, S., Barbera, K., Giglio, E., Deorsola, F., Bensaid, S., Perathoner, S., Pirone, R., Centi, G., 2016. Synthesis, characterization, and activity pattern of Ni−Al hydrotalcite catalysts in CO2 methanation. Ind. Eng. Chem. Res. 55 (30), 8299−8308.

Abelló, S., Bolshak, E., Montané, D., 2013. Ni−Fe catalysts derived from hydrotalcite-like precursors for hydrogen production by ethanol steam reforming. Appl. Catal., A 450, 261−274.

Aldana, P.A.U., Ocampo, F., Kobl, K., Louis, B., Thibault-Starzyk, F., Daturi, M., Bazin, P., Thomas, S., Roger, A.C., 2013. Catalytic CO2 valorization into CH4 on Ni-based ceria-zirconia. Reaction mechanism by operando IR spectroscopy. Catal. Today 215, 201−207.

Andersson, M.P., Bligaard, T., Kustov, A., Larsen, K.E., Greeley, J., Johannessen, T., Christensen, C.H., Nørskov, J.K., 2006. Toward computational screening in heterogeneous catalysis: Pareto-optimal methanation catalysts. J. Catal. 239 (2), 501−506.

Aziz, M.A.A., Jalil, A.A., Triwahyono, S., Ahmad, A., 2015. CO2 methanation over heterogeneous catalysts: recent progress and future prospects. Green Chem. 17 (5), 2647−2663.

Bailera, M., Lisbona, P., Romeo, L.M., Espatolero, S., 2017. Power to Gas projects review: Lab, pilot and demo plants for storing renewable energy and CO2. Renew. Sustain. Energy Rev. 69, 292−312.

Bartholomew, C.H., 1975. Alloy catalysts with monolith supports for methanation of coal-derived gases. Quarterly Progress Report to ERDA.

Beierlein, D., Häussermann, D., Pfeifer, M., Schwarz, T., Stöwe, K., Traa, Y., Klemm, E., 2019. Is the CO2 methanation on highly loaded Ni-Al2O3 catalysts really structure-sensitive? Appl. Catal., B 247, 200−219.

Bengaouer, A., Ducamp, J., Champon, I., Try, R., 2018. Performance evaluation of fixed-bed, millistructured, and metallic foam reactor channels for CO2 methanation. Can. J. Chem. Eng. 96 (9), 1937−1945.

Bette, N., Thielemann, J., Schreiner, M., Mertens, F., 2016. Methanation of CO2 over a (Mg,Al)Ox supported nickel catalyst derived from a (Ni,Mg,Al)-Hydrotalcite-like precursor. ChemCatChem 8 (18), 2903−2906.

Cavani, F., Trifirò, F., Vaccari, A., 1991. Hydrotalcite-type anionic clays: preparation, properties and applications. Catal. Today 11 (2), 173−301.

Cullity, B.D., 1956. Elements of X-Ray Diffraction. Addison-Wesley Pub. Co.

Delidovich, I., Palkovits, R., 2015. Structure−performance correlations of Mg−Al hydrotalcite catalysts for the isomerization of glucose into fructose. J. Catal. 327, 1−9.

Di Cosimo, J.I., Dıez, V.K., Xu, M., Iglesia, E., Apesteguıa, C.R., 1998. Structure and surface and catalytic properties of Mg-Al basic oxides. J. Catal. 178 (2), 499−510.

Fan, G., Li, F., Evans, D.G., Duan, X., 2014a. Catalytic applications of layered double hydroxides: recent advances and perspectives. Chem. Soc. Rev. 43 (20), 7040−7066.

Fan, M.-T., Miao, K.-P., Lin, J.-D., Zhang, H.-B., Liao, D.-W., 2014b. Mg-Al oxide supported Ni catalysts with enhanced stability for efficient synthetic natural gas from syngas. Appl. Surf. Sci. 307, 682−688.

Gao, J., Wang, Y., Ping, Y., Hu, D., Xu, G., Gu, F., Su, F., 2012. A thermodynamic analysis of methanation reactions of carbon oxides for the production of synthetic natural gas. RSC Adv. 2 (6), 2358−2368.

Ghaib, K., Ben-Fares, F.-Z., 2018. Power-to-Methane: a state-of-the-art review. Renew. Sustain. Energy Rev. 81, 433−446.

Graça, I., González, L.V., Bacariza, M.C., Fernandes, A., Henriques, C., Lopes, J.M., Ribeiro, M.F., 2014. CO2 hydrogenation into CH4 on NiHNaUSY zeolites. Appl. Catal., B 147, 101−110.

Guo, J., Lou, H., Zhao, H., Chai, D., Zheng, X., 2004. Dry reforming of methane over nickel catalysts supported on magnesium aluminate spinels. Appl. Catal., A 273 (1), 75−82.

He, L., Lin, Q., Liu, Y., Huang, Y., 2014. Unique catalysis of Ni-Al hydrotalcite derived catalyst in CO2 methanation: cooperative effect between Ni nanoparticles and a basic support. J Energy Chem 23 (5), 587−592.

Jia, X., Zhang, X., Rui, N., Hu, X., Liu, C.-j., 2019. Structural effect of Ni/ZrO2 catalyst on CO2 methanation with enhanced activity. Appl. Catal., B 244, 159−169.

Khodakov, A.Y., Griboval-Constant, A., Bechara, R., Zholobenko, V.L., 2002. Pore size effects in fischer tropsch synthesis over cobalt-supported mesoporous silicas. J. Catal. 206 (2), 230−241.

Kopyscinski, J., Schildhauer, T.J., Biollaz, S.M.A., 2010. Production of synthetic natural gas (SNG) from coal and dry biomass − a technology review from 1950 to 2009. Fuel 89 (8), 1763−1783.

Kustov, A.L., Frey, A.M., Larsen, K.E., Johannessen, T., Nørskov, J.K., Christensen, C.H., 2007. CO methanation over supported bimetallic Ni−Fe catalysts: from computational studies towards catalyst optimization. Appl. Catal., A 320, 98−104.

Li, J., Lin, Y., Pan, X., Miao, D., Ding, D., Cui, Y., Dong, J., Bao, X., 2019. Enhanced CO2 methanation activity of Ni/Anatase catalyst by tuning strong metal−support interactions. ACS Catal. 9 (7), 6342−6348.

Liu, J., Bing, W., Xue, X., Wang, F., Wang, B., He, S., Zhang, Y., Wei, M., 2016. Alkaline-assisted Ni nanocatalysts with largely enhanced low-temperature activity toward CO2 methanation. Catal. Sci. Technol. 6 (11), 3976−3983.

Marocco, P., Alexandru Morosanu, E., Giglio, E., Ferrero, D., Asmelash, C., Lanzini, A., Abate, S., Bensaid, S., Perathoner, S., Santarelli, M., Pirone, R., Centi, G., 2018. CO2 methanation over Ni/Al hydrotalcite-derived catalyst: experimental characterization and kinetic study. Fuel 225, 230−242.

Mebrahtu, C., Krebs, F., Perathoner, S., Abate, S., Centi, G., Palkovits, R., 2018. Hydrotalcite based Ni−Fe/(Mg, Al)Ox catalysts for CO2 methanation − tailoring Fe content for improved CO dissociation, basicity, and particle size. Catal. Sci. Technol. 8 (4), 1016−1027.

Mette, K., Kühl, S., Düdder, H., Kähler, K., Tarasov, A., Muhler, M., Behrens, M., 2014. Stable performance of Ni catalysts in the dry reforming of methane at high temperatures for the efficient conversion of CO2 into syngas. ChemCatChem 6 (1), 100−104.

Mutz, B., Belimov, M., Wang, W., Sprenger, P., Serrer, M.-A., Wang, D., Pfeifer, P., Kleist, W., Grunwaldt, J.-D., 2017. Potential of an alumina-supported Ni3Fe catalyst in the methanation of CO2: impact of alloy formation on activity and stability. ACS Catal. 7 (10), 6802−6814.

Nørskov, J.K., Bligaard, T., Rossmeisl, J., Christensen, C.H., 2009. Towards the

computational design of solid catalysts. Nat. Chem. 1, 37.
Othman, M.R., Helwani, Z., Martunus, Fernando, W.J.N., 2009. Synthetic hydrotalcites from different routes and their application as catalysts and gas adsorbents: a review. Appl. Organomet. Chem. 23 (9), 335–346.
Pandey, D., Deo, G., 2016. Determining the best composition of a Ni–Fe/Al2O3 catalyst used for the CO2 hydrogenation reaction by applying response surface methodology. Chem. Eng. Commun. 203 (3), 372–380.
Pandey, D., Ray, K., Bhardwaj, R., Bojja, S., Chary, K.V.R., Deo, G., 2018. Promotion of unsupported nickel catalyst using iron for CO2 methanation. Int. J. Hydrogen Energy 43 (10), 4987–5000.
Rashid, K., Ellingwood, K., Safdarnejad, S.M., Powell, K.M., 2019. Designing flexibility into a hybrid solar thermal power plant by real-time, adaptive heat integration. In: Muñoz, S.G., Laird, C.D., Realff, M.J. (Eds.), Computer Aided Chemical Engineering. Elsevier, pp. 457–462.
Rashid, K., Mohammadi, K., Powell, K., 2020. Dynamic simulation and techno-economic analysis of a concentrated solar power (CSP) plant hybridized with both thermal energy storage and natural gas. J. Clean. Prod. 248, 119193.
Ray, K., Deo, G., 2017. A potential descriptor for the CO2 hydrogenation to CH4 over Al2O3 supported Ni and Ni-based alloy catalysts. Appl. Catal., B 218, 525–537.
Rönsch, S., Schneider, J., Matthischke, S., Schlüter, M., Götz, M., Lefebvre, J., Prabhakaran, P., Bajohr, S., 2016. Review on methanation – from fundamentals to current projects. Fuel 166, 276–296.
Rostrup-Nielsen, J.R., 1984. Catalytic steam reforming. In: Anderson, J.R., Boudart, Michel (Eds.), Catalysis. Springer, p. 1.
Sabatier, P., Senderens, J.-B., 1902. Nouvelles syntheses du methane. Comptes Rendus Des Séances De L'Académie Des Sciences, Section VI – Chimie 134, 514–516.
Song, C., 2006. Global challenges and strategies for control, conversion and utilization of CO2 for sustainable development involving energy, catalysis, adsorption and chemical processing. Catal. Today 115 (1), 2–32.
Song, H., Yang, J., Zhao, J., Chou, L., 2010. Methanation of carbon dioxide over a highly dispersed Ni/La2O3 catalyst. Chin. J. Catal. 31 (1), 21–23.
Tathod, A.P., Gazit, O.M., 2016. Fundamental insights into the nucleation and growth of Mg–Al layered double hydroxides nanoparticles at low temperature. Cryst. Growth Des. 16 (12), 6709–6713.
U.S. Geological Survey, 2019. Mineral commodity summaries 2019. U.S. Geological Survey. https://doi.org/10.3133/70202434.
Vogt, C., Monai, M., Kramer, G.J., Weckhuysen, B.M., 2019. The renaissance of the Sabatier reaction and its applications on Earth and in space. Nat. Catal. 2 (3), 188–197.
Zhou, R., Rui, N., Fan, Z., Liu, C.-j., 2016. Effect of the structure of Ni/TiO2 catalyst on CO2 methanation. Int. J. Hydrogen Energy 41 (47), 22017–22025.
Agora Energiewende and Sandbag (2019): The European Power Sector in 2018. Up-to-date analysis on the electricity transition.

Appendix E – Paper V

Structured NiFe catalysts derived from in-situ grown layered double hydroxides on ceramic monolith for CO_2 methanation

H. L. Huynh, W. M. Tucho, and Z. Yu

Green Energy & Environment **2020**, *5*, 423-432

DOI: 10.1016/j.gee.2020.09.004

Available online at www.sciencedirect.com

ScienceDirect

Green Energy & Environment 5 (2020) 423–432

www.keaipublishing.com/gee

Research paper

Structured NiFe catalysts derived from in-situ grown layered double hydroxides on ceramic monolith for CO_2 methanation

Huong Lan Huynh [a], Wakshum Mekonnen Tucho [b], Zhixin Yu [a,*]

[a] Department of Energy and Petroleum Engineering, University of Stavanger, 4036 Stavanger, Norway
[b] Department of Mechanical and Structural Engineering and Material Science, University of Stavanger, 4036 Stavanger, Norway

Received 29 July 2020; revised 11 September 2020; accepted 17 September 2020
Available online 28 September 2020

Abstract

Monolithic catalysts for CO_2 methanation have become an active research area for the industrial development of Power-to-Gas technology. In this study, we developed a facile and reproducible synthesis strategy for the preparation of structured NiFe catalysts on washcoated cordierite monoliths for CO_2 methanation. The NiFe catalysts were derived from in-situ grown layered double hydroxides (LDHs) via urea hydrolysis. The influence of different washcoat materials, i.e., alumina and silica colloidal suspensions on the formation of LDHs layer was investigated, together with the impact of total metal concentration. NiFe LDHs were precipitated on the exterior surface of cordierite washcoated with alumina, while it was found to deposit further inside the channel wall of monolith washcoated with silica due to different intrinsic properties of the colloidal solutions. On the other hand, the thickness of in-situ grown LDHs layers and the catalyst loading could be increased by high metal concentration. The best monolithic catalyst (COR-AluCC-0.5M) was robust, having a thin and well-adhered catalytic layer on the cordierite substrate. As a result, high methane yield was obtained from CO_2 methanation at high flow rate on this structured NiFe catalysts. The monolithic catalysts appeared as promising structured catalysts for the development of industrial methanation reactor.

Keywords: CO_2 methanation; Structured catalysts; In-situ growth; Layered double hydroxides; Ceramic honeycomb monolith

1. Introduction

The ever-growing concern on carbon dioxide mitigation has drawn much attention to sustainable solutions in the past decades. Carbon capture, utilization, and storage (CCUS) plays a major role to tackle this global climate change challenge. Most interestingly, carbon-neutral industrial processes in which renewable energy sources are utilized to convert CO_2 into valuable fuels and chemicals with no carbon footprint emerge as promising approaches for CO_2 utilization [1]. One of many potential processes is Power-to-Gas (PtG) technology which can produce methane or synthetic natural gas (SNG), an important chemical energy carrier with high heating value [2]. In this process, hydrogen produced via water electrolysis by excessive renewable electricity and captured carbon dioxides are catalytically converted to methane via the Sabatier reaction Eq. (1), also called CO_2 methanation.

$$CO_2 + 4H_2 \leftrightarrow CH_4 + 2H_2O,\ \Delta H_{298\ K} = -165.0\ kJ\ mol^{-1} \quad (1)$$

Catalytic CO_2 methanation is an exothermic reaction which thermodynamically favored at low temperatures and elevated pressures. However, due to unfavorable kinetics, high conversion rates are difficult to be achieved at low-temperature region of 200–350 °C. On the other hand, the reaction mechanism is still under debate despite being discovered for more than a hundred years [3,4]. Metals in group VIII are well-known as active catalysts for the CO_2 methanation. Although noble metals (i.e., Ru, Rh) have excellent activity and stability, Ni-

* Corresponding author.
E-mail address: zhixin.yu@uis.no (Z. Yu).

https://doi.org/10.1016/j.gee.2020.09.004

based catalysts are widely used for CO_2 methanation due to the affordable price and good performance [5–8].

A large number of research studies have been devoted to improving the activity of Ni-based catalysts for CO_2 methanation, especially at low temperatures over powder/pellet catalysts in fixed-bed reactor [9]. Many efforts have been dedicated to studying different type of supports, from single (e.g., Al_2O_3, TiO_2, SiO_2) to composite (e.g., Al_2O_3-SiO_2, CeO_2-ZrO_2) or novel type (e.g., mesoporous materials, molecular sieves, nanotubes, graphene, zeolite, etc.), often with different additives, such as alkaline and rare earth metal oxides, transition and noble metals. For example, Fe has been recognized as an excellent promoter, significantly improving the activity of Ni-based catalysts for low-temperature CO_2 methanation [10–12]. Besides, it should be emphasized that the performances of Ni-based catalysts are strongly impacted by the preparation methods. It has been recognized that catalysts prepared by layer double hydroxides precursors (LDHs, general formula $[M^{2+}_{1-x}M^{3+}_{x}(OH)_2](A^{n-})_{x/n} \cdot mH_2O$, where M are metals, and A is anion) exhibited higher activity and selectivity than catalysts prepared by conventional methods due to better dispersion of metal active sites [8,13].

The development of laboratory research into industrial practice is essential for the commercialization of PtG technology. One of the most recent development trends of methanation unit is structured reactors equipped with monolithic catalysts [14]. Structured catalysts and reactors have been widely used for environmental applications, such as automotive catalysts, volatile organic compounds incinerators, etc. Honeycomb monoliths have become the common catalyst shape after their commercial success for automobile exhaust treatment [15]. Therefore, the use of structured catalysts for other heterogeneous catalytic reactions has been highly motivated. Monolithic catalysts offer many advantages over conventional pelletized catalysts, such as lower pressure drop associated with the high flow rates and small size of the reactor, which are typical concerns for gas-phase chemical processes. For CO_2 methanation, monolithic catalysts can handle large volumetric flow of CO_2 during industrial applications with more efficient heat and mass transfer.

In terms of preparation methods, there are two types of structured catalysts. Catalysts in which an active phase is deposited on inert monolithic support are classified as coated catalysts, whereas catalysts in which the whole structure is made from the active compounds are bulk catalysts. Most structured catalysts used for CO_2 methanation were coated catalysts [13]. Cordierite ($2Al_2O_3 \cdot 5SiO_2 \cdot 2MgO$) is the most widely used ceramic material for the production of commercial monoliths with different dimensions and cell densities. Cordierite has high thermal stability and low thermal expansion coefficient, but ultralow surface area. Therefore, it is advantageous to coat a layer of support material on cordierite in order to increase the surface area prior to the deposition of active catalyst layer. The active layer can be deposited by different methods such as impregnation or deposition–precipitation [16].

The main concern is the homogeneous distribution of the active phase on monolithic support. Recently, a novel synthesis using urea hydrolysis to deposit LDHs layer in-situ on structured supports as precursors for structured catalysts has been reported. In the presence of a basic retardant, i.e., urea, LDHs consisting of Ni-Al, Co-Al, Co-Fe, etc., were successfully coated on a variety of supports such as metal mesh and foams (e.g., Ni foam, Fe mesh, FeCrAl fiber, Al foils, etc.) with great potentials for different catalytic reactions [17–21]. Moreover, in-situ grown LDHs layers appeared to have strong adherence and mechanical stability between the layer and the metal substrate [22–24]. Notably, the formation of LDHs was influenced by different parameters such as reaction temperature, urea amount, metal concentration, and the ratio of trivalent and divalent ions [25,26]. However, researches on structured catalysts from in-situ grown precursors on the ceramic substrate via urea hydrolysis are rarely reported.

Recent innovative applications using structured catalysts and reactors for CO_2 methanation has been reviewed elsewhere [13]. Different catalytic systems were investigated, for example, the superior performance of honeycomb-type over powdered catalysts for the Sabatier reaction was confirmed at a very high gas space velocity (up to 50,000 h^{-1}) by Vita et al. [27] The authors studied Ni/Gd-CeO_2 catalysts on cordierite monolith prepared by solution combustion synthesis. Besides most honeycomb catalysts were prepared by washcoating the ready-made powdery catalysts onto monolithic surface using slurry solution. Janke et al. prepared cordierite honeycomb catalysts by slurry coating a commercial 10% Ru/γ-Al_2O_3 catalysts on the monolith [28]. Similar preparation was carried out by Fukuhara et al. that powder-type Ni-CeO_2 catalysts were slurry coated on aluminum honeycomb substrate [29,30]. Ahn et al. further studied the impact of different coating liquids when washcoating Ni-CeO_2 catalysts on the ceramic honeycomb monolith for CO_2 methanation [31]. To the best of our knowledge, monolithic catalysts derived from in-situ grown LDHs have not been employed for CO_2 methanation. Since the preparation of monolithic catalysts could significantly influence the catalytic performance [32,33], it would be important to study different synthesis methods.

In this work, we report a facile synthetic strategy of structured catalysts derived from in-situ grown NiFe LDHs precursors on washcoated cordierite monoliths. In general, the monolith was firstly washcoated using colloidal solutions, followed by urea hydrolysis in which a stable LDHs layer was formed. The influence of different colloidal coating, i.e., alumina or silica, on the synthesis of NiFe LDHs was studied. The impact of the metal concentration during urea hydrolysis was also investigated. After calcination and reduction, the well-dispersed NiFe active phases on cordierite monoliths were obtained and tested for CO_2 methanation under industrial relevant conditions.

2. Experimental

2.1. Materials

The cylindrical honeycomb monoliths were made of cordierite (Versagrid™, $MgO:SiO_2:Al_2O_3$ = 13.8:50:34 wt%,

and traces amount of iron and zinc oxide) supplied by Applied Ceramics Inc. (USA). The dimension of monoliths was 19 mm in diameter and 20 mm in length. The monoliths had 230 cells per square inch (cpsi), channel wall thickness of 200 ± 50 μm, average pore diameter of 4.5 μm, open frontal area of 72%, and geometric surface area of 2220 m^2 m^{-3}. All monoliths were washed with ethanol and water in an ultrasonic bath three times and dried at 90 °C overnight prior to further synthesis steps.

All reagents used for the synthesis of LDHs, i.e., urea, $Ni(NO_3)_2 \cdot 6H_2O$, $Fe(NO_3)_3 \cdot 9H_2O$ were analytical grade (Merck Millipore) and used as received without purification.

2.2. Coating on ceramic monoliths using colloidal solutions

In order to increase the surface area of the cordierite monolith, a washcoat layer of support material was deposited by dip coating method. Two different colloidal solutions were investigated, i.e., alumina and silica. Colloidal Al_2O_3 (Alfa Aesar, 20 wt% suspension in water, viscosity of 10 cps) has a particle size of 50 nm, while colloidal SiO_2 (LUDOX TM-50, 50 wt% suspension in water, viscosity of 55 cps) has a particle size of around 22–25 nm. In a typical dip coating cycle, the monolith was immersed in the colloidal solution for 3 min, then dried at 250 °C for 15 min. Several cycles were made to achieve the desired washcoat loading. Finally, the monolith was calcined at 600 °C for 6 h (heating rate of 2 K min^{-1}) in a muffle furnace. The washcoated monoliths are named COR-AluCC and COR-SiCC.

2.3. In-situ grown of LDHs layers on washcoated ceramic monoliths

Typically, aqueous stock solutions consisting of nickel nitrate, iron nitrate, and urea with a total molar concentration of 0.5 M or 0.05 M were used. The molar ratio of Ni^{2+}/Fe^{3+} was maintained at 4 and the molar ratio of urea and metal ion was 9.9, corresponding to a urea/nitrate ion ratio of 4.5. The selected urea/metal compositions had been optimized experimentally in order to obtain a pure LDHs structure.

The pretreated monolith was immersed in 45 mL of the stock solution, and subsequently transferred into a 90-mL Teflon-lined hydrothermal autoclave and heated at 110 °C for 24 h. After cooling the autoclave to room temperature, the monolith was washed with deionized water and dried at 90 °C for 1 h. Calcination was carried out at 600 °C for 6 h (heating rate of 2 K min^{-1}) in a muffle furnace. The final monolithic catalysts were designated as COR-AluCC-*x*M and COR-SiCC-*x*M, where *x* is the total metal concentration used in urea hydrolysis.

For comparison, the same synthesis procedure was conducted without the addition of washcoated monoliths. The solid precipitate was collected by centrifugation, washed, and dried. These LDHs powders are denominated as LDH-*x*M, where *x* is the total metal concentration used in urea hydrolysis. Also, the dry LDHs powders were calcined at 600 °C for 6 h.

2.4. Catalysts characterization

X-ray diffraction (XRD) diffractograms were recorded on a Bruker D8 Advance micro-diffractometer, equipped with CuKα radiation source. The scanning speed was 1° min^{-1} over the range from 5° to 70°. The average crystallite size *d* was calculated by the Scherrer equation [34].

Temperature programmed reduction (TPR) of the calcined catalyst powders was carried out on Micromeritics Autochem II ASAP 2020 instrument, equipped with a thermal conductivity detector (TCD). In order to obtain reliable data [35], approximately 35 mg of the samples was used, which was degassed at 200 °C for 30 min prior to measurement. The TPR profiles were recorded from 50 °C to 950 °C in flowing H_2 (10 vol% H_2/Ar) at a heating rate of 10 K min^{-1}.

Simultaneous thermogravimetric (TG) and differential scanning calorimetry (DSC) analysis were conducted using Netzsch STA449 Jupiter F3 instrument. A 10-mg sample was used and heated up to 800 °C at a heating rate of 10 K min^{-1} in He flow (20 mL min^{-1}).

The adherence of the coating layer was evaluated by measuring the weight loss after ultrasonic treatment. The monolith catalysts were immersed in ethanol and then transferred to the ultrasonic bath (45 kHz, 600 W) at room temperature for 30 min. The monolith catalysts were dried at 90 °C for 1 h and the total weight loss was calculated.

The specific surface area was measured from the N_2 adsorption–desorption isotherms at −196 °C using the Brunauer-Emmet-Teller (BET) equation [36]. The samples were degassed at 150 °C overnight before the analysis was carried out on the Micromeritics Tristar II 3020 instrument. The pore volume and pore size distribution were estimated using the Barrett–Joyner–Halenda (BJH) method [37].

The coating morphology of the structured catalysts was examined by scanning electron microscopy (SEM, ZEISS Gemini Supra 35VP) equipped with energy dispersive X-ray spectrometry (EDX) for elemental mapping. Prior to analysis, the monolith was polished and coated with Pd plasma to inhibit charging.

2.5. Activity tests on the structured reactor

The structured reactor was made from stainless steel with an inner diameter of 21.1 mm and an outer diameter of 25.4 mm. The reactor was horizontally installed and heated by an electric oven, where the temperature was controlled by a thermocouple (type K) inside the reactor. The schematic representing the reactor setup is shown in Fig. 1a. Since the outer diameter of the monolith was 20 mm, an in-house designed catalyst holder with an inner diameter of 19.1 mm was used. Therefore, the structured catalysts were inserted in the holder and could be easily placed inside and removed from the reactor, avoiding any potential for gas channeling. Fig. 1b

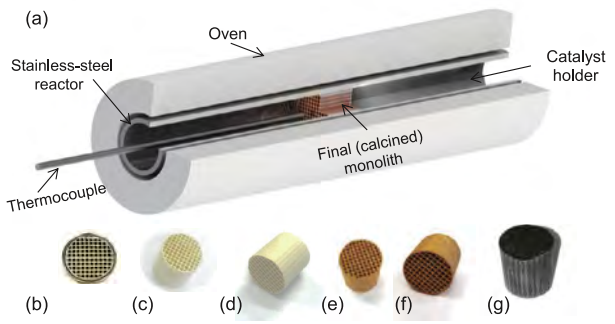

Fig. 1. (a) Schematic diagram of structured reactor setup; (b) photograph of monolith located inside the holder; (c-d) photograph of fresh cordierite monolith; (e-f) photograph of calcined monolith before reaction; (g) photograph of monolith after reaction.

illustrates the monolith inside the holder while photographs of fresh, calcined and spent monoliths are shown in Fig. 1c–f.

Prior to the reaction, the monolithic catalyst was reduced at 600 °C for 2 h in 50 vol% H_2/N_2 with a total flow of 200 mL min^{-1} (STP). Thereafter, the reactor was cooled down in pure N_2 flow for 2 h. Subsequently, a total flow of reactant gases of 500 mL min^{-1} (STP) was introduced, corresponding to a gas hourly space velocity (GHSV) of 7,760 h^{-1}. The ratio of $H_2/N_2/CO_2$ was 64/20/16 (i.e., $H_2/CO_2 = 4/1$). The reaction was carried out at 200–500 °C at ambient pressure and kept at each temperature for 1 h. Water formed during the reaction was removed by a cold trap. The outgas was analyzed using an online gas chromatograph (Agilent 7890A). A blank test was conducted, and no conversion was found over pure cordierite monolith in the stainless-steel reactor.

The CO_2 conversion (X_{CO_2}), CH_4 selectivity (S_{CH_4}), and CH_4 yield (Y_{CH_4}) were defined in Eqs. (2)–(4), where F^{in} and F^{out} are the molar flow rates in and out of the reactor (mol/h).

$$X_{CO_2}(\%) = \frac{F^{in}_{CO_2} - F^{out}_{CO_2}}{F^{in}_{CO_2}} \times 100 \quad (2)$$

$$S_{CH_4}(\%) = \frac{F^{out}_{CH_4}}{F^{in}_{CO_2} - F^{out}_{CO_2}} \times 100 \quad (3)$$

$$Y_{CH_4}(\%) = \frac{F^{out}_{CH_4}}{F^{in}_{CO_2}} \times 100 \quad (4)$$

3. Results and discussion

3.1. Characterization of NiFe LDHs

The XRD diffractograms of the dry powder obtained after urea hydrolysis were shown in Fig. 2. The characteristic peaks of LDHs structures were observed for both LDH-0.5M and LDH-0.05M samples with symmetric and sharp reflections of the basal (003), (006), (012) planes at 2θ of 11.3°, 22.9°, and 34.4°, respectively (MgAl-CO_3 LDHs, JCPDS 01-089-0460). Other peaks were ascribed to the nonbasal (015), (018), (110), and (113) planes. No other impure phases such as $Ni(HCO_3)_2$

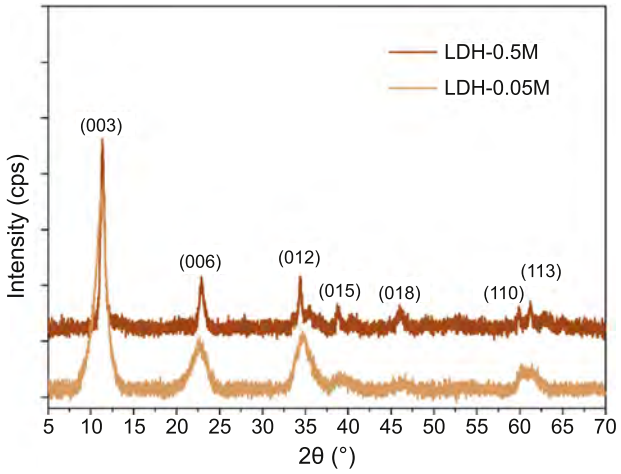

Fig. 2. XRD diffractograms of NiFe LDHs prepared by urea hydrolysis.

were detected [38]. Therefore, it can be confirmed that NiFe LDHs with high purity and crystallinity were successfully synthesized via urea hydrolysis at both total metal concentration of 0.5 M and 0.05 M.

The crystallite size in the stacking direction of LDH-0.5M was 16 nm, calculated by the Scherrer equation on the (003) diffraction. By diluting the stock solution, the LDHs particle size reduced significantly to only 6 nm. Moreover, it is worth mentioning that the pH of the stock solution was initially around 2.4–2.7. After 24 h of decomposition at 110 °C, the pH of the solution underwent a steep increase to 8.8–8.5, confirming the precipitation of both Ni^{2+} and Fe^{3+} ions [38].

The thermal decomposition of NiFe LDHs was analyzed by TG and DSC (Fig. 3). The TG curves of both LDHs sample shows common features for the decomposition of the layered structure [39]. Initially, physisorbed water and water in the interlayer were removed at 150–250 °C. Subsequently, dehydroxylation and decarbonation occurred simultaneously up to 500 °C. The total weight loss of LDH-0.05M was higher than LDH-0.5M, which could be ascribed to a higher amount of

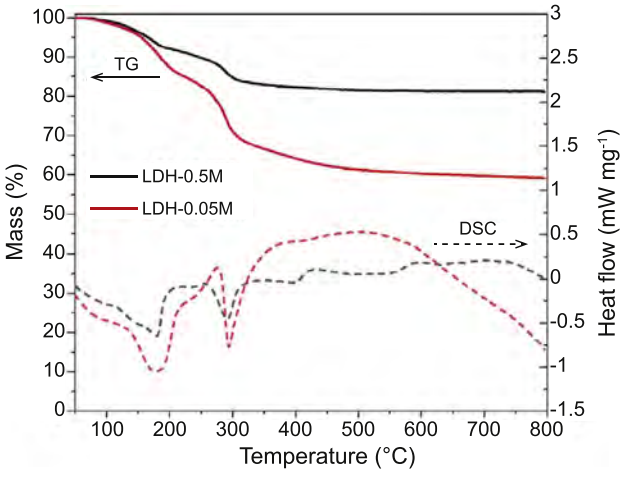

Fig. 3. Thermal analysis (TG and DSC) of NiFe LDHs.

water, hydroxyl, and anion in the interlayer [40,41]. In addition, the DSC curves display two endothermic peaks for both samples, corresponding to the two stages of weight loss. The high intensity of the peaks was also related to the high crystallinity of the samples, which is consistent with the XRD analysis (Fig. 2).

From the TG analysis, calcination at 600 °C would be sufficient for the decomposition of LDHs. Moreover, XRD analysis of calcined LDHs confirmed that LDHs structures were completely transformed into mixed metal oxides since only diffraction patterns of $NiFe_2O_4$ (JCPDS 00-054-0964) and NiO (JCPDS 01-089-5881) were identified (Fig. 4). The crystallite size of calcined LDH-0.5M was 22 nm, estimated by the Scherrer equation at 2θ of 43.4°. On the other hand, the crystallite size of LDH-0.05M was only 11 nm. Overall, increasing the concentration of stock solution would enlarge the particle size of LDHs [26].

To study the reducibility of the mixed oxides derived from LDHs, H_2-TPR analysis was performed (Fig. 5). Pure NiO was reported to be reduced at 340–410 °C, while Fe_2O_3 had a sequential reduction at 380 °C, 620 °C, and 715 °C [12,42]. However, the reduction of Fe was strongly enhanced in the presence of Ni that a gradual shift to lower temperature of reduction peaks would be observed [43]. As the theoretical weight percentage of Ni was 79 wt.%, the TPR profiles would show a similar pattern to the reduction of Ni species [44]. The first peak and the last peak in Fig. 5 could be assigned to the reduction of Fe^{3+} to $Fe^{8/3+}$ and Fe^{2+} to Fe, respectively. Two peaks at 350–450 °C were ascribed to the reduction of $Fe^{8/3+}$ and Ni^{2+} species in $NiFe_2O_4$ and NiO [45]. The peaks of LDH-0.05M were located at lower temperatures than that of LDH-0.5M, implying that the former was easier to be reduced than the latter.

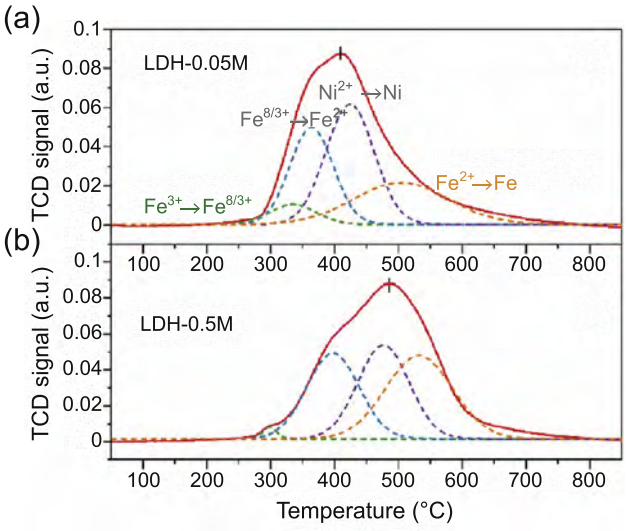

Fig. 5. TPR profiles of calcined (a) LDH-0.05M, and (b) LDH-0.5M.

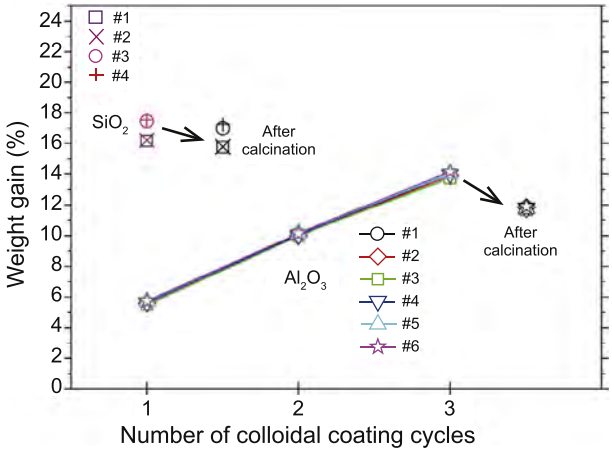

Fig. 6. The weight gain of monoliths after colloidal coating and calcination.

3.2. Characterization of the structured catalysts

3.2.1. Synthesis of the structured catalysts

The first step of structured catalysts preparation was dip coating support materials onto cordierite monoliths using colloidal solutions. The weight gain of monoliths after several colloidal coating cycles are presented in Fig. 6. For alumina coating, the washcoat layer reached 14 ± 0.5 wt% after three times of dip coating and drying. The weight gain of six

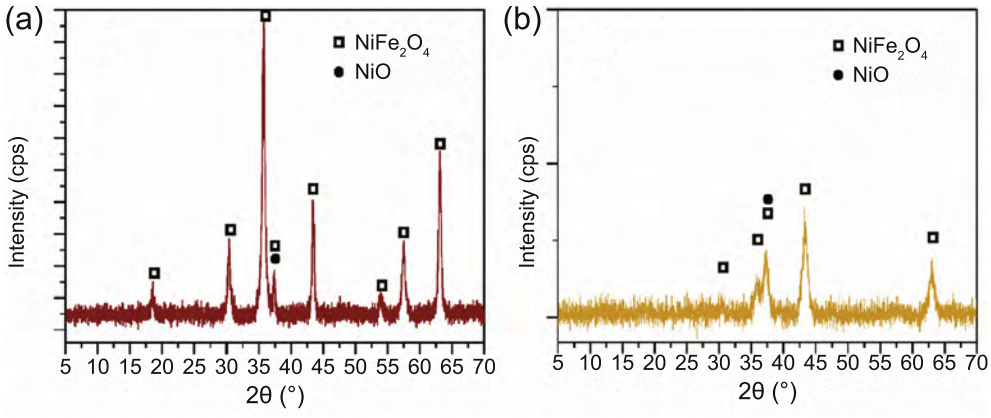

Fig. 4. XRD diffractograms of calcined NiFe LDHs: (a) LDH-0.5M and (b) LDH-0.05M.

different monoliths as shown in Fig. 6 demonstrates the high reproducibility of the synthesis procedure. On the other hand, one coating cycle was sufficient to achieve a washcoat layer of 17 ± 1 wt% for SiO_2, where the reproducibility was also confirmed by four monolith samples. Calcination was subsequently conducted for the fixation of the support materials onto cordierite. As a result, the weight of washcoat layers was reduced to 12 wt% for COR-AluCC and 16 wt% for COR-SiCC.

In the second step, NiFe LDHs were in-situ grown on the washcoated monoliths by urea hydrolysis at 110 °C for 24 h. After washing, drying, and calcination, the mixed oxides layer was fixed on the cordierite monoliths. The catalyst loading was defined as the percentage of the catalytic mass (mixed oxides) on the total weight of the final monolith, and the results are summarized in Table 1. It can be seen that Al_2O_3 was more advantageous for the deposition of the catalyst layer than SiO_2, even though SiO_2 was easier to be washcoated on the monolith.

3.2.2. Mechanical stability of the catalytic layers on the monoliths

In industrial applications, monolithic catalysts may experience different severe stresses such as thermal, chemical, and mechanical stresses. For gas-phase processes like methanation unit in PtG technology under stationary operating conditions, thermal and chemical stresses could be ruled out. However, mechanical stress can affect the amount of active phase on the washcoated monoliths. Ultrasonic vibration test is often used to estimate the effect of mechanical stress on the monoliths [46]. The adherence of the catalytic layer, calculated by the weight loss percentage, is reported in Table 1 for the calcined structured catalysts.

The adherence of the NiFe oxides layer on alumina-washcoated cordierite substrate was relatively high at 99.2% for COR-AluCC-0.5M and 99.6% for COR-AluCC-0.05M. By using stock solutions of 0.05 M, less amount of LDHs was deposited, which could be the reason for the stronger anchoring forces on the substrate. On the other hand, the COR-SiCC-0.5M showed slightly weaker adhesion. Nevertheless, the catalyst layer prepared by hydrothermal synthesis on the ceramic monoliths had good mechanical stability, similar to those prepared on metallic monoliths [22,23].

3.2.3. Textural properties of the structured catalysts

It is well-known that cordierite monoliths have an ultralow BET surface area, which was 1.2 $m^2\ g^{-1}$ in this study. After washcoating alumina and silica on the substrate, the surface area of COR-AluCC and COR-SiCC was larger at 18.3 $m^2\ g^{-1}$ and 17.0 $m^2\ g^{-1}$, respectively (Table 2). Thereafter, when LDH-0.5M was grown on the monolith and calcined, the surface area of both COR-AluCC and COR-SiCC further increased to 30.7 $m^2\ g^{-1}$ and 34.8 $m^2\ g^{-1}$, respectively. The pore volume of the final monolithic catalysts was larger than that of washcoated monoliths. For COR-AluCC-0.05M, the structured catalyst had a similar surface area yet slightly smaller pore volume than COR-AluCC.

Table 2
Textural properties of the washcoated monoliths and final calcined structured catalysts.

Samples	BET specific surface area ($m^2\ g^{-1}_{\text{total COR}}$)	BJH pore volume ($cm^3\ g^{-1}$)
COR-AluCC	18.3	0.064
COR-SiCC	17.0	0.045
COR-AluCC-0.5M	30.7	0.069
COR-AluCC-0.05M	18.3	0.047
COR-SiCC-0.5M	34.8	0.070

Cordierite monolith had a very low macropore volume with an average macropore size of 4.5 μm. In this study, the micro-mesopore size of washcoated and final monoliths was calculated from the N_2 physisorption isotherms using the BJH method. The COR-AluCC washcoated monoliths had an average pore size of 9 nm, while it was smaller at 7 nm for COR-SiCC (Fig. 7). After LDHs layers were formed and calcined, the pore sizes were reduced for both COR-AluCC-0.5M and COR-AluCC-0.05M, and obviously less for the latter. A bimodal pore size distribution of 4 nm and 6 nm was observed for COR-SiCC-0.5M and the pore sizes were also reduced compared to COR-SiCC.

3.2.4. Morphology of the structured catalysts

The in-situ grown LDHs structure was examined by SEM characterization (Fig. 8). For COR-AluCC-0.5M, the monolithic surface contained numerous hexagonal platelets intercrossed with each other, which was typical morphology of LDHs prepared by urea hydrolysis [47]. The lateral size of these platelets was around 1 μm (900 ± 100 nm), while the thickness was 30 ± 10 nm. When LDHs were formed using a diluted stock solution, the hexagonal platelets were smaller with a lateral diameter at 300 ± 50 nm, while the thickness was maintained at 35 ± 10 nm (COR-AluCC-0.05M, Fig. 8b). This is also consistent with the observed trend based on XRD study (Fig. 2). Hence, smaller LDHs particles were obtained at a lower metal concentration [24,26,48]. For COR-SiCC-0.5M

Table 1
Synthesis parameters, mass of in-situ grown LDHs, catalyst loading and the adherence of structured catalysts.

Structured catalysts	Colloidal solution	Total metal concentration	Mass of LDHs (mg)	Catalyst loading (wt%)	Adherence % (Weight loss %)
COR-AluCC-0.5M	Al_2O_3	0.5 M	175.8	2.85%	99.2% (0.8%)
COR-AluCC-0.05M	Al_2O_3	0.05 M	60.1	0.58%	99.6% (0.4%)
COR-SiCC-0.5M	SiO_2	0.5 M	112.8	2.24%	98.9% (1.1%)

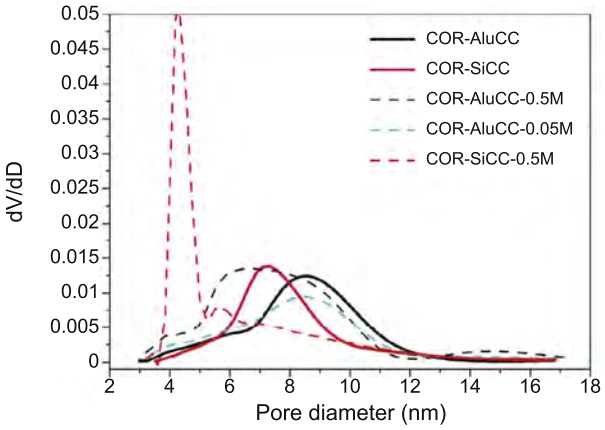

Fig. 7. Pore size distribution of washcoated monoliths and final structured catalysts.

(Fig. 8c), the regular flower-like clusters of NiFe LDHs were 2–3 times smaller as compared to COR-AluCC-0.5M. The thickness of the platelets was about 20–30 nm while the lateral dimension was difficult to measure.

The morphology of the final monolithic catalyst was also of great interest. Fig. 8d reveals that although significantly reduced in lateral size, the mixed oxides particles were still in its original hexagonal shape after calcination. This is beneficial for the dispersion of Ni and Fe active sites. Moreover, the ordered interconnection between the platelets was maintained, providing sufficient exposed surface area for reactant molecules to access to the active sites.

Furthermore, the cross-sectional SEM images of the channel wall were captured, and EDX elemental mapping was conducted. It is noteworthy that the washcoat layer using colloidal solutions of alumina and silica could not be observed or differentiated from cordierite ($2MgO \cdot 5SiO_2 \cdot 2Al_2O_3$). For COR-AluCC-0.5M, the deposition–precipitation of LDHs occurred on the porous exterior. Fig. 9a combined with Fig. 8a suggests that the LDHs platelets were grown perpendicularly on the cordierite surface, which could be explained by the evolution selection mechanism [22].

The LDHs layer on COR-AluCC-0.5M was around 20 μm, which was relatively thin compared to the channel wall thickness of 200 ± 50 μm. Moreover, the EDX mapping images show a spatial distribution of Ni and Fe on the LDHs region without visible segregation, demonstrating well-dispersed metal ions of LDHs.

For COR-SiCC-0.5M, the thickness of LDHs layers located outside the cordierite wall was similar at 15–27 μm. However, the elemental mapping detected both Ni and Fe even inside the pores of cordierite, which was not the case for COR-AluCC-0.5M. Thus, it could be assumed that Ni and Fe were diffused into the porous structure and LDHs layer deposited both inside the pore and on the surface of the monolith. This further explains why smaller pores were obtained for COR-SiCC-0.5M from the pore size distribution analysis (Fig. 7).

LDHs could only deposit due to chemical bonding between the material itself and the substrate surface, especially on a polar substrate [49]. Reports showed that LDHs were not feasible to grow on an un-anodized aluminum substrate [23], or FeCrAl-fiber without Al_2O_3 washcoat [20]. In this work,

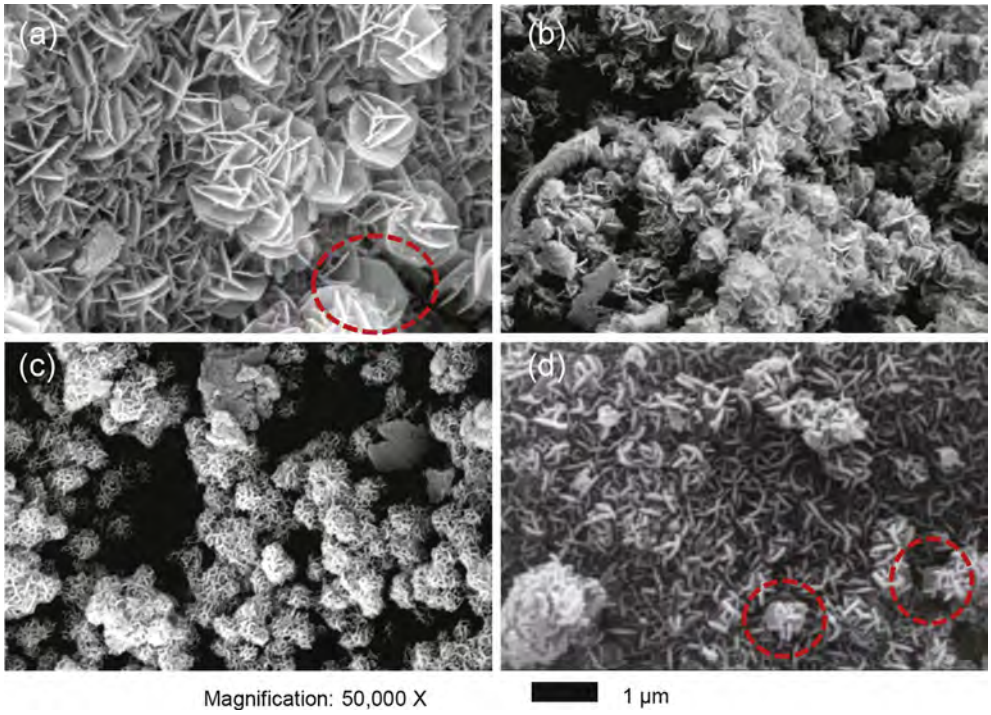

Fig. 8. SEM images of in-situ grown LDHs on monoliths of (a) COR-AluCC-0.5M, (b) COR-AluCC-0.05M, (c) COR-SiCC-0.5M and (d) calcined COR-AluCC-0.5M.

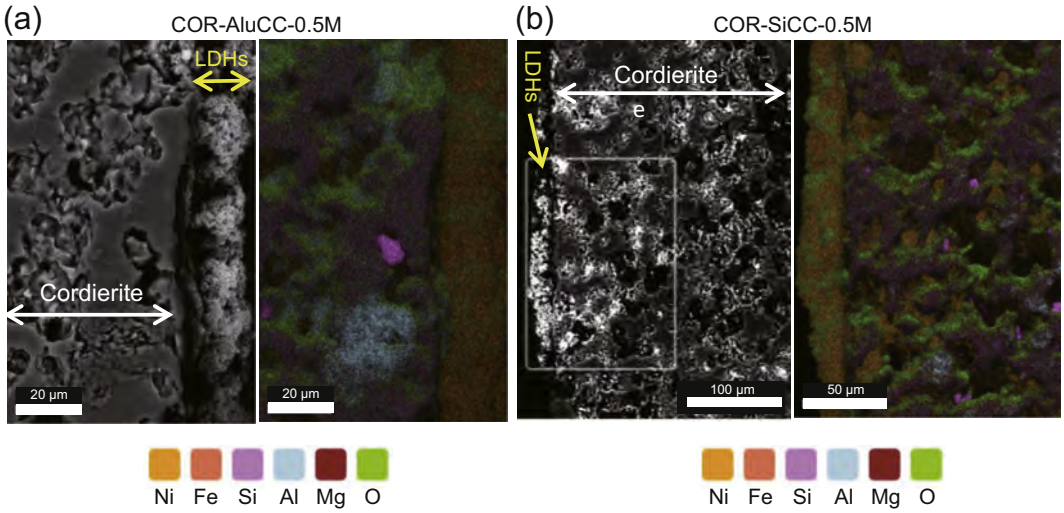

Fig. 9. SEM images and corresponding EDX elemental mapping of the cross-sectional channel wall of (a) COR-AluCC-0.5M and (b) COR-SiCC-0.5M monolith.

colloidal solutions with conductive properties should have played an important role in the anchoring of NiFe LDHs on the ceramic monoliths. In fact, SiO_2 nanoparticles (~25 nm, high viscosity) had a negative charge while Al_2O_3 nanoparticles (~50 nm, low viscosity) had a positive charge. The higher viscosity of silica colloidal could explain the successful ~17 wt% loading after one washcoating cycle, compared to three cycles of COR-AluCC [50]. Smaller silica particles could have diffused further inside the pore of cordierite monolith.

For COR-AluCC-0.05M, since a very diluted stock solution was used during urea hydrolysis, the in-situ grown LDHs layer at very low weight loading was unable to be observed from SEM imaging (Fig. 10). Although the thickness was not measurable, LDHs were found to be distributed on the surface of the porous cordierite, similar to COR-AluCC-0.5M.

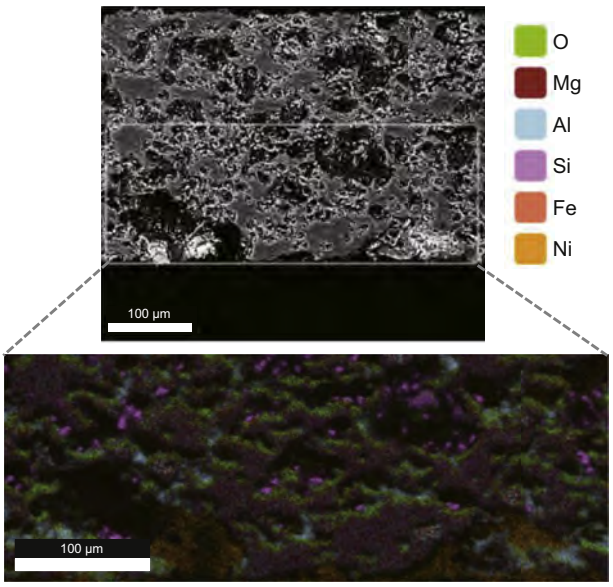

Fig. 10. SEM images and corresponding EDX elemental mapping of the cross-sectional channel wall of COR-AluCC-0.05M monolith.

3.3. Catalytic performance of the structured catalysts

The reaction was carried out at a temperature range of 200–500 °C with a total gas flow of 500 mL min^{-1} (STP). Although the monoliths had different coating thickness, the final monolithic catalysts were considered to have the same bulk volume. Accordingly, GHSV was calculated to be 7,760 h^{-1}. The active phase on the monoliths was assumed to be stable during the reaction at this high GHSV due to insignificant weight loss, as summarized in Table 3. Furthermore, the weight losses were mainly due to the reduction of oxides into metallic phases.

CO_2 conversion, CH_4 selectivity and CH_4 yield from CO_2 methanation over the monolithic catalysts are shown in Figs. 11, 12 and 13, respectively. Although CO_2 methanation was thermodynamically favored at low temperatures, it was difficult to achieve high CO_2 conversion due to kinetic barriers. As expected, all monolithic catalysts exhibited low activity at 200–250 °C. Interestingly, at 300 °C, COR-AluCC-0.5M showed excellent activity with the highest CO_2 conversion of 70%, while the other two showed poorer performance (Fig. 11). Although COR-SiCC-0.5M had much higher catalyst loading than COR-AluCC-0.05M, the former exhibited lower CO_2 conversion, especially at 350–450 °C. At higher temperature of 400–500 °C, the conversion started to decrease following the thermodynamic equilibrium curve.

During CO_2 hydrogenation to CH_4, reverse water gas shift reaction ($CO_2 + H_2 \leftrightarrow CO + H_2O$) could simultaneously

Table 3
Weight loss of structured catalysts after temperature-programmed CO_2 methanation at GHSV of 7,760 h^{-1}, atmospheric pressure.

Structured catalysts	Weight loss (%)[a]
COR-AluCC-0.5M	0.7
COR-AluCC-0.05M	0.4
COR-SiCC-0.5M	0.5

[a] weight loss = (weight $_{\text{total COR before}}$ − weight $_{\text{total COR after}}$)/ weight $_{\text{total COR before}}$.

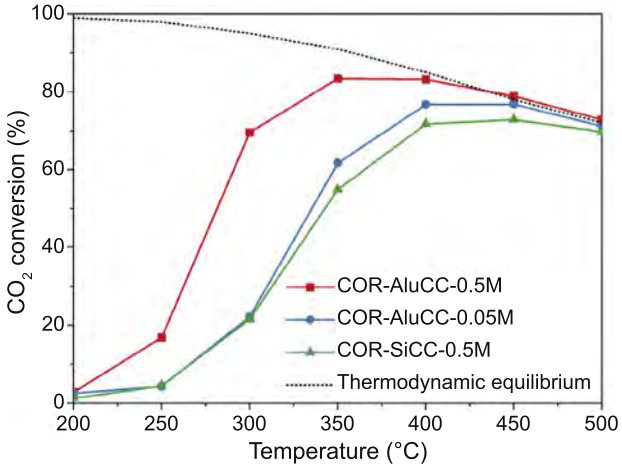

Fig. 11. CO_2 conversion of structured catalysts in CO_2 methanation at atmospheric pressure, GHSV of 7,760 h^{-1}, $H_2/N_2/CO_2$ = 64/20/16 vol%. The thermodynamic equilibrium conversion curve is also included for comparison.

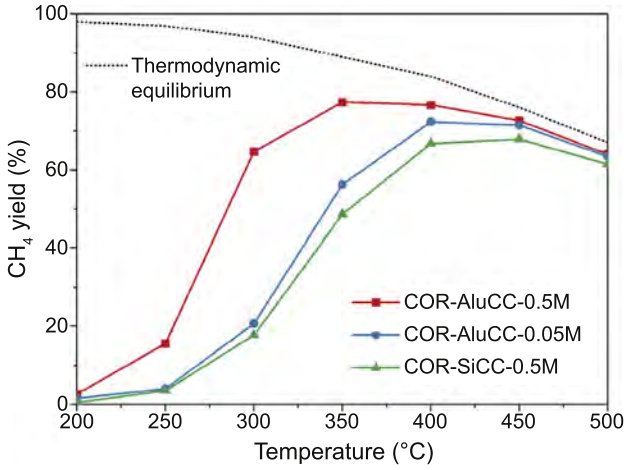

Fig. 13. CH_4 yield of structured catalysts in CO_2 methanation at atmospheric pressure, GHSV of 7,760 h^{-1}, $H_2/N_2/CO_2$ = 64/20/16 vol%. The thermodynamic equilibrium of CH_4 yield is also included for comparison.

occur which suppressed the formation of CH_4. Thus, CH_4 selectivity was an important indicator when evaluating structured catalysts for CO_2 methanation. The catalysts on COR-AluCC monoliths showed good selectivity towards methane (>90%) at 250–500 °C, demonstrating that CO_2 methanation was dominant under the reaction condition (Fig. 12). On the other hand, at 250–400 °C, lower CH_4 selectivity was obtained over COR-SiCC-0.5M.

The best catalytic performance of COR-AluCC-0.5M amongst others was confirmed by the methane yield (Fig. 13). This could be explained by the fact that COR-AluCC-0.5M had the highest catalyst loading with a thin and well-adhered layer on the honeycomb substrate. As for COR-AluCC-0.05M, the low-loading monolith exhibited even higher methane yield than that of COR-SiCC-0.5M.

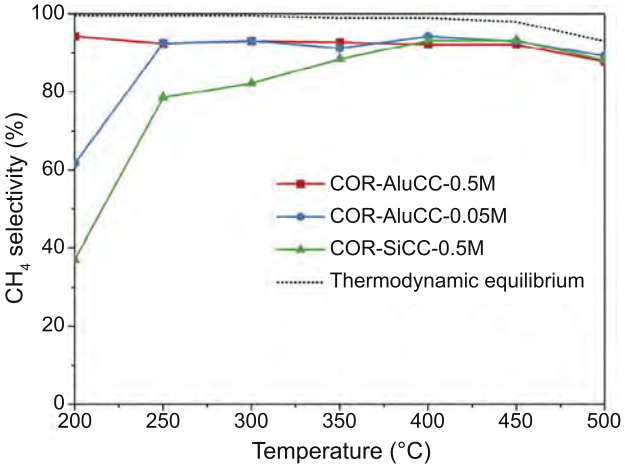

Fig. 12. CH_4 selectivity of structured catalysts in CO_2 methanation at atmospheric pressure, GHSV of 7,760 h^{-1}, $H_2/N_2/CO_2$ = 64/20/16 vol%. The thermodynamic equilibrium of CH_4 selectivity is also included for comparison.

Interestingly, COR-SiCC-0.5M contained similar content of the active phase as COR-AluCC-0.5M but its catalytic performance was much poorer. The EDX elemental mapping (Fig. 9b) revealed a large amount of Ni and Fe penetrated inside the pore structure of cordierite. These active sites would be more difficult to be reached by gaseous molecules. As a result, the diffusion path could be extended from the exterior (20 μm) to the whole channel wall thickness (200 ± 50 μm). Therefore, COR-SiCC-0.5M had lower methane yield even compared to COR-AluCC-0.05M. It is noteworthy that the higher activity of COR-AluCC-0.5M could also be due to the stronger metal-support interaction of Al_2O_3 than SiO_2 in supported catalysts [51,52].

It is important to note that a high reproducibility was achieved in terms of preparation and activity test of structured catalysts. The reproduced experimental data are reported in Table S1 and Fig. S1 in the supporting information.

4. Conclusions

A facile preparation method of structured catalysts for CO_2 methanation was developed. The thin layer of NiFe LDHs was successfully in-situ grown with excellent adherence to the washcoated cordierite monoliths via urea hydrolysis. Under CO_2 methanation reaction at high gas velocity, the catalytic layer exhibited higher activity on Al_2O_3-washcoated than SiO_2-washcoated monolith. It could be due to Al_2O_3 was only washcoated on the exterior of the monolith and the diffusion path for reactant gases was much shorter during methanation. A suitable high-concentration stock solution is also advantageous to achieve high catalyst loading on the ceramic monolith, thus high methane yield in CO_2 methanation. Therefore, COR-AluCC-0.5M monolithic catalyst is promising for the development of industrial high-throughput methanation reactor, an important unit of the PtG technology. The synthetic

strategy developed in this work could also be utilized to prepare structured catalysts for other catalytic processes.

Conflict of interest

The authors declare no conflict of interests.

Acknowledgments

The authors would like to thank the Norwegian Ministry of Education and Research for financial support.

Appendix A. Supplementary data

Supplementary data to this article can be found online at https://doi.org/10.1016/j.gee.2020.09.004.

References

[1] D. Reichle, J. Houghton, B. Kane, J. Ekmann, Carbon sequestration research and development, Oak Ridge National Lab., TN (US), 1999.
[2] S. Rönsch, J. Schneider, S. Matthischke, M. Schlüter, M. Götz, J. Lefebvre, P. Prabhakaran, S. Bajohr, Fuel 166 (2016) 276–296.
[3] P. Sabatier, J.B. Senderens, Comptes Rendus Acad. Sci. 1902, Section VI - Chimie 514–517.
[4] C. Vogt, M. Monai, G.J. Kramer, B.M. Weckhuysen, Nat. Catal. 2 (2019) 188–197.
[5] M.a.A. Aziz, A.A. Jalil, S. Triwahyono, A. Ahmad, Green Chem. 17 (2015) 2647–2663.
[6] M. Bailera, P. Lisbona, L.M. Romeo, S. Espatolero, Renew. Sustain. Energy Rev. 69 (2017) 292–312.
[7] K. Ghaib, F.Z. Ben-Fares, Renew. Sustain. Energy Rev. 81 (2018) 433–446.
[8] P. Frontera, A. Macario, M. Ferraro, P. Antonucci, Catalysts 7 (2017) 59.
[9] C. Lv, L. Xu, M. Chen, Y. Cui, X. Wen, Y. Li, C.E. Wu, B. Yang, Z. Miao, X. Hu, Q. Shou, Front. Chem. (2020). https://www.frontiersin.org/articles/10.3389/fchem.2020.00269/full.
[10] M.P. Andersson, T. Bligaard, A. Kustov, K.E. Larsen, J. Greeley, T. Johannessen, C.H. Christensen, J.K. Nørskov, J. Catal. 239 (2006) 501–506.
[11] A.L. Kustov, A.M. Frey, K.E. Larsen, T. Johannessen, J.K. Nørskov, C.H. Christensen, Appl. Catal. Gen. 320 (2007) 98–104.
[12] D. Pandey, K. Ray, R. Bhardwaj, S. Bojja, K.V.R. Chary, G. Deo, Int. J. Hydrogen Energy 43 (2018) 4987–5000.
[13] H.L. Huynh, Z. Yu, Energy Technol. 8 (2020) 1901475.
[14] M. Lehner, R. Tichler, H. Steinmüller, M. Kopper (Eds.), in: The Power-to-Gas Concept, SpringerBriefs in Energy. Springer, Cham. 2014, pp. 41–61.
[15] E. Tronconi, G. Groppi, C.G. Visconti, Curr. Opin. Chem. Eng. 5 (2014) 55–67.
[16] T.A. Nijhuis, A.E.W. Beers, T. Vergunst, I. Hoek, F. Kapteijn, J.A. Moulijn, Catal. Rev. 43 (2001) 345–380.
[17] H. Chen, L. Hu, M. Chen, Y. Yan, L. Wu, Adv. Funct. Mater. 24 (2014) 934–942.
[18] W. Li, G. Fan, L. Yang, F. Li, ChemCatChem 8 (2016) 2724–2733.
[19] H. Li, D. Zhang, P. Maitarad, L. Shi, R. Gao, J. Zhang, W. Cao, Chem. Commun. 48 (2012) 10645–10647.
[20] R. Chai, S. Fan, Z. Zhang, P. Chen, G. Zhao, Y. Liu, Y. Lu, ACS Sustain. Chem. Eng. 5 (2017) 4517–4522.
[21] H. Chen, F. Zhang, S. Fu, X. Duan, Adv. Mater. 18 (2006) 3089–3093.
[22] X. Guo, S. Xu, L. Zhao, W. Lu, F. Zhang, D.G. Evans, X. Duan, Langmuir 25 (2009) 9894–9897.
[23] Z. Lü, F. Zhang, X. Lei, L. Yang, S. Xu, X. Duan, Chem. Eng. Sci. 63 (2008) 4055–4062.
[24] T. Xue, R. Li, Y. Gao, Q. Wang, Chem. Eng. J. 384 (2020) 123284.
[25] M. Adachi-Pagano, C. Forano, J.-P. Besse, J. Mater. Chem. 13 (2003) 1988–1993.
[26] M. Ogawa, H. Kaiho, Langmuir 18 (2002) 4240–4242.
[27] A. Vita, C. Italiano, L. Pino, P. Frontera, M. Ferraro, V. Antonucci, Appl. Catal. B Environ. 226 (2018) 384–395.
[28] C. Janke, M.S. Duyar, M. Hoskins, R. Farrauto, Appl. Catal. B Environ. 152–153 (2014) 184–191.
[29] C. Fukuhara, K. Hayakawa, Y. Suzuki, W. Kawasaki, R. Watanabe, Appl. Catal. Gen. 532 (2017) 12–18.
[30] S. Ratchahat, M. Sudoh, Y. Suzuki, W. Kawasaki, R. Watanabe, C. Fukuhara, J. CO_2 Util. 24 (2018) 210–219.
[31] J.Y. Ahn, S.W. Chang, S.M. Lee, S.S. Kim, W.J. Chung, J.C. Lee, Y.J. Cho, K.S. Shin, D.H. Moon, D.D. Nguyen, Fuel 250 (2019) 277–284.
[32] V. Meille, Appl. Catal. Gen. 315 (2006) 1–17.
[33] P. Avila, M. Montes, E.E. Miró, Chem. Eng. J. 109 (2005) 11–36.
[34] U. Holzwarth, N. Gibson, Nat. Nanotechnol. 6 (2011) 534-534.
[35] A. Gervasini, A. Auroux, Ed. UK (2013).
[36] S. Brunauer, P.H. Emmett, E. Teller, J. Am. Chem. Soc. 60 (1938) 309–319.
[37] E.P. Barrett, L.G. Joyner, P.P. Halenda, J. Am. Chem. Soc. 73 (1951) 373–380.
[38] X. Wu, Y. Du, X. An, X. Xie, Catal. Commun. 50 (2014) 44–48.
[39] F. Cavani, F. Trifirò, A. Vaccari, Catal. Today 11 (1991) 173–301.
[40] H. Wang, G. Fan, C. Zheng, X. Xiang, F. Li, Ind. Eng. Chem. Res. 49 (2010) 2759–2767.
[41] H. Wang, J. Gao, Z. Li, Y. Ge, K. Kan, K. Shi, CrystEngComm 14 (2012) 6843–6852.
[42] D. Beierlein, D. Häussermann, M. Pfeifer, T. Schwarz, K. Stöwe, Y. Traa, E. Klemm, Appl. Catal. B Environ. 247 (2019) 200–219.
[43] D. Shi, R. Wojcieszak, S. Paul, E. Marceau, Catalysts 9 (2019) 451.
[44] R. Brown, M.E. Cooper, D.A. Whan, Appl. Catal. 3 (1982) 177–186.
[45] T. Li, H. Wang, Y. Yang, H. Xiang, Y. Li, Fuel Process. Technol. 118 (2014) 117–124.
[46] D. Wu, Y. Zhang, Y. Li, J. Ind. Eng. Chem. 56 (2017) 175–184.
[47] Y. Han, H. Li, X. Ma, Z.H. Liu, Solid State Sci. 11 (2009) 2149–2155.
[48] J. Liu, Y. Li, X. Huang, G. Li, Z. Li, Adv. Funct. Mater. 18 (2008) 1448–1458.
[49] J.A. Gursky, S.D. Blough, C. Luna, C. Gomez, A.N. Luevano, E.A. Gardner, J. Am. Chem. Soc. 128 (2006) 8376–8377.
[50] C. Agrafiotis, A. Tsetsekou, I. Leon, J. Am. Ceram. Soc. 83 (2000) 1033–1038.
[51] D. Pandey, G. Deo, Chem. Eng. Commun. 203 (2016) 372–380.
[52] I. Wysocka, J. Hupka, A. Rogala, Catalysts 9 (2019) 540.

Supporting information

Structured NiFe catalysts derived from in-situ grown layered double hydroxides on ceramic monolith for CO_2 methanation

Huong Lan Huynh[a], Wakshum Mekonnen Tucho[b], Zhixin Yu[a,*]

[a] Department of Energy and Petroleum Engineering, University of Stavanger, 4036 Stavanger, Norway

[b] Department of Mechanical and Structural Engineering and Material Science, University of Stavanger, 4036 Stavanger, Norway

***Corresponding author:**

Prof. Zhixin Yu

E-mail address: zhixin.yu@uis.no

Department of Energy and Petroleum Engineering,

University of Stavanger, 4036 Stavanger, Norway

Tel: +47 51 83 22 38

Fax: +47 51 83 20 50

Table S1. Repeatability on catalyst preparation of structured catalysts.

Samples	Catalysts loading of monolith #1	Catalysts loading of monolith #2
COR-AluCC-0.5M	2.85%	2.95%
COR-AluCC-0.05M	0.58%	0.56%
COR-SiCC-0.5M	2.30%	1.87%

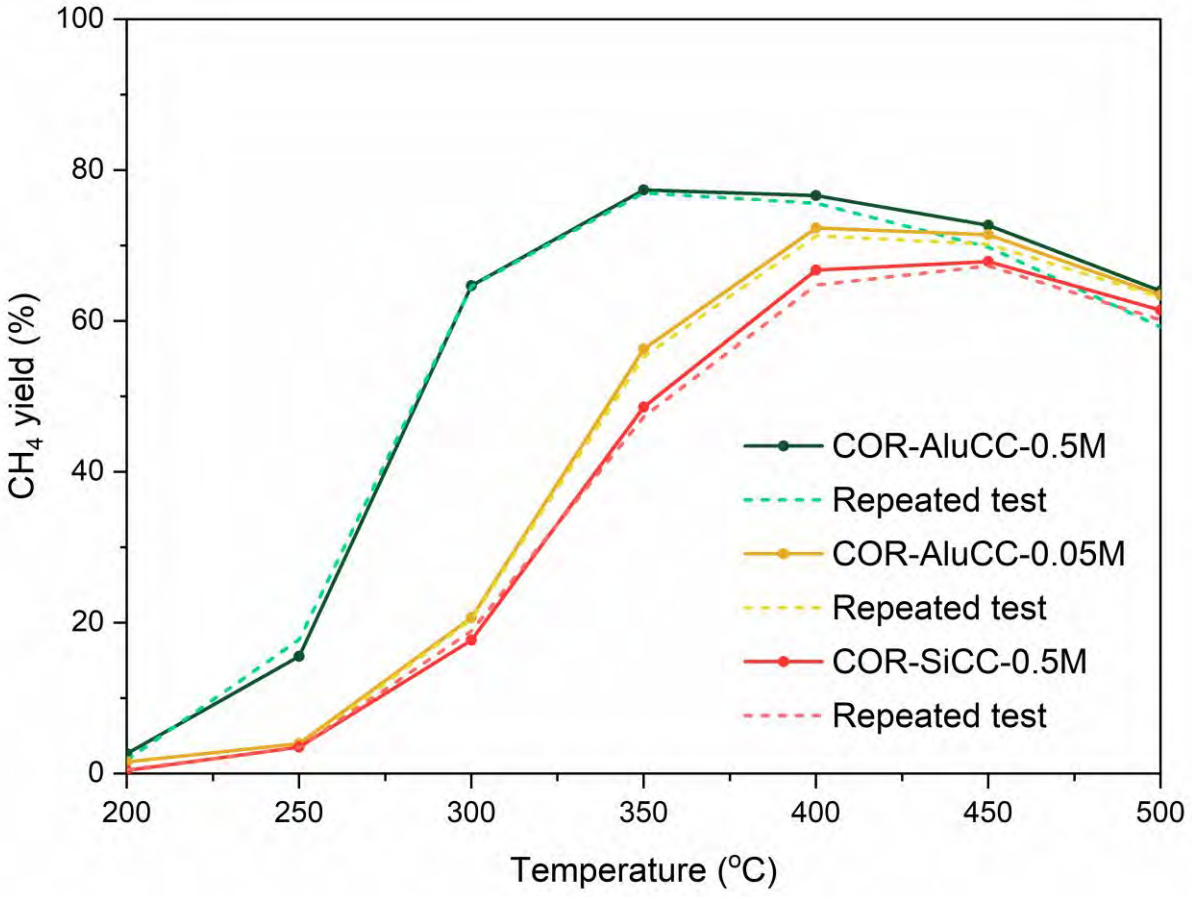

Figure S1. Repeatability on CH_4 yield of structured catalysts in CO_2 methanation at 7,760 h^{-1}, $H_2/N_2/CO_2$ = 64/20/16 vol.%, atmospheric pressure.

Appendix F – Paper VI

Bed packing configuration and hot-spot utilization for low-temperature CO_2 methanation on monolithic reactor

H. L. Huynh, W. M. Tucho, Q. Shen and Z. Yu

Chemical Engineering Journal **2022**, *428*, 131106

DOI: 10.1016/j.cej.2021.131106

Chemical Engineering Journal 428 (2022) 131106

Contents lists available at ScienceDirect

Chemical Engineering Journal

journal homepage: www.elsevier.com/locate/cej

Bed packing configuration and hot-spot utilization for low-temperature CO_2 methanation on monolithic reactor

Huong Lan Huynh [a], Wakshum Mekonnen Tucho [b], Qi Shen [c,*], Zhixin Yu [a,*]

[a] Department of Energy and Petroleum Engineering, University of Stavanger, Stavanger 4036, Norway
[b] Department of Mechanical and Structural Engineering and Material Science, University of Stavanger, Stavanger 4036, Norway
[c] Institute of New Energy, School of Chemistry and Chemical Engineering, Shaoxing University, Shaoxing 312000, China

ARTICLE INFO

Keywords:
CO_2 methanation
Hot-spot
Bed packing
Monolithic reactor
Low-temperature

ABSTRACT

The revival of CO_2 methanation (Sabatier reaction) as part of the large-scale Power-to-Gas technology has stimulated the development of novel reactor concepts for better heat management due to its exothermic nature. The generation of hot-spots in fixed bed reactors could reduce methane yield, accelerate catalyst deactivation, and potentially cause thermal runaway. However, hot-spots could be utilized to achieve outstanding CO_2 methanation performance at low temperatures and high gas flow rate in monolithic reactors, whereas strategic bed packing configurations could boost the performance of low-activity catalytic beds. We prepared NiFe catalysts derived from in-situ grown layered double hydroxides via urea hydrolysis on washcoated cordierite honeycomb substrate with varying activities. Temperature profiles by both experimental and computational fluid dynamic (CFD) studies revealed hot-spot formation along catalytic beds. Hot-spots increased the catalytic beds' temperature due to high thermal conductivity of cordierite monolith, thus accelerated the reaction. The monolithic reactor with a single-monolith bed exhibited a methane yield of 16.5% at 250 °C, which was significantly increased to 80.4% on the reactor with three-monolith bed of the same catalyst at similar reaction condition with a constant ratio of catalyst mass to gas flow rate. A combined low-high activity monolithic bed was proposed which demonstrated high methane yield and excellent stability. Interestingly, the methane yields were higher at a gas flow rate of 1500 mL/min than that at 500 mL/min, again ascribed to the beneficial effect of hot-spot formation on monolithic reactors. Therefore, strategic bed packing configuration plays an important role in the optimization of monolithic methanation reactors, and hot-spot formation could be exploited to achieve excellent CO_2 methanation performance at low temperatures.

1. Introduction

Discovered more than one hundred years ago by Nobel laureate Paul Sabatier, CO_2 methanation reaction which converts carbon monoxide (CO) or carbon dioxide (CO_2) and hydrogen (H_2) into methane (CH_4) is one of the most important chemical reactions for heterogeneous catalysis research [1,2]. It has been used as an important purification step to remove traces of CO and CO_2 from H_2-rich gases for ammonia production, for example. Recently, renewed interest in methanation has been driven by the energy transition towards renewable sources, e.g., solar and wind power [3]. As renewable energies become an important part of the transitional energy system, the inherent intermittency of wind and solar power has appeared to be problematic since it affects the balance between energy supply and demand. Power-to-Gas (PtG) technology has been proposed as a promising solution for large-scale energy storage of renewable electricity, in which CO_2 methanation is an important process [4,5]. The concept aims to use surplus renewable electricity to produce hydrogen via water electrolysis. The green hydrogen is further reacted with carbon dioxide to produce synthetic natural gas (SNG).

$$CO_2 + 4H_2 \leftrightarrow CH_4 + 2H_2O,\ \Delta H_{298K} = -165.0\ \text{kJ/mol} \quad (1)$$

The Sabatier reaction (Equation. (1)) is thermodynamically favored at low temperatures and high pressures. However, it is difficult to obtain high conversion at low temperatures of 200–350 °C due to kinetic limitations. Thus, supported catalysts such as noble metals (e.g., Ru, Rh) or earth-abundant metals (e.g., Ni, Fe, Co) are applied in the process. Because of affordable cost and good catalytic performance, Ni-based catalysts are widely used in most industrial applications [6,7]. The

* Corresponding authors.
E-mail addresses: zhixin.yu@uis.no (Q. Shen), zhixin.yu@uis.no (Z. Yu).

https://doi.org/10.1016/j.cej.2021.131106
Received 5 May 2021; Received in revised form 15 June 2021; Accepted 28 June 2021
Available online 3 July 2021

Sabatier reaction is highly exothermic thus a large amount of heat could be generated during large-scale PtG process. This would cause hot-spots inside the reactor and potentially lead to thermal runaway. In addition, the CO_2 conversion and CH_4 selectivity will be reduced [8]. It has been reported that a temperature spike of 227 °C was recorded in an annular fixed-bed reactor filled with commercial Ni/Al_2O_3 trilobes catalysts during CO_2 methanation at an operating temperature of 225 °C, pressure of 0.4 MPa and gas hourly space velocity (GHSV) of 6000 h^{-1} [9]. Although a high methane yield of 83% was obtained, hot-spot formation appears to be the big challenge that should be tackled by proper reactor heat management.

New reactor concepts are focusing on improving the heat management of reactors in two-phase systems such as wall-cooled fixed bed, fluidized bed, coated honeycombs, or three-phase systems such as bubble column [10]. One of the most recent strategies to improve the methanation performance is the introduction of monolithic honeycomb catalysts. Structured reactors have the advantage of low pressure drop due to the channeling nature. The tunable thickness of catalyst layer which affects the diffusion length could be beneficial to optimize the efficiency of the catalysts. Moreover, high volumetric flow rates of feed gases can be handled by structured reactors with improved heat and mass transfer, especially for better heat transfer since monolithic substrates typically have good thermal conductivity [11]. There has also been an increasing application of structured catalysts and reactors for CO_2 methanation. For instance, Fukuhara *et al.* reported that under similar methanation conditions, honeycomb-type catalytic bed showed a flat temperature profile while granular-type catalytic bed showed a temperature rise of 20 °C due to poor heat dissipation of the conventional fixed bed [12]. However, at a higher gas flow rate, hot-spot formation was observed on the honeycomb monolithic bed. Great efforts to further improve heat and mass transfer along the monolithic bed have been devoted [13,14]. It was found that a less severe hot-spot formation could be obtained while high CO_2 conversion and CH_4 selectivity were maintained on a multi-stacked catalyst bed [15]. The researchers have been innovative by designing the bed packing configuration containing a sequence of coated and uncoated Ni/CeO_2 aluminum honeycomb-fin monolithic catalysts. Thus, the catalytic activity was discretely distributed along the reactor bed length which resulted in an optimal heat transfer and reaction rate. Kosaka *et al.* has recently reported that an increasing catalytic activity along the tubular catalyst bed could also prevent hot-spot formation compared to the uniform catalytic bed [16,17]. However, it was not anticipated that the performance of the low-activity catalysts was boosted by the observed hot-spots. Apparently, controlled hot-spot formation could be utilized for a more sustainable catalytic process and has been deliberately employed in certain reactor designs [18,19]. Therefore, it is important to fundamentally understand the effect of catalytic activity along the catalytic bed on the reactor temperature profiles.

We have recently developed a novel, highly reproducible and easily scalable synthesis procedure to prepare NiFe catalysts derived from layered double hydroxides (LDHs) precursors on cordierite (ceramic) honeycomb substrate [20]. The bimetallic honeycomb catalysts have shown excellent performance in CO_2 methanation. In this study, the preparation parameters were optimized to obtain honeycomb catalysts with different activities. We studied the effect of metal concentrations on catalyst loading and its performance in CO_2 methanation. The temperature profiles of the structured reactor packed with monolithic catalysts were investigated. Hot-spot formation was detected on the catalytic bed during CO_2 methanation at different operating temperatures and gas flow rates. We then investigated the effect of bed packing configurations on the formation of hot-spot and the overall CO_2 methanation performance. A computational fluid dynamic (CFD) model was developed to verify the experimental results. Long-term stability tests were also carried out to evaluate the monolithic catalysts for industrial applications of PtG technology. To the best of our knowledge, this is the first study to report CO_2 methanation on ceramic honeycomb monolithic reactors with different bed packing configurations.

2. Experimental

2.1. Catalyst preparation

The preparation method has been adapted from our previous work [20]. The honeycomb cordierite substrates (Applied Ceramics Inc., USA) were cylindrical with an outer diameter of 19 mm and a length of 20 mm. It consists of 230 cells per square inch (cpsi) with a channel wall thickness of 200 ± 50 μm. Prior to the synthesis steps, the substrates were washed with ethanol and distilled water and dried at 90 °C overnight. In order to increase the surface area, the ceramic substrates were dip-coated with alumina colloidal (Alfa Aesar, 20 wt% suspensions in water, particle size of 50 nm) three times with subsequent drying to obtain a washcoated layer with 14 wt% alumina. The washcoated substrate was calcined at 600 °C for 6 h with a heating ramp of 2 °C/min.

For the formation of NiFe-CO_3 LDHs, aqueous stock solutions consisting of nickel (II) nitrate hexahydrate, iron (III) nitrate nonahydrate, and urea (all from Merck Millipore) with total molar concentrations from 0.05M to 2M were used. The molar ratio between urea and total metal ion of Ni^{2+} and Fe^{3+} was 9.9 while the Fe^{3+}/Ni^{2+} molar ratio was kept constant at 0.25. The washcoated honeycomb was then immersed in a 45-mL stock solution contained by a Teflon-lined hydrothermal autoclave. Urea hydrolysis was carried out at 110 °C for 24 h. Subsequently, the obtained monolith was washed, dried, and calcined at 600 °C for 6 h with a ramp rate of 2 °C/min. The final monoliths are denoted as COR-*x*M, where *x* is the total metal concentration during preparation.

To characterize the as-prepared NiFe-CO_3 LDHs precursors, the solid precipitate in the autoclave after urea hydrolysis was collected, washed, and dried. These LDHs powders are named LDH-*x*M, where *x* is also the total metal concentration. The dry LDHs powders were calcined at similar conditions as the monolithic catalysts.

2.2. Catalyst characterization

X-ray diffraction (XRD) diffractograms of the LDHs powder precursors were recorded using D8 Advance micro-diffractometer (Bruker) equipped with CuKα radiation. The scanning speed was 1°/min over a 2θ range from 5° to 70°.

Temperature programmed reduction (TPR) of the calcined precursors was carried out on Autochem II (Micromeritics) equipped with a thermal conductivity detector (TCD). In a typical experiment, 35 mg of the calcined sample was firstly degassed at 200 °C for 30 min. H_2 gas flow (10 vol% H_2/Ar) was then introduced and the sample was heated from 50 °C to 950 °C at a heating rate of 10 °C/min.

The adsorption–desorption isotherms of N_2 at −196 °C was measured using Tristar II 3020 (Micromeritics) instrument. The monolithic sample was degassed at 150 °C overnight prior to the analysis. The surface area was then calculated using the Brunauer-Emmet-Teller (BET) equation [21] while the pore volume was estimated using the Barrett-Joyner-Halenda (BJH) method [22].

The morphology and elemental mapping of the catalytic layers were characterized with scanning electron microscopy (SEM), Gemini SUPRA 35VP (Carl Zeiss Jena) equipped with EDAX energy dispersive X-ray spectroscopy (EDS). For better image analysis, the monolithic samples were polished using very fine SiC abrasive grits. After cleaning with ethanol and drying, the samples were then coated with Pd to inhibit charging.

The inductive coupled plasma optical emission spectrometry (ICP-OES) method was applied to analyze the elemental compositions of dried LDHs precursors. The samples were dissolved in chloric acid and nitric acid prior to analysis by Optima 4300 DV (PerkinElmer) instrument.

2.3. Catalytic activity tests and temperature profile studies

CO_2 methanation tests were performed in a stainless steel structured reactor (inner diameter of 21.1 mm) heated by an electric tubular oven. An in-house designed catalyst holder (inner diameter of 19.1 mm) was used so that the monolith could be inserted inside the reactor without any gas channeling or flow bypass effect.

The catalytic performance of individual monolithic catalyst was carried out at a total gas flow of 500 mL/min (STP), corresponding to a GHSV of 7760 h^{-1}. The ratio of $H_2/N_2/CO_2$ in the gas mixture was 64/20/16 vol% (i.e., H_2/CO_2 = 4/1). Temperature-programmed reaction was conducted from 200 to 500 °C at ambient pressure with a temperature step of 50 °C. The temperature was controlled by a type-K thermocouple installed inside the reactor at the gas inlet. Prior to the reaction, the monolithic catalyst was in-situ reduced at 600 °C for 4 h in flowing H_2 gas (50 vol% H_2/N_2, 200 mL/min, STP).

For the study of temperature profiles along the catalytic bed, a multi-point thermocouple (Watlow) was installed to measure temperatures at 6 different positions, as illustrated in Fig. 1. The catalytic bed contained three monoliths with a total length of 60 mm. The monoliths were drilled through at the center (hole diameter of 3 mm) so that the multi-point thermocouple could be inserted. The temperature of the oven was controlled by another thermocouple (T_{oven}) located outside of the reactor. The temperature of the gas inlet was also monitored by the thermocouple at the gas inlet (T_{gas_in}). The reaction temperature was varied from 200 to 300 °C at ambient pressure with different gas flow rates of up to 3000 mL/min (STP). The stability test was carried out at T_{oven} of 250 °C at a gas flow rate of 1500 mL/min (STP) for 100 h.

At the reactor gas outlet, a cold trap was used to remove water formed during reaction before the outgases were introduced into the online gas chromatograph (GC 7890A, Agilent) for analysis. A blank test of the pure honeycomb substrate was conducted, and no catalytic conversion was observed. The CO_2 conversion (X_{CO2}), CH_4 yield (Y_{CH4}), and CH_4 productivity (P_{CH4}) were defined in Eqs. (2), (3), (4), where F^{in} and F^{out} are the molar flow rates in and out of the reactor (mol/h).

$$X_{CO2}(\%) = \frac{F^{in}_{CO2} - F^{out}_{CO2}}{F^{in}_{CO2}} \times 100 \quad (2)$$

$$Y_{CH4}(\%) = \frac{F^{out}_{CH4}}{F^{in}_{CO2}} \times 100 \quad (3)$$

$$P_{CH4}\left(mol/h.g_{cat}\right) = \frac{F^{out}_{CH4}}{m_{cat}} \quad (4)$$

2.4. CFD model development

Numerical simulations were developed to verify the thermal profiles along the monolithic beds obtained from experimental studies. A discretized three-dimensional (3D) computational geometry of one-eighth of a monolith with the same dimensions as lab-scale experiments was built (Fig. 2), which consisted of channel blocks and porous walls. Governing equations of the CFD models are reaction rate, continuity, momentum, mass, and energy equations as described in detail in Table S1 in the supporting information. All boundary conditions and parameters are listed in Table S2 and S3. The equations were solved by finite element based multiphysics simulation software COMSOL Multiphysics® version 5.5.

The model presents channels in monolithic reactor with a pseudo-homogeneous approach. The reaction rate and equilibrium equation were adapted from Koschany *et al.* [23,24]. The fluid flow was assumed as a fully developed laminar flow with weak compressibility, and the average gas velocity was set at the inlet. The temperature-dependent transport properties of the multicomponent gas mixtures (heat capacity, thermal conductivity, and viscosity) were automatically calculated by the software with a mass-fraction weighted rule. The gas diffusivity was estimated using Fuller-Schettler-Giddings equations while the effective binary diffusion coefficients in the porous walls were calculated with the Bruggeman correction model [25–27]. Atmospheric pressure was applied, and the pressure drop was neglected. The energy equation defines the reacting gas temperature in the channels and conductive heat transfer in the wall structure. The gas mixture was set at desired inlet temperature and heat generated from the reaction was the main heat source, while the ambient temperature was set as the oven temperature. Moreover, no-slip conditions were also applied together with a symmetric boundary condition since the modeling domain was reduced to one-eighth of the full reactor geometry.

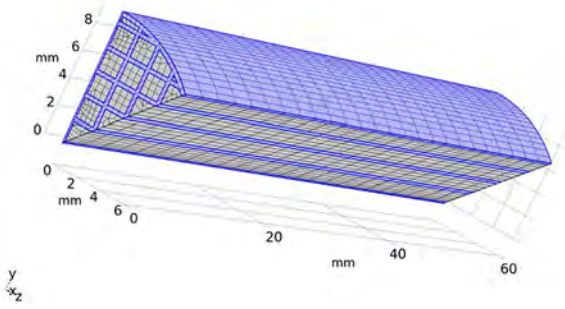

Fig. 2. Discretized one-eighth of the full monolithic reactor geometry; the structured mesh has 13296 elements.

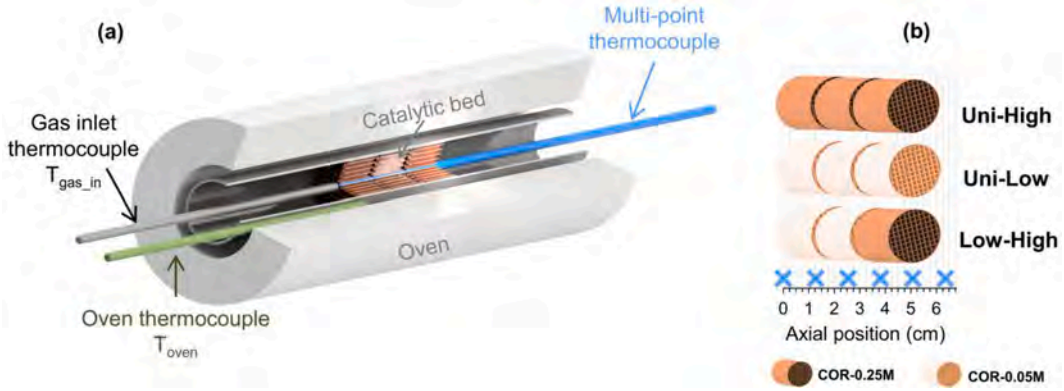

Fig. 1. (a) Illustration of upgraded structured reactor setup for temperature profile studies. (b) The axial position of measuring points by the multi-point thermocouple with respect to the gas inlet position of three different bed packing configurations, i.e., Uni-High, Uni-Low, and Low-High.

3. Results and discussion

3.1. Characterization of NiFe-CO_3 LDHs prepared at different metal concentrations

The influence of total metal concentrations during urea hydrolysis on the synthesis of as-prepared precursors was revealed by XRD analysis. The XRD diffractograms of dry precursors (Fig. 3) showed that highly crystalline LDHs materials were formed by using metal concentrations of up to 1M. Characteristic peaks of LDHs structures were observed for all samples except for LDH-2M, e.g., symmetric and sharp reflections at 2 of 11.5°, 23.3°, and 34.5° could be ascribed to the basal (003), (006), (012) planes, respectively (NiFe-CO_3 LDHs, JCPDS 00–051-0463). LDH-0.25M has the best crystallinity thus probably the most perfect LDH structure. As for LDH-2M, the precursor was amorphous since no diffraction peaks were observed. It has been reported that LDHs synthesized at high metal concentrations had poorer crystallinity [28]. Moreover, to form a pure LDHs structure, the Fe^{3+}/Ni^{2+} molar ratio should be in the range of 0.2–0.33 [29–31]. However, at high Fe^{3+} concentrations, it was more favorable for Fe^{3+} ion to precipitate as insoluble $Fe(OH)_3$ in aqueous ammonia [32]. Indeed, the elemental analysis via ICP-OES showed that precursors prepared at metal concentrations above 1M had high Fe content compared with the nominal value (Table S4 in the supporting information). Therefore, it can be concluded that 0.25M was the most ideal metal concentration to prepare NiFe-CO_3 LDHs.

Upon calcination at 600 °C, it was expected that a mixed metal oxide of Ni and Fe would form from LDHs precursors [20]. The diffractograms of the calcined LDHs were presented in Fig. 4. It confirmed that LDHs structures were completely decomposed since only the diffraction patterns of $NiFe_2O_4$ (JCPDS 00-054-0964) and NiO (JCPDS 01-089-5881) were identified. It can also be observed that the XRD pattern of the calcined LDH-2M showed mostly reflections of $NiFe_2O_4$ due to higher Fe content compared to the other samples.

The reducibility of the calcined catalysts was investigated by H_2-TPR analysis (Fig. 5). With increasing metal concentrations, the main reduction temperature of the metal oxides was increased. It has been reported that pure NiO could be reduced at 340–410 °C and Fe_2O_3 is reduced sequentially at 380, 620, and 715 °C [33,34]. In this study, the TPR peaks of calcined LDH-0.05M, LDH-0.25M and LDH-0.5M were at 415, 430 and 485 °C, respectively. It is reasonable that the reduction temperature of Ni species would be increased due to the interaction with Fe species in the mixed oxides [35]. As for LDH-1M and LDH-2M samples, small reduction peaks were observed at 310–330 °C which could be attributed to the reduction of NiO, while the main peaks were recorded at high temperatures of 540–545 °C. It was in good agreement with the previous assumption that these two samples contained more iron oxides.

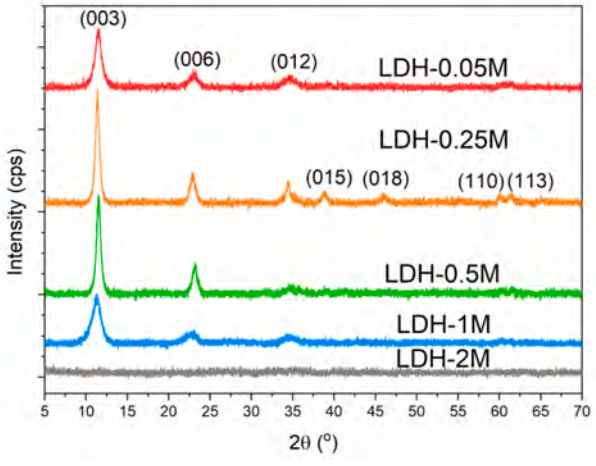

Fig. 3. XRD diffractograms of NiFe-CO_3 LDHs prepared by urea hydrolysis at different metal concentrations.

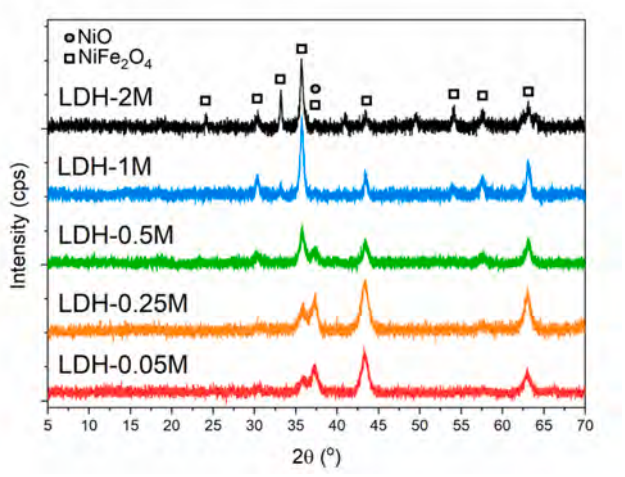

Fig. 4. XRD diffractograms of the calcined NiFe-CO_3 LDHs.

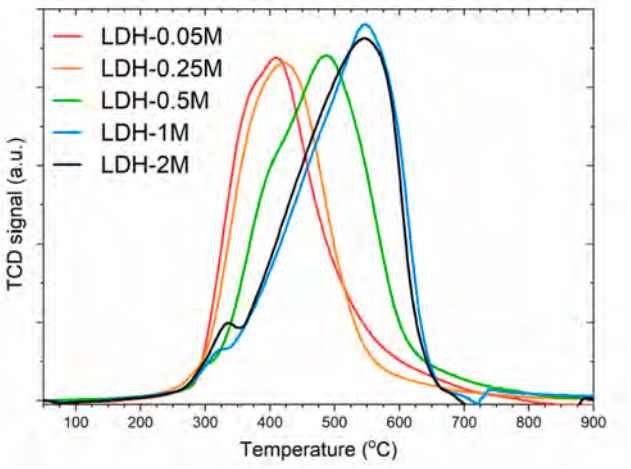

Fig. 5. TPR profiles of calcined NiFe-CO_3 LDHs.

3.2. Characterization of monolithic catalysts

The NiFe-CO_3 LDHs layer was in-situ grown on the washcoated honeycomb ceramic substrate via urea hydrolysis at different metal concentrations from 0.05M to 2M. The amount of deposited LDHs layers on the monoliths as well as catalyst loading are summarized in Table 1. Noted that the catalyst loading was calculated as the percentage of the catalyst mass after calcination on the total weight of final monoliths. It

Table 1
The mass of in-situ grown LDHs, corresponding catalyst loading and textural properties of the final calcined monolithic catalysts.

Structured catalysts	Mass of LDHs (mg)	Catalyst loading (wt %)	BET specific surface area ($m^2/g_{total\ COR}$)	BJH pore volume (cm^3/g)
COR-0.05M	60.1	0.52	18.3	0.047
COR-0.25M	192.9	3.51	24.4	0.051
COR-0.5M	175.8	2.63	30.7	0.069
COR-1M	168.3	1.87	22.6	0.047
COR-2M	163.5	1.12	18.6	0.047

was found that the highest amount of LDHs precursor could be deposited on monolith prepared at metal concentration of 0.25M. It is also the sample with the most crystalline LDHs structure. Thus, increasing metal concentrations could not increase the amount of in-situ grown LDHs precursors on washcoated substrate. As discussed in the XRD analysis, the formation of pure and high crystalline LDH structure was not favored at metal concentrations above 1M.

Cordierite honeycomb substrate is one of the most popular materials for the synthesis of structured catalysts thanks to its availability and low costs. However, cordierite substrate originally has a very low surface area, which was 1.2 m^2/g in our study. Thus, the substrate was washcoated with colloidal alumina three times to reach a washcoat layer loading of 14 wt%. After calcination, the washcoated monolith had a higher surface area of 18.3 m^2/g and pore volume of 0.064 cm^3/g. The surface area and pore volume of final monoliths after urea hydrolysis are summarized in Table 1. It shows that the surface area was significantly improved after urea hydrolysis, especially for monolith prepared at 0.25M, 0.5M and 1M.

The morphology of catalytic layer deposited on cordierite monoliths upon urea hydrolysis was observed by SEM. Numerous hexagonal platelets of LDHs were found on the exterior wall of the monolithic channels, in good agreement with earlier studies [36]. As shown in Fig. 6, the lateral size and thickness of these platelets on COR-0.25M and COR-1M were around 1 μm and 25 ± 10 nm. The morphology of LDHs precursors on COR-0.05M was almost three-time smaller in lateral size (Fig. S1a), while the platelet dimensions of COR-0.25M, COR-0.5M and COR-1M (Figs. 6 and S1b) was similar.

The thickness of the catalytic layer was estimated using the cross-sectional SEM images of the channel wall. As shown in Fig. 7, the deposition of LDHs occurred on the porous exterior of the cordierite channel walls. The LDHs platelets were assumed to grow perpendicularly on the surface, resulting in a layer thickness of around 20–30 μm. Notably, the catalytic layer on COR-0.25M, COR-0.5M, and COR-1M had similar thicknesses (Fig. 7 and Fig. S1d). As for COR-0.05M, it was unable to measure the LDHs layer due to very low catalyst loading (Fig. S1c). In addition, EDS elemental mapping was conducted and revealed a uniform spatial distribution of Ni and Fe on the layer, indicating that the metal ions were well dispersed on the monolithic surface.

3.3. Catalytic performance of monolithic catalysts

The temperature-programmed reaction was carried out at 200–500 °C for all monolithic catalysts. Due to kinetic limitations, high conversion of CO_2 could not be obtained at low temperature region of 200–250 °C, even though CO_2 methanation is thermodynamically favored. The conversion was much improved at 300 °C, especially for COR-0.25M monolith which achieved a CO_2 conversion of 70.1% (Fig. 8). COR-0.5M and COR-1M also exhibited good activity at 300 °C with CO_2 conversion of 65.6% and 59.6%, respectively. The conversions peaked at 350 °C and gradually decreased at elevated temperatures, following the thermodynamic equilibrium. On the other hand, COR-0.05M showed a poorer performance, and COR-2M presented the poorest activity.

In addition to the main reaction, the reverse water gas shift reaction (RWGS, $CO_2 + H_2 \leftrightarrow CO + H_2O$, $\Delta H_{298K} = 41$ kJ/mol) could occur to produce the byproduct CO. Hence, the CH_4 selectivity or CH_4 yield is also an important indicator for the performance of the catalysts. In this study, CH_4 yield is reported together with the loading of catalysts (Fig. 9). The best performance of COR-0.25M amongst others was confirmed by the CH_4 yield at different reaction temperatures. This could be due to the highest catalyst loading of COR-0.25M with a thin and well-adhered layer on the honeycomb substrate. Interestingly, CO_2 conversion over the COR-2M catalyst was always increasing with temperature, distinct from the other catalysts as it did not follow the thermodynamic curve for methanation. This could be explained by the high Fe content of COR-2M, which promotes the endothermic RWGS reaction and favors CO_2 conversion at high temperatures [37]. Indeed, the CH_4 selectivity was very low over the COR-2M monolith.

3.4. Temperature profiles of structured reactor

3.4.1. Temperature profiles with increasing oven temperatures

The exothermic nature of the methanation reaction could be influenced by different catalytic activities of the monolithic catalysts. Thus, the temperature along the catalytic bed containing high and low activity catalysts (COR-0.25M and COR-0.05M, respectively) was measured by the multi-point thermocouple at the center of the bed. At first, the reaction was carried out on uniform catalytic beds containing three COR-0.25M monoliths (Uni-High bed) or three COR-0.05M monoliths (Uni-Low bed). Fig. 10 shows the temperature profile and the methane yield of the catalytic beds at steady state when T_{oven} was 200, 250 and 300 °C, respectively.

At T_{oven} = 200 °C and a total gas flow rate of 500 mL/min, the CH_4 yield on both monolithic beds was relatively low at less than 3.5% (Fig. 10a). As expected, no hot-spot formation was observed from the axial temperature profiles. When the oven temperature ramped up to 250 °C (Fig. 10b), hot-spot appeared along the Uni-High bed with a maximum temperature increase (ΔT) of 42 °C in the middle of the bed. The catalytic performance also improved with a CH_4 yield of 50.9%. In contrast, a CH_4 yield of only 8.9% was achieved on the Uni-Low bed, and there was obviously no hot-spot formation at this low conversion. When T_{oven} was increased from 250 to 300 °C, the hot-spot on Uni-High bed shifted from the center axial position to near the gas inlet region with a significant ΔT = 86 °C, whereas the CH_4 yield increased to 84.1% (Fig. 10c). A CH_4 yield of 59.5% was achieved on the Uni-Low bed at T_{oven} = 300 °C, and hot-spot was also observed with ΔT = 44 °C. The thermal profile of catalytic beds could result from the balance between the exothermic heat from methanation which increased exponentially with reaction temperature due to reaction rate acceleration, and heat transfer by conduction in the cordierite channel wall and by convection from the bed to the gas flow. The shift of hot-spot location at increasing operating temperature has also been reported by Kosaka *et al.* [17]. It

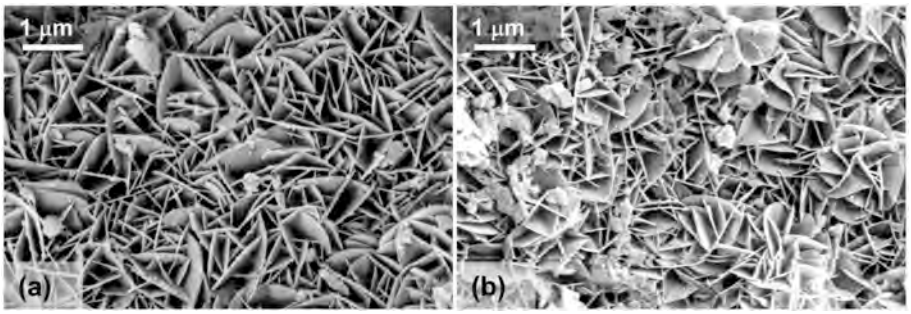

Fig. 6. SEM images of in-situ grown NiFe-CO_3 LDHs on (a) COR-0.25M and (b) COR-1M monolith.

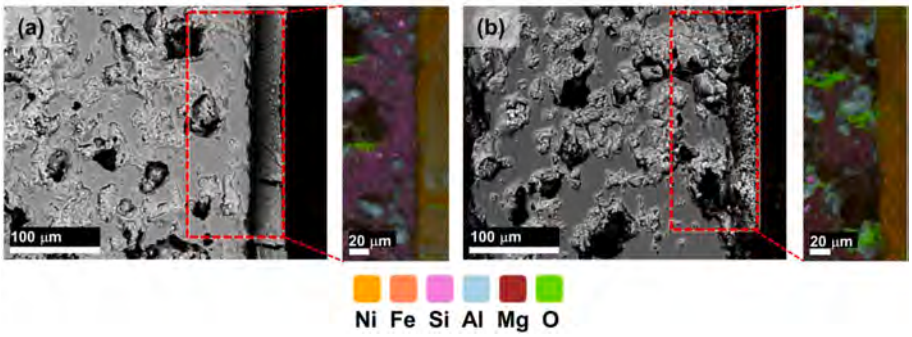

Fig. 7. SEM and corresponding EDS elemental mapping images of the cross-sectional channel wall on (a) COR-0.25M and (b) COR-1M.

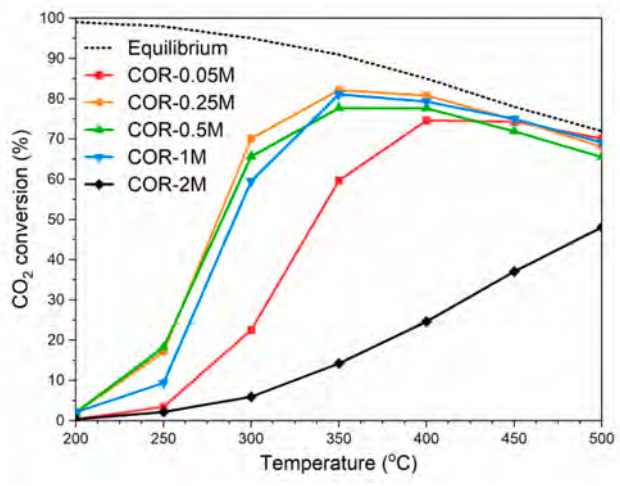

Fig. 8. CO_2 conversion over structured catalysts in temperature-programmed CO_2 methanation at atmospheric pressure, total gas flow rate of 500 mL/min (STP), $H_2/N_2/CO_2$ = 64/20/16 vol%; The thermodynamic equilibrium was added for comparison.

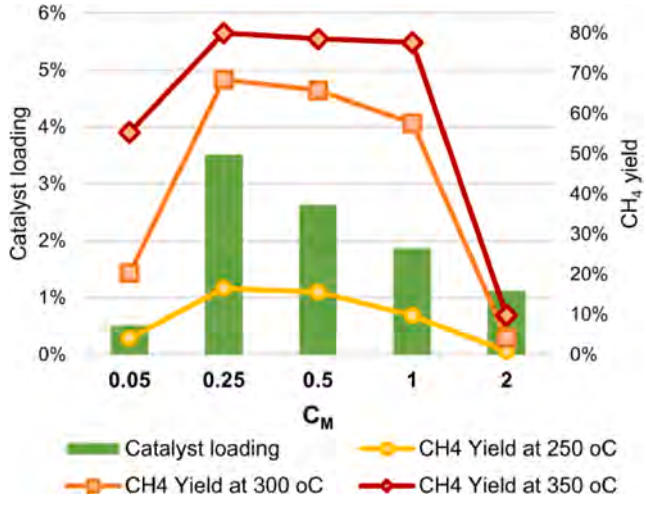

Fig. 9. CH_4 yield obtained over structured catalysts at different reaction temperatures (200, 250 and 300 °C); The CO_2 methanation reaction was at atmospheric pressure, total gas flow rate of 500 mL/min (STP), $H_2/N_2/CO_2$ = 64/20/16 vol%.

could be due to the higher heat conductivity of the catalytic cordierite monolith bed compared to that of the flowing gas. Thus, heat transfer along the monolithic bed was faster than that between the catalytic bed and the gas. Subsequently, monolith at the near gas inlet was further heated and accelerated methanation reactions. Simultaneously, a large amount of exothermic reaction heat was released.

It was proposed that the excellent thermal conductivity of monolithic substrate could be utilized to boost up the performance of low activity catalysts in methanation [17]. We therefore configured a monolithic bed with increasing catalytic activity, i.e., Low-High bed consisting of two COR-0.05M and one COR-0.25M. Hot-spot was not observed at T_{oven} = 200 °C (Fig. 10a) but was measured with ΔT = 26 °C and a CH_4 yield of 32.1% at T_{oven} = 250 °C. Notably, at T_{oven} = 300 °C, the CH_4 yield of the Low-High bed was almost close to that of the Uni-High bed (83.1% vs 84.1%) while a lower ΔT of 69 °C was recorded. Thus, although the Low-High bed contained less catalyst loading than the Uni-High bed, the CH_4 yield was almost similar at T_{oven} = 300 °C. As shown in Fig. 8, while COR-0.25M slowly dropped its performance at 350 °C and above, the CO_2 conversion over COR-0.05M still increased and reached a maximum at 400–450 °C. It seems that hot-spot generated in the reaction could be exploited to improve the overall performance of the Low-High bed. In terms of methane productivity when catalyst mass was taken into account, P_{CH4} was 0.9 mol/(h.g_{cat}) on Uni-High and 1.6 mol/(h.g_{cat}) on Low-High bed. Hence, it can be assumed that the Low-High bed packing strategy could enhance the catalytic efficiency of the monolithic reactor with a lower hot-spot temperature.

3.4.2. CFD simulation results

The experimental results for all three catalytic beds were verified by a 3D CFD consisted of reaction kinetics, fluid dynamics, heat transfer and mass transport. The simulated temperature profiles at a gas inlet temperature of 250 °C along three catalytic beds (Fig. 11) showed similar patterns of hot-spot formation compared to the experimental results at T_{oven} = 250 °C (Fig. 10b). The simulation demonstrated that the highest temperature of 290 °C on Uni-High bed was at the middle of the bed (Fig. 11a), while on Low-High bed the maximum temperature T_{max} of 258 °C was detected at the third monolith COR-0.25M near the gas outlet (Fig. 11c). As expected, the temperature profile of the Uni-Low bed was quite flat without any hot-spot formation (Fig. 11b). Thus, the proposed bed packing strategy by combining catalysts with low and high activity appeared to be a promising approach to manage bed temperatures.

3.4.3. Temperature profiles with increasing gas flow rates

We further studied the effect of GHSV on the catalytic conversion and temperature profile of Uni-High and Low-High beds at T_{oven} = 250 °C (Fig. 12). For comparison, the CH_4 yield and temperature profile at 500 mL/min were also included as Fig. 12a. The hot-spot formation was more pronounced at higher gas flow rate of 1500 mL/min (corresponding to a GHSV of 7760 h^{-1}). The Uni-High bed reached a T_{max} of 458 °C with a remarkable CH_4 yield of 80.4% (Fig. 12b). It is worth emphasizing that the ratio of the catalyst mass to volumetric gas flow rate was the same for the single-bed at 500 mL/min and Uni-High bed at

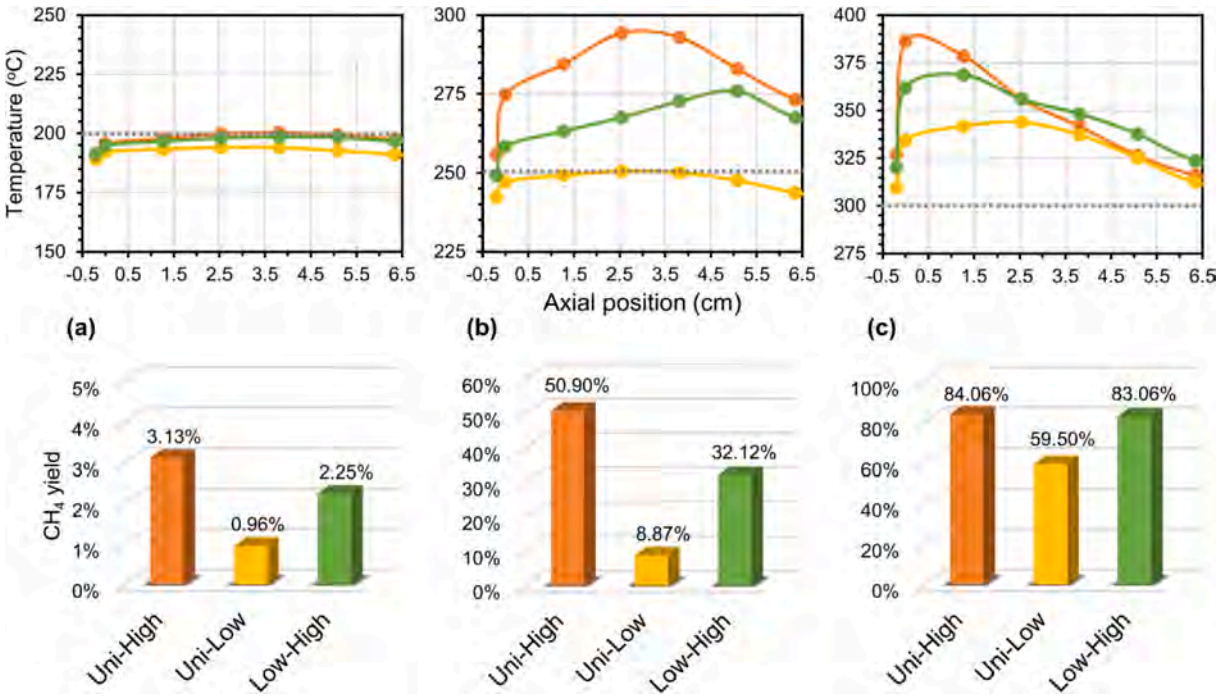

Fig. 10. Temperature profiles of reactor (top) and methane yield (bottom) obtained from CO_2 methanation over different catalytic beds at T_{oven} of (a) 200 °C, (b) 250 °C, (c) 300 °C; The reaction was at atmospheric pressure, total gas flow rate of 500 mL/min (STP), $H_2/N_2/CO_2$ = 64/20/16 vol%.

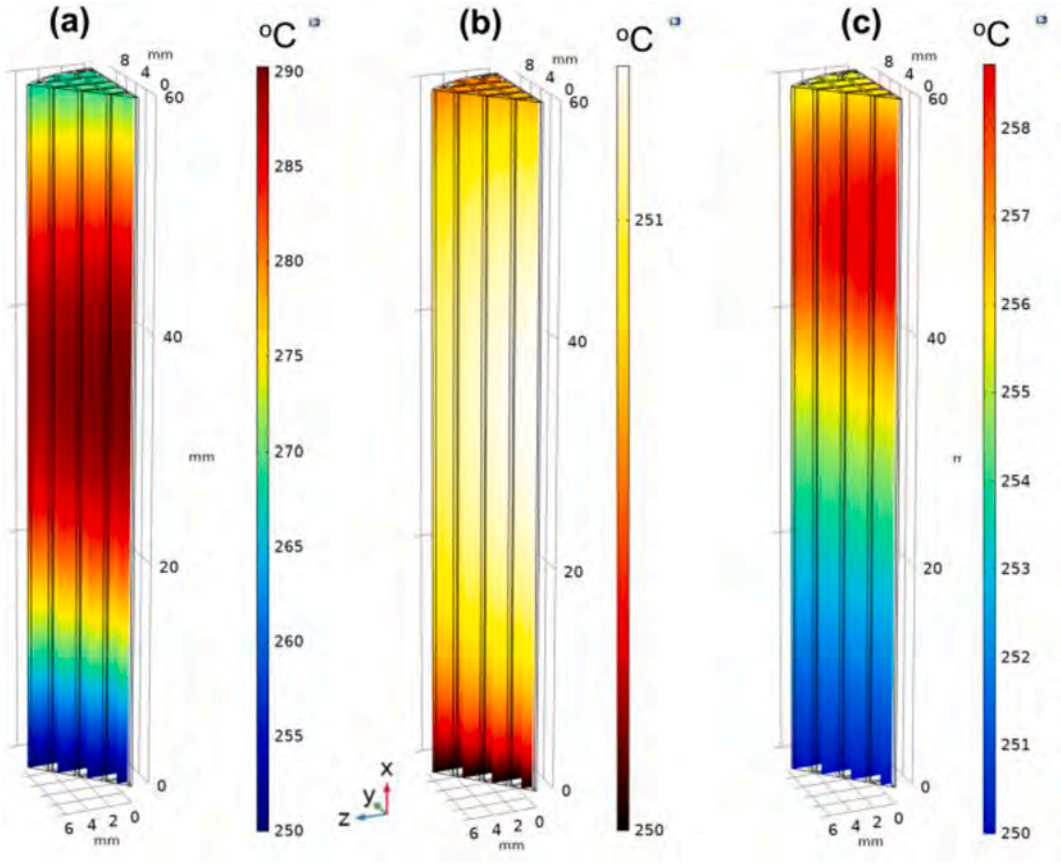

Fig. 11. Simulated temperature profiles of monolithic reactor using (a) Uni-High, (b) Uni-Low and (c) Low-High bed at operating temperature of 250 °C, atmospheric pressure, total gas flow rate of 500 mL/min (STP).

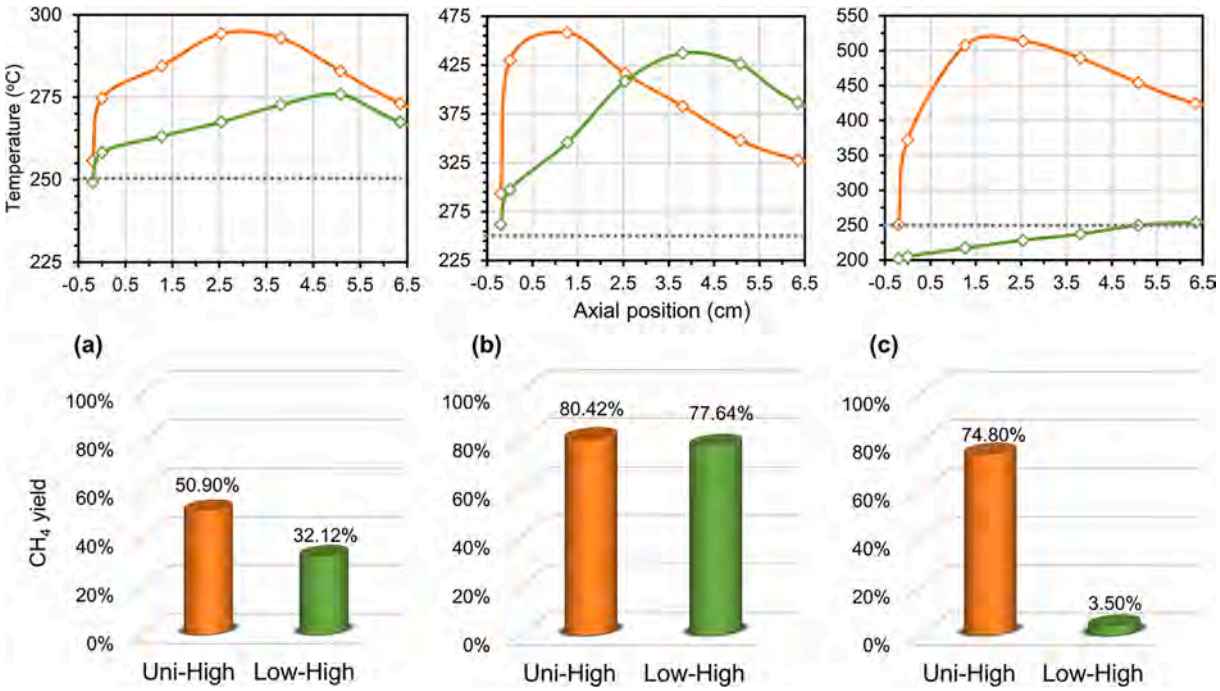

Fig. 12. Temperature profiles of reactor (top) and methane yield (bottom) obtained from CO_2 methanation over Uni-High and Low-High bed at different gas flow rates of (a) 500 mL/min, (b) 1500 mL/min and (c) 3000 mL/min (STP). The temperature of the oven was set at 250 °C. The reaction was at atmospheric pressure, $H_2/N_2/CO_2$ = 64/20/16 vol%.

1500 mL/min, whereas the CH_4 yield was only 16.5% for the former (Fig. 9). Obviously, the hot-spot generated on the Uni-High bed had significantly boosted the overall CH_4 yield to 80.4%. Thus, while hot-spot formation is a big concern for many chemical reactions [18], it could also be utilized to boost the performance of exothermic monolithic reactors. As for the Low-High bed, it showed a lower T_{max} of 437 °C at a gas flow rate of 1500 mL/min while the CH_4 yield was only marginally lower at 77.6%, apparently due to the hot-spot formed on the reactor bed. The strategic Low-High packing was again demonstrated to be a promising alternative to the uniform Uni-High bed.

Lower CO_2 conversion and CH_4 yield are generally expected at higher GHSV at the same reaction temperature. Interestingly, the catalytic performance of both monolithic beds was significantly improved at a higher gas rate of 1500 mL/min compared to 500 mL/min. This could also be explained by the hot-spot observed in the reactor: the initial CO_2 conversion was probably lower at 1500 mL/min, but the amount of heat released and the heat transfer coefficient would be larger at higher flow rate, which increased the bed temperature thus further accelerated the reaction. Consequently, the monolithic bed was operated at a much higher temperature at 1500 mL/min than that at 500 mL/min, as shown in Fig. 12a and Fig. 12b.

We also investigated the reactor performance at 3000 mL/min at T_{oven} = 250 °C. For Uni-High bed, a higher T_{max} of 513 °C, corresponding to a ΔT of 263 °C could be observed, whereas the CH_4 yield decreased to 74.8%. Indeed, a larger amount of heat was released at 3000 mL/min which led to a higher temperature spike. However, at 450–500 °C, COR-0.25M exhibited a lower conversion of only 75–68% (Fig. 8). As for the Low-High bed, the CH_4 yield was merely 3.5%. The residence time at this condition could be too short for the two low-activity COR-0.05M catalytic beds, thus CO_2 was not reacted and no heat was released to form hot-spot (Fig. 12c). To sum up, at a very high gas flow of 3000 mL/min, extreme hot-spot formation was not favorable for the conversion on Uni-High bed while it was too harsh condition for Low-High bed to produce methane.

3.4.4. Stability tests

Long-term stability test was carried out on both Uni-High and Low-High beds at T_{oven} = 250 °C and a gas flow rate of 1500 mL/min (STP). The T_{max} on Low-High bed was maintained at 440 °C during the 100-h long-term test. On Uni-High bed, the high hot-spot temperature was slightly decreased from 468 to 460 °C, which could be explained by the loss of activity during 100 h. Regardless, it was consistent with previous tests that Low-High bed had a lower hot-spot compared to that of Uni-High bed (Fig. 13). This could also explain the lower but more stable methane yield with a slight drop of 0.02%/h on the Low-High bed compared to a deactivation rate of 0.05%/h on the Uni-High bed. Nevertheless, both bed configurations have shown quite stable performance throughout 100 h of reaction. Therefore, CO_2 methanation could be effectively carried out on monolithic reactors at a very low operating temperature of 250 °C.

4. Conclusions

NiFe catalytic active layer was in-situ grown on washcoated ceramic substrate via urea hydrolysis, which is a novel preparation method to obtain thin and well-adhered catalytic layer on monoliths. It was found that catalysts prepared by 0.25M solution, i.e., COR-0.25M with the highest metal loading exhibited the best CO_2 conversion and CH_4 yield. The formation of hot-spot during exothermic methanation reaction was observed on monolithic reactors and further verified by CFD simulations. Although a temperature increase of 86 °C was observed on Uni-High bed reactor, a remarkable methane yield of 80.4% was achieved at low operating temperature of 250 °C. In contrast, the methane yield was merely 16.5% on single COR-0.25M bed at this temperature. Therefore, controlled hot-spot formation was beneficial for the overall catalytic performance via bed packing. A strategic bed packing configuration was proposed that combined low and high activity monolith, i.e., Low-High bed. Amazingly, this bed achieved ~83% methane yield and the hot-spot formation was less severe compared to that of the Uni-High bed at 300 °C. It was also revealed that hot-spot formation could be exploited to achieve high methane yield at high gas flow rate during

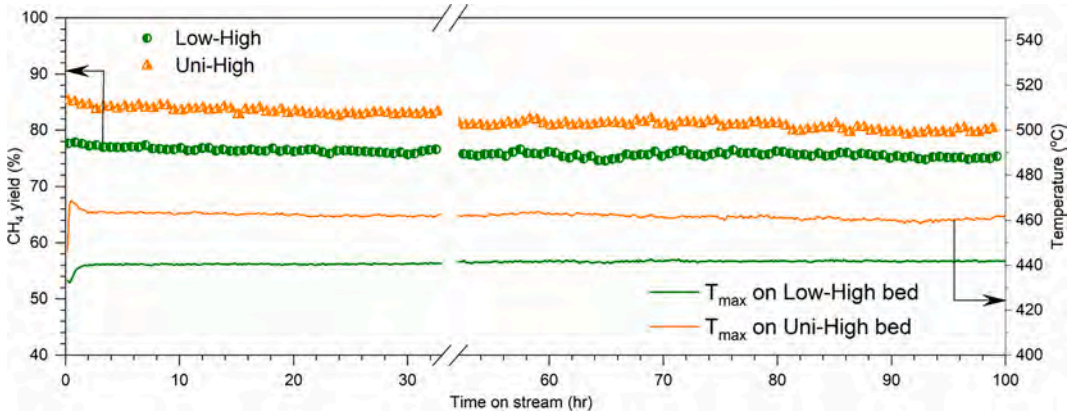

Fig. 13. Methane yield and maximum temperature of the Low-High and Uni-High bed during long-term tests. The oven temperature was set at 250 °C. The reaction was at atmospheric pressure, total gas flow rate of 1500 mL/min (STP), $H_2/N_2/CO_2$ = 64/20/16 vol%.

low-temperature CO_2 methanation on honeycomb monolithic reactors. In conclusion, hot-spot and strategic bed packing could be utilized to achieve excellent CO_2 methanation performance on monolithic reactors at low temperatures. These results demonstrated a promising approach for the development of industrial monolithic CO_2 methanation reactors as part of large-scale PtG process.

Declaration of Competing Interest

The authors declare that they have no known competing financial interests or personal relationships that could have appeared to influence the work reported in this paper.

Acknowledgments

The authors would like to thank the Norwegian Ministry of Education and Research for the financial support.

Appendix A. Supplementary data

Supplementary data to this article can be found online at https://doi.org/10.1016/j.cej.2021.131106.

References

[1] J. Artz, T.E. Müller, K. Thenert, J. Kleinekorte, R. Meys, A. Sternberg, A. Bardow, W. Leitner, Sustainable conversion of carbon dioxide: an integrated review of catalysis and life cycle assessment, Chem. Rev. 118 (2) (2018) 434–504, https://doi.org/10.1021/acs.chemrev.7b00435.

[2] P. Sabatier, J.-B. Senderens, Nouvelles syntheses du methane, Comptes Rendus Des Séances De L'Académie Des Sciences, Section VI – Chimie 134 (1902) 514–516.

[3] C. Vogt, M. Monai, G.J. Kramer, B.M. Weckhuysen, The renaissance of the sabatier reaction and its applications on earth and in space, Nat. Catal. 2 (3) (2019) 188–197, https://doi.org/10.1038/s41929-019-0244-4.

[4] M. Götz, J. Lefebvre, F. Mörs, A. McDaniel Koch, F. Graf, S. Bajohr, R. Reimert, T. Kolb, Renewable power-to-gas: a technological and economic review, Renew. Energy 85 (2016) 1371–1390, https://doi.org/10.1016/j.renene.2015.07.066.

[5] M. Bailera, P. Lisbona, L.M. Romeo, S. Espatolero, Power to gas projects review: Lab, pilot and demo plants for storing renewable energy and CO2, Renew. Sustain. Energy Rev. 69 (2017) 292–312, https://doi.org/10.1016/j.rser.2016.11.130.

[6] C. Lv, L. Xu, M. Chen, Y. Cui, X. Wen, Y. Li, C.-E. Wu, B. Yang, Z. Miao, X. Hu, Q. Shou, Recent progresses in constructing the highly efficient ni based catalysts with advanced low-temperature activity toward co2 methanation, Front. Chem. 8 (269) (2020), https://doi.org/10.3389/fchem.2020.00269.

[7] P. Frontera, A. Macario, M. Ferraro, P. Antonucci, Supported catalysts for co2 methanation: a review, Catalysts 7 (2) (2017) 59, https://doi.org/10.3390/catal7020059.

[8] D. Türks, H. Mena, U. Armbruster, A. Martin, Methanation of CO2 on Ni/Al2O3 in a structured fixed-bed reactor—a scale-up study, Catalysts 7 (5) (2017) 152, https://doi.org/10.3390/catal7050152.

[9] A. Bengaouer, J. Ducamp, I. Champon, R. Try, Performance evaluation of fixed-bed, millistructured, and metallic foam reactor channels for CO2 methanation, Can. J. Chem. Eng. 96 (9) (2018) 1937–1945, https://doi.org/10.1002/cjce:23140.

[10] M. Lehner, R. Tichler, H. Steinmüller, M. Koppe, Methanation, in: M. Lehner, R. Tichler, H. Steinmüller, M. Koppe (Eds.), Power-to-gas: technology and business models, springer international publishing, Cham, 2014, pp. 41–61, https://doi.org/10.1007/978-3-319-03995-4_4.

[11] F. Kapteijn, J.A. Moulijn, Structured catalysts and reactors – perspectives for demanding applications, Catal. Today (2020), https://doi.org/10.1016/j.cattod.2020.09.026.

[12] C. Fukuhara, K. Hayakawa, Y. Suzuki, W. Kawasaki, R. Watanabe, A novel nickel-based structured catalyst for CO2 methanation: a honeycomb-type Ni/CeO2 catalyst to transform greenhouse gas into useful resources, Appl. Catal. A 532 (2017) 12–18, https://doi.org/10.1016/j.apcata.2016.11.036.

[13] H.L. Huynh, Z. Yu, CO2 Methanation on hydrotalcite-derived catalysts and structured reactors: a review, Energy Technol. 8 (5) (2020) 1901475, https://doi.org/10.1002/ente.201901475.

[14] S. Hwang, P. Linke, R. Smith, Heterogeneous catalytic reactor design with optimum temperature profile II: application of non-uniform catalyst, Chem. Eng. Sci. 59 (20) (2004) 4245–4260, https://doi.org/10.1016/j.ces.2004.05.036.

[15] S. Ratchahat, M. Sudoh, Y. Suzuki, W. Kawasaki, R. Watanabe, C. Fukuhara, Development of a powerful CO2 methanation process using a structured Ni/CeO2 catalyst, J. CO2 Util. 24 (2018) 210–219, https://doi.org/10.1016/j.jcou.2018.01.004.

[16] F. Kosaka, T. Yamaguchi, Y. Ando, T. Mochizuki, H. Takagi, K. Matsuoka, K. Kuramoto, Thermal management of CO2 methanation with axial staging of active metal concentration in Ni-YSZ tubular catalysts, Int. J. Hydrog. Energy 46 (5) (2020) 4116–4125, https://doi.org/10.1016/j.ijhydene.2020.10.247.

[17] F. Kosaka, T. Yamaguchi, Y. Ando, T. Mochizuki, H. Takagi, K. Matsuoka, Y. Fujishiro, K. Kuramoto, Effect of Ni content on CO2 methanation performance with tubular-structured Ni-YSZ catalysts and optimization of catalytic activity for temperature management in the reactor, Int. J. Hydrog. Energy 45 (23) (2020) 12911–12920, https://doi.org/10.1016/j.ijhydene.2020.02.221.

[18] W. Wang, C. Duong-Viet, G. Tuci, Y. Liu, A. Rossin, L. Luconi, J.-M. Nhut, L. Nguyen-Dinh, G. Giambastiani, C. Pham-Huu, Highly nickel-loaded γ-alumina composites for a radiofrequency-heated, low-temperature co2 methanation scheme, ChemSusChem 13 (20) (2020) 5468–5479, https://doi.org/10.1002/cssc.202001885.

[19] J. Jenkins, E. Shutt, The hot spot™ reactor, Platinum Met. Rev. 33 (3) (1989) 118–127.

[20] H.L. Huynh, W.M. Tucho, Z. Yu, Structured NiFe catalysts derived from in-situ grown layered double hydroxides on ceramic monolith for CO2 methanation, Green Energy Environ. 5 (4) (2020) 423–432, https://doi.org/10.1016/j.gee.2020.09.004.

[21] S. Brunauer, P.H. Emmett, E. Teller, Adsorption of gases in multimolecular layers, J. Am. Chem. Soc. 60 (2) (1938) 309–319, https://doi.org/10.1021/ja01269a023.

[22] E.P. Barrett, L.G. Joyner, P.P. Halenda, The Determination of pore volume and area distributions in porous substances. I. computations from nitrogen isotherms, J. Am. Chem. Soc. 73 (1) (1951) 373–380, https://doi.org/10.1021/ja01145a126.

[23] F. Koschany, D. Schlereth, O. Hinrichsen, On the kinetics of the methanation of carbon dioxide on coprecipitated NiAl(O)x, Appl. Catal. B 181 (2016) 504–516, https://doi.org/10.1016/j.apcatb.2015.07.026.

[24] G. Tauer, C. Kern, A. Jess, Transient effects during dynamic operation of a wall-cooled fixed-bed reactor for co2 methanation, Chem. Eng. Technol. 42 (11) (2019) 2401–2409, https://doi.org/10.1002/ceat.201900367.

[25] E.N. Fuller, P.D. Schettler, J.C. Giddings, New method for prediction of binary gas-phase diffusion coefficients, Ing. Eng. Chem. 58 (5) (1966) 18–27, https://doi.org/10.1021/ie50677a007.

[26] E.N. Fuller, K. Ensley, J.C. Giddings, Diffusion of halogenated hydrocarbons in helium. The effect of structure on collision cross sections, J. Phys. Chem 73 (11) (1969) 3679–3685.

[27] T. Fuller, Proton exchange membrane fuel cells 8, Electrochem. Soc. (2008).

[28] Z. Chang, D.G. Evans, X. Duan, C. Vial, J. Ghanbaja, V. Prevot, M. de Roy, C. Forano, Synthesis of [Zn–Al–CO3] layered double hydroxides by a

coprecipitation method under steady-state conditions, J. Solid State Chem. 178 (9) (2005) 2766–2777, https://doi.org/10.1016/j.jssc.2005.06.024.
[29] M.V. Bukhtiyarova, A review on effect of synthesis conditions on the formation of layered double hydroxides, J. Solid State Chem. 269 (2019) 494–506, https://doi.org/10.1016/j.jssc.2018.10.018.
[30] F. Cavani, F. Trifirò, A. Vaccari, Hydrotalcite-type anionic clays: preparation, properties and applications, Catal. Today 11 (2) (1991) 173–301, https://doi.org/10.1016/0920-5861(91)80068-K.
[31] V. Rives, María Angeles Ulibarri, Layered double hydroxides (LDH) intercalated with metal coordination compounds and oxometalates, Coord. Chem. Rev 181 (1) (1999) 61–120.
[32] N.J. Tro, Chemistry A Molecular Approach, Pearson, 2003.
[33] D. Pandey, K. Ray, R. Bhardwaj, S. Bojja, K.V.R. Chary, G. Deo, Promotion of unsupported nickel catalyst using iron for CO2 methanation, Int. J. Hydrog. Energy 43 (10) (2018) 4987–5000, https://doi.org/10.1016/j.ijhydene.2018.01.144.
[34] D. Beierlein, D. Häussermann, M. Pfeifer, T. Schwarz, K. Stöwe, Y. Traa, E. Klemm, Is the CO2 methanation on highly loaded Ni-Al2O3 catalysts really structure-sensitive? Appl. Catal. B 247 (2019) 200–219, https://doi.org/10.1016/j.apcatb.2018.12.064.
[35] D. Shi, R. Wojcieszak, S. Paul, E. Marceau, Ni promotion by Fe: what benefits for catalytic hydrogenation? Catalysts 9 (5) (2019) 451, https://doi.org/10.3390/catal9050451.
[36] Y. Han, H. Li, X. Ma, Z.-H. Liu, Preparation and formation process of Ni2+–Fe3+ CO32− LDHs materials with high crystallinity and well-defined hexagonal shapes, Solid State Sci. 11 (12) (2009) 2149–2155, https://doi.org/10.1016/j.solidstatesciences.2009.08.016.
[37] C.-S. Chen, W.-H. Cheng, S.-S. Lin, Study of iron-promoted Cu/SiO2 catalyst on high temperature reverse water gas shift reaction, Appl. Catal. A 257 (1) (2004) 97–106, https://doi.org/10.1016/S0926-860X(03)00637-9.

Supporting information

Bed packing configuration and hot-spot utilization for low-temperature CO_2 methanation on monolithic reactor

Huong Lan Huynh[a], Wakshum Mekonnen Tucho[b], Qi Shen [c,*], Zhixin Yu[a,*]

[a] Department of Energy and Petroleum Engineering, University of Stavanger, 4036 Stavanger, Norway

[b] Department of Mechanical and Structural Engineering and Material Science, University of Stavanger, 4036 Stavanger, Norway

[c] Institute of New Energy, School of Chemistry and Chemical Engineering, Shaoxing University, Shaoxing 312000, China

***Corresponding author:**

Prof. Zhixin Yu

E-mail address: zhixin.yu@uis.no

Department of Energy and Petroleum Engineering, University of Stavanger, 4036 Stavanger, Norway

Tel: +47 51832238

Qi Shen

Email address: shenqi@usx.edu.cn

Institute of New Energy, School of Chemistry and Chemical Engineering, Shaoxing University, Shaoxing 312000, China

Tel: +86 18888795648

Figure S1. SEM images of in-situ grown LDHs on (a) COR-0.05M and (b) COR-0.5M. SEM and corresponding EDS elemental mapping images of cross-sectional channel wall on (c) COR-0.05M and (d) COR-0.5M. [1]

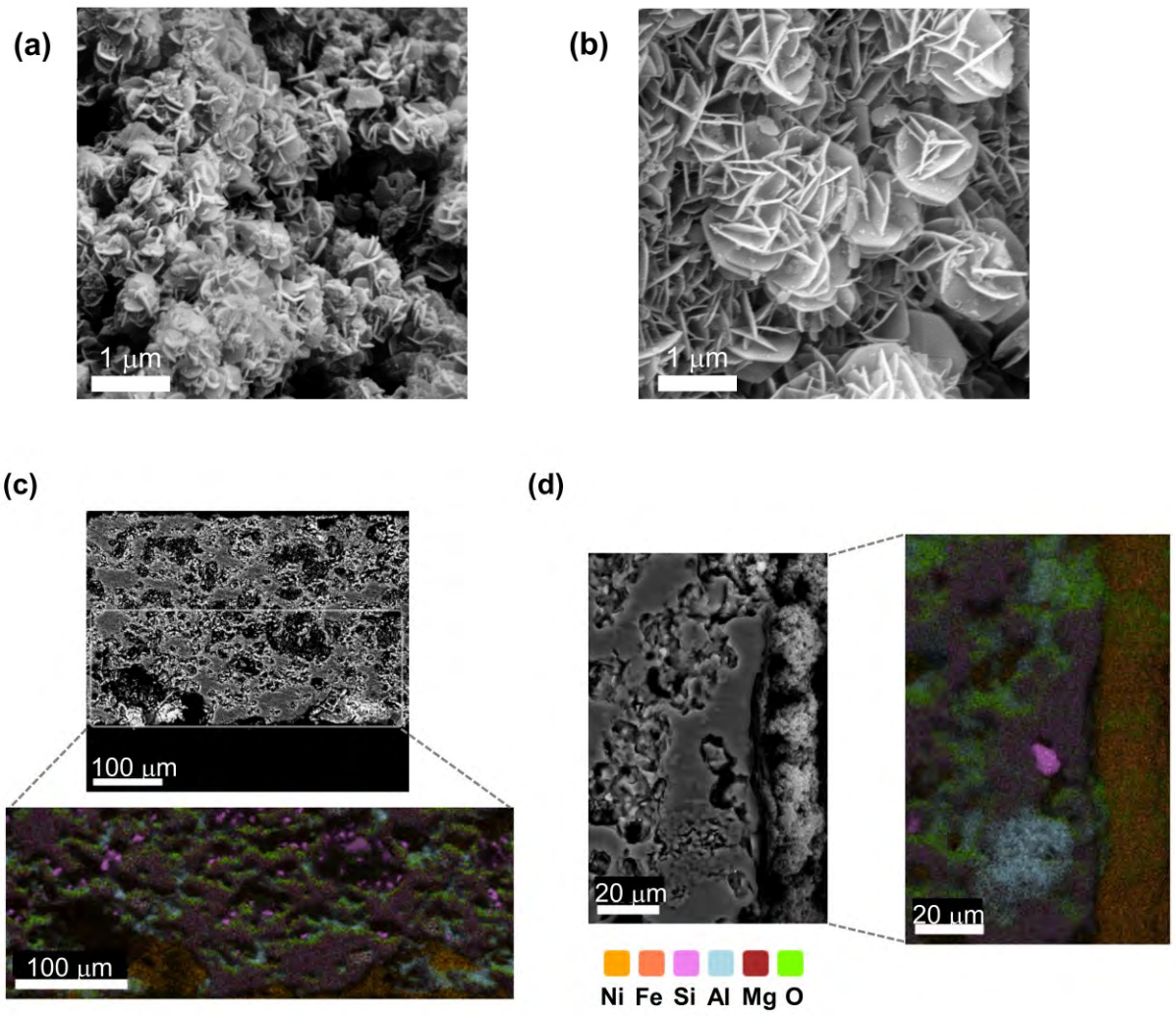

Table S1. Governing equations for the numerical simulation of the monolithic reactor.

Equations	Expression
Reaction rate [2, 3]	$r_{CO2} = \frac{k_m p_{CO2}^{0.5} p_{H2}^{0.5} \left(1 - \frac{p_{CH4} p_{H2O}^2}{p_{CO2} p_{H2}^4 K_p}\right)}{\left(1 + K_1 p_{CO2}^{0.5} + K_2 p_{H2}^{0.5} + K_3 \frac{p_{H2O}}{p_{H2}^{0.5}}\right)^2}$
Reaction rate constant	$k_m = k_{0,m} e^{\left(-\frac{Ea}{RT}\right)}$ $k_{0,m} = 9.2 \times 10^{-2}\ mol/(kg.s.Pa)$
Equilibrium constant	$K_p = 137 \times 10^{-10}\ T^{-3.998} e^{\left(-\frac{158.7 \times 10^3 J/mol}{RT}\right)}$ (Pa^{-2})
Activation energy	$Ea = 46.8 \frac{kJ}{mol}$ for COR-0.05M; $Ea = 39.3 \frac{kJ}{mol}$ for COR-0.25M
Adsorption rate constant	$K_i = k_{0,i} e^{\left(-\frac{\Delta H_{ads,i}}{RT}\right)}$ $k_{0,1} = 4.5 \times 10^{-6}\ Pa^{-0.5}$; $k_{0,2} = 1.7 \times 10^{-5}\ Pa^{-0.5}$; $k_{0,3} = 1.5 \times 10^{-6}\ Pa^{-0.5}$
Adsorption enthalpy	$\Delta H_{ads,1} = -29.4 \frac{kJ}{mol}$; $\Delta H_{ads,2} = -23.4 \frac{kJ}{mol}$; $\Delta H_{ads,3} = -34.7 \frac{kJ}{mol}$
Mass transport [4] u is fluid velocity field c is species concentration D is diffusion coefficient V is atomic diffusion volume of species M is molar mass of species θ_p is porosity	$\boldsymbol{u}\nabla \cdot c_i + \nabla \cdot \left(-D_{ij} \nabla c_i\right) = r_i$ $D_{ij} = \frac{0.001 \times T^{1.75} \left(\frac{1}{M_i} + \frac{1}{M_j}\right)^{0.5}}{P \left(V_i^{1/3} + V_j^{1/3}\right)^2}$ $D_{ij,eff} = D_{ij} \left(\frac{T}{T_{ref}}\right)^{1.5} {\theta_p}^{1.5}$
Navier-Stokes Momentum equation	$\rho(\boldsymbol{u} \cdot \nabla)\boldsymbol{u} = \nabla \cdot \left[-p2\boldsymbol{I} + \mu(\nabla \boldsymbol{u} + (\nabla \boldsymbol{u})^T) - \frac{2}{3}\mu(\nabla \cdot \boldsymbol{u})\boldsymbol{I}\right] + F$
Continuity equation	$\nabla \cdot (\rho \boldsymbol{u}) = 0$
Heat balance	$\rho C_p \boldsymbol{u} \boldsymbol{\nabla} T - \boldsymbol{\nabla}\left[\{\theta_p k_p + (1 - \theta_p)k\}\boldsymbol{\nabla} T\right] = Q$
Heat transfer at reactor surface [5]	$q = h(T_{\text{external}} - T)$

Table S2. Boundary conditions for the numerical simulation of the monolithic reactor.

Mass transport	Inlet: $c = c_{in}$ $c_{in\,CO2} = 7.14\frac{mol}{m^3}$ $c_{in\,H2} = 28.56\frac{mol}{m^3}$ $c_{in\,N2} = 8.93\frac{mol}{m^3}$ Outlet: $n \cdot (-D\nabla c) = 0$
Heat transfer	Inlet: $T = T_0$ = 250 °C Outlet: $n \cdot (k\nabla T) = 0$

Table S3. Parameters for the numerical simulation.

Parameters		Value
T_0	Temperature at inlet	250 ^{o}C
T_{external}	Temperature outside reactor surface	250 ^{o}C
T_{ref}	Temperature for reference	273 K
v	Volumetric flow rate	1.042×10^{-6} m^3/s
θ_p	Porosity of cordierite monolith	0.3
ρ	Density of cordierite monolith	2970 kg/m^3
C_p	Heat capacity at constant pressure of cordierite monolith	850 J/(kg.K)
k_p	Thermal conductivity of cordierite monolith	2.5 W/(m.K)
k	Thermal conductivity of fluid flow	0.05 W/(m.K)
h	Heat transfer coefficient at reactor surface	30 $W/(m^2.K)$

Table S4. Fe/Ni molar ratio from elemental analysis using inductively coupled plasma optical emission spectrometry (ICP-OES).

Catalysts	Fe/Ni molar ratio
LDH-0.05M	0.36
LDH-0.25M	0.38
LDH-0.5M	0.78
LDH-1M	2.19
LDH-2M	3.35

References

[1] H.L. Huynh, W.M. Tucho, Z. Yu, Structured NiFe catalysts derived from in-situ grown layered double hydroxides on ceramic monolith for CO2 methanation, Green Energy & Environment, 5 (2020) 423-432.

[2] F. Koschany, D. Schlereth, O. Hinrichsen, On the kinetics of the methanation of carbon dioxide on coprecipitated NiAl(O)x, Applied Catalysis B: Environmental, 181 (2016) 504-516.

[3] G. Tauer, C. Kern, A. Jess, Transient Effects during Dynamic Operation of a Wall-Cooled Fixed-Bed Reactor for CO2 Methanation, Chemical Engineering & Technology, 42 (2019) 2401-2409.

[4] N. Engelbrecht, S. Chiuta, R.C. Everson, H.W.J.P. Neomagus, D.G. Bessarabov, Experimentation and CFD modelling of a microchannel reactor for carbon dioxide methanation, Chemical Engineering Journal, 313 (2017) 847-857.

[5] F. Kosaka, T. Yamaguchi, Y. Ando, T. Mochizuki, H. Takagi, K. Matsuoka, Y. Fujishiro, K. Kuramoto, Effect of Ni content on CO2 methanation performance with tubular-structured Ni-YSZ catalysts and optimization of catalytic activity for temperature management in the reactor, International Journal of Hydrogen Energy, 45 (2020) 12911-12920.